2023

Data Collection in Two-Tier IoT Networks with Radio Frequency (RF) Energy Harvesting Devices and Tags

Muchen Jiang

Data Collection in Two-Tier IoT Networks with Radio Frequency (RF) Energy Harvesting Devices and Tags

A thesis submitted in partial fulfilment of the requirements for the award of the degree

Doctor of Philosophy

from

UNIVERSITY OF WOLLONGONG

by

Muchen Jiang

Bachelor of Degree (Computer Engineering)

School of Electrical, Computer and Telecommunications Engineering

February 2023

Statement of Originality

I, Muchen Jiang, declare that this thesis, submitted in partial fulfilment of the requirements for the award of Doctor of Philosophy, in the School of Electrical, Computer and Telecommunications Engineering, University of Wollongong, is wholly my own work unless otherwise referenced or acknowledged. The document has not been submitted for qualifications at any other academic institutions.

Signed

Muchen Jiang

February 04, 2023

Abstract

The Internet of things (IoT) is expected to connect physical objects and end-users using technologies such as wireless sensor networks and radio frequency identification (RFID). In addition, it will employ a wireless multi-hop backhaul to transfer data collected by a myriad of devices to users or applications such as digital twins operating in a Metaverse. A critical issue is that the number of packets collected and transferred to the Internet is bounded by limited network resources such as bandwidth and energy. In this respect, IoT networks have adopted technologies such as time division multiple access (TDMA), signal interference cancellation (SIC) and multiple-input multiple-output (MIMO) in order to increase network capacity. Another fundamental issue is energy. To this end, researchers have exploited radio frequency (RF) energy-harvesting technologies to prolong the lifetime of energy-constrained sensors and smart devices. Specifically, devices with RF energy harvesting capabilities can rely on ambient RF sources such as access points, television towers, and base stations. Further, an operator may deploy dedicated power beacons that serve as RF-energy sources. Apart from that, in order to reduce energy consumption, devices can adopt ambient backscattering communication technologies. Advantageously, backscattering allows devices to communicate using negligible amount of energy by modulating ambient RF signals.

To address the aforementioned issues, this thesis first considers data collection in a two-tier MIMO ambient RF energy-harvesting network. The first tier consists

of routers with MIMO capability and a set of source-destination pairs/flows. The second tier consists of energy harvesting devices that rely on RF transmissions from routers for energy supply. The problem is to determine a minimum-length TDMA link schedule that satisfies the traffic demand of source-destination pairs and energy demand of energy harvesting devices. It formulates the problem as a linear program (LP), and outlines a heuristic to construct transmission sets that are then used by the said LP. In addition, it outlines a new routing metric that considers the energy demand of energy harvesting devices to cope with routing requirements of IoT networks. The simulation results show that the proposed algorithm on average achieves 31.25% shorter schedules as compared to competing schemes. In addition, the said routing metric results in link schedules that are at most 24.75% longer than those computed by the LP.

This thesis then considers ambient backscattering tags. Specifically, it considers a two tier IoT network where its first tier is a multi-hop wireless backhaul and its second tier contains a multi-hop ambient backscattering communication network. Both tiers have a set of flows. The *goal* is to maximize the total flow rate in both tiers. The main problem is to jointly determine the data rate at each source router and tag, a TDMA-based schedule for RF links and backscattering links, the amount of traffic routed over each link, and the transmit power/backscattering coefficient at each router/tag. This thesis formulates the problem as a mixed-integer linear program (MILP). It then outlines a heuristic to construct transmission sets for both RF links and backscattering links as well as to optimize the transmit power of router and tags. For large scale IoT networks, it outlines a novel heuristic that jointly optimizes scheduling and routing in the said two-tier network. The simulation results show that the proposed link scheduler results in network throughput that is on average 29.80% higher as compared to competing link scheduling methods that do not consider backscattering. In addition, the proposed heuristic leads to network throughput that is on average 21.36% lower than the throughput computed by MILP.

Lastly, this thesis considers a power beacon that uses RF to charge devices on

a multi-hop path to a sink. The problem is to optimize the total transmit power of the power beacon. A challenging aspect is that the power beacon has imperfect CSI. Further, it must ensure samples arrive at the sink by a deadline with a given probability. To this end, this thesis formulates a chance-constrained stochastic model to optimize the charging policy of the power beacon. It also contains two novel practical algorithms that can be used to approximate the optimal charging policy that meets the said probabilistic deadline requirement. The simulation results show that the performance of S-POPA and BO-POPA is on average 86.91% and 79.25% of the transmit power computed by Sample Average Approximation (SAA).

Acknowledgments

First and foremost, I would like to thank my supervisor, Associate Professor Kwan-wu Chin. My largest honor and luck is to meet him as an undergraduate and a candidate for PhD. I am very grateful that he has been willing to guide me all the way. His generous guidance, kind encouragement, profound knowledge, and rigorous research attitude have all promoted and motivated my PhD studies. In any situation, including during COVID-19, he has done many things to guide me, facilitate me, and help me improve my work. Without his help, I would not be able to finish the current research work and can not grow as an independent researcher. He is a role model as an excellent researcher, a responsible supervisor, and also a close friend. I will never forget the experience studying under him. My largest respect for him will last all my future work and study life.

Second, I also thank my co-supervisor, Associate Professor Raad Raad, for his help and contributions.

Third, I also have special thanks to Dr SieTeng Soh, for his serious review and useful comments of my research works.

During my PhD years at University of Wollongong, I have met many good seniors and friends. We have fun together in our free time, and they help me through the negative moments in my life. In addition, they also provide instructions when I meet problems during research. To this end, special thanks to my best friends Dr Tengjiao He, Dr Changlin Yang, Dr Ying Liu, Dr Yishun Wang, Dr Tianle Liu, Dr

Honglin Ren, and Dr Hang Yu. Thanks to my close friend, Longji Zhang, who I have spent the longest time together in Wollongong.

Lastly, I would like to thank my parents and my wife, Ms. Xueqi Yang, for their love, support, and encouragement. They bring me happiness and will always be my most solid backers.

Contents

List of Figures

List of Tables

Abbreviations

AoI	Age of Information
AP	Access Point
BO	Bayesian Optimization
BER	Bit Error Rate
BTTN	Backscattering Tag-to-Tag Network
CDF	Cumulative Distribution Function
CSI	Channel State Information
CSMA/CA	Carrier-Sense Multiple Access with Collision Avoidance
DoF	Degree of Freedom
EH	Energy Harvesting
FM	Frequency Modulation
FS	Frequency-Shift
HAP	Hybrid Access Point
HTT	Harvest-Then-Transmit
IoT	Internet of Things
MDP	Markov Decision Process
MILP	Mixed Integer Linear Programming
MIMO	Multiple-Input Multiple-Output
MAC	Medium Access Control
LP	Linear Programming

QoS	Quality of Service
RF	Radio-Frequency
RFID	Radio-Frequency Identification
SAA	Sample Average Approximation
SIC	Successive Interference Cancellation
SISO	Single-Input Single-Output
SNR	Signal to Noise Ratio
SINR	Signal to Interference plus Noise Ratio
SWIPT	Simultaneous Wireless Information and Energy Transfer
TDMA	Time-Division Multiple Access
TV	Television
OFDM	Orthogonal Frequency Division Multiplexing
PB	Power Beacon
PSK	Phase-Shift Keying
PMF	Probability Mass Function
WSN	Wireless Sensor Network
WPCN	Wireless Power Communication Network
WPT	Wireless Power Transfer

Chapter 1

Introduction

1.1 Background

The Internet of things (IoT) provides a communication channel to a myriad of "things", such as physical objects instrumented with a transceiver, one or more sensors or/and actuators [1]. Further, IoT facilitates cooperative operation and management of "things" by leveraging their information sharing and communication capabilities to provide high-quality services to users. Consequently, IoT networks have a broad range of applications; see Table 1.1 for details. For example, in [2], a smart home application allows users to remotely monitor and control lights, smart furniture and a security system via a smartphone. Further, IoT networks will play a key role in the upcoming Metaverse [3], whereby heterogeneous IoT devices collect and update digital twins that model physical objects or processes.

Figure 1.1 shows a three-layer IoT architecture [13] that consists of a perception, network and application layer. The perception layer consists of devices that transmit samples to access points. Further, these devices may receive control messages from access points to affect an environment. The network layer helps with the exchange of information between devices in the perception layer and the application layer via communication technologies such as Wi-Fi [14], Bluetooth [15], Zigbee [15] and WiMAX [16] to name a few. Moreover, access points or routers may form a multi-

Field	IoT applications
Smart home	Environment monitoring, IoT devices operation control, and security systems control [2].
	Energy management and electrical loads control in smart homes [4].
Smart city	Real-time traffic monitoring and tracking systems [5].
	Low-cost purchasing and product delivery systems [6].
	Real-time smart parking systems that find open parking spaces for drivers in a short time [7].
Smart agriculture	Remote controlled robot systems to perform agriculture tasks such as spraying and crop protection [8].
	Cloud computing and wireless sensor networks to monitor agriculture-related data, e.g., temperature and humidity[9].
Healthcare	Low-power and low-latency healthcare monitoring and alarm systems, e.g., cloud services assisted wearable sensor platforms [10].
Industrial	Air, soil, water, plant and animal monitoring systems [11].
	Food safety monitoring and quality control systems, which allows users to access food supply chains, freshness, and logistics information[12].

Table 1.1: Examples of IoT networks and applications.

hop wireless backhaul to help relay samples generated by devices. The application layer visualizes and processes data from devices, provides inference services, and may sell collected data [17]. It also provides an interface between IoT applications and users.

Data collection is a major function of IoT networks. To do so, an IoT network can employ one or both of the following wireless network architectures: *single-hop* or/and *multi-hop* [18]. In *single-hop* IoT networks, a device communicates directly with a sink/gateway. However, a limitation of *single-hop* communications is that devices far from a sink may require a high transmit power [19]. By contrast, in a *multi-hop* wireless IoT network, devices are interconnected, meaning each device can help route data from devices to a sink [20]. Advantageously, a *multi-hop* wireless network provides better connectivity and coverage. In addition, devices are able to reduce their transmit power and have a high data rate.

Interference is a major factor that limits capacity as well as the amount of data collected in a multi-hop wireless network. Devices in a multi-hop network may interfere with each other because they share limited wireless channel resources. Interference degrades channel quality. As a result, a high interference level can cause

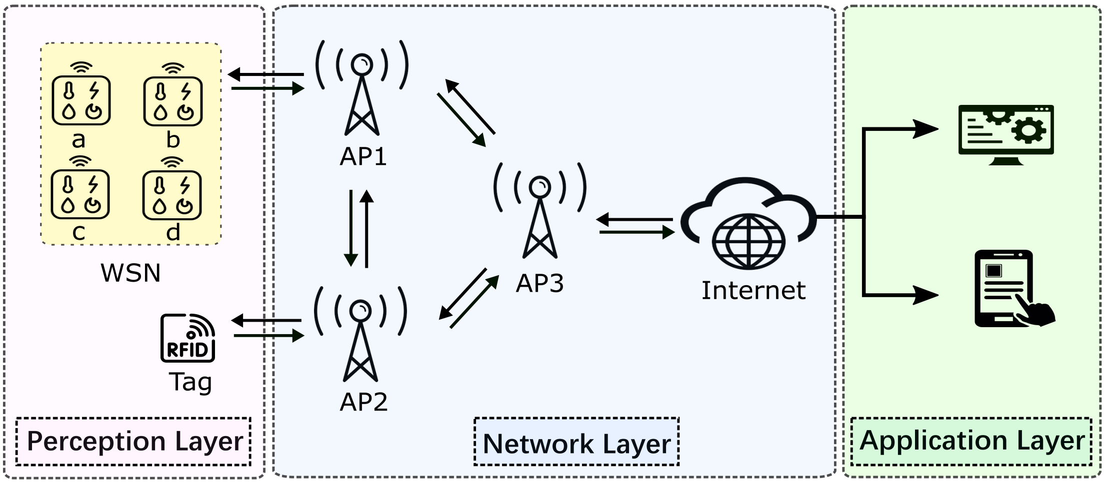

Figure 1.1: An example three-layer IoT architecture. Sensors a, b, c, and d form a wireless sensor network (WSN); see yellow box. Each arrow denotes a direct link between two devices. In the network layer, access points (APs) form a wireless multi-hop backhaul to relay data from IoT devices to the Internet.

packet loss. Further, it reduces capacity as per the Shannon-Hartley theorem [21], which relates the theoretical capacity of a channel to the signal-to-interference-radio (SINR) at a receiver. To this end, a key research direction is to design physical and channel access technologies that embrace interference such as successive interference cancellation [22]. Another direction is the development of link schedulers that aim to derive a time division multiple access (TDMA) schedule that minimizes interference as well as ensure high network capacity [23].

Limited energy resource is another critical challenge that impacts data collection [24]. This is because IoT devices powered by batteries have a limited operation time, i.e., a device that transmits frequently will experience an energy outage quickly. In multi-hop networks, devices that are close to a sink or connected with multiple other devices may transmit more frequently to help relay data packets to a sink. As a result, a multi-hop network may be disconnected once these devices experience an energy shortfall [24]. To this end, many prior works focus on energy-aware routing [25] and transmit power control schemes [26]. Their goal is to balance the energy utilization of devices in order to maximize network lifetime. Of interest in this thesis is wireless power transfer (WPT) technologies [27] and ambient backscattering [28].

These technologies are elaborated in the following sections.

1.1.1 Wireless Power Transfer

Wireless power transfer (WPT) technologies allow an energy source to deliver energy to a device via an electric field, magnetic field, or electromagnetic radiation [27]. The energy transfer range of WPT can be classified into near-field and far-field [27].

Near-field WPT techniques include inductive, magnetic, resonant, and capacitive coupling. Their most significant feature is that they provide efficient transfer of power in the kilowatts range [29]. Thus near-field WPT techniques are suitable for charging electric vehicles [30]. Near-field WPT, however, suffers from severe energy attenuation and has a short energy transfer distance, e.g., from millimeters to several centimeters [31]. In addition, near-field WPT technologies require alignment of transmission and reception coils [32]. To this end, there are works that aim to improve charging efficiency via coils alignment, e.g., [33]. However, a disadvantage is a charger cannot track and serve multiple harvesters simultaneously.

Far-field WPT exploits electromagnetic radiation, i.e., RF signals, which operate in frequencies ranging from 3 kHz to 30 GHz. Compared with near-field techniques, far-field WPT technologies promise a longer energy transfer distance, e.g., from meters to several kilometers [31]. Advantageously, far-field WPT technologies do not require alignment between energy charger and energy harvester. Further, a charger can serve multiple harvesters simultaneously. However, compared with near-field WPT, far-field WPT circuits achieve a lower energy conversion efficiency and limited output power [34], which mainly depend on the received power strength at a harvester. For example, for the harvester in [35] and input power -20 dBm, its energy conversion efficiency reaches only 18.2%. To this end, far-field techniques are suitable for charging low-power sensor networks.

RF energy harvesting/charging technologies can be classified into ambient and dedicated charging [36]. Ambient RF energy charging allows IoT devices to obtain energy from existing RF sources, e.g., television signals, Wi-Fi signals (2.4 GHz/5 GHz), and GSM signals (900 - 950 MHz). As a downside, the energy delivered by an ambient RF source is unpredictable and uncontrollable. Hence, dedicated RF chargers are useful as devices can request energy whenever they experience an energy shortfall. However, employing dedicated RF chargers incur additional infrastructure costs. To date, existing works have focused on antenna circuits design [37], waveform design [38] and beamforing [39] technologies in order to improve energy transfer efficiency. Another direction focuses on technologies that improve the spectrum efficiency of dedicated RF-charging systems, e.g., simultaneous wireless information and power transfer (SWIPT) [40].

1.1.2 Backscatter communication systems

Backscatter communication systems play a significant role in ultra-low-power IoT networks; see reference [28] and therein. A backscatter transceiver/tag harvests and reflects external RF signals from transmitters. For example, a tag absorbs or reflects an RF signal to represent bits in a two-state modulation mechanism [41]. This means backscatter tags do not need an RF chain for transmission. As a result, they consume orders of magnitude less power than devices with a conventional RF radio. For example, tags that are equipped with a Wi-Fi backscatter transmit with power as low as 1 μW [28]. The downside is that they have a low data rate and limited transmission range, see Table 1.2.

Backscatter communication systems can be classified into three categories based on their architectures, e.g., monostatic, bistatic, and ambient backscatter communication systems; as shown in Figure 1.2. Monostatic backscatter systems are similar to conventional RFID systems, whereby a reader emits an RF carrier to activate backscatter and collects data simultaneously. This, however, causes self-interference at the reader's end. In addition, radio signals experience attenuation twice, i.e., from a reader to a backscatter and from a backscatter to a reader, which leads

Prototype	Frequency	Max Data Rate (range)	Consumption
Wi-Fi Backscatter [42]	2.4 GHz	1 kbps (2.1 meter)	$\leq 1\ \mu$W
BackFi [43]	2.4 GHz	1/5 Mbps (5/1 meter)	N/A
Frequency-shift backscatter [44]	2.4 GHz	48.7 kbps (4.8 meter)	45 μW
Television backscatter [45]	536-542 MHz	10 kbps (2.5 meter)	0.79 μW
Phase-shift keying backscatter [46]	539 MHz	20 kbps (0.75 meter)	N/A
LoRa Backscatter [47]	900 MHz	37.5 kbps (2.8 km)	9.25 μW
Frequency-Modulation backscatter [48]	98.5 MHz	2.5 kbps (5 meter)	1.4 μJ/bit
Backscattering tag-to-tag network [49]	915 MHz	5 kbps (3 meter)	260 μW

Table 1.2: Example backscatter prototypes and their performance.

to significant loss and causes the doubly near-far problem [28]. Consequently, a backscatterer must be deployed near a reader in monostatic backscatter systems. This means monostatic backscatter systems have a limited communication range.

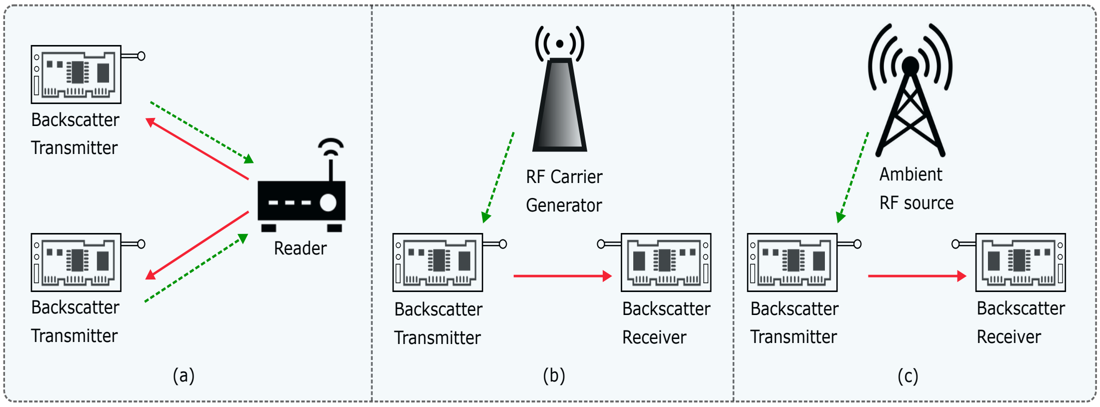

Figure 1.2: Example backscatter communication systems: (a) monostatic, (b) bistatic and (c) ambient. The green and red arrow denote the RF carrier signal and backscattered signal, respectively.

In bistatic backscatter communication systems, RF sources and backscatter receivers are physically separately. This avoids self-interference at a reader. In addition, compared with monostatic systems, bistatic backscatter communication systems achieve a longer transmission range as one or multiple RF sources can be placed near to tags [50]. However, a disadvantage of bistatic backscatter communication systems is they require more infrastructure costs.

Ambient backscatter communication systems allow tags to exploit existing modulated RF signals from television towers, Wi-Fi access points, and cellular base stations; see Table 1.2. To this end, ambient backscatter communication systems do not require dedicated RF sources, thereby reducing infrastructure costs. In addition, they have a higher spectrum utilization efficiency as compared to bistatic backscatter communication systems [51]. However, ambient RF signals generated by access points or television towers may interfere with backscatter signals. In particular, the signal strength of RF signals is usually much higher than that of a backscattered signal at a backscatter receiver. To this end, many works have focused on physical layer solutions, e.g., frequency-shift [44], multi-phase transmitter [49], and modulation schemes [46], to enable a backscatter receiver to decode backscattered signals in the presence of external modulated RF signals. Another issue is that ambient RF sources are unpredictable and uncontrollable, which may result in a short transmission range and limited amount of generated data.

Recently, researchers have shown the possibility of tag-to-tag backscatter communications. It differs from the above backscatter communication technologies because it does not require a dedicated reader for data collection. In addition, a multi-hop tag-to-tag communication system achieves wider coverage than monostatic and bistatic backscatter technologies. A major application of a tag-to-tag backscatter system is to overcome interruption of data collection due to energy outages. As demonstrated in [52], multi-hop tag-to-tag communication can assist in relaying data when devices do not have sufficient energy to emit an RF signal. Existing works have also investigated centralized or distributed multi-access control protocols [53], resource allocation methods [52], and routing protocols [54] to maximize the throughput of multi-hop tag-to-tag systems.

1.2 Research Statement

This thesis focuses on data collection in a two-tier IoT network. An example is shown in Figure 1.3, which consists of routers at Tier-1 and devices/tags at Tier-2. The first tier is a multi-hop wireless backhaul that consists of routers powered by the grid, i.e., routers have an unlimited power supply. Routers are responsible for forwarding data packets from source to destination routers or a sink. In addition, routers can collect data packets from devices located in the second tier. Specifically, the second tier consists of an RF energy-harvesting network and an ambient backscatter communication network. Energy-harvesting devices are powered by ambient or dedicated RF signals from routers. They use a *harvest-then-transmit* protocol; they first harvest energy from routers, then transmit data packets if they have a sufficient energy. In other words, they have an energy requirement for data transmission. In addition, they are able to perform multi-hop communications; see path $e - f - g$. Tier-2 also consists of tags that use multi-hop tag-to-tag communications. There is a flow from tag a to tag d, which is routed over path $a - b - c - d$. They are battery-free and can be activated only when their neighboring routers, e.g., router A and C, are transmitting.

Given the above IoT network, this thesis aims to investigate the following research questions:

- *How to jointly optimize energy provision and device activation in a two-tier multi-hop IoT network for data collection?* This question relates to the development of algorithms that ensure ambient RF energy-harvesting devices and ambient backscatter tags have sufficient energy for data transmissions. A challenge is that devices transmit data via multi-hop communications, meaning a sink can collect from a source device only when *all* devices on a path have sufficient energy. To this end, a major problem is to meet the energy demand of devices. Another problem is to schedule the transmission of devices according to their energy arrival and channel conditions. Specifically, devices

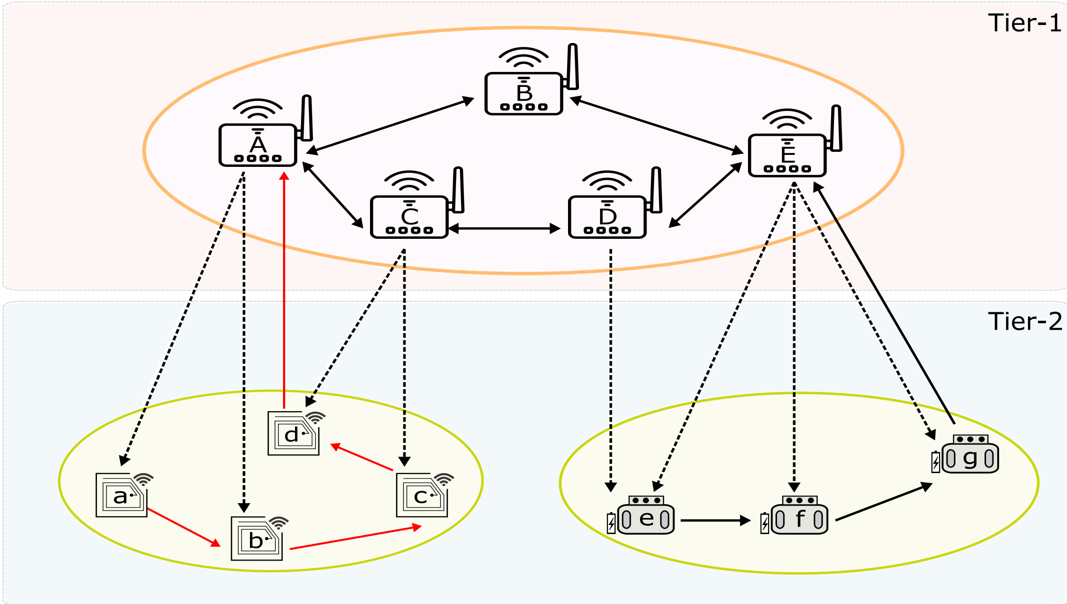

Figure 1.3: An example IoT network. Router A, B, C, D, E form a multi-hop wireless backhaul network. Ambient tag a, b, c, d form a backscattering communication network. IoT device e, f, g form an energy-harvesting network. Each solid and dotted arrow represent a direct data link and an ambient energy link, respectively. Each red arrow represents a backscattering link.

with high energy arrivals can be allocated more transmission opportunities. Alternatively, devices can wait for a good channel. However, this may cause high transmission latencies. Alternatively, they can transmit as soon as they can. This, however, may require a high transmit power.

- *How to optimize routing and antenna power allocation of routers in a two-tier multiple-input multiple-output (MIMO) network for both data transmission and energy harvesting?* Routing affects data transmissions and energy delivery to devices. Specifically, routing has an impact on the traffic load of links. The traffic load over each link will determine how often a link is activated, which in turn determines the energy arrivals at devices located in the second tier of the network. For example, referring to Figure 1.3, assume router A aims to transmit to router E, and there are two available paths: $A-B-E$ and $A-C-D-E$. Router A can route all traffic over the shorter path. However, devices d, c, and e will experience an energy shortage due to the lack of RF sources. Antenna allocation in a MIMO system is another challenge. Specifically, routers with MIMO will have diversity gain, whereby each transmit antenna has a random channel gain towards each receive antenna. This means a random antenna allocation may cause low SINR at routers and low harvestable energy at devices. To this end, routers must decide their antenna power allocation to maximize energy transfer efficiency and the number of concurrent links.

- *How to construct a link schedule for both RF links and backscatter links in a two-tier ambient backscattering network?* The major challenge is that the length of a link schedule is limited by interference. In addition, link scheduling is a classic NP-hard problem [55]. Deriving the optimal link schedule requires an exhaustive collection of transmission sets; each transmission set includes a group of transmitting links. This is challenging because the number of transmission sets grows exponentially with the network scale. For example, there are ten links in Tier-1 of Figure 1.3. This can result in $2^{10} - 1$ possible transmission sets. Another challenge is that the active time of backscattering links is closely associated with the transmission time of their neighboring routers. For example, referring to Figure 1.3, a sink can collect more data from tags when routers A and C are given more transmission opportunities. In addition, tags also need to share channel resources and avoid interference. To this end, a major problem is to jointly determine the active time of RF links and backscattering links in order to maximize network throughput.

- *How to efficiently deliver energy to devices for multi-hop data collection with imperfect CSI?* A router is able to power *all* energy harvesting devices with switch-beam antennas; see Figure 1.4. The goal is to minimize the energy consumption of a transmitting router and ensure energy-harvesting devices can forward a sample to a sink by a deadline with a given probability. The key problem is to decide the switched-beam pattern used by a transmitting router in each time frame. The major challenge is imperfect CSI knowledge for RF-charging. This means a transmitting router cannot decide its switched-beam pattern based on channel power gains and the amount of harvested energy at devices. Another challenge is that the required energy to transmit a sample also varies with random channel gains in each frame. As shown in Figure 1.3, the sample is forwarded in a multi-hop manner, i.e., over path $e - f - g$, meaning an energy shortage at any node will result in a sample delivery failure.

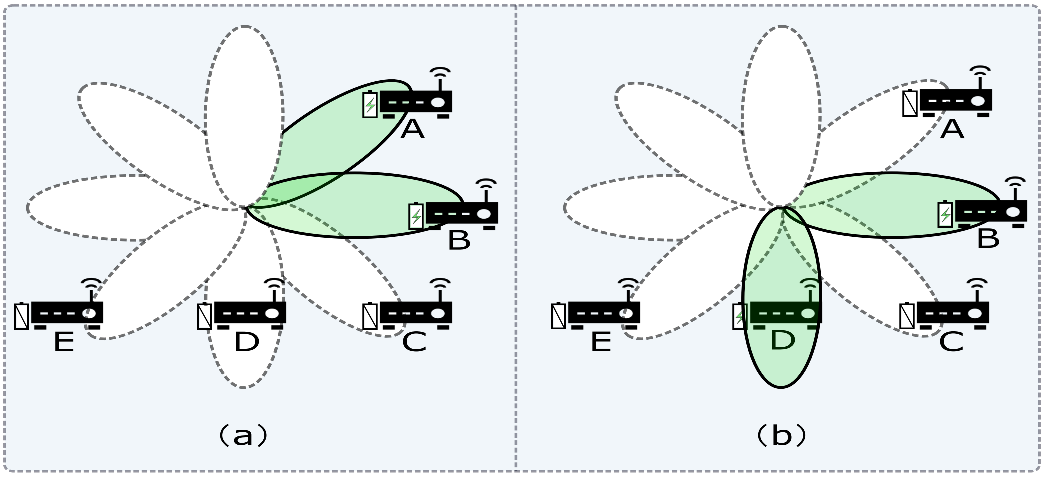

Figure 1.4: Example switched-beam antenna patterns for RF-charging. There are five energy-harvesting devices, namely A, B, C, D, E, in pattern (a) and (b). The selected single-lobes are colored by green and form a beam pattern. Note that beam pattern (a) only allows device A and B to harvest energy and device B and D are able to harvest energy in pattern (b).

1.3 Contributions

This thesis aims to jointly optimize energy delivery and device activation in a two-tier multi-hop IoT network for data collection. It presents solutions to the following problems: (i) joint routing, link scheduling, and antenna power allocation in a two-tier MIMO RF energy-harvesting network, (ii) joint routing, link scheduling, transmit power/backscattering coefficient control in a two-tier IoT network with ambient backscattering tags, and (iii) transmit power control of a power beacon that is used to charge energy-harvesting devices efficiently with imperfect CSI. Figure 1.5 illustrates the connection among these topics.

1.3.1 Joint link scheduling and routing in two-tier RF energy-harvesting IoT Networks

This thesis first aims to answer the first and second research questions. It considers a two-tier ambient RF energy-harvesting IoT network. The first tier is a multi-hop wireless backhaul network that consists of routers with MIMO capability. The *goal* is to derive the minimum-length link schedule and routing policy to meet a given traffic and energy demand of routers and energy harvesting devices, respectively. Specifically, the problem is to determine the active time of each link, the antenna power allocation of routers, and the amount of traffic routed over each link.

The major challenge is that link scheduling is NP-hard. The second challenge is to optimize antenna power allocation of routers with MIMO capability to maximize network capacity and energy transfer efficiency. The third challenge is that routing must ensure routers transmit sufficiently frequently to deliver energy to devices located at Tier-2 of the network.

To achieve the said goal, this thesis first outlines a linear program (LP) that jointly optimizes the active time of transmission sets and also the routing of each session. As link scheduling is NP-hard, it presents a novel heuristic called Transmission Set Generator (TSG) to generate transmission sets for use by the LP. In addition to considering the SINR of links, it also maximizes *both* the number of links and energy delivered to energy-harvesting nodes. Lastly, it outlines a novel routing metric that quantifies the number of energy-harvesting nodes that are charged on a given path. Advantageously, this metric can then be used by the well-known Dijkstra's algorithm [56] to select a path for each session.

1.3.2 Maximizing flow rates in multi-hop two-tier IoT networks with ambient backscattering tags

The second major work considers a two-tier IoT network with routers and ambient backscattering tags. Specifically, the first tier has a set of flows/source-destination pairs. The second tier consists of ambient tags that rely only on the RF signals emitted by routers for backscattering. In addition, tags are equipped with a frequency-shift transmitter, which allows tags to shift the backscattered signal to an adjacent channel of incident RF signal from routers. The *goal* is to derive the optimal TDMA link schedule and routing policy to maximize the sum throughput of both tiers over a given time duration. The major challenge is that the optimal link schedule must consider the active time of both RF links and backscattering links.

To achieve the said goal, this thesis presents a mixed integer linear program (MILP) to jointly optimize the active time of RF links, the active time of backscattering links, and multi-hop routing. Next, it outlines a novel heuristic called Algorithm Transmission Set Generator (ALGO-TSG) that constructs a set of transmission sets for active RF links and backscattering links. ALGO-TSG aims to maximize the number of concurrent links and activates additional *power* links to assist backscatter communications. The transmission sets generated by ALGO-TSG are used by MILP to derive a final schedule that maximizes network throughput at both tiers. Lastly, it outlines a novel heuristic called Centralized Max-Flow (CMF), which jointly considers scheduling and routing in a two-tier network. It aims to maximize flow rates at both tiers by determining: (i) the transmission set activated in each time slot, (ii) a path used by each session, and (iii) flow rates.

1.3.3 Optimizing sample delivery in RF-charging multi-hop IoT networks

The third work considers a power beacon that is deployed to deliver RF energy to devices on a multi-hop path. A source device generates a sample and other devices on the path help forward the sample to the sink. In this setup, the main aim is to ensure a sample arrives at the sink by a deadline with a given probability. To do so, the power beacon must supply sufficient energy to all devices. However, a key challenge is that the power beacon has imperfect CSI knowledge of channel gains and energy level at devices. The problem at hand is to minimize the power beacon's transmit power when charging devices. A key constraint is that samples must arrive at the sink by a given deadline with a given probability.

To address the said problem, this thesis formulates a chance-constrained stochastic program to determine the transmit power allocation of the power beacon. This program is then solved using the sample average approximation (SAA) method [57]. In addition, this thesis contains two algorithms named sampling based probabilistic optimal power allocation (S-POPA) and Bayesian Optimization based probabilistic optimal power allocation (BO-POPA) to approximate the optimal solution for our problem. Briefly, S-POPA generates a set of candidate solutions and iteratively learns the solution that returns a high probability of success. On the other hand, BO-POPA applies the Bayesian Optimization framework to construct a surrogate model to predict the reward value of each transmit power allocation.

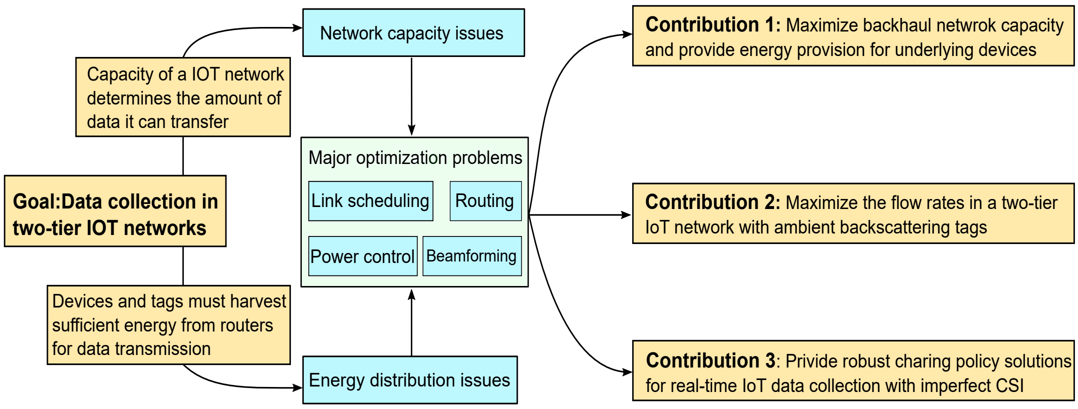

Figure 1.5: Connections among the topics and contributions in this thesis.

1.4 Publications

The research carried out in this thesis has appeared or submitted to the following venues:

1. **M. Jiang**, K-W Chin, T He, S. Soh, L. Wang, *Joint Link Scheduling and Routing in Two-Tier RF-Energy-Harvesting IoT Networks*, in IEEE Internet of Things Journal, vol.9, no. 1, pp. 800-812, Jan. 2022.

2. **M. Jiang**, K-W Chin, S. Soh, *Maximizing Flow Rates in Multi-hop Two-Tier IoT Networks With Ambient Backscattering Tags*, in IEEE Internet of Things Journal, vol.9, no. 24, pp. 24628 - 24642, Dec. 2022.

3. **M. Jiang**, K-W Chin, *Optimizing Sample Delivery in RF-Charging Multi-Hop IoT Networks*, in IEEE Transactions on Green Communications and Networking, 2023. *Under major revision.*

1.5 Thesis Structure

1. *Chapter 2.* This chapter provides a comprehensive literature review of existing works on resource allocation, routing and scheduling works in RF energy-harvesting networks and backscattering networks. It also discusses multi-hop packet delivery with timeliness or energy harvesting requirement. It also highlight the novelties of this thesis.

2. *Chapter 3.* This chapter answers the first and second research questions. It outlines an LP for a joint routing and link scheduling problem in a two-tier RF energy harvesting MIMO network. It also outlines a heuristic to generate transmission sets for the LP, and proposes a new metric to compute paths for routers to charge energy harvesting devices.

3. *Chapter 4.* This chapter answers the first and third research questions. It outlines a MILP. In addition, it also proposes a heuristic to generate RF trans-

mission sets and backscattering sets in order to maximize network capacity. Lastly, it outlines a heuristic to jointly compute a link scheduling and a single path for each flow.

4. *Chapter 5.* This chapter answers the first and the last research questions. It presents a chance-constrained stochastic program to cope with the uncertainty in imperfect CSI in a real-time packet delivery system. It approximates the optimal solution by using the SAA method and two novel proposed sampling methods.

5. *Chapter 6.* This chapter concludes this thesis and outlines future works.

Chapter 2

Literature Review

This chapter first discusses resource allocation in multi-user RF energy-harvesting networks, including works that consider one or more hybrid access points or power beacons, multi-hop RF energy-harvesting networks, and cognitive radio RF energy-harvesting networks. Next, it focuses on link scheduling with routing works that consider SISO, MIMO, and RF energy-harvesting networks. Thirdly, ambient backscatter networks, backscatter-aided WPCNs, and a novel passive tag-to-tag network are highlighted. Fourth, it reviews packet delivery strategies in real-time multi-hop networks that consider information freshness and timeliness metrics under uncertainty. Lastly, it provides an analysis of prior works and highlights the novelties of this thesis.

2.1 Multi-user RF energy-harvesting networks

This section presents multi-user RF energy powered networks. These works focus on optimizing energy utilization, whereby their major aims are divided into two general categories: (i) maximize sum-throughput subject to energy constraints, or achieve throughput fairness among energy-constrained users, and (ii) minimize the energy consumption of RF sources subject to certain quality of service (QoS) demands at rechargeable users, or achieve a fair energy distribution among users. The following

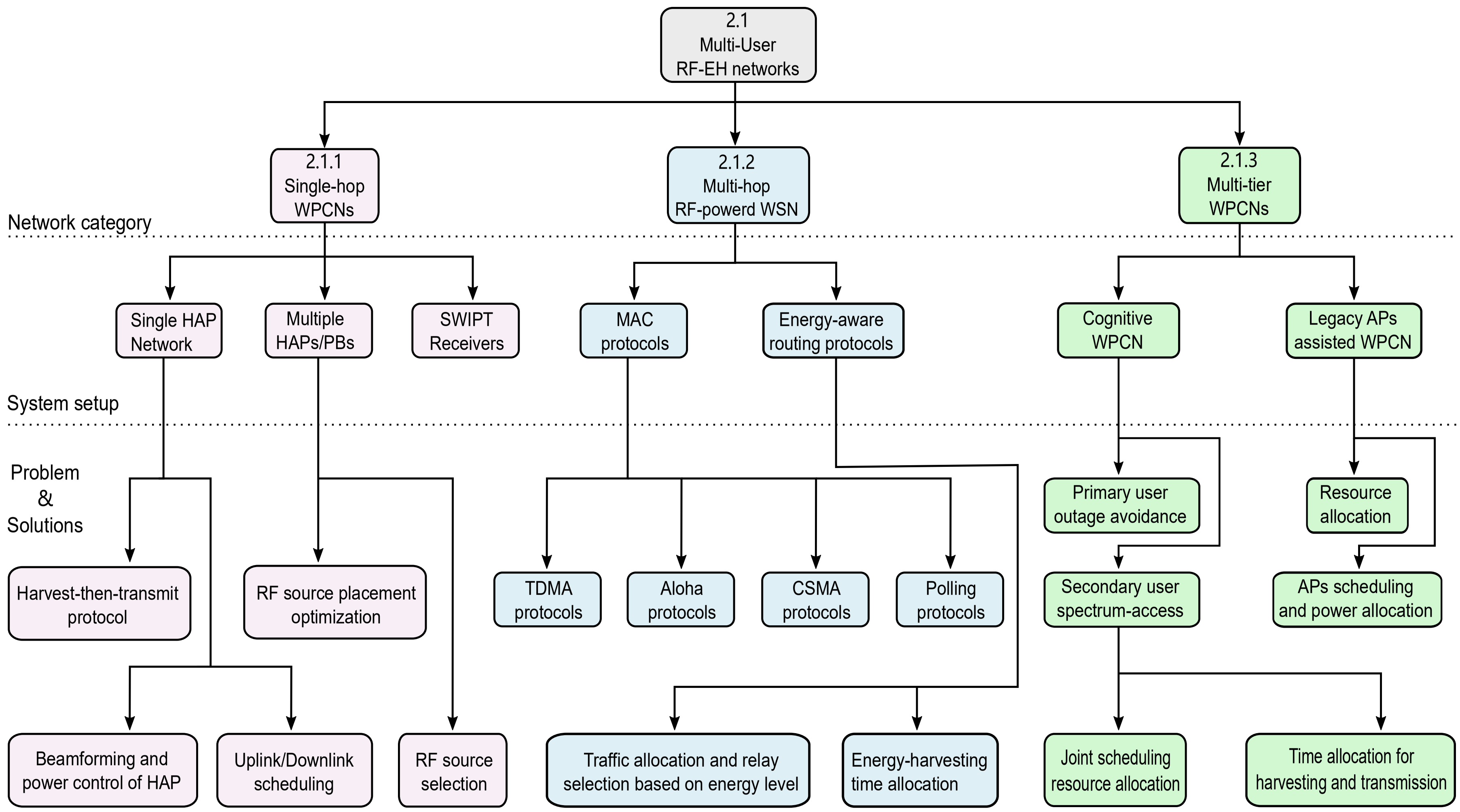

Figure 2.1: Taxonomy of prior works that consider multi-user RF energy-harvesting networks.

sections discuss three categories of works based on their network: (i) single-hop RF energy-harvesting networks, (ii) RF energy powered wireless sensor networks (WSNs), and (iii) multi-layer RF energy-harvesting networks.

2.1.1 Single-hop RF energy-harvesting networks

This section presents research into *single-hop* wireless energy and information transfer. This section first discusses a simple network where a hybrid access point (HAP) broadcasts energy signals to charge all energy-harvesting users, and collects data from all users via *single-hop* transmissions [58, 59]. However, the amount of harvested energy and the transmit power of users for data transmissions are highly dependent on the distance to the HAP. This means users that are far away from the HAP harvest less RF energy, and have to transmit to the HAP with a high power to overcome significant path loss. This phenomenon is known as the doubly-near far problem. To this end, this section next focuses on works that aim to improve *single-hop* energy transfer efficiency by adopting multiple HAPs [60–63] or beamforming [64–68]. The focus is to optimize the placement or beamforming vectors of HAP(s). Lastly, this section reviews works that consider simultaneous wireless information and energy transfer (SWIPT) systems with *single-hop* communications [69–71]. The main focus is to optimize a so-called power-splitting ratio and a time-switching ratio to maximize energy utilization.

Prior works that study single-hop RF energy-harvesting networks where a HAP charges all energy-harvesting devices aim to maximize network throughput. Typically, a HAP has a constant power supply, e.g., from power grids, and serves as a dedicated RF source. Users leverage their harvested energy to power their circuits. There are two types of links: (i) downlink, which is used for charging devices by the HAP, and (ii) data uplinks from users. The example work in [58] considers a half-duplex HAP, and proposes a harvest-then-transmit protocol to schedule both wireless energy transfer and information transmission. Briefly, all users first simultaneously harvest energy in a charge slot. Next, each user transmits to the HAP using time-division multiple-access (TDMA). Advantageously, each user only transmits in an assigned data slot to avoid any redundant energy consumption due to collisions. In [59], the authors extend the said RF energy-harvesting network with a full-duplex HAP. A full-duplex HAP broadcasts downlinks and receives uplinks at the same time. Advantageously, users are able to continuously harvest energy until it transmits in an assigned slot. This promises a higher amount of harvested energy for users and thus supports a higher data rate. The authors consider a weighted throughput maximization problem in two scenarios, i.e., the HAP has either perfect or imperfect self-interference cancellation. The problem is to jointly optimize the transmit time of energy transfers and uplink transmissions.

There are also works that consider the use of multiple omni-directional HAPs or PBs to overcome the doubly-near far problem. The focus is to determine the number of HAPs or PBs and their placement in order to maximize energy transfer efficiency and achieve fairness in energy distribution. An example work in [60] aims to minimize the number of PBs subject to a given number of users with given energy demand. The location of energy-harvesting users is also given. Users transmit data packets to APs. The authors consider two network scenarios. In the first scenario, APs have a fixed location. The authors proposed a greedy algorithm to iteratively deploy PBs and determine their location. In the second scenario, the problem is to jointly optimize the location of each PB and each AP. In [61], the authors investigate a trade-off between the maximum energy harvested by users and the fairness of distributed energy among users. The goal is to maximize a utility value that is jointly determined by the sum harvested energy of users and the minimum harvestable energy among users. In a different work [62], the authors consider a network where users harvest energy from both a HAP and multiple PBs. Three energy-harvesting modes are considered: (i) users only harvest energy from the HAP, (ii) users harvest energy from all PBs until they transmit, and, (iii) each user only requests energy from the nearest PB. The authors aim to optimize the location of a given number of PBs to minimize the SNR outage probability of users. In [63], the authors consider the PB deployment problem under imperfect CSI. In addition, the PB does not know the location of nodes. The goal is to minimize the number of PBs while ensuring energy outage occurs within a given probability.

Another key issue is to use beamforming to overcome path loss. The goal is to maximize energy-harvesting efficiency or maximize the sum network throughput by optimizing the beamforming vector at HAP. In their systems, a multi-antenna HAP is responsible for charging all users and collecting data from them. Under static channel state information, the HAP decides the optimal beamforming pattern that allows the transmit signal from multiple antennas to constructively combine at users and maximize the amount of harvestable energy. Advantageously, the HAP is able to focus its energy on users that experience an energy shortage thereby preventing network outages. There are works that consider to charge a single user at a time with beamforming. An example is [64], where users contend to request energy or transmit data from/to the HAP based on CSMA/CA. Each user maintains a probability of sending an RTS frame to request energy from the HAP, whereby the probability is inversely proportional to its residual energy level. The goal is to minimize throughput degradation due to energy requests. In a different work [65], the HAP is able to charge all users in an energy-harvesting phase. Next, users transmit to the HAP via space-division-multiple-access in a data transmission phase. The authors present a mathematical program to jointly optimize the beamforming vectors, the duration of the energy-harvesting phase and transmission phase, and the transmit power at users. As the problem is proven to be non-convex, the authors present a two-step solution. In the first step, they determine the transmit and receive beamforming vectors and the transmit power allocation among users under a given charging and transmission schedule. In the second step, they compute the optimal duration of charging and transmission by an exhaustive search in order to maximize the minimum throughput among users.

Prior works such as [64, 65] assume the CSI knowledge is perfectly known at the HAP. In practice, HAPs are not able to operate by using perfect CSI knowledge due to many factors, such as channel estimation error, feedback error, and delay. To this end, there are a number of works that focus on beamforming design to provide robust transmissions over imperfect CSI. The main consideration is to avoid network outages or allow network outages to occur only within a given probability. There are works that consider stochastic models to characterize imperfect CSI, whereby CSI errors are modeled as a zero-mean Gaussian variable with a given variance. Their aim is to maximize network throughput in the presence of channel estimation error. Example works include [66] and [67]. In [66], the CSI information for both charging and collecting data is imperfect at the HAP. In each time slot, users are assigned into two groups based on their operation: only transmit data to the HAP or only harvest energy from the HAP. They formulate a non-convex program to jointly optimize the transmit and receive beamforming vector of the HAP, grouping strategy and transmit power of users, and convert the problem to an equivalent weighted minimum-mean-square error minimization problem. In [67], the objective is to maximize the sum throughput at users, whereby the SNR of each user must meet a threshold value at a given probability. The authors present a chance-constrained program that jointly optimizes the beamforming vector and the transmission time of users. In a different work [68], the authors use a deterministic model to characterize imperfect CSI. Specifically, the authors give the worst-case channel realization instead of a distribution of channels. To this end, they focus on avoiding network outages for the worst channel realization. The authors consider a HAP that uses imperfect CSI knowledge to transmit data to an information receiver and transfer energy to an energy receiver. The objective is to maximize the energy harvested by the energy receiver. In addition, the data rate at the information receiver must exceed a threshold for any channel condition. The problem is to optimize the beamforming vector of the HAP. The problem cannot be directly solved as it requires all possible CSI realizations. To this end, the authors capture the optimal solution by reformulating the problem as a semidefinite program.

Works that study resource allocation in SWIPT systems aim to balance the information rate and the harvestable energy at users. Typically, SWIPT consists of two architectures, namely time-switching and power-splitting receivers. Time-switching receivers dedicate time to harvest energy as well as communication. The fraction of time between energy harvesting and information decoding over a given period of time is adjusted by a time-switching ratio. Alternatively, receivers can split a received signal to decode information and harvest energy. The amount of power dedicated for each part is determined by a power-splitting ratio. In [69], the authors study the achievable rate-energy region for time-switching receivers and power-splitting receivers in different network settings, respectively.

Reference [70, 71] considers optimizing the time-switching ratio and power-splitting ratio at receivers. In [70], each user decides its power-splitting ratio. In addition, each user maintains a minimum harvested energy threshold and a minimum SINR threshold. The aim is to minimize the transmit power at a HAP subject to a given energy and SINR requirement of users. The work in [71] studies SWIPT in a multi-user orthogonal frequency division multiplexing (OFDM) system. Users employ TDMA or OFDM. Specifically, time-switching receivers use TDMA, and those that use power-splitting employ OFDM. The aim is to maximize the sum-throughput subject to the energy demand of users.

2.1.2 RF powered WSNs

This section presents RF energy powered WSNs. Of interest are works on designing energy-efficient MAC protocols [72–75]. The objective of these works is to maximize the throughput of rechargeable users and maximize their harvested energy. Different from conventional MAC protocols, these energy-efficient MAC protocols consider metrics such as energy arrivals and energy level at devices. In WSNs, employing relays shortens transmission distances, which helps to improve energy efficiency and overcome the doubly near-far problem. To this end, there are many works that consider a RF energy powered WSN with multi-hop communications [76–83], whereby some works also consider routing protocol, beamforming, MIMO, and SWIPT. The major objectives of these works are to maximize network throughput or minimize energy consumption subject to QoS demands.

Example works such as [72–75] study the design of medium access control (MAC) protocol for RF powered WSNs. The work in [72] considers a WSN where sensors are powered by one or multiple PBs. The authors present a CSMA/CA-based MAC protocol to maximize the average harvested energy by users. The protocol jointly controls (i) the transmission schedule of PBs and their transmit power, (ii) the charging time of users, and (iii) the priority of nodes to transmit data and request energy. A major challenge is that the RF signals from multiple power beacons can combine destructively at some users due to phase cancellation, thereby degrading the energy harvested by these users. To this end, PBs are assigned into two groups upon receiving an energy request from a user, whereby PBs in different groups transmit at a different center frequency.

Many works consider energy-harvesting in slotted Aloha-based networks [73, 74]. In [73], Moradian et al. designed a slotted Aloha-based MAC protocol to maximize throughput. Energy arrives randomly at a node. Energy-harvesting nodes transmit data by choosing a random waiting time in a contention window. The problem is to optimize the energy arrival rate and contention window size to avoid collision and maximize throughput. In [74], the authors propose a distributed harvest-until-access protocol based on slotted Aloha. This work aims to maximize network capacity without knowledge of full channel state information. A HAP charges all users and collects data from users. They focus on determining the optimal number of random access slots in each frame. In each frame, users randomly select a slot to access the channel, continuously harvest energy until they are allowed to access the channel. The energy-harvesting time of nodes depends on when these nodes start to transmit data. To avoid collisions, at any random access slot, only one wireless device transmits data to a hybrid access point while other wireless devices continuously harvest energy from a hybrid access point.

The work in [75] presents a probabilistic polling-based MAC for multi-hop RF powered WSNs. The goal is to maximize network throughput. There are a set of rechargeable users. Users continuously harvest ambient RF sources and have random energy arrivals. Each active sensor first waits for a random time to access channel, and transmits a poll packet to request data from other active users. Upon receiving a poll packet, an active user transmits its data packet according to a probability, whereby the probability is inversely proportional to the estimated number of neighboring active users. Users store received data packets and transmit in response to poll packets.

The work in [76, 77] studies multi-hop WSNs powered by ambient RF sources. The goal is to design energy-aware routing schemes for WSNs. In [76], the authors present a distributed energy-harvesting-aware routing algorithm (EHARA) to jointly manage the energy-harvesting time of users and a path used for each source-destination pair. In terms of routing, the authors define a new metric to calculate the cost of each link, where it takes both the energy level of the transmitter and receiver on the link and their spatial distance into consideration. EHARA ensures nodes with a high energy level are used for routing. The work in [77] outlines a routing protocol named energy-harvesting Aware Ad hoc On-Demand Distance Vector (AODV-EHA). It aims to minimize the total transmission cost for routing; the transmission cost of a node is defined by the energy it uses for data transmission minus its harvested energy.

Works that studied multi-hop WSNs powered by dedicated RF sources include [78–80]. Their aim is to improve network throughput. The main focus is to study the optimal charging policy in order to satisfy the energy demand of energy-harvesting devices. An example work is [78], where relays first broadcast RF energy signals to charge energy-harvesting users. After that, they collect data from users and forward data to a sink. The author aims to maximize network throughput by jointly optimizing the transmit power at each relay and user. The work in [79] considers a two-hop

WSN that consists of a source node, a relay, and a sink. The sink harvests energy from the relay and decodes information via SWIPT. The authors aim to jointly optimize the transmit power and relay placement to minimize a given data rate outage probability. In [80], the authors consider a two-hop network. Relays harvest energy from the HAP and operate in two modes, namely, amplify-and-forward and decode-and-forward. The authors aim to maximize the sum throughput by determining the optimal transmission time of relays. Next, the authors present algorithms when relays operate in amplify-and-forward and decode-and-forward mode, respectively.

A major direction is to adopt energy beamforming technology in RF-powered multi-hop WSNs to improve energy transfer efficiency. Some works consider a HAP/power beacon with multiple antennas to charge sensors with beamforming. The major problem is to determine the beamforming pattern and charging time of the HAP. Example works include [81] and [82]. In [81], a HAP uses beamforming and focuses its beam on one user at a time. Each user is able to transmit to the HAP via one-hop or two-hops. In addition, the authors prove that users have a higher throughput and energy efficiency under TDMA. In [82], the authors consider a WSN that consists of multiple sensors, PBs, and a sink. PBs use beamforming to charge sensors and each sensor transmits to the sink via multi-hops. The authors aim to maximize the minimum data rate among users by jointly optimizing the data rate and routing of users, beamforming vectors of PBs and their charging time. The challenge is the data rate and route for sensors are dependent on their energy level. The authors first present a centralized algorithm given by a set of pre-defined beamforming vectors, then outline a distributed algorithm for large-scale networks. There are also works that consider joint energy sharing and energy beamforming problems in multi-hop RF-powered WSNs. An example work is [83]. Relays are equipped with multiple antennas and have SWIPT capability. Hence, each relay only harvests energy upon receiving the RF signal transmitted by a neighboring relay. The authors consider beamforming optimization in a power-splitting case and a time-switching case. For both cases, the authors optimize the beamforming vector at relays to maximize the data rate subject to energy storage and transmit power constraints.

2.1.3 Multi-layer RF energy-harvesting networks

This section presents works that consider multi-layer RF energy-harvesting networks. In multi-layer RF energy-harvesting networks, rechargeable users harvest energy directly from devices in an existing network rather than from dedicated HAPs or PBs. Multi-layer RF energy-harvesting networks enable spectrum reuse, which advantageously ensures efficient energy and spectrum utilization. This section considers two categories of multi-layer RF energy-harvesting networks: (i) cognitive wireless powered communication networks [84–90], and (ii) WSNs powered by co-operative APs [91–93].

Past works aim to maximize the sum throughput of secondary users, while protecting the transmissions of primary users in cognitive wireless powered communication networks [84–90]. A typical cognitive wireless powered communication network consists of a primary network and an underlying energy-constrained secondary network. The transmissions in the primary network power a set of underlying secondary users, e.g., a WSN. Primary users share the spectrum with secondary users, meaning secondary users access the channel opportunistically as the transmission of a secondary user may interfere with primary users. The main problems relate to (i) channel access for secondary users [84–86], which determines the time and spectrum used by users for channel access, and (ii) determining forwarding path(s) for each source-destination pair, and the data rate of relays, e.g., [87–90].

References [84–86] study channel access in cognitive wireless powered communication networks. In [84], the secondary network consists of a HAP and multiple secondary users. Secondary users harvest RF energy from the HAP and primary transmitter, and send data packets to the HAP. Secondary users access the channel via TDMA. The authors consider two spectrum sharing models. Their main difference lies in whether the HAP has the CSI from the primary transmitter to the primary receiver and to the HAP. The authors jointly optimize the time allocation for energy-harvesting and information transmission, and the transmit power of each secondary user. In [85], the authors extend the system in [84] with MIMO, i.e., secondary users have multiple antennas. The goal is to maximize the sum throughput of secondary users by optimizing the beamforming vector at the HAP, and the time allocation for energy-harvesting and information transmission. In a different work, the authors of [86] study a dynamic spectrum access problem. Primary users operate on orthogonal channels. In each time slot, a secondary user accesses a channel licensed to a primary user and switches between energy harvesting and data transmission. Specifically, the secondary user sends data only when the primary user is idle. The authors aim to maximize the long-term throughput by optimizing the channel selection policy of the secondary user.

The following works consider cognitive wireless powered communication networks with relays. The work of [87] and [88] studies a relay selection problem, where the secondary network is a multi-hop WSN. In [87], secondary users are provided with a set of orthogonal channels. To improve spectrum utility, secondary users are also able to sense idle channels licensed to primary users. The authors aim to maximize the spectrum utilization subject to an SINR requirement of primary users. To this end, the authors propose algorithms to sequentially compute the shortest path for a flow, the transmit power of users over the path, and the channel allocation of users. In another work [88], Nguyen et al. consider relay selection problems with imperfect CSI. The aim is to minimize network outage probability by jointly optimizing the time allocation for energy harvesting and transmission, the path for a flow in the secondary network, and the transmit power of relays. In addition, they present two relay selection metrics to minimize the outage probability over two consecutive hops, and minimize the end-to-end outage probability of the flow.

Many works study collaborative relaying systems in cognitive wireless powered communication networks. This means secondary users are able to help relay data from a primary transmitter to a primary receiver in order to primary network outage. The objective of these works is to maximize the secondary network throughput subject to a rate outage requirement of the primary receiver. In [89], a primary transmitter splits its transmit power into two portions. One portion is used to support its transmission, and the other portion is used to charge a secondary transmitter. The problem is to jointly optimize the beamforming vector of the secondary transmitter, and the power allocation at the primary transmitter. In [90], primary users harvest RF energy from a HAP and secondary users. The bandwidth of secondary users is split into two portions: one portion is used for cooperative data relay by primary users, and the other portion is used for secondary data transmissions. The problem is to jointly determine the time allocation of primary users that is used for energy-harvesting and data transmissions, the bandwidth allocation of secondary users, and the density of secondary users in an energy-harvesting area of primary users.

The following works consider a novel two-layer RF-EHN, where the primary layer is a set of APs or routers, and the underlying layer is a set of RF energy-harvesting devices; see [91–93]. Devices are only powered by the transmissions of APs. The focus is to schedule the RF transmissions of APs subject to the energy demands of energy-harvesting devices. For example, reference [91] considers a network that consists of multiple APs and energy-harvesting sensors. The data arrival at each AP is random. The objective is to maximize an expected reward value, whereby the reward is a function of the sum throughput of APs and sum-energy harvested at sensors. To this end, the authors of [91] formulate the problem as a Markov decision process (MDP) and optimize the transmission schedule of APs. In [92], routers operate on the same channel and need to decide their transmit power in order to avoid interference. In addition, routers are able to transmit dedicated energy links to charge energy-harvesting devices. The authors aim to derive the minimum schedule length that activates each data link once subject to the energy demands of underlying sensors. To this end, the author presents a heuristic to jointly optimize the transmission order of data links and energy links, and the transmit power of routers. In [93], the authors consider a two-tier OFDMA RF energy-harvesting network. The bandwidth is divided into multiple sub-carriers. Links over the same sub-carrier may interfere with each other. The aim is to minimize the sum transmit power of APs subject to data rate demand and energy demand at underlying users. The problem is to jointly determine the sub-carrier allocation for each AP to transmit data links and energy links, and the transmit power of each AP over each sub-carrier.

To date, numerous standards exist to help facilitate the implementation of RF-energy harvesting networks. For example, the Zigbee protocol cluster [94] specifies that battery-less devices in a wireless mesh network are able to perform ambient energy harvesting to support communications and other operations such as sensing and computing. Another industry standard concerns RF energy charging is AirFuel RF [95]. AirFuel RF provides commercial RF energy chargers and receivers, whereby a single charger is able to simultaneously charge multiple mobile energy harvesters located several meters away. In addition, it also specifies regulation for the use of RF energy harvesting technologies in terms of application scenarios, frequency bands, and human safety concerns.

2.2 Joint routing and link scheduling

This section presents works that jointly consider link scheduling and routing issues. Link scheduling is a data link layer technique that exploits spatial reuse in order to activate as many links as possible simultaneously. However, finding the optimal link schedule for a given network is an NP-hard problem [96]. To this end, many efforts have been devoted to developing efficient link scheduling algorithms. In addition, there are many works that propose cross-layer solutions that jointly consider routing and link scheduling, whereby the derived link schedule must ensure links have the capacity to route a given amount of traffic.

Next, this section categorizes cross-layer solutions based on their network architecture: (i) in single-in single-out (SISO) networks, where both transmitters and receivers are equipped with a single antenna. In addition, all transmissions operate on a single frequency band, (ii) multiple-input multiple-output (MIMO) networks, where nodes are equipped with multiple antennas. As compared with SISO networks, nodes are able to actively cancel co-channel interfering streams by consuming antenna elements, and (iii) in RF energy-harvesting networks, whereby nodes are energy-constrained and powered by ambient or dedicated RF sources.

2.2.1 Cross-layer approaches

This section divides cross-layer approaches into two categories. The works in the first category employ the protocol interference model; see in [97–102]. These works consider nodes that maintain a transmission range and an interference range. The works in the second category employ the physical interference model [96, 103–111]. A link can be activated if the SINR at its receiver meets a threshold. The remainder of this section discusses these works in detail.

In general, link scheduling works that study the protocol interference model aim to maximize network throughput [97–102]. Typically, these works construct a conflict graph based on the interference range of nodes to derive an interference-free schedule. The interference range of nodes depends on their transmit power. There are a set of works that aim to optimize STDMA links schedule for a routing strategy, which specifics paths for flows and their traffic demand. For example, reference [97] considers a wireless mesh network where routers operate on a fixed number of orthogonal channels. The problem is to jointly determine link scheduling, channel assignment, and routing. To this end, they first determine a joint channel assignment and traffic routing solution to minimize interference between nodes. Next, a link schedule is computed based on the given traffic routing. Similarly, the work in [98] considers a joint link scheduling, transmit power control, and routing prob-

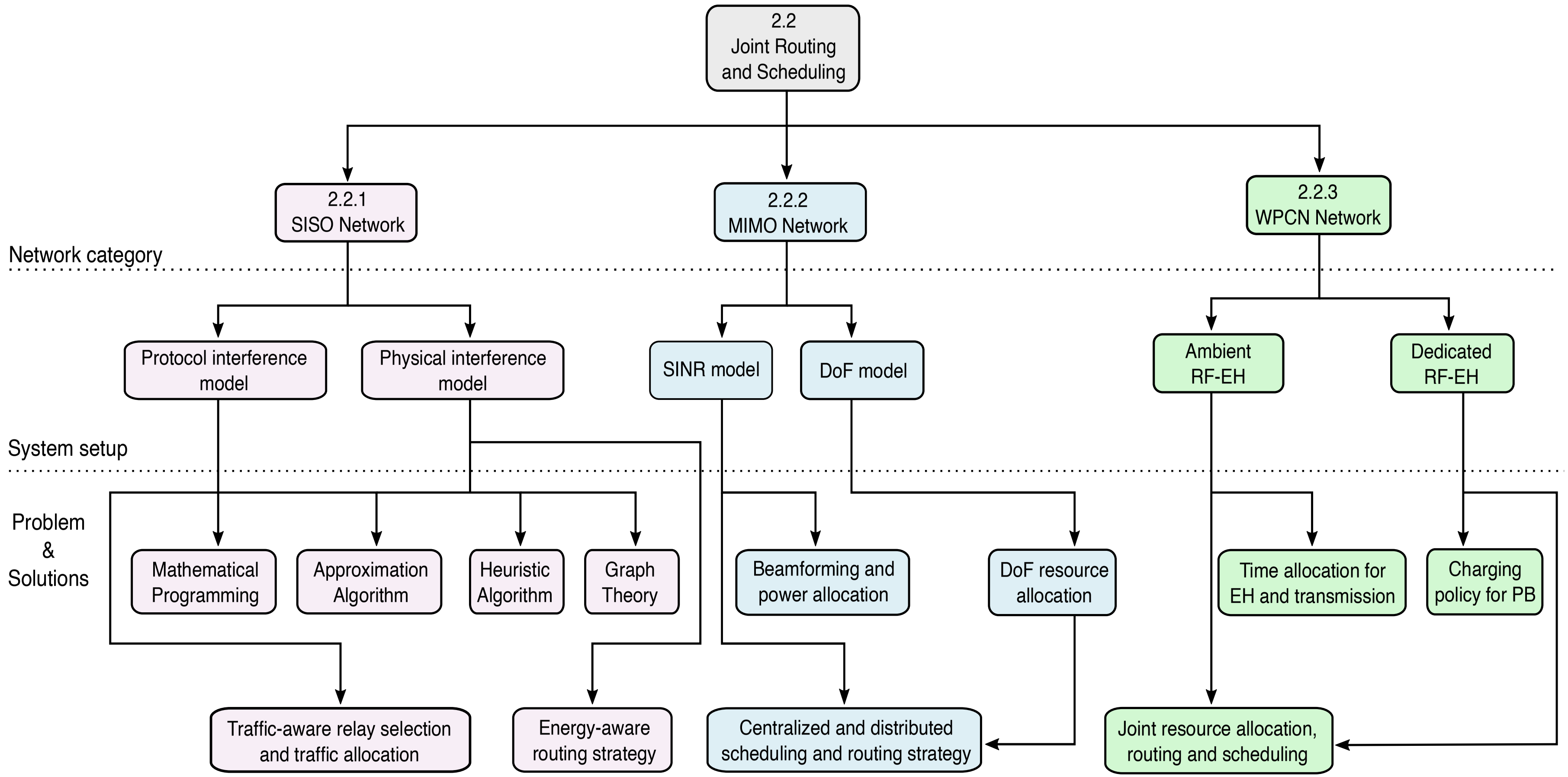

Figure 2.2: Taxonomy of joint routing and scheduling works.

lem. The throughput maximization problem is decomposed into sub-problems: the first sub-problem is to determine the traffic over each link. The second sub-problem is to determine the transmit power of nodes in order to ensure links have sufficient capacity for their routed traffic. In another work [99], the authors propose a cross-layer solution, whereby links that interfere with the least number of neighboring transmissions are first scheduled. For a given routing that specifies the amount of traffic routed over links, links carrying more traffic will be activated in multiple time slots. In [102], the authors propose a delay-aware routing and link scheduling scheme. The aim is to minimize the maximum end-to-end delay among flows subject to flow deadline. To this end, the authors propose a Lagrangian scheme, where in each iteration, it checks whether there is a feasible link schedule for a computed path.

The works that consider routing for a computed STDMA schedule aim to maximize network throughput. Specifically, these works first compute a schedule that meets a certain link QoS demand, which also reveals the capacity of links. Next, they determine the optimal traffic allocation scheme that maximizes the sum flow rate. For example, in [100], the authors study both sum-throughput maximization and throughput fairness maximization for a WSN. They propose a polynomial-time scheduling method that preferentially activates links with a small interference range. Next, the author formulates a linear program to determine the amount of traffic placed over links. In [101], Sivrikaya et al. aim to minimize the end-to-end delay from a source to a destination. The problem is to find the optimal routing for a computed STDMA schedule. To this end, the authors propose routing protocols that aim to ensure fairness in terms of data distribution over links and minimize path length. Further, they consider two cases: nodes can or cannot aggregate packets from multiple transmitters.

Another category of works aims to maximize network throughput based on the physical interference model [112]. Specifically, these works address the problem of constructing a minimum-length schedule subject to end-to-end traffic demands or maximizing the long-term flow rates over a frame with a fixed number of time slots. Many works consider constructing a non-interfering links schedule based on column generation algorithms. Specifically, a set of non-interfering links form a column/transmission set. This means the capacity of links is dependent on the activation of a set of computed transmission sets. Example works that propose a column-generation-based scheme for joint routing and scheduling problems include [96, 103–109]. In [103], the aim is to compute the minimum-length schedule subject to flow demand. The authors formulate a dual problem to minimize the schedule length. Specifically, there is a master problem that aims to determine the active time of transmission sets and the traffic routed over each link subject to a set of end-to-end traffic demands. The slave problem is to determine the activation of links to construct a new transmission set that improves the objective of the master problem. In [104], the goal is to minimize the schedule length subject to flow demand. To this end, the authors first compute a set of transmission sets and their length. The length of each transmission set is minimized subject to the data demand of all links in the transmission set. Next, the problem is to determine the activation of transmission sets to form the minimum-length link schedule. Similarly, reference [105] derives a traffic-aware link schedule by considering a dual problem. The master problem is to determine the active time of each given transmission set. The sub-problem is to generate a new transmission set. The aim is to activate links that lead to the maximum sum data rate. In [106], the problem is joint path selection and links schedule. The authors propose an algorithm to iteratively select a path for each session, and compute a link schedule given the selected paths in order to maximize the sum throughput of sessions. The work in [107] considers the joint routing and scheduling problem with dynamic routing conditions. The aim is to find a schedule that minimizes the worst-case network congestion level among all possible end-to-end traffic demand realizations. The problem is to jointly determine the amount of traffic routed over links and the active time of transmission sets.

Research into joint routing and link scheduling problems has also considered graph-theory based schemes. In some prior works, link scheduling is solved by a vertex coloring algorithm, whereby each vertex is a direct link. Two vertices are connected by an edge only if links on the vertices interfere with each other based on the physical interference model [112]. Next, the algorithm aims to minimize the number of colors used for vertices so that no two vertices connected by an edge share the same color. A transmission set includes a set of links with the same color. Consequently, a link schedule is computed by determining the activation of each transmission set in order to support the traffic of flows. An example work is [108], whereby the aim is to maximize network throughput subject to a node lifetime requirement. To this end, the authors formulate a problem to jointly determine the traffic routed over each path of each session and the active time of each transmission set. The authors in [109] consider a joint transmit power control, routing, and link scheduling problem based on vertex coloring, whereby the aim is to construct a link schedule subject to the traffic of flows. Paths are computed by a weighted Dijkstra's algorithm [56], and routers use the minimum transmit power to meet SINR in the link schedule. In [96], the authors propose an approximation algorithm to schedule links with traffic demand. The idea is first to assign links with similar SNR values into a cluster. Next, non-interfering links in a cluster are scheduled in the same time slot based on vertex coloring; the length of a time slot is depended on the traffic demand of active links. The algorithm terminates if all links are scheduled into a certain time slot.

Many works have considered energy-efficient routing over the physical interference model. In general, these works aim to minimize the sum transmit power at nodes subject to flow rate demands. For example, in [110], Cruz et al. consider a network with multiple routers and a set of links. The authors first generate transmission sets by optimizing the transmit power of routers. For each given transmission set, the goal is to minimize the sum average transmit power of nodes subject to the minimum capacity of links. Next, the authors compute a link schedule by determining the active time of each transmission set. Given the computed link schedule and the shortest path for each session, the authors optimize routing by allocating traffic routed over links. In [111], the authors propose an algorithm to jointly determine the path for a session, link scheduling and transmit power of nodes. Briefly, the algorithm first determines a path for a session, where links over the path use the minimum data rate to meet the traffic demand of a session. Next, the link scheduling problem is solved by an edge coloring algorithm, whereby each edge represents a direct link between two nodes. The goal is to minimize the number of colors used for edges so that no adjacent edges share the same color. Links that share the same color can be active at the same time.

2.2.2 MIMO Networks

This section reviews works that consider joint link scheduling and routing issues in MIMO networks. Unlike SISO networks, MIMO networks additionally concern antenna allocation at a transmitter and a receiver in order to suppress co-channel interference. In particular, antenna elements are allocated depending on the number of streams transmitted over a link as well as interfering streams from neighboring nodes. In addition, the use of antenna elements can be characterized by the degree-of-freedom (DoF) model proposed in [113]; the available DoF resource at a node is equivalent to the number of antenna elements.

This section considers two categories of works based on their antenna allocation model. For works that employ the DoF model, e.g., [114–121], the main problem is to allocate DoF resources at nodes. On the other hand, the works that do not employ DoF focus on beamforming optimization and transmit power control at nodes; e.g., [122–125].

In DoF-based MIMO works, the data rate of a link is dependent on the number of DoF resources. Specifically, both the transmitter and receiver of a link consume a DoF to transmit a data stream, where streams have an identical data rate. The sum rate of a MIMO link depends on the number of data streams received at the receiver of the link. In addition, a MIMO receiver is able to null a co-channel interfering stream for a neighboring transmitter by consuming one DoF. To this end, prior works have studied DoF allocation for spatial multiplexing and interference suppression, along with MIMO links scheduling and routing. The main aim is to maximize network sum throughput. An example work is [114], whereby the authors formulate a linear program to select a single path for each flow, and determine the DoF allocation at each node. The work in [115] extends [114] to a multi-path routing case. The aim is to minimize the TDMA schedule length subject to traffic demand. To this end, the authors jointly determine relay selection, MIMO link scheduling, and antenna allocation. In [116], the authors consider a multi-hop MIMO system with multiple nodes and gateways. Each transmitter exploits spatial multiplexing to communicate with different neighboring receivers. The goal is to derive the minimum-length schedule so that each node receives data packets from a gateway. The problem is to determine the path for each flow, activation of links, and DoF allocation for data transmission and interference cancellation. In [117], the authors consider a multi-radio MIMO network. Each node is equipped with multiple radios that operate on orthogonal channels, whereby each radio has multiple antennas. Nodes are able to simultaneously transmit to multiple receivers, where the outgoing links at a transmitter cannot exceed the number of its antennas. The aim is to minimize the schedule length subject to traffic demand of flows. The problem is to jointly optimize the link scheduling, the traffic routed over each link, the channel assignment, and the DoF allocation.

Many past DoF-based works aim to achieve rate fairness by maximizing the minimum source rate of flows; see [118–121]. Their main concern is to optimize DoF allocation for data transmission and interference cancellation, along with routing and MIMO links scheduling. In [118], the authors consider both spatial multiplexing and diversity, whereby each antenna experiences a different path loss. Consequently, streams on different spatial paths have different rates. The problem is to determine DoF allocation for both data transmission and interference cancellation based on the interference level at nodes, the path for each flow, and the activation of links. In [119], the authors propose an efficient ordering model to allocate DoF resources during interference cancellation. Specifically, nodes are arranged in an order. Each node only suppresses interference streams from/to nodes that are ordered before it. The problem is to explore the optimal DoF allocation at nodes, the ordering metric of all nodes, links scheduling, and the routes of flows. The authors propose a distributed protocol, whereby nodes are allowed to exchange their DoF allocation with their neighbors. In another work [120], the authors aim to achieve a fair rate allocation among flows. They first propose a heuristic to generate a set of transmission sets for MIMO links, whereby each transmission set also specifies the DoF allocation over links and their link rate. Next, the authors use a relaxed linear program to jointly optimize the traffic of each flow routed over each link, the source rate of each flow, and the active time of each transmission set. Reference [121] considers a multi-ratio multi-channel MIMO network, where each node has one or multiple radios that operate on orthogonal channels. The challenge is the dynamic traffic of flows. The problem is to jointly optimize the channel assignment of nodes, links activation, DOF allocation, relay selection, and traffic allocation.

The following works concern MIMO links scheduling and routing along with beamforming and antenna power allocation; see [122–125]. In this set of works, the data rate of a MIMO link depends on the actual SINR value at receivers, which is determined by a beamforming vector and MIMO channel gains matrix. They address a problem of beamforming vector and power allocation optimization at the transmitters end, in order to minimize network energy consumption or improve network throughput. For example, in [122], the authors consider a multi-hop network that consists of a set of sources and destinations. Each link has a pre-defined weight of activation. The objective is to maximize a weighted sum network throughput. To this end, the authors jointly optimize the beamforming vector of nodes, relay selection for sources, and the traffic of each flow routed over each link. The work of [123] studies resource allocation based on a column generation method. A set of pre-defined interference-free transmission sets for MIMO links are given, along with the power allocation over antennas of transmitters and the data rate of MIMO links in each transmission set. This means the transmit power at nodes and network throughput is determined by the activation and active time of transmission sets. The aim is to maximize the minimum fairness among flows, whereby the fairness of a flow refers to the ratio between the actual data rate and the rate demand on it. The problem is to jointly determine the active time of each transmission set, and the fraction of traffic of each flow routed over each link. In [124], Lin et al. propose a distributed resources allocation mechanism in multi-hop MIMO networks. The challenge is that spatial channels between transmit and receive antennas are time-varying. This means the data rate of links in each time slot depends on the beamforming vector at their transmitter and channel conditions. The aim to minimize the sum transmit power of all nodes subject to the rate demand of flows. To this end, the authors formulate a dual problem to jointly determine the beamforming vector, links scheduling, and routing. In [125], the authors consider a robust resource allocation mechanism against imperfect CSI. The authors consider an orthogonal frequency division multiplexing MIMO network. The objective is to maximize the worst case network throughput subject to flow rate demand and co-channel interference constraint. The problem is to jointly optimize the scheduling, channel assignment, and power allocation among nodes and beamforming vector at each node.

2.2.3 RF energy-harvesting networks

This section reviews works that consider joint routing and link scheduling in RF energy-harvesting networks. Unlike the works in the previous two sections, this section reviews works that consider both network capacity and energy provision requirements. Their main objectives include (i) maximizing network sum-throughput [126–129], or ensuring fair data transmissions [130–133], and, (ii) developing energy-efficient routing and links scheduling schemes [134–136].

References [126–128] aim to maximize network sum-throughput in RF energy-harvesting networks. In this set of works, devices harvest energy from ambient energy sources or dedicated power beacons that emit a signal with a fixed power level, meaning nodes experience different energy arrival. They address the problem of optimizing links scheduling, relay selection, and energy distribution at devices. For example, in [126], the authors consider a multi-hop network that has a set of rechargeable nodes and routers. Rechargeable nodes rely on data transmission among routers to replenish their battery level. To assist energy-harvesting devices, routers also use energy links to charge these nodes. Energy links carry no information and cause interference. The work in [126] aims to minimize the schedule length subject to the data demand of flows and the energy demand of rechargeable nodes. The problem is to determine the active time of each link, and the traffic of each flow routed over each link. In [127], the authors consider a network powered by a single power beacon. Links are scheduled based on the protocol interference model. In addition, each flow uses a path determined by a tree routing protocol. Nodes send data packets to a sink via multi-hop communications. The aim is to maximize a utility function, which is determined by the sum data rate of all source nodes. The problem is to jointly optimize the sampling rate of each source node and the amount of data routed over each link. In [128], multiple power beacons are used to charge an energy-harvesting multi-hop network. Nodes transmit to an access point based on an ad-hoc on-demand distance vector routing protocol [137]. The access point assigns the best path for use by each source node. The authors aim to maximize throughput subject to the rate demand of links and the lifetime demand of nodes. The problem is to jointly determine the routing of flows, data transmission, and energy-harvesting time of each node. In another work of [129], nodes harvest ambient energy and have finite energy storage. This means the consumed power of each node in a time slot cannot exceed an upper bound. In addition, each node is able to decide whether to harvest energy in each slot. The goal is to maximize the average network sum-throughput subject to limited energy arrivals at nodes. The problem is to jointly determine the transmit power allocation of nodes and links activation in each time slot and the traffic of flows placed on each link.

Works consider joint routing and link scheduling in dedicated RF energy-harvesting networks aim to maximize network throughput. The main focus is to derive the optimal charging policy to dedicate energy to devices that have data to transmit. In addition, these works also concern path selection, link scheduling, and transmit power control of nodes subject to their energy level. An example work is [130], Roh et al. consider a WSN powered by a single PB that transmits with a fixed power level. The problem is to determine the activation of links in each slot, and transmit power of nodes and relays selected by each source. Works including [131–133] further consider to improve charging efficiency by optimizing the deployment of PBs or their beamforming vectors, in order to distribute energy to nodes according to their assigned data traffic. For example, in [131], the authors consider an RF energy powered WSN, where sensors transmit data to a sink via multi-hop transmissions. The problem is to jointly determine the active time of links, the traffic of each flow routed over each link, and the deployment of PBs. There are also works that consider the use of energy-constrained power beacons. For example, in [132] and [133], power beacons are powered by solar and experience random solar energy arrival. In addition, they are equipped with multiple antennas and charge nodes via beamforming. In [132], the authors consider a non-linear energy conversion rate, whereby the harvested energy at a node depends on its incident power level. The problem is to jointly determine links scheduling, beamforming vector at PBs, transmit power of nodes, and routing. In [133], He et al. consider distributed resource allocation scheme in a cognitive wireless powered network. The secondary network consists of PBs/nodes, which are able to operate on orthogonal channels licensed to primary users. In each time slot, a PB/node only operates on one channel, thereby each node only harvests RF energy from PBs in the same channel. The problem is to jointly determine the channel assignment of PBs and nodes, the beamforming vector of PBs, the transmit power of nodes, the traffic allocated to links, and the active time of links.

The following works aim to study energy-efficient routing schemes. The main aim of these works is to minimize energy consumption subject to flow rate demand and QoS demand of users. They address problems such as charging time allocation, transmit power control, and relay selection and link scheduling. For example, in [134], the authors consider a multi-hop network where nodes are powered by a charger. The authors consider an energy-balanced routing scheme for flows. Specifically, each node selects a relay by jointly considering the energy level of the next-hop relay and the distance between nodes. The aim is to maximize the minimal residual energy among nodes. The problem is to jointly optimize the charging policy, path selection and links activation over time slots. In [135], the authors propose an energy-aware cluster-based routing scheme. They consider an RF energy-harvesting network with a set of nodes and two sinks. In addition, nodes are divided into multiple non-overlapping clusters. In each cluster, a cluster head collects data from all nodes via multi-hop transmissions, then sends the aggregated data to a sink. Each node maintains a probability to be a cluster head, which is determined by its residual energy. The problem is to jointly optimize cluster head selection, link activation in each cluster, and routing in each cluster. In another work [136], the authors propose an energy-efficient routing framework to jointly optimize network lifetime and throughput. Nodes have a fixed energy-harvesting rate. Links access channel by TDMA. The aim is to maximize network throughput while avoiding energy outages, i.e., to achieve perpetual network lifetime. The problem is to jointly determine a path for each flow, the transmission order of links and their data rate, and the transmit power of nodes.

2.3 Passive backscatter communication networks

This section presents works that consider resource allocation issues in passive backscatter communication systems. Rather than using conventional radios, a passive backscattering node relies on an external RF signal to power its circuit and transmits by reflecting incident RF signals.

Prior works can be divided into three categories according to their system. The first category of works focuses on single-hop communication systems where passive tags communicate with a reader directly. These works consider bistatic and ambient backscatter communications systems, whereby an energy source can either be an access point or a dedicated power beacon, or an ambient RF source. A disadvantage of single-hop backscatter communication systems is that they have small coverage due to the short transmission range of backscatter transceivers.

The works in the second category consider multi-hop passive tag-to-tag systems, whereby passive backscatters are able to communicate with each other when assisted by RF energy sources. Advantageously, multi-hop backscatter communication systems have better network coverage and energy efficiency than single-hop backscatter systems.

The third category concerns backscatter-assisted WPCNs. The works in this category consider hybrid devices that have both an RF signal transmitter and a passive backscatter module. Advantageously, hybrid devices are able to transmit when they harvest sufficient amount of energy, or perform passive backscatter communications, which help reduce communication cost. The remainder of this section will present resource allocation issues in backscatter communication networks in detail.

2.3.1 Single-hop passive backscatter communications

This section reviews works that consider single-hop passive backscatter communication systems in two categories: bistatic [138–140], and ambient [141–145]. Unlike conventional RFID works, readers and RF energy emitters are separated. Readers

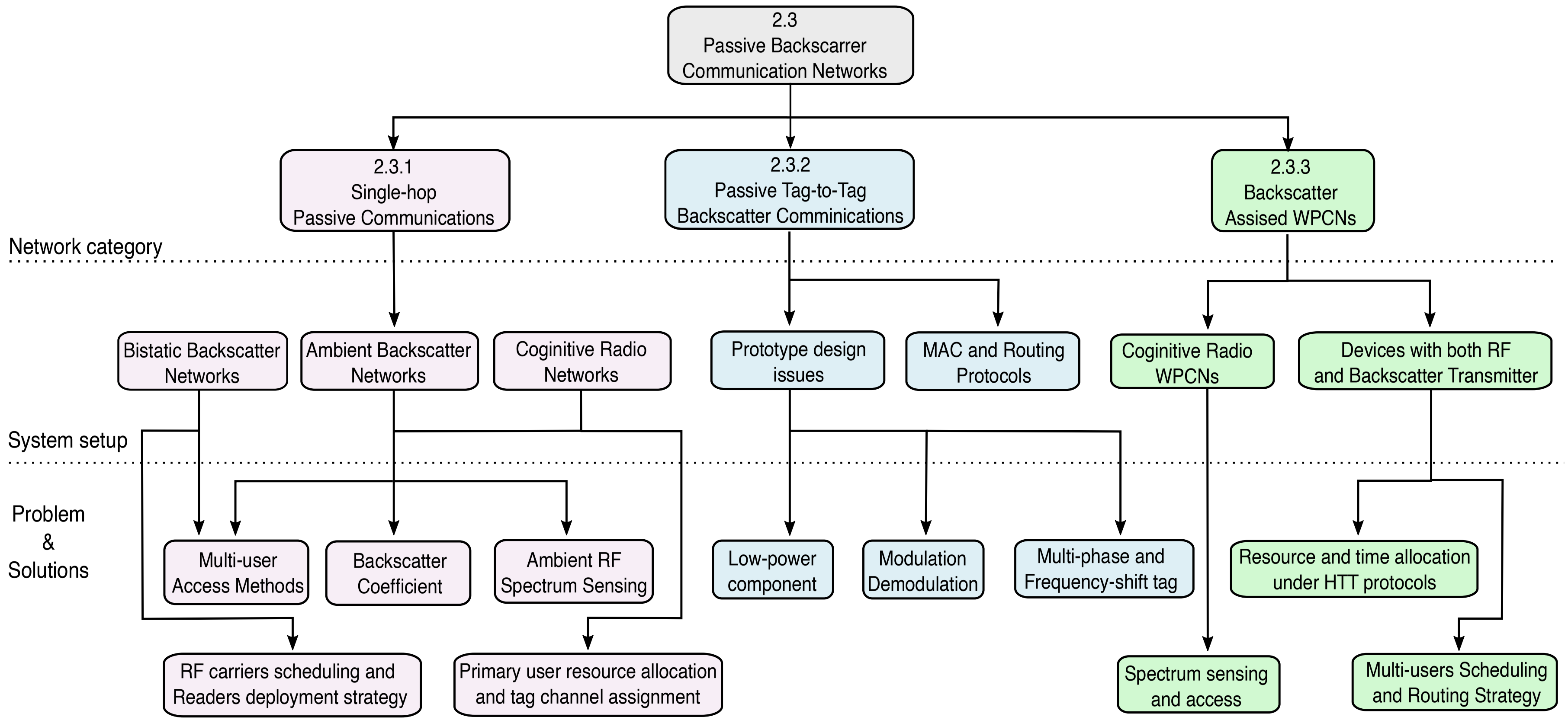

Figure 2.3: Taxonomy of prior works that consider passive backscatter communication networks.

have unlimited energy supply and collect data from tags directly. Passive backscatters/tags are battery-free and rely solely on external RF signals to backscatter their data to a reader.

The first category of works considers resource allocation problems in bistatic backscatter communication systems, whereby the aim is to improve energy efficiency or throughput. In their system, one or multiple RF sources are used to power tags. In addition, one or multiple readers collect data from tags. The main problem is to schedule backscatter communications and the transmit power of RF sources. For example, the work in [138] jointly determines the transmit power of an RF source, and the backscatter coefficient of tags. The authors of [138] further consider imperfect CSI and network outage requirement.

Prior works that consider multiple RF emitters and readers in bistatic communication systems aim to improve network throughput and energy efficiency. Unlike works with a single reader, tags are able to communicate with and harvest energy from a nearby reader. Further, these works address the doubly near-far problem [58]. The main focus of these works is RF carriers and backscatter communications scheduling. Specifically, carrier scheduling methods aim to determine which RF emitters are active in each time so that the data demand of tags is satisfied with the maximum energy efficiency. In addition, a scheduler is used to ensure tags backscatter without interference in the presence of RF carriers. Example scheduling works include [139] and [140]. Their major aim is to maximize the energy efficiency of readers subject to the QoS demand of tags. In their system, readers are half-duplex, meaning each reader either collects data from tags or emits an RF carrier to enable backscatter communications in each time slot. To this end, these works consider an RF carrier scheduling problem to determine which readers simultaneously emit an RF carrier in each time slot in order to minimize the sum-energy consumption of readers. In addition, tags scheduling is needed to improve network throughput. For example, the work in [140] constructs a minimum-length tag schedule assuming the protocol interference model, where they also minimize the number of readers used to power tags in each time slot.

A common aim is to maximize network throughput in ambient backscatter communication systems. A major issue is spectrum sensing. In each time slot, a tag needs to first perform spectrum sensing in order to detect a strong ambient frequency signal to enable passive backscatter communications. After that, the tag carries out channel access in the presence of an ambient RF signal. The length for each time slot is usually fixed. Consequently, there is a trade-off between the duration allocated to spectrum sensing and backscattering communications, which respectively decides the number of detected RF signals and backscattering data rate. Example works that consider the said optimal time allocation include [141, 142], whereby they also optimize the power split ratio at tags. The power split ratio determines the amount of harvested energy used for spectrum sensing and backscattering communications. In addition, the work in [142] considers imperfect spectrum sensing process, meaning tags may experience energy shortage when a detected RF signal has a low power. Another issue is that tags need to perform spectrum sensing to avoid interfering with legacy RF users. This means tags only backscatter when neighboring RF users are idle. An example work is [143], where tags adopt a backoff mechanism during channel sensing.

Multi-user scheduling is a key problem in ambient backscatter communication systems. The main focus is on network throughput optimization via contention-free or contention-based protocols. Firstly, works such as [146–149] study TDMA-based multi-user scheduling algorithms for ambient backscatter communication systems. Usually, a centralized controller governs the channel access of tags. These works aim to design tag selection rules for a controller to compute a TDMA schedule in order to maximize network throughput and improve energy efficiency. For example, a scheduler activates a backscattering link with the maximum SNR [146] or best channel gain [148] in each time slot. However, these approaches result in unfair channel access among tags, i.e., only links with the best channel quality are activated. To address this problem, there are also works that study a scheduler that allows tags to backscatter opportunistically. For instance, the authors of [147] propose fairness-based schedulers. Briefly, the probability of activating a backscattering link is proportional to its SNR value. In [149], the authors use reinforcement learning to construct a TDMA schedule, whereby a tag with new data transmits at a higher probability in each time slot. There are also works that consider contention-based protocols. For example, works such as [150] and [151] respectively study Aloha-based protocol and CSMA-based protocols for multi-user access, along with channel assignment and backscatter coefficient optimization problems.

Research into passive backscatter communications has also considered cognitive radio networks. A typical system consists of one or multiple primary users, which serve as ambient RF sources for a set of underlying tags. Tags are able to transmit whenever primary users transmit. The major issue is the interference caused by secondary users at primary receivers. To this end, the research goal of these works is to enable backscatter communication systems and prevent primary users outage, i.e., to meet certain rate or SINR at primary receivers. Example works such as [144, 145] aim to maximize the throughput of a secondary network. In [144], the problem is to jointly determine the transmit power of a primary transmitter, backscattering coefficient of tags, and time allocation for each tag to backscatter. In [145], a reader performs spectrum sensing and controls channel access for all tags. The authors consider imperfect CSI between primary transmitters and tags, meaning a reader is unaware of the incident power level at a tag. To this end, they aim to maximize the average data rate by optimizing the transmission schedule of tags.

Note that a number of industry standards have been developed for passive backscattering communication systems. Existing global industry standards for passive backscattering communication systems include EPCglobal Gen2 [152] and ISO 18000-6C [153], whereby tags are able to communicate with readers over ultra-high-frequency bands via one-hop communication. These standards specify regulations for passive backscattering communication systems in terms of equipment architecture and functionality, physical layer parameters such as modulation coding schemes, and data link layer technologies such as multiple access control (MAC) protocols. Specifically, they apply slotted Aloha to avoid collisions among backscattering links.

2.3.2 Passive tag-to-tag communication systems

In passive tag-to-tag communication systems, backscatter transceivers communicate with each other. Unlike monostatic and bistatic communication systems, dedicated readers are optional. A typical tag-to-tag backscatter network consists of an RF energy source and a set of passive backscatter transceivers/tags. Passive tags have no battery or energy storage for communications. To establish communication, a transmitter tag backscatters external RF signals to a receiver tag. In practice, the incident power strength at a receiving tag must exceed a sensitivity level to enable demodulation and to meet a certain SNR demand, which has a range from -25 dBm to -5 dBm. Moreover, in multi-hop tag-to-tag communication systems, a reader serves as both an RF energy source, and a controller to coordinate the operation of tags. In addition, a reader is able to collect data from tags via either direct or multi-hop transmissions, which is a promising solution to the doubly near-far problem [58].

The next set of works consider hardware design issues [45, 49, 154, 155] and routing protocols for multi-hop tag-to-tag communication systems [53, 156–159]. Their major design goal is to reduce the energy consumption of backscatter transceivers and enable tag-to-tag communications. They consider the use of low-power consumption components. As the received power level of an external RF carrier at a receiving tag is usually much higher that of a backscattered signal, a challenge is to extract backscattered information in the presence of excitation RF signals. To this end, many works consider modulation schemes for backscatter communications. For example, in [154], tags adopt an amplitude modulation scheme. Specifically, a backscattered signal is successfully decoded only when its modulation depth meets a threshold; the modulation depth at a receiver is the ratio of two voltage levels that respectively represent two modulation states. In addition, tags are equipped with an envelope detector and analog-to-digital converter to decode backscatter signals. However, analog-to-digital demodulators consume significant amount of energy, which is not suitable for battery-free passive backscatter transceivers. To this end, there are also works further consider energy-efficient modulation and decoding methods. For example, in [45], Liu et al. avoid the use of any high-power components such as analog-to-digital modules and oscillators. In their work, receivers are equipped with an envelope detector to decode backscattered information with an averaging mechanism. The proposed averaging mechanism allows receivers to identify backscattered signals and RF signals due to the fact that their data rate are significantly different.

Another major concern is the phase cancellation problem in tag-to-tag communication systems. In practice, RF excitation signals and backscattered signals arrive at a receiver with different phases, which can combine destructively resulting in a decoding failure. Example works include [49] and [155]. In [49], the authors design a multi-phase backscatter modulator that allows transmitters to decide the phase of their backscattered signal, called a phase channel. In addition, they integrate ultra-low power consumption circuits at tags for both modulation and demodulation. Further, in [155], the authors propose a collaborative multi-phase backscatter system. Briefly, only one pair of transmit and receive tag communicate at a time. Other tags decide their phase channel and collaboratively backscatter to a transmitting tag, which aims to increase the incident power at a transmit tag. This in turn increases the backscattered signal strength at a receiving tag.

There are also works that consider multi-user access and routing protocols design for multi-hop tag-to-tag communication networks. The main focus is on the optimization of network throughput and end-to-end transmission reliability. Similar to routing in conventional networks, routing methods in tag-to-tag communication networks can either be performed in a centralized or distributed manner. In centralized routing protocols, a reader serves as a controller, whereby the reader computes the optimal path for flows. There are numerous issues when designing centralized routing protocols for tag-to-tag communications. The first issue is tag identification. To this end, a reader first queries all tags in order to check whether they have a packet to transmit. Next, the reader computes the best path for each flow. For example, in [157], a reader first runs a depth-first-search algorithm to compute all possible paths for each flow. Next, the reader selects a path that has the minimum end-to-end bit error rate. In [156], a reader computes paths that lead to the maximum network sum-throughput. The second issue is co-channel interference between tags. This means a reader needs to schedule the transmission of tags so that any interfering tags cannot backscatter simultaneously. To this end, past works have employed channel access schemes such as TDMA or STDMA under the physical interference model, see [156]. In another work [158], the authors consider a frequency shift design for multi-hop tag-to-tag communications, which allows tags to backscatter at different frequencies. The third issue is the optimization of backscatter coefficients. For example, in [156], tags have an adjustable backscattering coefficient, meaning they are able to reduce interference caused at neighboring receivers by attenuating their backscattered power.

There are a number of works that aim to develop distributed routing methods. Each tag maintains a routing table. To establish their routing table, tags need to sense neighboring tags and exchange their local information. An example work is [159], whereby the aim is to reduce the energy consumption of multi-hop tag-to-tag communications. To this end, tags preferentially route traffic over a path with the shortest distance. In another work [53], tags operate based on a continuous carrier sensing mechanism. To reduce power consumption, tags switch between listening and sleep mode periodically. Rather than adopting any specific routing protocol, a flooding-based mechanism is used to forward data.

2.3.3 Backscatter Assisted WPCNs

This section reviews works that consider backscatter assisted WPCNs. Unlike tags in previous sections, the devices in these works simultaneously backscatter and harvest energy in the presence of ambient RF signals, or actively initiate a RF transmission by exploiting their stored energy without the help of RF sources. These works consider backscatter communications in single-hop networks [160–163], relay networks [164, 165] and cognitive radio networks [166–170].

Numerous works use the harvest-then-transmit protocol in [171] to schedule active RF and passive backscatter transmissions. Briefly, a time slot consists of three sub-slots, namely energy-harvesting phase, backscattering phase and active transmission phase. In some works, energy-harvesting and backscattering phase are merged into the same sub-slot, namely two-phase harvest-then-transmit protocol [171]. In the first phase, a set of devices perform backscatter communications in the presence of RF sources while other devices harvest energy for future active transmissions. In the second phase, devices access channel to transmit. To this end, the main focus of these works is on time allocation for each phase in order to improve network performance. For example, the work in [160] and [163] considers a network with a single hybrid device, a receiver and an ambient RF source. In [160], the problem is to optimize the time allocation for each phase. Further, the authors of [160] study how a fixed and variable backscattering coefficient affects the performance of a hybrid device. However, this work assumes non-causal CSI. In practice, future CSI knowledge is not available. To this end, many works have considered causal CSI. For example, in [163], each device is unaware of its future battery level. To this end, the authors formulate a stochastic program to maximize the average long-term network throughput over a fixed number slots. The problem is to determine the operation mode selection of a hybrid device in each time slot, and time allocated to each operation mode.

Multi-user scheduling is another key issue. The main aim is to maximize the sum-throughput of a set of hybrid devices in WPCNs. These works consider the use of multiple hybrid devices that directly communicate with a hybrid access point via either active RF or passive backscatter commendations. As these works consider a harvest-then-transmit protocol, hybrid devices first backscatter and then initiate RF transmissions in each time slot. To this end, a common problem is to construct an interference-free schedule for both backscatter communications and RF transmissions. A classic multi-access control method is TDMA; see in [161]. Each device sequentially accesses the channel and operates under the harvest-then-transmit protocol [171], meaning there is no interference among each type of links. The problem is to jointly determine the time allocated for energy-harvesting, backscattering and RF transmission of each hybrid device. There are also works consider to improve network throughput by constructing a STDMA schedule. An example is [162], where Liu et al. schedule backscatter communications assuming the protocol interference model. The problem is to jointly determine sensing time, backscattering time, energy-harvesting time and RF transmission time of devices.

Past works that consider backscatter-assisted relaying in WPCNs aim to maximize end-to-end flow rates. Unlike previous backscatter-assisted WPCNs works, devices communicate via multiple hops. In addition, hybrid devices are able to route data over both passive backscattering links and active RF transmissions. Compared with conventional WPCNs, hybrid devices are able to route data when they do not have sufficient energy level to transmit RF signals. In practice, hybrid devices perform backscattering and harvesting in the same time phase. This means that the more time allocated to backscattering, the less energy is harvested for future active transmissions. To this end, these works mainly focus on developing a scheduling and routing strategy, i.e., to optimize the active time of each backscattering link and RF link, along with the amount of traffic of each flow routed over each types of link. For example, in [164] and [165], the authors consider multi-path routing, i.e., multiple hybrid devices are able to serve as relays to cooperatively forward data towards a receiver. The combination of incident RF signals and backscattered signals jointly determines the data rate of a receiver. The problem of the work [164] is to jointly optimize the traffic routed over each link, and the active time of each RF link and backscattering link, which in turn decides the data rate of each link. The same problem as [164] is considered in [165] along with the optimal charging problem. A charging policy used at each power beacon affects the available energy at each hybrid devices, which further affect the data rate of each type of links.

Some prior works consider backscatter assisted wireless powered cognitive radio networks. Unlike wireless powered cognitive radio networks, secondary users rely on active RF to backscatter their data and carry out active transmissions. In addition, secondary users adopt the harvest-then-transmit protocol [171], whereby they backscatter or harvest energy when licensed or primary users transmit, and initiate active RF transmission when channels are idle. The general research aim of these works is to maximize secondary network throughput subject to primary network outage conditions. The first set of works consider time allocation for each phase in a harvest-then-transmit protocol, along with joint RF transmissions and backscattering communications scheduling [166], or joint transmit power of primary users and backscatter coefficient of tags optimization [167].

A major issue is that channel conditions in primary and secondary networks are dynamic. In practice, future CSI knowledge is not available. However, solutions of previous works in [166] and [167] assume non-causal and complete CSI knowledge, meaning they are not practical. To this end, there are also works that study solutions based on dynamic optimization with causal CSI. Their main aim is to maximize long-term network throughput. An example work [168] considers reinforcement learning against random CSI, whereby the problem is to optimize the energy-harvesting time, backscattering time, and RF transmission time of a secondary user in each time slot. The authors of [169] address the same problem by formulating a Markov decision process (MDP) based stochastic programming.

Another issue is imperfect spectrum sensing; see in [170, 172]. As a result, backscatter communications in a secondary network can interfere with primary receivers. To this end, the authors in [170] consider an imperfect spectrum sensing process as a Stackelberg game; primary receivers tolerate a certain interference level. The aim is to maximize a utility function, which is dependent on the throughput of secondary users and interference price of primary users. The problem is to jointly optimize time allocation for each phase in the harvest-then-transmit protocol, and the interference price of primary users. Another work in [172] considers opportunistic and imperfect spectrum sensing of ambient backscatters in cognitive radio systems. The problem is to jointly optimize a detection threshold for spectrum sensing, and time allocation for each phase, subject to probabilities of spectrum sensing errors.

2.4 Real-time packet delivery

This section reviews resource allocation issues in multi-hop real-time communications. A major goal is to derive energy-efficient packet delivery policies to guarantee network performance in terms of delay and information freshness. To this end, works with real-time considerations are classified into two general categories. The first category considers delay-sensitive networks with a timeliness requirement, i.e., packets must arrive at their destination by an end-to-end deadline. A major challenge is packet delivery under dynamic network conditions. Works in the second category aim to optimize the freshness of packets characterized by an age of information (AoI) metric. Unlike delay or latency metric, AoI denotes the time elapsed at a destination since the latest update packet was generated by a source. The remainder of this section discusses these works in details.

Works that study routing issues with a hard timeliness requirement aim to minimize network power consumption. A key requirement is that the worst-case end-to-end delay is less than some threshold. In these studies, devices are usually energy-constrained, meaning relays that route more packets are likely to experience energy shortfall and cause network outage. In addition, the power consumption for a relay to transmit also varies with dynamic network conditions. Consequently, routing decisions may vary with the energy level of relays. To this end, the problem is to jointly determine one or more paths for flows and the amount of packets of each flow routed by each relay. For example, the work in [173] considers a dynamic flow rate scheduler under pre-defined paths, whereby flows with the earliest deadline are assigned a higher flow rate in each time slot. In [174], the authors propose a reinforcement learning approach based energy-efficient routing scheme against dynamic relay topology, whereby the routing decision for each time slot is based on the energy level of relays and their deadline.

Another category of works considers energy-efficient routing policies with probabilistic or soft timeliness requirements. The main aim of these works is to minimize network power consumption under dynamic network conditions. Unlike previous works that consider a hard timeliness requirement, these works assume a network is able to tolerate an end-to-end packet delivery failure within a certain probability. Many works consider distributed energy-efficient routing protocols against dynamic channel conditions. Example works include [175] and [176]. In these works, relays maintain a neighbor table, whereby the neighbor table records the estimated one-hop delay for each feasible forwarding decision. Using such a neighbor table, a routing protocol determine one or more paths that satisfy the deadline of flows with the minimum total energy consumption under certain uncertainties. Another energy-aware routing protocol is [177], whereby a source first identifies a set of paths that are able to meet a deadline with a probability, and selects a path according to a computed probability. Specifically, the probability of selecting a path is inversely proportional to the total energy consumption of relays over the path. Apart from routing protocols, there are also works on studying the trade-off between network reliability and power consumption under dynamic network environments. For example, the aim of the work in [175] and [176] is to maximize the probability of a sample being delivered by a deadline and minimize relay energy consumption. To this end, they derive the optimal routing policy based on a Markov decision process. Moreover, there are established industry standards apply to real-time data collection in IoT networks, e.g., IEEE 802.15.4 [178] and 6LoWPAN [179]. However, thses existing industry standards do not include a joint data collection solution with both network capacity and energy provision considerations.

Prior research has also consider multi-hop packet delivery policy that optimizes AoI. Specifically prior works aim to minimize the average or the maximum AoI over multiple time frames. The problem is to optimize packet delivery policy for multi-hop networks, which can include packet rate control, path selection, links scheduling and transmit power control. An example work is [180], whereby the authors aim to maximize network throughput and minimize AoI across multiple flows. They propose a linear program to determine the optimal routing and scheduling solution subject to interference and transmit power constraints. A limitation of these works is that they do not consider the energy level of relays. To this end, works such as [181, 182] consider AoI minimization in ambient energy-harvesting networks. In these works, both data packet arrivals and energy arrivals at relays are known. In addition, packet delivery decisions are subject to the energy level of relays. For example, in [181], the authors consider a two-hop ambient energy-harvesting network. The problem is to determine the transmission time of each packet at a source and a relay subject to causal energy and data constraints. Another work in [182] considers a multi-hop linear topology. The problem is to optimize links schedule and transmit power control based on both the physical and the protocol interference model. Rather than using a given packet arrival rate, the work in [183] considers multi-hop packet delivery based on the *just-in-time* policy [184], i.e., a source immediately generates a new packet whenever the current packet arrives a destination. The main problem is to optimize the beamforming weight of power beacons to charge relays that forward data. A sub-problem is to determine the route of flows.

2.5 Research gaps

In summary, this chapter has reviewed resource allocation problems in WPCNs, joint routing and scheduling problems in SISO, MIMO and RF-energy-harvesting networks. Next, it examines past works that consider resource allocation problems in passive backscatter communication networks. Lastly, it discussed real-time multi-hop packet delivery problems. The following sections outline how the works in this thesis differ from prior works.

2.5.1 Resource allocation, routing and link scheduling

The works in Section 2.1 that consider resource allocation problems in multi-user WPCNs only focus on either the MAC or network layer, meaning they do not have a cross-layer solution that addresses routing and link scheduling jointly. In addition, they aim to use one or multiple hybrid access points, power beacons or ambient RF sources to power energy-harvesting devices. This means their systems are single-tier, i.e., they do not leverage RF transmissions in an existing network to power energy-harvesting devices. Existing works such as [84–93] consider resource allocation problems in multi-tier WPCNs, e.g., time allocation, channel assignment and transmit power control. They, however, do not consider the trade-off between routing and the transmission opportunities of primary users, which affect the energy provision of energy-harvesting devices.

Table 2.1 compares prior joint routing and links scheduling problems and their system. Past research into the classic joint link scheduling and routing problem in SISO and MIMO networks does not consider energy-harvesting nodes. Thereby their solutions cannot be applied in RF-energy-harvesting networks because their solutions do not take harvestable energy and energy level of devices into consideration. Some prior works further study joint routing and scheduling in RF-energy-harvesting networks. However, they only focus on energy-aware routing or charging policy in single-tier ambient or dedicated RF-energy-harvesting networks instead of multi-tier networks. In addition, they do not consider MIMO technology.

To fill these research gaps, Chapter 3 studies joint resource allocation, routing and link scheduling in a two-tier RF-energy-harvesting MIMO network. Different to prior works, energy-harvesting devices harvest energy from RF-transmissions of routers in a MIMO network. The aim is to construct the minimum-length schedule of MIMO links, along with routing and antenna power allocation of routers in order to meet any traffic demand of flows and energy demand of energy-harvesting devices.

Reference	Power Control	EH Devices	MIMO	Energy-aware Routing	Charging	Multi-Tiers
[97, 99–102]	✗	✗	✗	✗	✗	✗
[96, 103–108]	✓	✗	✗	✗	✗	✗
[110, 111]	✓	✗	✗	✓	✗	✗
[114–121]	✗	✗	✓	✗	✗	✗
[122, 123, 125]	✓	✗	✓	✗	✗	✗
[124]	✓	✗	✓	✓	✗	✗
[126–129]	✓	✓	✗	✓	✗	✗
[130–136]	✓	✓	✓	✓	✗	✗

Table 2.1: A comparison of cross-layer joint scheduling and routing works.

2.5.2 Passive backscatter communication networks

Table 2.2 shows a comparison between prior works related to passive backscatter communications. The work in [141–145] only studies link scheduling over *single-hop* networks. Although some past works consider multi-hop tag-to-tag communication systems, they focus on hardware prototype or routing protocol design. Their systems do not involve RF transmissions.

Prior works that study backscatter-assisted WPCNs, e.g., [160–165], assume the harvest-then-transmit protocol [171]. Consequently, RF transmissions and backscattering links cannot co-exist simultaneously in their systems as they are activated in a distinct phase. Moreover, these works only consider single-tier networks, i.e., backscatter transmissions are powered by an HAP rather than data signals from an existing RF network. Hence, they do not consider RF carrier scheduling and power control for multiple RF sources/readers.

To this end, no prior work has investigated how the traffic allocated to routers and their transmissions affect the flow rates of an underlying passive multi-hop tag-to-tag network. In addition, a router that transmits at a high power can enable more passive backscatter communications at the expense of causing higher interference to neighbouring routers. Therefore, router collaboration in terms of power control and interference management is necessary. To fill these research gaps, Chapter 4 aims to construct a joint activation schedule and routing strategy for routers, along with a backscattering links schedule, in order to maximize the sum-network throughput of both router and tag tier.

Reference	Schedule	Power Control	Routing	Multiple Tier	Tag-to-Tag	Multiple Reader
[138]	✗	✓	✗	✗	✗	✗
[139, 140]	✓	✓	✗	✗	✗	✓
[141, 142]	✗	✓	✗	✗	✗	✗
[146–149]	✓	✗	✗	✗	✗	✗
[143–145]	✓	✗	✓	✓	✓	✗
[45, 53] [49, 154, 155]	✗	✗	✗	✗	✓	✗
[156–159]	✓	✓	✓	✗	✓	✗
[160–163]	✓	✓	✗	✗	✗	✗
[164, 165]	✓	✓	✓	✗	✓	✗
[166–170]	✓	✓	✗	✓	✗	✗

Table 2.2: A comparison of passive backscatter communication networks.

2.5.3 Real-time packet delivery

Existing works on real time multi-hop sample delivery consider a hard [173, 174] or soft [175–177] timeliness requirement. However, these works do not involve energy-harvesting, i.e., devices are battery-powered.

Prior works that study AoI optimization in multi-hop RF-energy-harvesting networks focus on routing. For example, the work in [180–182] considers ambient RF-energy-harvesting. They do not consider any energy allocation and charging policy to avoid energy outage at devices. Although the work in [183] studies charging policy, the authors assume causal data/energy arrival information and perfect CSI knowledge. This means their solutions do not guarantee any robustness against uncertainty in imperfect CSI.

In summary, no prior work has studied energy-efficient charging policy for a multi-hop RF-energy-harvesting network with imperfect CSI knowledge, dynamic channel conditions and probabilistic timeliness requirement; see Table 2.3. To fill these research gaps, Chapter 5 presents a charging policy with imperfect CSI for a power beacon with switched-beam antennas in order to support real-time sample delivery over energy-harvesting devices.

Reference	Uncertainty	Harvesting	Dynamic CSI	Imperfect CSI	Charging Policy
[173, 174]	✗	✗	✓	✗	✗
[175–177, 185]	✓	✗	✓	✗	✗
[180]	✗	✗	✗	✗	✗
[181, 182]	✗	✓	✗	✗	✗
[183]	✗	✓	✗	✗	✓

Table 2.3: A comparison of real-time multi-hop communication networks.

Given the aforementioned research gaps, in the following chapters, this thesis considers data collection in the following multi-hop IoT networks: (i) Chapter 3 aims to jointly optimize link scheduling and routing in a two-tier RF energy-harvesting MIMO network, (ii) Chapter 4 aims to jointly consider link scheduling and routing in a two-tier ambient backscattering communication network, and (iii) Chapter 5 aims to optimize the energy delivery policy of a power beacon that is responsible for charging devices on a multi-hop path.

Chapter 3

Data collection in a two-tier RF energy harvesting network

This chapter considers data collection in a two-tier IoT RF energy-harvesting network. It considers two types of nodes: (i) routers with MIMO capability, and (ii) RF energy-harvesting devices that rely on routers for energy. The *goal* is to determine a link schedule that satisfies the traffic and energy demand of routers and energy-harvesting devices, respectively. The problem at hand is to determine the active time of links, the amount of traffic routed over each link, and the antenna power allocation of transmitting routers. To this end, it proposes an LP to jointly derive the minimum-length schedule and routing in a centralized manner. It also outlines a heuristic link scheduler to generate a set of transmission sets along with antenna power allocation of routers. Lastly, it outlines a new routing metric for routers to maximize the amount of energy harvested by devices.

To illustrate the said research problem and its corresponding challenges, consider the example two-tier IoT network shown in Figure 3.1. All routers have two antennas. Routers B, C, and D are able to charge energy-harvesting device N whenever they transmit. There are two paths from router A to the sink. Figure 3.2 shows two example link schedules. First consider *Schedule-1*. Observe that router A is able to route its traffic over both paths. This is because all links have a transmission opportunity in *Schedule-1*. Further, notice that in slot-3, both link $(C, \star)$ and $(D, \star)$ are active, meaning both routers are able to charge energy-harvesting device N together. Now consider *Schedule-2*. We see that links (A, D) and $(D, \star)$ have not been given an opportunity to transmit. Hence, their link capacity is zero. This means router A can only route its traffic on path A–B–C–$\star$. Moreover, energy-harvesting device N is only able to harvest energy from one router. Hence, *Schedule-1* is preferred given that all links have non-zero link capacity and energy-harvesting device N receives energy from two routers. Moreover, *Schedule-1* has a high capacity as each slot has two active links.

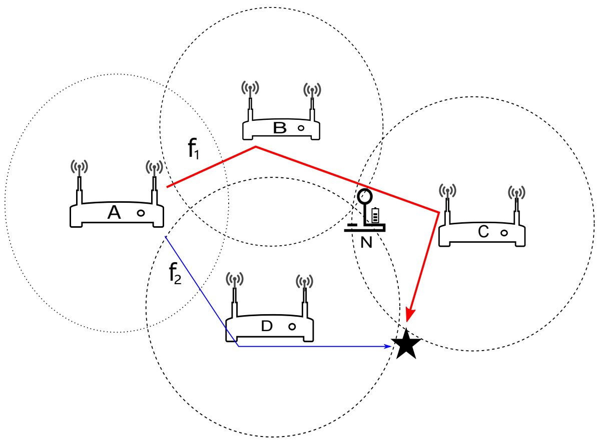

Figure 3.1: An example of a two-tier RF-energy harvesting network. Each dotted circle denotes the transmission range of a router. There are two paths, denoted as a red or blue line, from source router A to the sink $\star$.

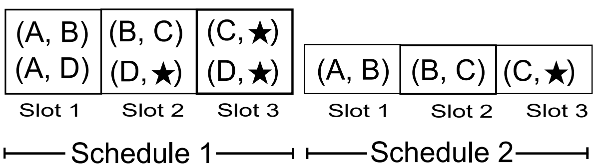

Figure 3.2: Example link schedules. Each block denotes a time slot.

In the previous example, given the respective traffic and energy demand from routers and energy-harvesting devices, the goal is to answer the following open questions:

- How does a source router forward its traffic to a destination router to ensure routers on a path have sufficient transmission opportunities to charge their energy-harvesting devices? As an example, in Figure 3.1, the amount of flow routed over f_1 and f_2 will determine how often router C and D charge energy-harvesting device N.

- How to construct a link schedule that meets the traffic demand of sources and energy requirement of energy-harvesting devices? Referring to Figure 3.1, one possible link schedule is to activate link (A, D) in Slot-t followed by link (D, $\star$) in Slot-$(t+1)$. Although this schedule affords path f_2 with a high capacity, it may not satisfy the energy requirement of energy-harvesting device N, especially if router D has a poor channel gain to energy-harvesting device N.

- When constructing a link schedule, how to optimize the transmit power of routers to meet the Signal-to-Interference-plus-Noise Ratio (SINR) requirement of links and also the energy delivered to energy-harvesting devices? A high transmit power benefits energy-harvesting devices but reduces link or network capacity, and vice-versa.

The remainder of the chapter is structured as follows. Section 3.1 and Section 3.2 formulate the system and problem, respectively. Section 3.3 presents the details of TSG, and Section 3.3.3 shows how it determines the transmit power allocation of routers. Section 3.5 presents some properties of the proposed LP and heuristic. After that, Section 3.6 presents numerical simulation results. Lastly, Section 3.7 concludes this chapter.

3.1 Preliminaries

Table 3.1 lists necessary notations. Consider a multi-hop two-tier network modeled as a directed graph $G(\mathcal{V}, \mathcal{E})$, where $\mathcal{V}$ and $\mathcal{E}$ denote the set of nodes and links, respectively. Let $\mathcal{V}_R$ and $\mathcal{V}_E$ denote the set of routers and energy-harvesting devices, respectively, where it has $\mathcal{V} = \mathcal{V}_R \cup \mathcal{V}_E$. The routers in set $\mathcal{V}_R$ are half-duplex and transmit on the same channel. Each router i has a set of antenna elements denoted by $\mathcal{K}_i$. The neighbors of router i are recorded in the set $\mathcal{R}_i = \{j \mid d_{ij} \leq r_d, j \in \mathcal{V}_R \setminus i\}$, where d_{ij} denotes the Euclidean distance between router i and j, and r_d is the communication range. Router i is able to charge energy-harvesting devices in the set $\mathcal{N}_i = \{j \mid d_{ij} \leq \bar{r}_d, j \in \mathcal{V}_E\}$; in practice, the charging range $\bar{r}_d$ is dependent on the RF input power of an RF-harvester; e.g., the harvesters reported in [186] have a received sensitivity range of -14 to -22 dBm. Let $\mathcal{F} = \{(s,t) \mid s,t \in \mathcal{V}_R, s \neq t\}$ be a set of sessions with source s and destination t. Its traffic demand is $\hat{D}_{st}$.

This chapter assumes block Rayleigh channel fading [187]. In other words, it assumes an environment with multi-path fading. Let h_{ij}^{xy} denote the channel gain between antenna x and y of router i and j, respectively. It thus has

$$h_{ij}^{xy} = \chi\alpha \left(\frac{d_{ij}}{d_0}\right)^{\beta}, \forall l_{ij} \in \mathcal{E}, \forall x, y \in \mathcal{K}_i, \mathcal{K}_j, \tag{3.1}$$

where χ is drawn from an Exponential distribution with unit mean, α is the path-loss at reference distance d_0 meter, and β is the path-loss exponent. Let $\mathbf{h}_{ijk} = \{h_{ij}^{xk}\}_{\forall x \in \mathcal{K}_i}$ be a vector of channel gains from router i to the k-th antenna of router j.

Let p_{ik} denote the transmit power on antenna k of router i. Define the vector of antenna weights as $\mathbf{p}_i$=$\{p_{ik}\}_{k \in \mathcal{K}_i}$. Each router has a maximum power threshold P_{max}. Formally, the transmit power of each router must satisfy

$$\sum_{k \in \mathcal{K}_i} p_{ik} \leq P_{max}, \forall i \in \mathcal{V}_R. \tag{3.2}$$

3.1.1 Link model

All links in the set $\mathcal{E}$ operate on the same frequency band. Each direct link is denoted as l_{ij}, where router i is the transmitter. Links are scheduled into a *transmission set*.

Table 3.1: A summary of notations

1.	**Sets**
$\mathcal{V}_R$	A set of routers
$\mathcal{V}_E$	A set of energy-harvesting devices
$\mathcal{E}$	A set of directed links
$\mathcal{F}$	A set of sessions
$\mathcal{K}_i$	A set of antennas on router i
$\hat{\mathcal{R}}_n$	The set of routers adjacent to energy-harvesting device n
2.	**Constants**
$\mathbf{h}_{ijk}$	A vector of channel gains from router i to the k-th antenna of router j
$\mathbf{g}_{in}$	A vector of channel gains from router i to energy-harvesting device n
γ_z	The SINR threshold of transmission set $\mathcal{S}_z$
σ^2	Noise power
E_n^{min}	The energy demand of energy-harvesting device n
$\hat{D}_{st}$	Traffic demand of session (s,t)
P_{max}	The maximum transmit power over all antennas of a router
C_{ij}^z	Capacity of link l_{ij} in transmission set $\mathcal{S}_z$
$\mathbf{A}$	Transmission set matrix
a_{ij}^z	Each entry of matrix $\mathbf{A}$
N	The total number of transmission sets
$\mathbf{\Phi}$	Antenna weights matrix
$\mathbf{p}_r^z$	The vector of antenna weights of router r in transmission set $\mathcal{S}_z$
$\mathcal{H}$	Energy harvesting rate matrix
3.	**Variables**
x_z	The activation time of transmission set $\mathcal{S}_z$
E_n^z	The harvested energy at node n from transmission set $\mathcal{S}_z$
f_{ij}^{st}	Traffic fraction of session (s,t) on link l_{ij}
δ_n^z	Energy harvesting rate at node n from $\mathcal{S}_z$
I_{nm}^z	An indicator to identify whether the input power at energy-harvesting device n falls into interval m in transmission set $\mathcal{S}_z$

Let the z-th *transmission set* be $\mathcal{S}_z = \{l_{ij}, l_{xy}, \dots\}$. To record transmission sets, this chapter uses a matrix called $\mathbf{A}$ that has dimension $|\mathcal{E}| \times N$, where column z represents transmission set $\mathcal{S}_z$, and N is the total number of transmission sets. Each element of $\mathbf{A}$ has value $a_{ij}^z \in \{0, 1\}$. Specifically, variable a_{ij}^z equals one if link l_{ij} belongs to transmission set $\mathcal{S}_z$; otherwise, it equals zero.

This chapter considers the physical interference model [188] when constructing a transmission set. Specifically, links can be activated only if their Signal-to-Interference-plus-Noise Ratio (SINR) exceeds a given threshold. Let γ_z be the SINR threshold of transmission set $\mathcal{S}_z$. Further, the capacity of link $l_{ij} \in \mathcal{S}_z$ operating in transmission set $\mathcal{S}_z$ is denoted as C_{ij}^z. In practice, the value of γ_z corresponds to the desired Modulation coding Scheme (MCS); e.g., an IEEE 802.11 radio requires a SINR threshold of 4 to 6 dB in order to support 6 Mbps. All links in transmission set $\mathcal{S}_z$ must satisfy

$$\frac{\sum_{k \in \mathcal{K}_j} \mathbf{p}_i^z \mathbf{h}_{ijk}^\mathsf{T}}{\sum_{l_{rs} \in \mathcal{S}_z \setminus l_{ij}} \sum_{k \in \mathcal{K}_j} \mathbf{p}_r^z \mathbf{h}_{rjk}^\mathsf{T} + \sigma^2} \geq \gamma_z, \forall l_{ij} \in \mathcal{S}_z, \tag{3.3}$$

where $\mathbf{p}_i^z$ denotes the antenna weights of router i when it is activated in transmission set $\mathcal{S}_z$. The term $^\mathsf{T}$ denotes the transpose and σ^2 is the noise power level.

A link schedule consists of one or more transmission sets. Each transmission set is associated with an active duration. Let x_z denote the proportion of time (in seconds) that the transmission set $\mathcal{S}_z$ is active in a link schedule. A link schedule is defined as $F = \{x_1, x_2, \dots, x_N\}$. The aim of this chapter is to generate a schedule length that is no more than a given time unit, which is normalized to one for ease of exposition as all link capacity is in units of bits per second. Further, it allows us to use the terms power and energy interchangeably. Formally, the total activation time of all transmission sets is

$$\sum_{z=1}^{N} x_z \leq 1. \tag{3.4}$$

3.1.2 Routing model

Let $f_{ij}^{st} \in [0,1]$ be the fraction of traffic demand from session (s,t) that is routed over link l_{ij}. All routers must satisfy the standard flow conservation constraint. That is, the total incoming and outgoing traffic flow of routers on the path of a session must be equal, except for the source and destination node. Formally, for each router $i \in \mathcal{V}_R$, and each session $(s,t) \in \mathcal{F}$, there is a flow conservation constraint as per

$$\sum_{j\in\mathcal{R}_i} f_{ij}^{st} - \sum_{j\in\mathcal{R}_i} f_{ji}^{st} = \begin{cases} 1 & i = s, \\ -1 & i = t, \\ 0 & \text{otherwise.} \end{cases} \tag{3.5}$$

The total traffic routed on each link cannot exceed its capacity; the capacity of a link depends on its total active time in each transmission set. Mathematically, there is the following capacity constraint for each link in set $\mathcal{E}$,

$$\sum_{(s,t)\in\mathcal{F}} \hat{D}_{st} f_{ij}^{st} \leq \sum_{z=1}^{N} a_{ij}^{z} x_z C_{ij}^{z}, \forall l_{ij} \in \mathcal{E}, \tag{3.6}$$

where the left side of (3.6) is the total traffic routed on a given link l_{ij} and the right side is the capacity of link l_{ij}.

3.1.3 Energy harvesting model

The energy harvested by energy-harvesting device n whenever router i transmits depends on (i) the antenna weights of router i in transmission set $\mathcal{S}_z$; i.e., $\mathbf{p}_i^z$, and (ii) the channel gain from each antenna of router i.

Let g_{ink} be the channel gain from the k-th antenna of router i to energy-harvesting device n. Define $\mathbf{g}_{in} = \{g_{ink}\}_{k\in\mathcal{K}_i}$ as a vector of channel gains. The receive power at energy-harvesting device n when router i transmits in transmission set $\mathcal{S}_z$ is

$$P_{in}^z = \mathbf{p}_i^z \mathbf{g}_{in}^\mathsf{T}. \tag{3.7}$$

Let $\hat{\mathcal{R}}_n = \{r \mid d_{nr} \leq \bar{r}_d, r \in \mathcal{V}_R\}$ be a set of routers that are able to charge energy-harvesting device n. Then its total received power P_n^z when transmission set $\mathcal{S}_z$ is active is calculated as follows:

$$P_n^z = \sum_{i \in \hat{\mathcal{R}}_n} P_{in}^z, \forall n \in \mathcal{V}_E, z = 1, 2, \ldots, N. \tag{3.8}$$

The energy conversion efficiency of energy-harvesting devices has the range $[0, 1]$. It varies non-linearly with the received power. Let η_n^z be the energy conversion efficiency used by energy-harvesting device n for transmission set $\mathcal{S}_z$. Let E_n^z denote the amount of harvested energy at energy-harvesting device n when transmission set $\mathcal{S}_z$ is active. The amount of energy harvested by energy-harvesting device n when transmission set $\mathcal{S}_z$ is active for x_z seconds is

$$E_n^z = \delta_n^z x_z, \forall n \in \mathcal{V}_E, z = 1, 2, \ldots, N, \tag{3.9}$$

where $\delta_n^z = \eta_n^z P_n^z$ is the energy harvesting rate.

Each energy-harvesting device has a minimum energy requirement of E_n^{min}, where $n \in \mathcal{V}_E$. Note, in practice, energy-harvesting devices will have a given energy budget to support their operation; e.g., an energy-harvesting device may be tasked with sampling and transmission over a given period of time. Thus, E_n^{min} corresponds to the amount of energy over the said time period. Specifically, for each energy-harvesting device $n \in \mathcal{V}_E$, there is an energy-harvesting constraint as per

$$\sum_{z=1}^{N} E_n^z \geq E_n^{min}, \forall n \in \mathcal{V}_E. \tag{3.10}$$

That is, the total energy harvested from the activation of transmission sets must be at least E_n^{min}.

3.2 Problem Definition

The aim of this chapter is to minimize the schedule length $\sum_{z=1}^{N} x_z$ subject to meeting the traffic demand of each session $(s,t) \in \mathcal{F}$ and also the energy requirement of energy-harvesting device n in $\mathcal{V}_E$. The problem at hand is to determine the active time x_z of each transmission set $\mathcal{S}_z$, and to determine the fraction of traffic f_{ij}^{st} routed on each link for all given sessions. Mathematically, the problem is

$$\begin{aligned} \underset{f_{ij}^{st},\, x_z}{\text{minimize}} \quad & \sum_{z=1}^{N} x_z \\ \text{subject to} \quad & (3.4) - (3.6), (3.9) - (3.10). \end{aligned} \tag{3.11}$$

This chapter concludes with a few remarks. First, problem (3.11) is an LP that accepts a given collection of transmission sets, i.e., matrix $\mathbf{A}$. Note that the number of transmission sets, i.e., N, increases exponentially with the number of links. Indeed, link scheduling is a classic NP-hard problem [188]. This motivates the heuristic in Section 3.3, which this chapter will use to generate a collection of transmission sets. In addition, note that LP (3.11) determines the active time of each transmission set. Once the activation of a transmission set is determined, the transmit power of active routers associated with this transmission set is used for data transmission and energy transfer. Second, in order to address (11), this chapter requires (i) topological information, which can be obtained during network deployment, (ii) channel state between routers and from routers to devices. This information can be obtained via a measurement campaign conducted during the deployment of routers and devices. The worst or nominal channel gain information can then be used in the proposed solution, and iii) session or flow information between routers, which can be obtained by polling routers periodically to determine the total traffic destined for a router acting as the gateway to the Internet. In this respect, the proposed solution will be critical to future software-defined wireless backhaul networks, see [189], where a controller gathers traffic statistics and computes one or more paths using the solution proposed in this chapter. Third, the antenna weights of routers and the energy conversion efficiency at energy-harvesting devices are computed when forming a transmission set; see Section 3.3. Lastly, the previous formulation assumes that traffic from a source can be split over multiple paths. In practice, a source uses only one path. This limitation is addressed in Section 3.4.

3.3 Transmission Set Generator (TSG)

This section now presents a heuristic called TSG. It has two phases. The *first* phase constructs N transmission sets by greedily adding links according to the number of energy-harvesting devices they are able to charge. That is, TSG prefers links that charge a high number of energy-harvesting devices. This ensures devices have a high energy harvesting rate whenever a transmission set is active. The *second* phase of TSG aims to improve link or network capacity by adding more links into each transmission set. Specifically, in the first phase, each link only exists in one of the N transmission sets. In this second phase, TSG attempts to add a link into multiple transmission sets.

3.3.1 Phase-1

Referring to Algorithm 1, TSG calls the function *Sort* ($\mathcal{E}$) to return a sorted set $\hat{\mathcal{E}}$; the links in $\mathcal{E}$ are sorted in descending order according to the number of energy-harvesting devices each link charges. After that, TSG proceeds to construct a transmission set by greedily adding a link l_{ij} from the set $\hat{\mathcal{E}}$. For each link l_{ij}, it calls the function *HalfDuplex* ($l_{ij}, \mathcal{S}_z$) to ensure all communications are half-duplex. Specifically, the function returns FALSE if neither router i nor j exists in the transmission set $\mathcal{S}_z$. In this case, link l_{ij} is added into the set $\hat{\mathcal{S}}_z$. After that, it calls the function *P-Allocation()* to determine the optimal antenna weights at all routers that lead to the highest energy harvesting rate at all energy-harvesting devices. It returns (i) a flag to indicate whether the link l_{ij} can be added into the transmission set $\mathcal{S}_z$, (ii) the antenna weights of routers, denoted as $\Phi_\star = \{\mathbf{p}_1^z, \ldots, \mathbf{p}_{|\mathcal{V}_R|}^z\}$, and (iii) the energy harvesting rate of energy-harvesting devices, denoted as $\mathcal{H}_\star = \{\delta_1^z, \ldots, \delta_{|\mathcal{V}_E|}^z\}$. If link l_{ij} can be added into $\mathcal{S}_z$, TSG adds it into $\mathcal{S}_z$, removes link l_{ij} from further consideration, and updates the antenna weights and energy harvesting rate of energy-harvesting devices in line-10.

3.3.2 Phase-2

In *Phase-1*, each link in $\mathcal{E}$ exists in one transmission set only. In *Phase-2*, TSG checks whether any other links can be added into a transmission set $\mathcal{S}_z$ from Phase-1.

Lines 18-27 of Algorithm 1 check whether a link in $\mathcal{E}$ can be added into transmission set $\mathcal{S}_w$. The function *P-Allocation()* and *HalfDuplex()* are then used to check whether a link can be added into $\mathcal{S}_w$. Lastly, in line 28, TSG updates transmission set $\mathcal{S}_w$ in matrix $\mathbf{A}$, antenna weights for $\mathcal{S}_w$, and the energy harvesting rate of energy-harvesting devices $\mathcal{H}_w$.

3.3.3 *P-Allocation*

TSG uses *P-Allocation()* to determine whether all links in a given transmission set, say $\hat{\mathcal{S}}_z$, satisfy their SINR threshold γ_z. It returns the corresponding antenna weights $\Phi_\star$ and energy harvesting rate $\mathcal{H}_\star$. To determine these quantities, *P-Allocation()* solves the following Non-Linear Program (NLP):

$$\max_{p_{ik}^z} \quad \sum_{n \in \mathcal{V}_E} \delta_n^z \tag{3.12a}$$

$$\text{s.t.} \quad \sum_{k \in \mathcal{K}_i} p_{ik}^z \leq P_{max}, \forall l_{ij} \in \hat{\mathcal{S}}_z, \tag{3.12b}$$

$$\frac{\sum_{k \in \mathcal{K}_j} \mathbf{p}_i^z \mathbf{h}_{ijk}^\mathsf{T}}{\sum_{l_{rs} \in \hat{\mathcal{S}}_z \setminus l_{ij}} \sum_{k \in \mathcal{K}_j} \mathbf{p}_r^z \mathbf{h}_{rjk}^\mathsf{T} + \sigma^2} \geq \gamma_z, \forall l_{ij} \in \hat{\mathcal{S}}_z \tag{3.12c}$$

The goal of NLP (3.12) is to optimize the antenna weights of routers in order to maximize the sum of energy harvesting rates at energy-harvesting devices; the sum

Algorithm 1: Transmission sets generation.

Input: $G(\mathcal{V}, \mathcal{E})$, γ_z
Output: Transmission set matrix $\mathbf{A}$
Antenna weight matrix $\mathbf{\Phi}$
Energy conversion efficiency matrix $\mathcal{H}$

```
// Phase-1
Set z = 1, Ê = Sort(E)
while Ê ≠ ∅ do
    S_z = Φ_z = H_z = ∅
    for l_ij ∈ Ê do
        if HalfDuplex (l_ij, S_z) == FALSE then
            Ŝ_z = S_z ∪ l_ij
            [Flag, Φ_⋆, H_⋆] = P-Allocation (Ŝ_z, γ_z)
            if Flag = TRUE then
                S_z = Ŝ_z, Φ_z = Φ_⋆, H_z = H_⋆
            end
        end
    end
    Ê = Ê \ S_z, z = z + 1
end
// Phase-2
for w = 1 → z − 1 do
    for l_ij ∈ E do
        if (l_ij ∉ S_w ∧ HalfDuplex (l_ij, S_w) == FALSE) then
            Ŝ_w = S_w ∪ l_ij
            [Flag, Φ_⋆, H_⋆] = P-Allocation(Ŝ_w, γ_w)
            if Flag = TRUE then
                S_w = Ŝ_w
                Φ_w = Φ_⋆, H_w = H_⋆
            end
        end
    end
    Update(A, S_w, Φ_w, H_w)
end
return A, Φ, H
```

of these weights must not exceed P_{max}, see (3.12b). An important constraint (3.12c) is to ensure links in $\hat{\mathcal{S}}_z$ satisfy their SINR threshold γ_z. Note that once the antenna weights of routers are decided, each energy harvesting rate δ_n^z can be then retrieved via Equ. (3.7) and (3.8).

3.3.4 Linearization of energy conversion efficiency

The objective of NLP (3.12) is non-linear because of the conversion process η_n^z of energy-harvesting device n. To this end, the conversion process is approximated using piece-wise linear segments. Specifically, it divides the domain of received power into M received power intervals; each interval m has a corresponding energy conversion efficiency η_{nm}^z. These intervals are non-overlapping, where each interval has the range $[l_m, h_m)$. For each received power P_n^z value, the goal is to determine the corresponding interval m that P_n^z falls into. To this end, define I_{nm}^z as a binary indicator that equals one when interval m is active. Further, only one of M intervals is allowed to be active. This can be formally represented as per

$$0 \leq \sum_{m=1}^{M} I_{nm}^z \leq 1, \forall n \in \mathcal{V}_E, z = 1, 2, \ldots, N, \tag{3.13}$$

For each transmission set $\mathcal{S}_z$ and energy-harvesting device $n \in \mathcal{V}_E$, the next expression calculates the received power P_n^z as

$$\sum_{m=1}^{M} [l_m I_{nm}^z + (h_m - l_m)\nu_{nm}^z] = P_n^z. \tag{3.14}$$

Here, ν_{nm}^z is a real variable constrained as

$$0 \leq \nu_{nm}^z \leq I_{nm}^z, 1 \leq m \leq M. \tag{3.15}$$

Expression (3.15) determines the interval that can be used to determine P_n^z. As an example, assume $P_n^z = 0.7$, and there are two ($M = 2$) intervals: $[0, 0.5]$ and $[0.5, 1.0]$. Hence, the received power falls in the interval $[0.5, 1.0]$. As per (3.14), only one interval is allowed to be active; in this example, it has $I_{n2}^z = 1$. This means (3.14) is written as $0.5(1) + 0.5\nu_{nm}^z = 0.7$, where it has $\nu_{nm}^z = 0.4$. This also means for the received power $P_n^z = 0.7$, this chapter uses the energy conversion efficiency associated with the second interval.

To linearize NLP (3.12), replace each non-linear term δ_n^z by variable $\hat{\delta}_n^z$. Formally, variable $\hat{\delta}_n^z$ is given by

$$\hat{\delta}_n^z = \sum_{m=1}^{M} \eta_{nm}^z I_{nm}^z P_n^z, \forall n \in \mathcal{V}_E. \tag{3.16}$$

The equation (3.16) is still non-linear due to the products of two decision variables, i.e., I_{nm}^z and P_n^z. In order to formulate the model as a MILP, an additional continuous variable $\hat{P}_{nm}^z$ is introduced. The equation (3.16) is then linearized by replacing the products of I_{nm}^z and P_n^z with $\hat{P}_{nm}^z$. For each energy-harvesting device $n \in \mathcal{V}_R$, the value $\hat{P}_{nm}^z$ is set as follows:

$$\hat{P}_{nm}^z \leq I_{nm}^z P_{max}, 1 \leq m \leq M, \tag{3.17}$$

$$\hat{P}_{nm}^z \leq P_n^z, 1 \leq m \leq M, \tag{3.18}$$

$$\hat{P}_{nm}^z \leq P_n^z - (1 - I_{nm}^z) P_{max}, 1 \leq m \leq M. \tag{3.19}$$

In the previous set of inequalities, i.e., constraint (3.17)-(3.19), observe that $\hat{P}_{nm}^z = P_n^z$ if $I_{nm}^z = 1$. Otherwise, variable $\hat{P}_{nm}^z$ is forced to zero.

Finally, after the above linearization process, NLP (3.12) can be formulated as the following mixed integer linear program (MILP):

$$\begin{aligned} \underset{p_{ik}^z, I_{nm}^z, \nu_{nm}^z}{\text{maximize}} \quad & \sum_{n \in \mathcal{V}_E} \hat{\delta}_n^z \\ \text{subject to} \quad & (3.12b) - (3.12c), \\ & (3.13) - (3.19). \end{aligned} \tag{3.20}$$

This chapter solves MILP (3.20) using Gurobi 9.0.1 [190].

3.4 A novel routing metric

In LP (3.11), routing paths are decision variables. Specifically, a source is allowed to divide its traffic onto all paths leading to its destination node. However, in practice, a source uses only one path. To this end, this chapter develops a novel routing metric that can be used to select a path for each session in $\mathcal{F}$ that charges the most RF-harvesting devices. This metric can then be used by Dijkstra's algorithm; this chapter refers to the version of Dijkstra's algorithm that uses the novel metric as W-Dijkstra. The path for each session then serves as an input to LP (3.11). Specifically, let $p^*_{(s,t)}$ be the path chosen by a routing protocol for session (s,t). Then the flow variable f^{st}_{ij} only exists for links on path $p^*_{(s,t)}$. Next, the following paragraphs show how to calculate $p^*_{(s,t)}$.

A novel weight is defined for each link. Specifically, let the weight of a link l_{ij} be W_{ij}, which is defined as the number of energy-harvesting devices charged by the link. Formally, the weight of a link is defined as

$$W_{ij} = |\mathcal{N}_i|, \forall l_{ij} \in \mathcal{E} \tag{3.21}$$

Let $\mathcal{P}(s,t)$ be a path for session (s,t) in $\mathcal{F}$. Further, denote $\mathbf{P}_{(s,t)}$ as the set of all paths for session (s,t). The weight of a path $\mathcal{P}(s,t)$ is defined as

$$\mathcal{W}_{\mathcal{P}(s,t)} = \sum_{l_{ij} \in \mathcal{P}(s,t)} W_{ij}, \forall (s,t) \in \mathcal{F}. \tag{3.22}$$

Then for each session $(s,t) \in \mathcal{F}$, it selects a path as per

$$p^*_{(s,t)} = \underset{p \in \mathbf{P}_{(s,t)}}{\arg\max}\, \mathcal{W}_p. \tag{3.23}$$

The previous problem can be solved using Dijkstra's algorithm by setting the weight of link $l_{ij} \in \mathcal{E}$ to W_{ij}.

3.5 Analysis

This section presents (i) the total number of decision variables and constraints of the LP (3.11); both of which affect the LP's computation time, (ii) the total number of decision variables and constraints in MILP (3.20), which affect the computation time of heuristic TSG, (iii), the time complexity of heuristic TSG, (iv) the lower and upper bound of the link schedule length.

Now first define a few necessary notations in this section. All routers have $|\mathcal{K}_i|$ number of antennas, and all links have a theoretical capacity of C. The maximum number of hops and traffic demand of sessions is $\hat{H}$ and D_{max}, respectively. The maximum energy demand of energy-harvesting devices is set to E_{max}. Let $\hat{\mathbf{h}}_{ij}$ and $\widetilde{\mathbf{h}}_{ij}$ be a vector of the best and worst channel gains vector from router i to router j, respectively. Similarly, define $\hat{g}_{in}$ and $\widetilde{g}_{in}$ to be the best and worst channel gains from router i to energy-harvesting device n, respectively. Lastly, let $\hat{\eta}$ and $\widetilde{\eta}$ to be the highest and lowest energy conversion efficiency, respectively.

Proposition 1. *LP (3.11) has $N + |\mathcal{E}||\mathcal{F}|$ decision variables and $|\mathcal{E}| + |\mathcal{V}_R||\mathcal{F}| + |\mathcal{V}_E|(N+1) + 1$ constraints.*

Proof. First, consider the decision variables of LP (3.11). The decision variable x_z exists for each transmission set $\mathcal{S}_z$, meaning there are N such decision variables. Next, for each session (s,t), the decision variable f_{ij}^{st} is used to represent the fraction of demand on each link l_{ij}, meaning there are $|\mathcal{E}||\mathcal{F}|$ such decision variables in total. Therefore, in total, there are $N + |\mathcal{E}||\mathcal{F}|$ decision variables for LP (3.11), as claimed. Next, consider the constraints of LP (3.11). There is a flow conservation constraint (3.5) for each router $i \in \mathcal{V}_R$ and each session $(s,t) \in \mathcal{F}$. This gives us $|\mathcal{V}_R||\mathcal{F}|$ constraints. Next, for each link in $\mathcal{E}$, there is a capacity constraint (3.6). For each energy-harvesting device $n \in \mathcal{V}_E$, constraint (3.9) and constraint (3.10) are used to calculate its total harvested energy and demand, respectively. This results in another $|\mathcal{V}_E|(N+1)$ constraints. Lastly, constraint (3.4) specifies the schedule length. In total, there are $|\mathcal{E}| + |\mathcal{V}_R||\mathcal{F}| + |\mathcal{V}_E|(N+1) + 1$ constraints, as claimed. This completes the proof. □

The next proposition shows the number of decision variables and constraints for MILP (3.20), which is used by TSG to validate a transmission set.

Proposition 2. *MILP (3.20) has* $|\mathcal{K}_i||\mathcal{V}_R| + 2|\mathcal{V}_E|M$ *decision variables and* $|\mathcal{E}| + |\mathcal{V}_R| + |\mathcal{V}_E|(4M + 3)$ *constraints.*

Proof. First, consider the decision variables of MILP (3.20). Given transmission set $\mathcal{S}_z$, TSG uses the function *P-Allocation()* to determine the transmit power at each antenna of each router. As there are $|\mathcal{K}_i|$ antennas per router, this gives a total of $|\mathcal{K}_i||\mathcal{V}_R|$ number of decision variables. For the non-linear conversion rate, there is a binary variable I^z_{nm} and an auxiliary real variable ν^z_{nm} for each energy-harvesting device n in a given transmission set. Given that M intervals, there are thus $2|\mathcal{V}_E|M$ decision variables. This gives a total of $|\mathcal{K}_i||\mathcal{V}_R| + 2|\mathcal{V}_E|M$ number of decision variables, as claimed.

As for constraints, there are $|\mathcal{V}_R|$ constraints of type (3.12b) and $|\mathcal{E}|$ constraints of each type (3.12c). Each energy-harvesting device n has a corresponding energy conversion efficiency η^z_{nm} in each interval $m \in M$ and in each transmission set $\mathcal{S}_z$. Hence, there is a total of $3|\mathcal{V}_E|$ constraints of each type (3.13), (3.14) and (3.16), respectively. Next, there are in total $4|\mathcal{V}_E|M$ constraints of type (3.15), (3.17), (3.18) and (3.19) as they consider each energy-harvesting device n in each interval M. In total, there are $|\mathcal{E}| + |\mathcal{V}_R| + |\mathcal{V}_E|(4M + 3)$ number of constraints for MILP (3.20). This completes the proof. □

The next proposition shows the time complexity of TSG.

Proposition 3. *TSG has time complexity* $\mathcal{O}(|\mathcal{E}|^2\epsilon)$.

Proof. Algorithm 1 first sorts $|\mathcal{E}|$ links, which takes time complexity $\mathcal{O}(|\mathcal{E}|\log(|\mathcal{E}|))$. After that, TSG generates each transmission set in an iterative manner. TSG checks $|\mathcal{E}|$ links to generate each transmission set in Phase-1; see lines 4-14. Note that the function *HalfDuplex()* has time complexity $\mathcal{O}(1)$. The function *P-Allocation()* takes time complexity $\mathcal{O}(\epsilon)$. The NLP (3.12) can be solved using the interior-point method that takes time complexity $\mathcal{O}(\epsilon) = \mathcal{O}(n^3/log(n))$ [191]. In the worst case, TSG checks $|\mathcal{E}|$ links to generate each transmission set. This requires a total time of $\mathcal{O}(|\mathcal{E}|^2\epsilon)$ for Phase-1. For lines 17-30, TGS checks $|\mathcal{E}|$ links for each transmission set in the worst case. As a result, it requires time $\mathcal{O}(N|\mathcal{E}|\epsilon)$ for Phase-2. Note that the number of transmission sets satisfies: $N \leq \mathcal{E}$. Hence, TSG in total takes $\mathcal{O}(|\mathcal{E}|^2\epsilon)$. □

The next proposition shows the lower bound of the schedule length generated by the LP (3.11).

Proposition 4. *The lower bound of schedule length is* $MAX\{\frac{2E_{max}}{|\mathcal{E}|\hat{\eta}P_{max}\hat{g}_{in}}, \frac{D_{max}}{C}\}$.

Proof. First, consider the lower bound of the schedule length. In the ideal case, all links are active simultaneously in one transmission set. As a result, all active routers perform charging and routing capabilities simultaneously. As routers are half-duplex, there are at most $\frac{|\mathcal{E}|}{2}$ links or routers that are able to charge energy-harvesting devices simultaneously. This results in all energy-harvesting devices harvesting at most $\frac{|\mathcal{E}|}{2}\hat{\eta}P_{max}\hat{g}_{in}x_s$ amount of energy. To this end, the shortest required time to simultaneously charge all energy-harvesting devices is $\frac{2E_{max}}{|\mathcal{E}|\hat{\eta}P_{max}\hat{g}_{in}}$ seconds. The schedule length is minimum when all sessions have only one hop. In this case, the time required to simultaneously route all sessions is $\frac{\mathbf{D_{max}}}{\mathbf{C}}$. Formally, the lower bound of schedule length is $MAX\{\frac{2E_{max}}{|\mathcal{E}|\hat{\eta}P_{max}\hat{g}_{in}}, \frac{D_{max}}{C}\}$. □

The next result shows the upper bound of schedule length generated by the LP (3.11).

Proposition 5. *The upper bound of schedule length is* $\frac{|\mathcal{V}_E|E_{max}}{\tilde{\eta}P_{max}\tilde{g}_{in}} + \frac{|\mathcal{F}|\hat{H}D_{max}}{C}$.

Proof. Now consider the upper bound of the schedule length. In the worst case, the routing and charging process of routers are separated into different transmission sets. As a result, the upper bound of schedule length is derived by combining the charging and routing time. This means each link is scheduled in a distinct transmission set to route sessions due to interference. In addition, energy-harvesting devices are not able to harvest ambient RF energy from transmission sets where routers route sessions. This means additional transmission sets that only consider energy transfer must be enabled to charge energy-harvesting devices. First, calculate the time required to satisfy the energy demand of energy-harvesting devices. In the worst case, an energy-harvesting device only harvests energy from one router over the worst channel. As a result, each energy-harvesting device harvests $\widetilde{\eta} P_{max} \widetilde{g}_{in} x_z$ amount of energy in transmission set $\mathcal{S}_z$. Hence, fully charging each energy-harvesting device n requires at most $\frac{E_{max}}{\widetilde{\eta} P_{max} \widetilde{g}_{in}}$ seconds. In the worst case, energy-harvesting devices are not able to harvest energy simultaneously. Consequently, to fully charge all energy-harvesting devices, the total required active time of transmission sets is $\frac{|\mathcal{V}_E| E_{max}}{\widetilde{\eta} P_{max} \widetilde{g}_{in}}$. Next, calculate the time required to route all sessions. Routing each session $(s,t) \in \mathcal{F}$ on each link l_{ij} requires a time of $\frac{D_{max}}{C}$ seconds at most. In the worst case, each link is able to route one session in each transmission set. As there are $|\mathcal{F}|$ sessions and each has $\hat{H}$ hops, routing all sessions requires at most $\frac{|\mathcal{F}| \hat{H} D_{max}}{C}$. Formally, by summing charging time and routing time, the upper bound of schedule length is $\frac{|\mathcal{V}_E| E_{max}}{\widetilde{\eta} P_{max} \widetilde{g}_{in}} + \frac{|\mathcal{F}| \hat{H} D_{max}}{C}$, as claimed. □

3.6 Evaluation

This chapter conducts all experiments in Python 3.8, and solves the proposed MILP (3.20) and LP (3.11) using Gurobi 9.0.1. Energy harvesting devices have one antenna and minimum energy requirement of $E_n^{min} = 20$ μJ, unless stated otherwise. In addition, each router i is equipped with $\mathcal{K}_i = 3$ antennas, unless otherwise specified. The RF energy conversion efficiency values, see Table 3.2, are derived from the datasheet of the Powercast RF harvester [192]. The noise power σ is set to -90 dBm; see Table 3.3 for details. TSG benchmarks against a simple scheduler called Set Division Link Scheduling (SDLS), whereby each transmission only has one distinct link. Moreover, in each transmission set $\mathcal{S}_z$, the transmitter of a link allocates a transmit power of $\frac{P_{max}}{|\mathcal{K}_i|}$ to each antenna. In each experiment, the same SINR threshold γ_z is used to calculate the link capacity for both TSG and SDLS. Additionally, W-Dijkstra will benchmark against the optimal routing solution where paths are determined as per constraints (3.4) and (3.5). Table 3.4 shows all proposed approaches. All these approaches use LP (3.11) to generate the final schedule. The main difference is how they construct transmission sets, determine the transmit power allocation of routers and select a path. Figure 3.3 illustrates how the proposed methods in Section 3.3 and 3.4 work cooperatively to solve the data collection problem in a two-tier RF energy harvesting network subject to given demands of routers and energy-harvesting devices.

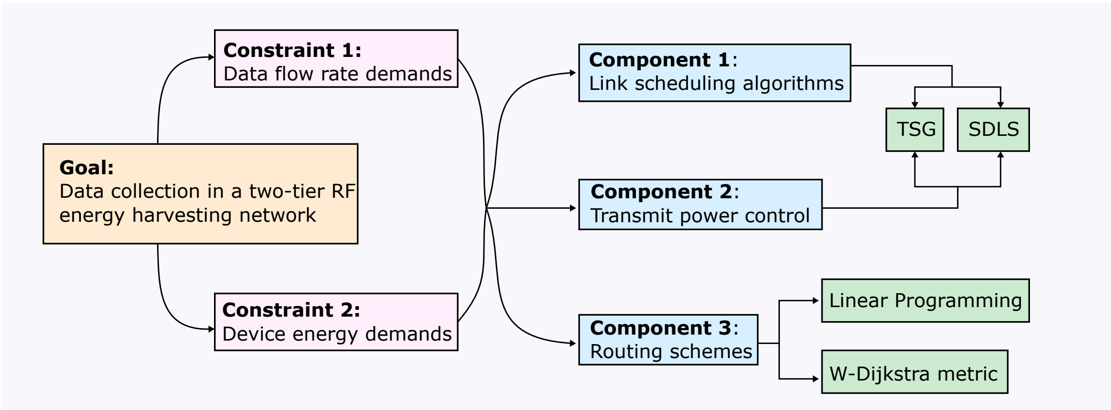

Figure 3.3: Approaches to derive the final schedule for data collection in a two-tier RF energy harvesting network.

Interval	**Received power (in mW)**	η
I_6	≥ 10.0	5%
I_5	[5.0, 10.0]	55%
I_4	[0.8, 5.0]	60%
I_3	[0.6, 0.8]	55%
I_2	[0.08, 0.6]	35%
I_1	[0.0, 0.08]	5%

Table 3.2: Received power and conversion rates.

3.6.1 Fixed Topology

This section studies all proposed solutions using a fixed topology, with five routers and one energy-harvesting device; see Figure 3.4. In addition, this section sets the transmission range of routers, namely r_d, and the energy harvesting range r_c of the energy-harvesting device to 10 meters. The SINR threshold γ_z is 3 dB, and there are four sessions, namely, $\mathcal{F} = \{(A, E), (C, E), (A, D), (C, B)\}$.

Parameter	Values	Parameter	Values
L	$50 \times 50\ m^2$	$\lvert\mathcal{K}_i\rvert$	1 to 9
$\lvert\mathcal{V}_R\rvert$	20	P_{max}	1 to 5 Watts
$\lvert\mathcal{V}_E\rvert$	5	B	20 MHz
r_c	10 m	r_d	10 to 17 m
γ_z	3 to 30 dB	σ	-90 dBm
E_n^{min}	20 to 50 μJ	$\hat{D}_{st}$	1 to 10 Mb/s
d_0	20 dB	β	2

Table 3.3: Parameter Values.

Approach	Scheduler	Power allocation	Routing
TSG-OP	TSG	MILP (3.20)	Optimal routing
SDLS-OP	SDLS	$\frac{P_{max}}{\lvert\mathcal{K}_i\rvert}$	Optimal routing
TSG-Dijkstra	TSG	MILP (3.20)	W-Dijkstra
SDLS-Dijkstra	SDLS	$\frac{P_{max}}{\lvert\mathcal{K}_i\rvert}$	W-Dijkstra

Table 3.4: Approaches to derive the final schedule.

This section first studies how the energy requirement of the energy-harvesting device affects the schedule length. This section sets the traffic demand of all sessions, namely $\hat{D}_{st}$, to 1 Mb/s. From Figure 3.5, we see that the schedule length of TSG-OP is on average 66.7% shorter than that of SDLS-OP. This is because TSG-OP activates on average two routers to simultaneously charge the energy-harvesting device during each active transmission set. Hence, the energy-harvesting device achieves a higher

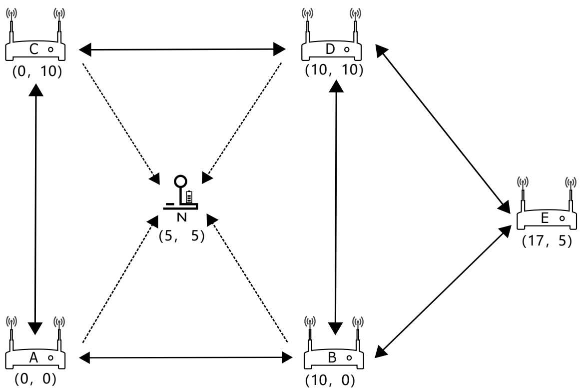

Figure 3.4: A fixed topology with five routers and one energy-harvesting device. Solid arrows denote direct communication, and dashed arrows denote RF-energy transfer. The coordinate of nodes is shown at the bottom.

energy-harvesting rate when using TSG-OP. When its energy demand is less than 25 μJ, the schedule length of TSG-Dijkstra and SDLS-Dijkstra does not change, which is 0.19 and 0.37, respectively. This is because the schedule length that they derived for supporting traffic demands is also sufficient to fulfill the energy requirement of the energy-harvesting device.

Next, this section considers to vary the traffic demand of sessions. Energy-harvesting device N has fixed energy demand of $E_N^{min} = 10$ μJ. Referring to Figure 3.6, the schedule length of TSG-OP is on average 92.3% shorter than that of SDLS-OP. This is because it uses transmission sets that contain multiple links. On the other hand, SDLS activates one link per transmission set. Hence, TSG-OP allows links to have a higher capacity (in bps) as compared to using SDLS-OP, meaning a shorter schedule length is sufficient to meet traffic demands. From Figure 3.6, both TSG-Dijkstra and SDLS-Dijkstra respectively have a longer schedule length than that of TSG-OP and SDLS-OP. This is because W-Dijkstra uses longer routing paths for session (A, E) and (C, E). Specifically, when the energy demand E_N^{min} is 10 μJ, LP (3.12) uses the path $A - B - E$ for session (A, E). By contrast, W-Dijkstra uses $A - C - D - B - E$. In both cases, a long schedule is required to support the links on both paths.

3.6.2 Random Topologies

Next, this section considers to study random typologies. In each run, 20 routers and five energy-harvesting devices are placed randomly in the given area. All routers are randomly deployed on a 50×50 m^2 square area. They have $|\mathcal{K}_i| = 3$ antennas and a maximum transmit power of $P_{max} = 30$ dBm, unless state otherwise. The channel bandwidth is $B = 20$ MHz. It considers the following SINR threshold γ_z (in dB): $\{3, 6, 10, 20, 30\}$. It deploys $|\mathcal{F}| = 2$ sessions, unless otherwise stated. In each experiment, a topology contains at least ten different flows that can be routed over a multi-hop path. Each energy-harvesting device is located within the charging

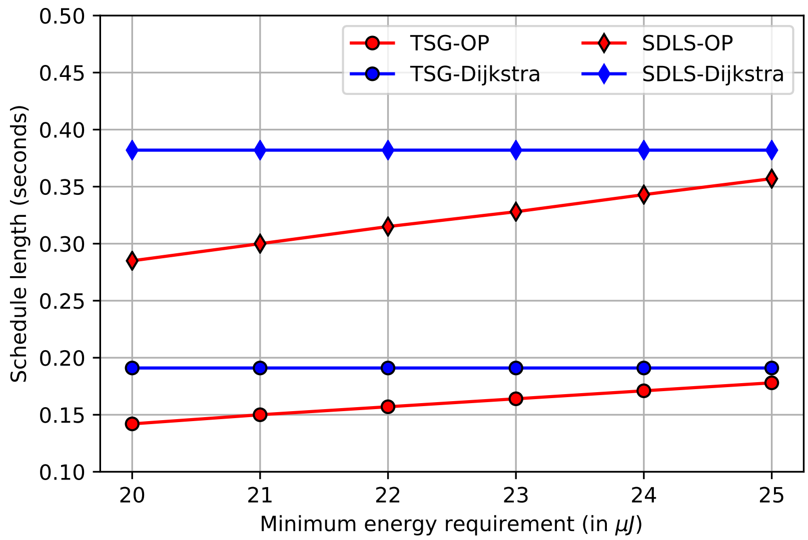

Figure 3.5: Schedule length with increasing energy requirements for the fixed topology.

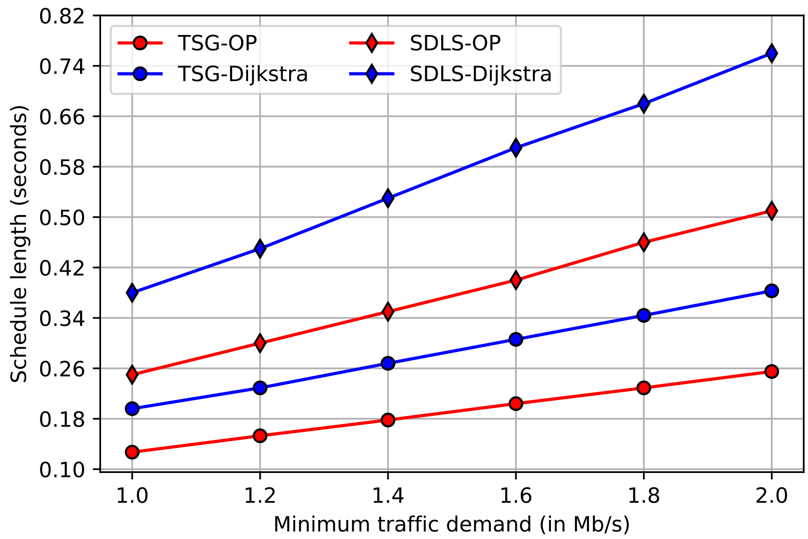

Figure 3.6: Schedule length with increasing traffic demands for the fixed topology.

range r_c of at least one router. Each result shows an averaged schedule length over 50 simulation runs.

Optimality gap

Recall that computing the optimal solution of problem (3.11) requires all possible transmission sets and realizations of power allocation, which is computationally intractable for large-scale networks. To this end, this section considers small-scale networks, whereby the number of routers ranges from five to ten and there is only one RF-energy harvesting device. The value of E_n^{min} and $\hat{D}_{st}$ is set to 20 μJ and 5 Mb/s, respectively. To compute the optimal solution of problem (3.11), this section applies exhaustive search to generate all possible transmission sets, and determines the transmit power allocation by solving MILP (3.12). Referring to Figure 3.7, as the number of routers increases from five to ten, the schedule length computed by exhaustive search reduces from 0.51 to 0.26 and the schedule length of TSG reduces from 0.51 to 0.29. This means the optimality gap between the optimal solution grows with network scale. This is because TSG only computes a portion of transmission sets, which grows linearly with network scale; see Algorithm 1. Further, the number of possible transmission sets grows exponentially with network scale. As a result, the gap between TSG-OP and the optimal solution increases accordingly with network scale, the gap between TSG-OP and the optimal solution also increases.

Impact of energy demand

In this experiment, the SINR threshold is set to $\gamma_z = 10$ dB, and each traffic demand is set to $\hat{D}_{st} = 1$ Mb/s.

As per Figure 3.8, the schedule length of TSG and SDLS increases when energy-harvesting devices have a higher energy demand E_n^{min}. This is reasonable because links need to be active longer to ensure energy-harvesting devices receive their required energy demand. The schedule length of TSG is on average 30.19% shorter than SDLS under the same energy requirement. This is because TSG allows multiple

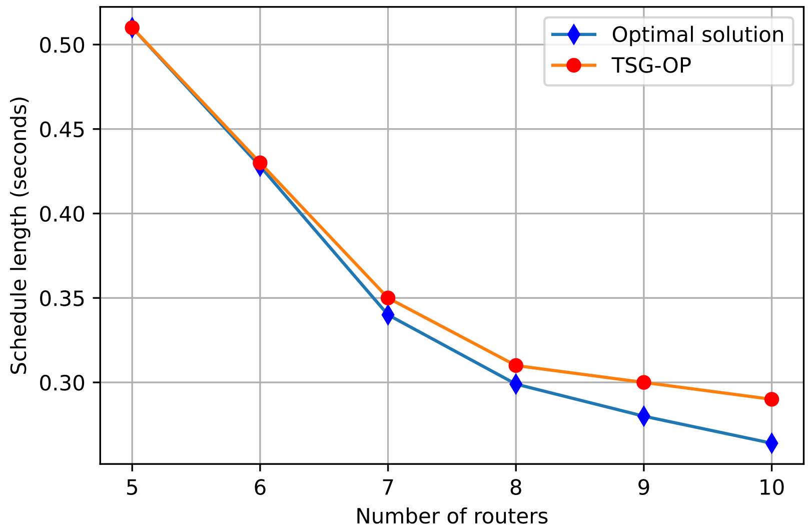

Figure 3.7: Optimality gap between TSG-OP and the optimal solution computed by exhaustive search.

links to charge energy-harvesting devices simultaneously in each transmission set. In addition, for TSG, its average transmit power per transmission set is larger than that of SDLS. On the other hand, although SDLS allows routers to transmit with the maximum power P_{max}, it only allows one router to charge energy-harvesting devices in each transmission set. This results in a longer charging time on average. Additionally, the overall performance of W-Dijkstra routing algorithm is within 98.5% of the optimal solution computed by LP (3.11). This means the paths computed by W-Dijkstra result in a near-optimal schedule when the flow demand is small, i.e., 1 Mb/s.

Impact of traffic demand

To study how traffic demands impact the schedule length, this section considers demands ranging from 1 Mb/s to 10 Mb/s. The energy demand E_n^{min} is set to 20 μJ, and the SINR threshold γ_z is 10 dB. Referring to Figure 3.9, for both TSG and SDLS, the schedule length increases significantly when the traffic demand increases from 1 to 10 Mb/s. This is because links need to be activated longer to transmit a higher amount of traffic. The difference between the schedule length achieved by

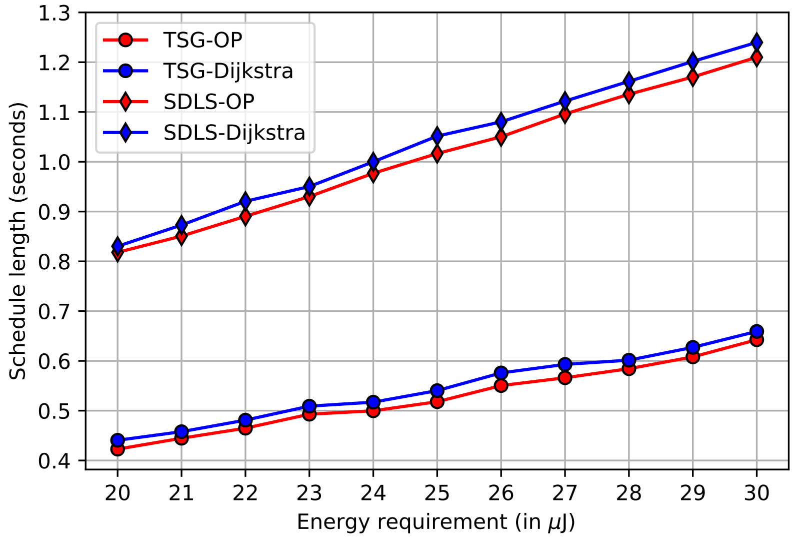

Figure 3.8: Average schedule length with increasing energy requirements.

LP (3.11) and W-Dijkstra becomes larger as traffic demand increases; see Figure 3.9. The reason is because W-Dijkstra computes longer paths. Recall that W-Dijkstra computes a path for each session that has the highest weight. Hence, more routers need to be activated to route sessions. Figure 3.10 shows the impact of increasing traffic demands, which ranges from 1 Mb/s to 2.4 Mb/s. There are two to 10 different sessions; see Figure 3.10. The schedule length of TSG-OP and SDLS-OP becomes longer under the same traffic demand $\hat{D}_{st}$. Referring to the link capacity constraint (3.6), a shorter schedule length is achieved when a network requires fewer transmission sets.

Impact of SINR threshold

Here, this section considers five SINR thresholds (in dB): $\gamma_z = \{3, 6, 10, 20, 30\}$. The energy demand of energy-harvesting devices is set to 30 μJ and each flow demand is set to 1 Mb/s. Referring to Figure 3.11, the schedule length of SDLS-OP and SDLS-Dijkstra decreases slightly by 4.81% and 9.2%, respectively. However, the schedule length generated by TSG-OP and TSG-Dijkstra increases significantly by 135% and 120%, respectively. The schedule length of TSG-OP is 60.19%, 54.91%,

Figure 3.9: Average schedule length with increasing traffic demands.

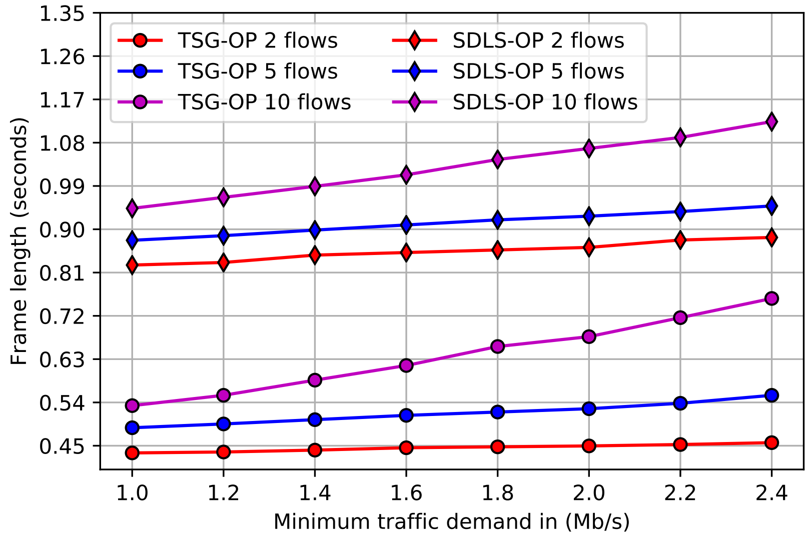

Figure 3.10: Average schedule length with different number of sessions.

47.64%, 16.13% and 3.4% lower than that of SDLS-OP when the SINR threshold is 3, 6, 10, 20 and 30 dB, respectively. This is because a higher SINR threshold γ_z translates to a higher theoretical link capacity, but smaller transmission sets for TSG. As expected, each active router transmits at a higher power to meet the higher γ_z value from 3 to 30 dB. However, each transmission set is smaller, meaning fewer routers are able to charge energy-harvesting devices when the SINR threshold is high. As a result, TSG generates more transmission sets to schedule $|\mathcal{E}|$ links. Moreover, each transmission set is active longer to satisfy the energy demand of energy-harvesting devices. When $\gamma_z = 30$ dB, each transmission set only contains one active router. Hence, for both TSG-OP and TSG-Dijkstra, further increases in SINR threshold do not cause longer schedule lengths. As compared to TSG, SDLS schedules each link into a distinct transmission set for each γ_z. Thus SDLS-OP and SDLS-Dijkstra are able to satisfy the traffic demand of links quicker. In addition, energy-harvesting devices continue to harvest RF energy from one active router in each transmission as each γ_z increases. Consequently, they have a shorter schedule length when links have a higher theoretical capacity.

The difference between the schedule length achieved by LP (3.11) and W-Dijkstra reduces from 3.61% to 0.52%. This is because W-Dijkstra's path is fixed. Hence, if the link capacity increases, routers will require a shorter active time to satisfy the traffic demand of sessions. Hence, the schedule length is mainly affected by the RF-energy harvesting time of energy-harvesting devices. In this respect, W-Dijkstra activates routers that charge the most number of energy-harvesting devices. This in turn improves the energy harvesting rate at energy-harvesting devices. As a result, the schedule length of W-Dijkstra is within 99.48% computed by LP (3.11) after γ_z reaches 30 dB.

Next, this section studies how SINR threshold γ_z affects the schedule length when each $\hat{D}_{st}$ is set to 10 Mb/s. Each energy demand is set to 20 μJ. From Figure 3.12, the schedule length of TSG-OP first gradually reduces from 0.69 to 0.55 as the SINR threshold increases from 3 to 10 dB, and reaches the lowest length at 10 dB. This is because each traffic demand $\hat{D}_{st}$ becomes higher as compared to 1 Mb/s. Further increasing each γ_z results in fewer transmitting routers to charge energy-harvesting devices per transmission set. This indicates a trade-off between network capacity and energy provisioning when using different SINR thresholds.

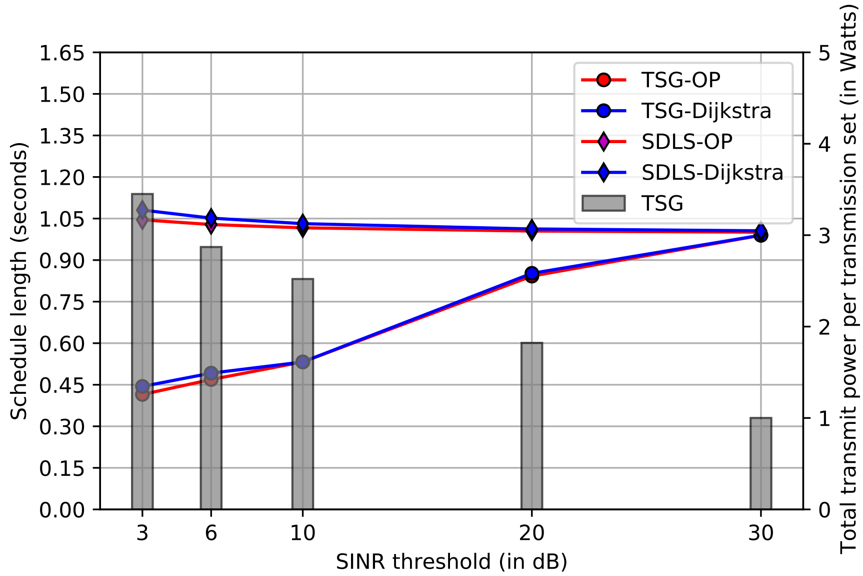

Figure 3.11: Average schedule length with different SINR thresholds for $E_n^{min} = 30$ μJ and $\hat{D}_{st} = 1$ Mb/s.

Number of antennas

To study the impact of antenna numbers, this section sets the traffic demand to 1 Mb/s and the energy demand is set to 20 μJ. The SINR threshold is set to 10 dB. Figure 3.13 shows the schedule length of TSG-OP and SDLS-OP with increasing $|\mathcal{K}_i|$ values. The schedule length of both TSG-OP first decreases, and stops decreasing when there are eight antennas. This is because channel diversity increases when routers have more antennas, which helps energy-harvesting devices harvest energy more efficiently. For instance, the average channel gain used for energy harvesting when $|\mathcal{K}_i| = 9$ is 1.31 times larger than when $|\mathcal{K}_i| = 1$; see Figure 3.13. On the contrary, we see the schedule length of SDLS-OP does not reduce consistently when the number of antennas at routers increases. This is because each antenna has the same transmit power of $\frac{P_{max}}{|\mathcal{K}_i|}$. Hence the transmit power per antenna reduces when

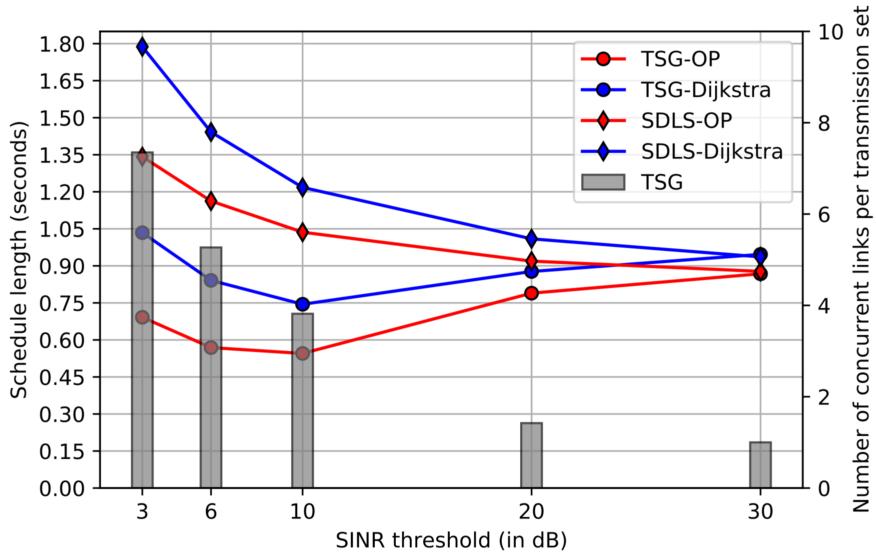

Figure 3.12: Average schedule length with different SINR thresholds for $E_n^{min} = 20$ μJ and $\hat{D}_{st} = 10$ Mb/s.

$|\mathcal{K}_i|$ increases, leading to a poorer received power at energy-harvesting devices from each antenna.

Maximum transmit power

Here, this section studies how the maximum transmit power of routers affects the frame length. To this end, it increases the value of P_{max} from 1 to 5 Watts, with an interval of 0.5. The session demand of each session is 1 Mb/s and the SINR threshold γ_z is 10 dB. Devices have an energy demand of 50 μJ.

Referring to Figure 3.14, when the maximum transmit power of routers increases from 1 to 5 W, the schedule length of TSG-OP, TSG-Dijkstra, SDLS-OP and SDLS-DIjkstra reduces by 84.33%, 82.72%, 84.64% and 83.92%, respectively. This is because energy-harvesting devices harvest more energy as they use a higher energy conversion efficiency; see Figure 3.15 and 3.16. For example, when using TSG, the percentage of received power that falls into the power interval I_3 increases from 6.34% to 28.92%. As devices harvest more energy, the schedule length of TSG is on average 47.43% shorter than that of SDLS. Furthermore, TSG is able to charge 2.96 times more energy-harvesting devices as compared to SDLS. This is because TSG

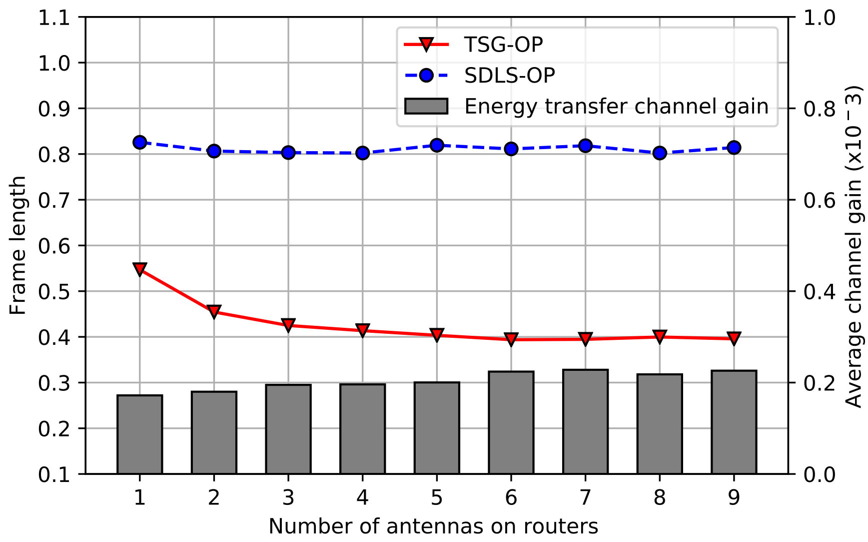

Figure 3.13: Average schedule length with different antenna numbers on routers.

uses multiple routers to cooperatively charge energy-harvesting devices. Hence, TSG requires fewer transmission sets and provides a higher amount of RF energy than SDLS. When the maximum transmit power at routers increases further, the schedule length of TSG-OP and TSG-Dijkstra will not reduce. This is because in MILP (3.20) routers control their transmit power so that energy-harvesting devices are able to harvest RF energy with the highest rate of 60%. Hence, the maximum energy harvested at each energy-harvesting device per second is $10 \times 0.55 = 5.5J$. However, in SDLS-OP and SDLS-Dijkstra, routers transmit at P_{max} Watts in each transmission set. Hence, when the maximum power P_{max} increases, the received power P_n^z at each node also increases as per constraints (3.7) and (3.8). Given that routers use a fixed transmit power, energy-harvesting devices may harvest less energy due to the non-linear energy conversion rate. For instance, the schedule length of SDLS-OP and SDLS-Dijkstra increases when the received power at energy-harvesting devices exceeds ten mW in each transmission set.

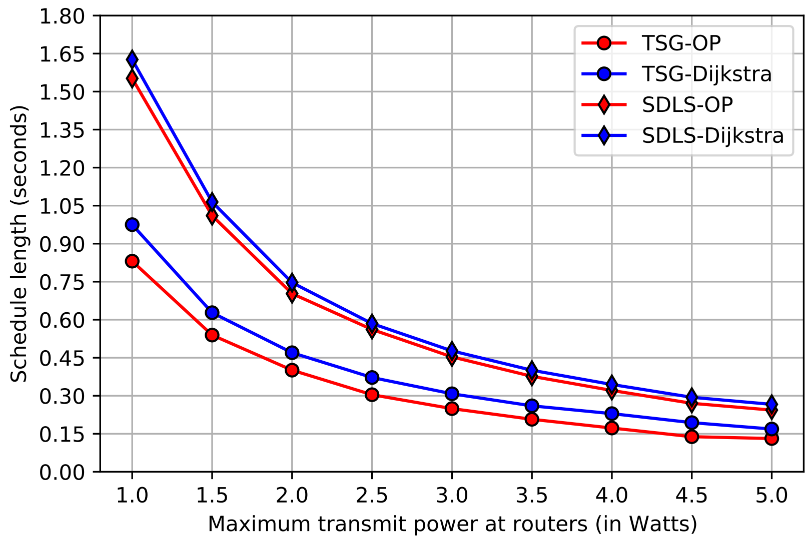

Figure 3.14: Average schedule length with different transmit power at routers.

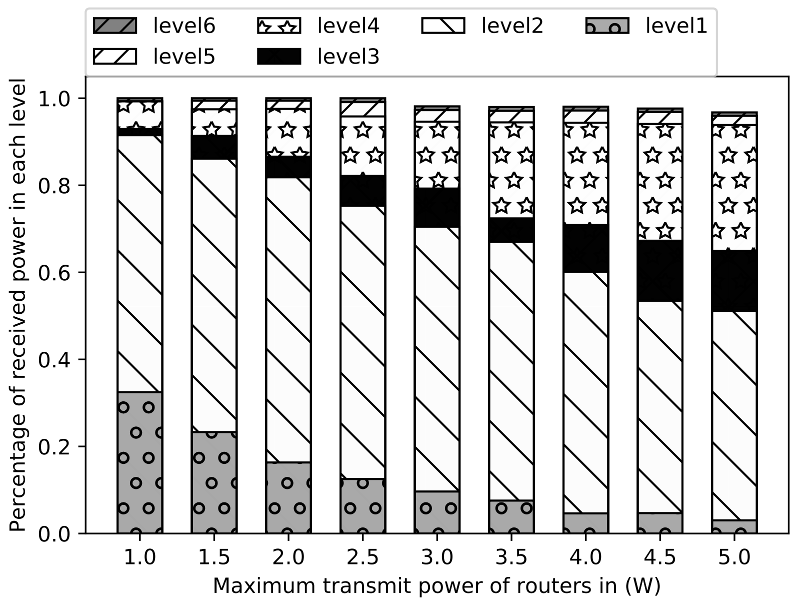

Figure 3.15: Percentage of received power in each power interval with different maximum transmit power of routers for SDLS-OP.

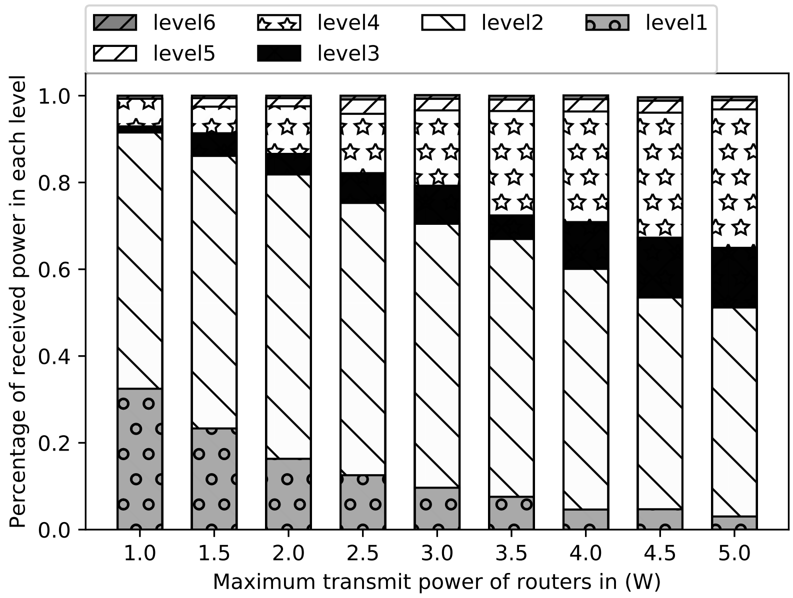

Figure 3.16: Percentage of received power in each power interval with different maximum transmit power of routers for TSG-OP.

Impact of router density

In this experiment, the traffic demand is set to 1 Mb/s and the energy demand is set to 30 μJ, respectively. In addition, routers have a 10-meter transmission range. The SINR threshold is set to 10 dB.

Figure 3.17 shows the schedule length when the number of routers ranges from 20 to 30. The schedule length of TSG-OP, TSG-Dijkstra, SDLS-OP and SDLS-Dijkstra on average reduces by 26.98%, 24.15%, 24.31%, 20.10%, respectively. This is because the number of links grows from 48 to 89 when the number of routers increases from 20 to 30. TSG and SDLS are able to generate more transmission sets when the number of links $|\mathcal{E}|$ becomes larger. For TSG-OP, referring to Figure 3.18, we see that (i) its average number of concurrent links per active transmission set rises from 3.42 to 5.16, (ii) its average total transmit power per active transmission set rises from 2.24 to 2.36 W. As a result, by using additional transmission sets that have more active routers and concurrent links, energy-harvesting devices are able to harvest energy quicker. Moreover, the number of paths increases for each session. This means there is a higher probability of establishing a short path for each session or a path that is able to charge energy-harvesting devices quicker. For SDLS-OP, the schedule length becomes shorter by activating routers that are able to charge more energy-harvesting devices or are located closer to energy-harvesting devices. We see the difference between the schedule length achieved by LP (3.11) and W-Dijkstra becomes larger with additional links. This is because W-Dijkstra computes longer paths that aim to charge more energy-harvesting devices. As a result, W-Dijkstra on average results in longer path lengths with additional links. For instance, the path length per session of 98 links is on average 3.34 times longer than the paths computed for 48 links. In addition, the path weight per session achieved under 98 links is 2.24 times longer than the weight for 48 links. Thus W-Dijkstra results in longer routing time as the number of routers increases. However, W-Dijkstra is able to reduce the required time for charging energy-harvesting devices; see Figure 3.17. Hence, we see a trade-off between charging time and routing time using W-Dijkstra.

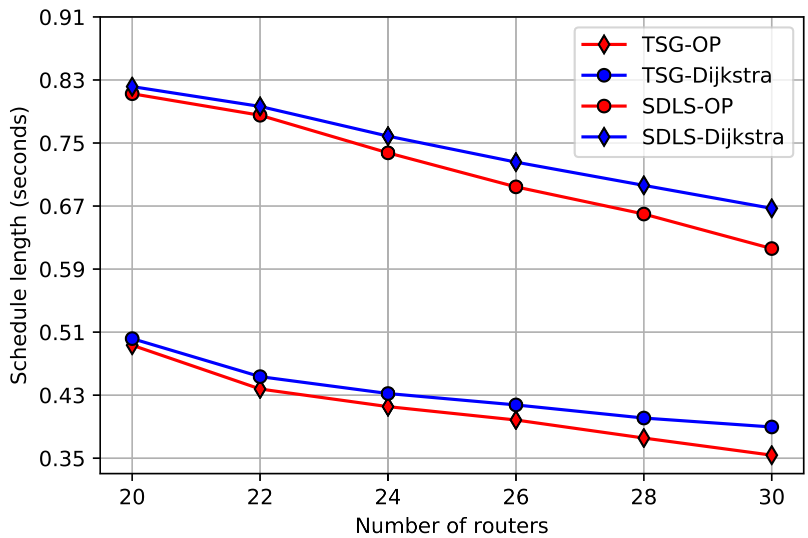

Figure 3.17: Average schedule length with different number of routers.

3.7 Conclusion

This chapter studies a novel challenging problem that requires joint optimization of routing, RF energy charging, transmit power allocation and link scheduling in a two-

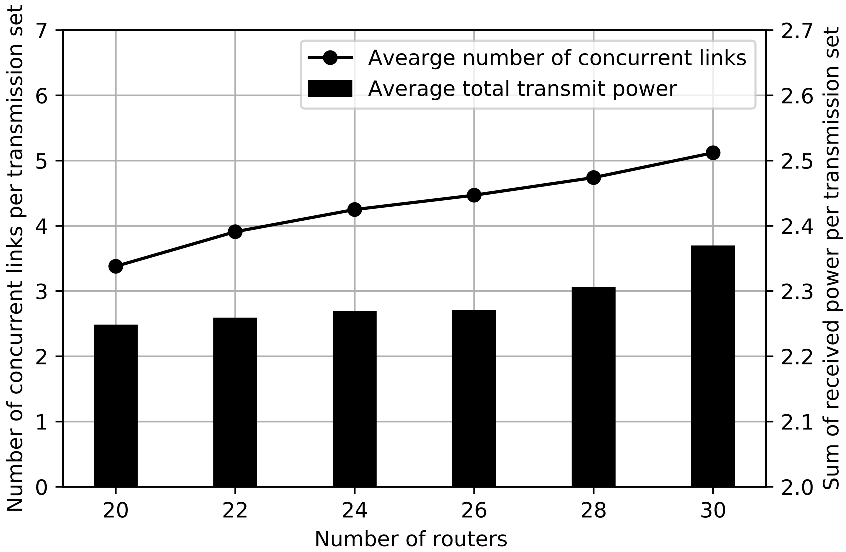

Figure 3.18: Average total transmit power and concurrent links per transmission set using TSG under different number of routers.

tier network. It presents the first LP, heuristic and a novel routing metric to solve the said problem. Advantageously, these solutions can be used to benchmark against future distributed solutions and applied in software defined wireless networks. The results show (i) TSG achieves shorter schedule as compared to other link schedulers, (ii) the proposed novel routing metric yields link schedule lengths that are 75.25% that of the LP solution, (iii) the schedule length is impacted directly by session and energy requirements, (iv) diversity gain improves both wireless power and data transfer.

This chapter only aims to meet the energy demand of energy-harvesting devices operating in tier-2. It does not consider scheduling the transmissions of these devices according to their energy arrival. In addition, it does not consider communication between energy-harvesting devices. To this end, the next chapter considers data transmissions in a multi-hop wireless backhaul with an underlying multi-hop ambient backscattering communication network.

Chapter 4

Data collection in a two-tier IoT network with ambient backscattering tags

This chapter considers data collection in a two-tier IoT network with ambient backscattering tags. The first tier is a wireless backhaul composed of routers and the second tier is an ambient backscattering communication network. The *goal* is to maximize the network throughput in both tiers. The problem at hand is to jointly determine: (i) the active time of each RF link and backscattering link, (ii) the amount of traffic routed by each link, (iii) the data rate of each flow, and (iv) the transmit power/backscattering coefficient of each transmitting router/passive tag. To this end, it outlines a MILP that jointly optimizes routing, link scheduling and transmit power control. As link scheduling is NP-hard [193], it presents a heuristic called ALGO-TSG to compute transmission sets for use by the proposed MILP. In addition, it also outlines a heuristic called CMF to maximize network throughput by jointly considering routing and link scheduling.

To elaborate on the said system and research problem, consider the two-tier IoT network shown in Figure 4.1. Assume there is a flow at *tier-1* from router A to D. It is routed over two paths $A - B - D$ and $A - C - D$. At *tier-2*, there are the following data flows: (i) $a - b - D$, and (ii) $c - d - e$. The *aim* of this chapter is to maximize the flow of router A, tag a and c. Observe that the flow rate of tags, which use backscatter communications, is dependent on the routing of router A. Specifically, the transmissions of these tags are determined by the amount of flow from router A that is routed to router B and C. To elaborate, assume router A only uses path $A-B-D$. This means only tags a and b will be able to backscatter their data. Alternatively, router A can choose to split its traffic by placing its data on both paths $A-B-D$ and $A-C-D$. Consequently, all sources A, a, and c have an opportunity to route data to their respective destination. Note that routers and tags may interfere with each other. Hence, a link schedule, which governs links that are active in each time slot. Further, it determines the capacity of links. This in turn limits the amount of flow on each link.

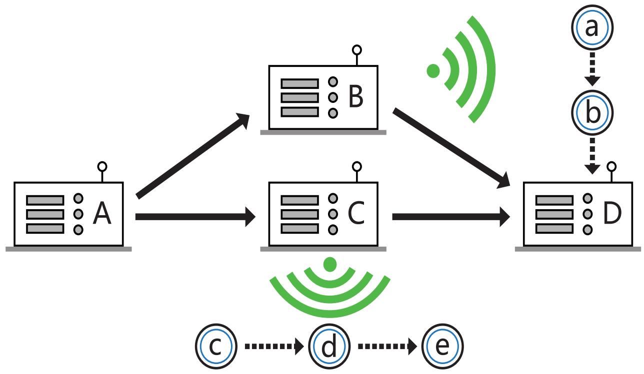

Figure 4.1: An example two-tier network with four routers and five tags. The transmission from router B enables the backscattering communication of tag a and b. Similarly, the transmission of router C enables backscattering communication of tag c, d and e. The routers are located in *tier-1*, whereas tags are in *tier-2*.

In the previous example, we see that there are flows at each tier of the IoT network. Specifically, there are flows from tags to gateways at tier-2, and flows between routers at tier-1. To this end, the *objective* of this chapter is to maximize the sum rate of these flows. This objective is significant because it allows an IoT operator to collect the maximum amount of data from devices. To this end, this chapter aims to (i) *derive a link schedule* that affords high link capacity between routers and also facilitates backscattering between tags. In particular, the link schedule will determine when routers transmit, and in turn, determines the set of backscattering links enabled by router transmissions. Further, when deriving a link schedule, a major problem is to ensure routers use a transmit power that minimizes co-channel interference, and provides sufficient power to tags for backscattering. Further, a short link schedule ensures a high link capacity, meaning links are able to transmit frequently [194], and (ii) *multi-hop routing*, which governs the flow between routers and their transmission time. Critically, the routing adopted by routers determines how often their surrounding tags initiate backscatter communications to forward sensed data. As we will see later, the routing adopted by routers has a direct impact on the link schedule, which in turn affects the transmission rate of both routers and tags.

The remainder of the chapter is organized as follows. Section 4.1 presents system model. The problem is formulated as an MILP in Section 4.2. Section 4.3 and 4.4 present the details of ALGO-TSG and CMF, respectively. The computational complexity of MILP, ALGO-TSG and CMF are discussed in Section 4.5. Section 4.6 presents simulation results. Section 4.7 concludes this chapter.

4.1 Preliminaries

4.1.1 Network Model

Consider a network or graph $\mathcal{G}(\mathcal{V}, \mathcal{E})$, where $\mathcal{V}$ is the set of nodes, and $\mathcal{E}$ contains links. There are two types of nodes: (i) routers at *Tier-1*, and (ii) tags at *Tier-2*. Let $\mathcal{V}_R$ and $\mathcal{V}_T$ denote the set of routers and tags, respectively; hence, $\mathcal{V} = \mathcal{V}_R \cup \mathcal{V}_T$. Let x or y denote either a router or a tag, i refers to a router, and n represents a tag. Each node x has a transmission range R_x. Let d_{xy} denote the Euclidean distance between transmitter x and receiver y. All neighbors of router or tag x are recorded in set $\mathcal{N}_x$, where $\mathcal{N}_x = \{y \mid d_{xy} \leq R_x, \ y \in \mathcal{V}\}$. Tags have no battery/energy storage. They rely solely on the transmissions of routers for communications. Define the set $\mathcal{N}(n)$ to record routers that enable tag n to backscatter, where $\mathcal{N}(n) = \{i \mid d_{in} \leq R_i,\ i \in \mathcal{V}_R\}$. All tags have an omni-directional antenna, and they are half-duplex.

Routing is carried out at both tiers, where at *Tier-1*, source routers forward traffic to their corresponding destination router, and similarly at *Tier-2*, source tags route their traffic to a corresponding destination tag or router. Lastly, let $\mathcal{T}$ be a set of discrete time slots indexed by $t \in \{1, \ldots, |\mathcal{T}|\}$. For convenience, assume each time slot has duration $\tau = 1$ second. Table 4.1 lists necessary notations.

4.1.2 Link Types

Let l_{xy} denote a link in $\mathcal{E}$, where $x, y \in \mathcal{V}$. There are three types of links in set $\mathcal{E}$: *inter-router*, *backscattering*, and *power*. These link types are defined as follows:

- *Inter-router*. Routers communicate via an *inter-router* link. Record all *inter-router* links in the set $\mathcal{E}_R$, where $\mathcal{E}_R = \{l_{ij} \mid d_{ij} \leq R_i, \forall i, j \in \mathcal{V}_R\}$. As an example, Figure 4.1 has $\mathcal{E}_R = \{l_{AB}, l_{AC}, l_{BD}, l_{CD}\}$.

- *Backscattering* links. Tags communicate over *inter-tag* backscattering links, and use an *uplink* to communicate with a router. They are recorded in the set $\mathcal{E}_B$, where $\mathcal{E}_B = \{l_{nx} \mid d_{nx} \leq R_n, \forall n \in \mathcal{V}_T, x \in \mathcal{V}\}$. For example, Figure 4.1 has $\mathcal{E}_B = \{l_{ab}, l_{cd}, l_{de}, l_{bD}\}$.

- *Power links*. These links are used by routers to transmit a dedicated RF signal to enable backscattering between tags. These *power* links are recorded in the set $\mathcal{E}_P$, where $\mathcal{E}_P = \{l_{in} \mid d_{in} \leq R_i, \forall i \in \mathcal{V}_R, n \in \mathcal{V}_T\}$.

4.1.3 Router Model

The routers in the set $\mathcal{V}_R$ are half-duplex. They transmit on channel f_1, and have an omni-directional antenna. In each time slot, a router activates either an *inter-router* link or a *power* link. For each router i, its transmit power is p_i, which is bounded

Table 4.1: A summary of notations

1.	**Sets**
$\mathcal{V}$	A set of nodes
$\mathcal{V}_R$	A set of routers
$\mathcal{V}_T$	A set of tags
$\mathcal{E}$	A set of all type of links
$\mathcal{E}_R$	A set of directed *inter-router* links
$\mathcal{E}_B$	A set of directed *backscattering* links
$\mathcal{E}_P$	A set of directed *power* links
$\mathcal{F}_R$	A set of sessions where routed via *inter-router* links
$\mathcal{F}_T$	A set of sessions where routed via *backscattering* links
$\mathcal{T}$	A set of discrete time slots
2.	**Constants**
$\mathcal{S}$	A collection of router transmission sets
$\mathcal{S}^z$	The z-th router transmission sets in collection $\mathcal{S}$
$\mathcal{B}$	A collection of backscattering sets
$\mathcal{B}^z_m$	The m-th backscattering sets derived from $\mathcal{S}^z$
p^z_i	The transmit power of router i in $\mathcal{S}^z$
P^z_{nxm}	The received power of backscatter x from the transmitting backscatter n in $\mathcal{B}^z_m$
C^z_{ij}	The capacity of RF link l_{ij} in $\mathcal{S}^z$
C^z_{nxm}	The capacity of backscattering link l_{nx} in $\mathcal{B}^z_m$
τ	Duration of each time slot
G_{ij}	Channel gains from router i to the router j in slot t
γ	The SINR threshold for RF links
θ	The SINR threshold for backscattering links
σ	Noise power
P_{max}	The maximum transmit power of a router
d_{ij}	The Euclidean distance between transmitter i and receiver j
a^z_{ij}	An indicator to show whether an *inter-router* link l_{ij} exists in transmission set $\mathcal{S}^z$
b^z_{nym}	An indicator to show whether a *backscattering* link l_{nx} exists in transmission set $\mathcal{B}^z_m$
3.	**Variables**
α^z_t	The activation of transmission set $\mathcal{S}^z$ in slot t
x^z_{mt}	The activation of backscattering set $\mathcal{B}^z_m$ in slot t
f^{st}_{ij}	Traffic fraction of session s on *inter-router* link l_{ij}
$\hat{f}^{st}_{nx}$	Traffic fraction of session s on *backscattering* link l_{nx}
$\hat{r}^s_n$	The data generated at source tag n of session s
r^s_i	The data generated at a source router i of session s

by P_{max}. Formally, the transmit power of each router must satisfy

$$0 \leq p_i \leq P_{max}, \forall i \in \mathcal{V}_R. \tag{4.1}$$

This chapter assumes Rayleigh fading for *inter-router* links [187]; i.e., it assumes environments with multi-path propagation. Let G_{ij}^t denote the channel power gain of the link between transmitter i and receiver j. Formally, it is

$$G_{ij} = \chi\alpha \left(\frac{d_{ij}}{d_0}\right)^{\beta}, \forall l_{ij} \in \mathcal{E}_R, \tag{4.2}$$

where χ is an Exponential distributed random variable with unit mean, where α is the path-loss at reference distance d_0 meter, and β is the path loss exponent.

4.1.4 Backscattering Links

As tags have a short communication range, this chapter only considers line-of-sight and free space propagation for backscattering communications [53]. They backscatter over frequency f_2. A *backscattering* link in set $\mathcal{E}_B$ only exists when the incident power of transmissions from routers at a tag is higher than the sensitivity threshold Ψ_{min}. As per [54], a modified Friis equation is employed to model the channel of backscattering links in set $\mathcal{E}_B$ and power links in set $\mathcal{E}_P$. The total received power P_n at tag n is calculated as

$$P_n = \sum_{i \in \mathcal{N}(n)} p_i \left(\frac{\lambda}{4\pi d_{in}}\right)^2, \forall n \in \mathcal{V}_T, \tag{4.3}$$

where λ denotes the wavelength. Note, Eq. (4.3) assumes tag n is able to backscatter multiple RF-signals from active routers in the set $\mathcal{N}(n)$.

Consider a tag n that is backscattering signals from routers. The received power of these signals at a neighboring router or tag x depends on P_n and is formally defined as

$$P_{nx} = P_n \rho_n \left(\frac{\lambda}{4\pi d_{nx}} \right)^2, \tag{4.4}$$

where $\rho_n \in [0, 1]$ is the backscattering coefficient of tag n when it transmits to receiver node x. This coefficient allows a tag to attenuate its backscattered power.

A set of backscattering links are created for each set of transmitting routers and transmit power configuration. Specifically, each set of *inter-router* links induces a corresponding set of backscattering links. Moreover, each transmit power setting of the said *inter-router* links yields a set of backscattering links. Let $\mathcal{S}^z$ denote a transmission set that contains a set of *inter-router* and *power* links, where z is its index. Define set $\mathcal{R}(\mathcal{S}^z)$ to contain the transmitting router of each link in transmission set $\mathcal{S}^z$. Let $\mathcal{P}(\mathcal{S}^z)$ record the transmit power of each router of links in set $\mathcal{S}^z$. Next, define a backscatter communication graph as $\mathcal{G}_{\mathcal{S}^z}(\mathcal{V}^z, \mathcal{E}_B^z)$, where $\mathcal{V}^z$ is a set of transmitting tags and their receiver. The set $\mathcal{E}_B^z$ contains *backscattering* links that are enabled by one or more routers in set $\mathcal{R}(\mathcal{S}^z)$, where $\mathcal{E}_B^z = \{l_{nx} | P_{nx} \geq \Psi_{min}, l_{nx} \in \mathcal{E}_B\}$. This means the incident power at the receiver of each link l_{nx} in set $\mathcal{E}_B^z$ meets a given receiver sensitivity Ψ_{min}. Note that in set $\mathcal{E}_B^z$, each P_{nx} is calculated as per Eq. (4.3) and (4.4).

Lastly, this section makes a few remarks. One main concern is that tags must be able to extract data from backscattered signals in the presence of ambient RF-signals. Hence, assume all tags are equipped with frequency shifting capability as per [44]. It allows a tag to shift a router's transmission frequency f_1 to f_2, where frequency f_1 and f_2 are orthogonal to one another. This means a *backscattering* link and an *inter-router* link do not interfere with each other. Hence, they are able to co-exist in the same time slot. In addition, as reported in [72], RF-signals from multiple routers may combine either constructively or destructively. To this end, methods such as [72] can be used to ensure the phases of RF-signals emitted by routers add constructively at tags.

4.1.5 Link Schedule Model

Recall that *inter-router* and *backscattering* links do not interfere because they operate on frequency f_1 and f_2, respectively, whereby $f_1 \neq f_2$. Hence, a fundamental problem is to ensure links operating on the same frequency do not interfere. To this end, define two transmission sets: (i) router transmission sets – they consist of non-interfering *inter-router* and *power* links, (ii) backscattering sets – they consist of non-interfering *backscattering* links. Next, the following sections make specific these transmission sets, and define constraints relating to active transmission sets in each time slot.

Router transmission sets

In total, there are $|\mathcal{S}|$ router transmission sets. Define a collection of router transmission sets as $\mathcal{S} = \{\mathcal{S}^1, \mathcal{S}^2, \ldots, \mathcal{S}^{|\mathcal{S}|}\}$; the z-th transmission set is $\mathcal{S}^z$. Let indicator $a_{ij}^z \in \{0, 1\}$ indicate whether a link l_{ij} exists in transmission set $\mathcal{S}^z$. Specifically, it equals one when link l_{ij} exists in transmission set $\mathcal{S}^z$. Otherwise, it equals zero.

Inter-router links must adhere to the physical interference model [112]. Specifically, a set of *inter-router* links that belong to transmission set $\mathcal{S}^z$ must meet a common Signal-to-Interference-Noise Ratio (SINR) threshold γ^z. In this respect, denote the theoretical capacity for SINR threshold γ^z as C_{ij}^z, which can be calculated using the Shannon-Hartley theorem. For each *inter-router* link l_{ij}, the SINR at receiver j must satisfy

$$\frac{p_i^z G_{ij}}{\sum_{u \in \mathcal{V}_R \setminus i} p_u^z G_{uj} + \sigma} \geq \gamma^z, \forall l_{ij} \in \mathcal{S}^z, \tag{4.5}$$

where the numerator is the received power at receiver j of link l_{ij}, and the denominator is the interference from other active routers with background noise σ. In addition, let p_i^z denote the transmit power of router i in transmission set $\mathcal{S}^z$.

Note that interfering *inter-router* links and *power* links must not be activated simultaneously in the same transmission set. Otherwise, activating *power* links will reduce network capacity because they carry no information and can interfere with data links. Hence, the last transmission set in collection $\mathcal{S}$ activates all *power* links simultaneously with maximum transmit power.

Backscattering transmission sets

A backscattering set contains backscattering links that are *only* activated whenever a router transmission set is active. Each router transmission set $\mathcal{S}^z$ results in a communication graph between tags; i,e., the transmitting routers in $\mathcal{R}(\mathcal{S}^z)$ enable a subset of backscattering links in $\mathcal{E}_B^z$. The goal of a link scheduler is to schedule all *backscattering* links in set $\mathcal{E}_B^z$ into a set of backscattering sets. Define M^z as the number of backscattering sets for a given router transmission set $\mathcal{E}_B^z$. Denote by $\mathcal{B}_m^z$ as the m-th backscattering sets. The collection of backscattering sets for transmission set $\mathcal{S}^z$ is defined as $B(\mathcal{S}^z) = \{\mathcal{B}_1^z, \mathcal{B}_2^z, \ldots, \mathcal{B}_{M^z}^z\}$. In addition, let indicator $b_{nxm}^z \in \{0, 1\}$ equal one if link l_{nx} exists in the backscattering set $\mathcal{B}_m^z$.

This chapter employs the physical interference model [112] to construct backscattering sets. Let θ^z be the SINR threshold for the collection of backscattering sets $B(\mathcal{S}^z)$. Formally, for each backscattering link l_{nx} in set $\mathcal{B}_m^z$, its SINR must satisfy

$$\frac{P_{nxm}^z}{\sum_{u\in\mathcal{V}_T\backslash n} P_{uym}^z + \sigma} \geq \theta_m^z, \forall l_{nx} \in \mathcal{B}_m^z, \tag{4.6}$$

where P_{nxm}^z denotes the received power of link l_{nx} at receiver x when tag n transmits in backscattering set $\mathcal{B}_m^z$.

To illustrate the construction of backscattering sets, see an example with topology in Figure 4.2. There are three router transmission sets: $\mathcal{S}^1 = \{l_{AB}\}$, $\mathcal{S}^2 = \{l_{BA}\}$ and $\mathcal{S}^3 = \{l_{Aa}, l_{Ba}\}$ Here, set $\mathcal{S}^3$ contains two *power* links. For transmission set $\mathcal{S}^1$, its router set is $\mathcal{R}^1 = \{A\}$. This in turn creates a graph $\mathcal{G}_{\mathcal{R}^1}(\mathcal{V}^1, \mathcal{E}_B^1)$, where set $\mathcal{E}_B^1 = \{l_{ab}, l_{aB}\}$. The corresponding collection of backscattering sets is $B(\mathcal{S}^1) = \{\mathcal{B}_1^1, \mathcal{B}_2^1\}$, where $\mathcal{B}_1^1 = \{l_{ab}\}$ and $\mathcal{B}_2^1 = \{l_{aB}\}$. Similarly for transmission set $\mathcal{S}^2$, there is $B(\mathcal{S}^2) = \{\mathcal{B}_1^2, \mathcal{B}_2^2\}$, where $\mathcal{B}_1^2 = \{l_{ab}\}$, and $\mathcal{B}_2^2 = \{l_{aA}\}$. Lastly, for set $\mathcal{S}^3$, there is $\mathcal{S}_1^3 = \{l_{ab}\}$.

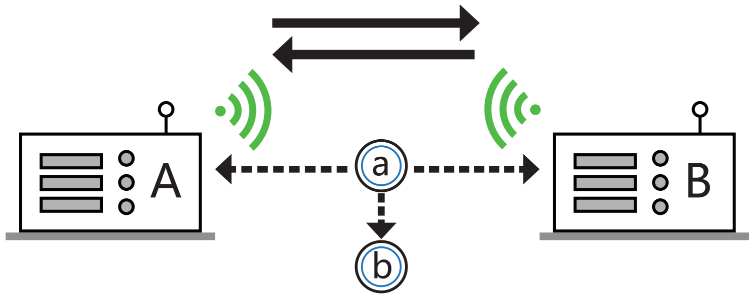

Figure 4.2: An example topology. Each arrow denotes an RF-signal. Each dash arrow denotes a backscattered signal. Tag b only receives from tag a.

Transmission sets activation

Define a binary variable $\alpha_t^z = \{0, 1\}$. It is equal to one when transmission set $\mathcal{S}^z$ is active in time slot t. Formally, for each time slot, transmission sets satisfy

$$\sum_{z=1}^{|\mathcal{S}|} \alpha_t^z = 1, \forall t \in \mathcal{T}. \tag{4.7}$$

Next, in each time slot, the active transmission set $\mathcal{S}^z$ allows one or multiple backscattering sets in collection $B(\mathcal{S}^z)$ to be active. Let $\mathbf{x}_t^z = [x_{1t}^z, x_{1t}^z, \ldots, x_{|M^z|t}^z]$ record the active time of each backscattering set that exists in collection $B(\mathcal{S}^z)$, where $x_{mt}^z \in [0, 1]$ denotes the active time of backscattering set $\mathcal{B}_m^z$ in time slot t. Note that in each time slot, the total active time of all backscattering set in collection $B(\mathcal{S}^z)$ cannot exceed the active duration of transmission set $\mathcal{S}^z$. Formally, for each time slot, there exists the following activation constraint for all backscattering sets:

$$\sum_{m=1}^{|M^z|} x_{mt}^z = \alpha_t^z, \forall t \in \mathcal{T}, 1 \le z \le |\mathcal{S}|. \tag{4.8}$$

4.1.6 Routing Model

Define $\mathcal{F}$ as a set of sessions, each of which is indexed by $s \in \{1, \ldots, |\mathcal{F}|\}$. Next, for each session s, define its source node and its destination node as S_s and D_s, respectively. Let $\mathcal{F}_R$ represent a set of sessions between routers[1]. Next, let $\mathcal{F}_T$ represent a set of sessions where each source is a tag, and the destination is either another tag or a router. In total, there exists $|\mathcal{F}| = |\mathcal{F}_R| + |\mathcal{F}_T|$.

Inter-router links

This section first considers the flow of sessions in set $\mathcal{F}_R$. The source router S_s of session s generates r^s bits of data over $|\mathcal{T}|$ time slots. Let variable f_{ij}^{st} denote the amount of flow of session s routed on link l_{ij} in time slot t.

The first set of constraints relates to flow conservation. For each session, its source router must transmit all generated data via its outgoing links over $|\mathcal{T}|$ time slots. Let $\mathcal{N}_i^R$ be neighboring routers of router i. Formally, for each session $s \in \mathcal{F}_R$ and its source $i = S_s$, they must satisfy

$$\sum_{t=1}^{|\mathcal{T}|} \sum_{j \in \mathcal{N}_i^R} f_{ij}^{st} = r^s, \tag{4.9}$$

where the left side of Eq. (4.9) is the total flow of session s transmitted by its source router i over duration $|\mathcal{T}|$. Second, for the destination of each session, it must receive all data generated by its source over $|\mathcal{T}|$ time slots. Formally, for each session $s \in \mathcal{F}_R$ and its destination $i = D_s$, they must satisfy

$$\sum_{t=1}^{|\mathcal{T}|} \sum_{j \in \mathcal{N}_i^R} f_{ji}^{st} = r^s. \tag{4.10}$$

For intermediate routers of sessions, their total incoming flow over $|\mathcal{T}|$ time slots must equal their total outgoing flow. Formally, for all sessions $s \in \mathcal{F}_R$, they must

[1] In practice, the sessions between routers are decided by a transport protocol. Further, a transport protocol such as multi-path transmission control protocol (TCP) [195] may create multiple connections to a destination router. In this case, this chapter treats each connection as an independent session.

satisfy

$$\sum_{t=1}^{|\mathcal{T}|} \sum_{j \in \mathcal{N}_i^R} f_{ij}^{st} = \sum_{t=1}^{|\mathcal{T}|} \sum_{j \in \mathcal{N}_i^R} f_{ji}^{st}, \forall i \in \mathcal{V}_R \setminus \{S_s, D_s\}. \tag{4.11}$$

The total data flow of all sessions placed on link l_{ij} cannot exceed its capacity. The capacity of an *inter-router* link depends on its theoretical capacity and the total active time over $|\mathcal{T}|$ time slots. Mathematically, for all time slots $t \in \mathcal{T}$, this is a link capacity constraint as per

$$\sum_{s=1}^{|\mathcal{F}_R|} f_{ij}^{st} \leq \sum_{z=1}^{|\mathcal{S}|-1} a_{ij}^z C_{ij}^z \alpha_t^z, \forall l_{ij} \in \mathcal{E}_R, \tag{4.12}$$

Backscattering links

Let the source tag of session s in $\mathcal{F}_T$ generate $\hat{r}^s$ bits of data over $|\mathcal{T}|$ time slots. Next, let $\hat{f}_{nx}^{st}$ denote the flow of session s routed over *backscattering* link l_{nx} in time slot t. Depending on whether a tag acts as a source, a destination, or an intermediate tag, there is a set of flow conservation constraints for each tag in set $\mathcal{V}_T$. Let $\mathcal{N}_x^T$ denote neighboring tags of a tag/router x. Formally, for each session $s \in \mathcal{F}_T$ and its source tag $n = S_s$, they must satisfy

$$\sum_{t=1}^{|\mathcal{T}|} \sum_{y \in \mathcal{N}_n} \hat{f}_{nx}^{st} = \hat{r}^s. \tag{4.13}$$

For each session $s \in \mathcal{F}_T$ and its destination $x = D_s$, formally, they must meet

$$\sum_{t=1}^{|\mathcal{T}|} \sum_{y \in \mathcal{N}_x^T} \hat{f}_{yx}^{st} = \hat{r}^s. \tag{4.14}$$

For intermediate tags of each session $s \in \mathcal{F}_T$, formally, they satisfy

$$\sum_{t=1}^{|\mathcal{T}|} \sum_{x \in \mathcal{N}_n^T} \hat{f}_{nx}^{st} = \sum_{t=1}^{|\mathcal{T}|} \sum_{x \in \mathcal{N}_n^T} \hat{f}_{xn}^{st}, \forall n \in \mathcal{V}_T \setminus \{S_s, D_s\}. \tag{4.15}$$

Lastly, the total flow over a *backscattering* link cannot exceed its total capacity in each time slot. The capacity of each *backscattering* link l_{nx} depends on its total active time in each backscattering set. Mathematically, there is the following link capacity constraint for all backscattering links $l_{nx} \in \mathcal{E}_B$ and for all $t \in \mathcal{T}$,

$$\sum_{s=1}^{|\mathcal{F}_T|} \hat{f}_{nx}^{st} \leq \sum_{z=1}^{|\mathcal{S}|} \sum_{m=1}^{M^z} b_{nxm}^z C_{nxm}^z x_{mt}^z, \tag{4.16}$$

where C_{nxm}^z denotes the theoretical capacity of *backscattering* link l_{nx} that is active in backscattering set $\mathcal{B}_m^z$.

4.2 Problem Definition

The *aim* of this chapter is to maximize the sum of flow rates at both tiers. The key decision variables include: (i) the *amount of data* generated by each source node; namely, r_i^s and $\hat{r}_n^s$, (ii) the *amount of flow* of each session routed over links in set $\mathcal{E}_R$ and $\mathcal{E}_B$; i.e., the quantity f_{xy}^{st} and $\hat{f}_{xy}^{st}$, (iii) the *active time* of each router transmission set and each backscattering set in a time slot; i.e., each α_t^z and x_{mt}^z. Formally, the problem can be formulated as the following MILP:

$$\begin{aligned} \underset{f_{xy}^{st}, \hat{f}_{xy}^{st}, r_i^s, \hat{r}_n^s, \alpha_t^z, x_{mt}^z}{\text{maximize}} \quad & \left(\frac{\sum_{s=1}^{|\mathcal{F}_T|} \hat{r}^s + \sum_{s=1}^{|\mathcal{F}_R|} r^s}{|\mathcal{T}|} \right) \\ \text{subject to} \quad & (4.8) - (4.16). \end{aligned} \tag{4.17}$$

This chapter concludes with a few remarks. First, MILP (4.17) requires a collection of transmission sets and backscattering sets as inputs. Second, MILP (4.17) can be solved by a commercial solver, e.g., Gurobi, for small-scale networks. Note that the optimal solution requires all possible transmission sets. However, the number of transmission sets grows exponentially with network scale $|\mathcal{E}|$. In particular, there are $2^{|\mathcal{E}|}$ possible transmission sets. Indeed, link scheduling is a well-known NP-hard problem [193]. This motivates the development of a heuristic solution named

ALGO-TSG to generate the said collection of transmission sets. Third, MILP (4.17) assumes source nodes are able to split a fractional amount of data onto multiple paths. However, in practice, a source node or router forwards an integral number of packets onto the least-cost path to a destination node.

The next section outlines a heuristic to generate a collection of transmission sets and backscattering sets. These sets are then used by a heuristic called CMF to compute a link schedule. In particular, CMF computes a single path for each session and the amount of data generated by each source. These quantities are then used to determine the transmission and backscattering set that are active in each time slot.

4.3 Heuristic algorithm: ALGO-TSG

ALGO-TSG outputs a collection of transmission sets. It requires the following inputs: (i) network topology, i.e., graph $\mathcal{G}(\mathcal{V}, \mathcal{E})$, and (ii) the SINR threshold for each transmission set, i.e., γ^z and θ^z, and (iii) channel gains.

ALGO-TSG consists of two other supporting algorithms, namely (i) Router Transmission Sets Generator (RTSG), and (ii) Backscattering Sets Generator (BSG). ALGO-TSG first runs RTSG to generate $|\mathcal{S}|$ router transmission sets. It then runs BSG to generate backscattering sets.

4.3.1 Router Transmission Sets Generator (RTSG)

RTSG outputs a collection of router transmission sets $\mathcal{S}$. It has two phases. In *Phase-1*, it constructs transmission sets by greedily adding *inter-router* links that have the highest channel gains. It then uses an LP to check whether a link is able to co-exist with other links in the transmission set. In *Phase-2*, it attempts to add non-interfering *power* links into the transmission sets constructed in *Phase-1*. This aims to activate more *backscattering* links. Apart from that, it creates a router transmission set containing **all** *power* links.

Phase-1 of RTSG

Algorithm 2 details *Phase-1*. In line 2, RTSG uses *SortChannel()* to sort all *inter-router* links in descending order of their channel gains. In lines 3-10, RTSG schedules each *inter-router* link in set $\hat{\mathcal{E}}_R$ once, where the schedules form collection $\mathcal{S}$. In lines 12-23, RTSG includes additional non-interfering *inter-router* links from set $\hat{\mathcal{E}}_R$ into each router transmission set $\mathcal{S}^z$ in collection $\mathcal{S}$. The function *HalfDuplex()* is used to check whether all communications in the selected transmission set $\mathcal{S}^z$ are half-duplex. Specifically, *HalfDuplex*($l_{ij}, \mathcal{S}^z$) returns *False* if neither transmitter i nor receiver j of input link l_{ij} exists in the router transmission set $\mathcal{S}^z$. After that, RTSG calls $\mathbf{LP_1}(\mathcal{S}^{\mathbf{z}}, \gamma^{\mathbf{z}})$ to check whether all links in $\mathcal{S}^z$ meet the SINR threshold γ^z; see line 17. Specifically, $\mathbf{LP_1}()$ outputs a *True* flag if the added link can co-exist with the other *inter-router* links in the input transmission set. Otherwise, $\mathbf{LP_1}()$ outputs a *False* flag.

The function $\mathbf{LP_1}()$ solves an LP to enable the maximum number of backscattering links. Let $\hat{b}_{nx}$ be a binary variable that is set to one if backscatter link l_{nx} can be enabled by router transmissions. Formally, there is the following LP:

$$\underset{p_i^z,\, \hat{b}_{nx}}{\text{maximize}} \quad \sum_{l_{nx} \in \mathcal{E}_B} \hat{b}_{nx} \tag{4.18a}$$

$$\text{subject to} \quad p_i^z \leq P_{max}, \forall i \in \mathcal{R}(\mathcal{S}^z), \tag{4.18b}$$

$$\frac{p_i^z G_{ij}}{\sum_{u \in \mathcal{R}^z \setminus i} p_u^z G_{uj} + \sigma} \geq \gamma^z, \forall l_{ij} \in \mathcal{S}^z, \tag{4.18c}$$

$$P_{nx} - \psi_{min} \geq \Phi(\hat{b}_{nx} - 1), \forall l_{nx} \in \mathcal{E}_B. \tag{4.18d}$$

We see that its objective is to maximize the sum of active backscatter links. To do so, it optimizes the transmit power of routers subject to the following constraints. Constraint (4.18b) ensures that the transmit power of each transmitting router does not exceed P_{max}. Constraint (4.18c) ensures the SINR of all inter-router links must meet the SINR threshold γ^z. Constraint (4.18d) ensures all enabled backscattering links meet a given sensitivity, where tags backscatter with the maximum coefficient

$\rho_n = 1$. Here, the constant Φ is used to disable a constraint, where $\Phi = \Psi_{min}$.

Algorithm 2: *Phase-1 of RTSG.*

Input: $G(\mathcal{V}, \mathcal{E})$, γ^z
Output: $\mathcal{S}$

// Schedule each link once
Set $z = 1$, $\hat{\mathcal{E}_R} = SortChannel(\mathcal{E}_R)$
for $l_{ij} \in \hat{\mathcal{E}_R}$ **do**
    $\mathcal{S}^z = \emptyset$
    $\mathcal{S}^z = \mathcal{S}^z \cup l_{ij}$
    if $z < |\mathcal{E}_R|$ **then**
        $z = z + 1$
        $|\mathcal{S}| = z$
    end
end
// Add additional data links
for $z = 1, \ldots, |\mathcal{S}|$ **do**
    for $l_{ij} \in \hat{\mathcal{E}_R}$ **do**
        if *HalfDuplex* $(l_{ij}, \mathcal{S}^z)$ == *False* **then**
            $\mathcal{S}^z = \mathcal{S}^z \cup l_{ij}$
            $Flag = \mathbf{LP_1}(\mathcal{S}^\mathbf{z}, \gamma^\mathbf{z})$
            if Flag == *False* **then**
                $\mathcal{S}^z = \mathcal{S}^z \setminus l_{ij}$
            end
        end
    end
    $\mathcal{S} = \mathcal{S} \cup \mathcal{S}^z$
end
return $\mathcal{S}$

Phase-2 of RTSG

In lines 3-13 of Algorithm 3, RTSG greedily adds *power* links in order maximize the number of tags in each existing transmission set. The function *SortR2T()* is used to sort links in descending order of their number of neighboring tags. The function *HalfDuplex*($l_{in}, \mathcal{S}^z$) is then used to ensure each transmitting router will not simultaneously have an outgoing *inter-router* link and a *power* link. In lines 15-18, it creates an additional router transmission set to activate all *power* links simultaneously. After that, RTSG terminates and returns a collection $\mathcal{S}$ that contains $|\mathcal{S}|$ router transmission sets.

Algorithm 3: *Phase-2 of RTSG.*

Input: $\mathcal{S}$,γ^z
Output: $\mathcal{S}$
$\hat{\mathcal{E}_P} = SortR2T(\mathcal{E}_P)$
// Add *power* links
for $z = 1, \ldots, |\mathcal{S}|$ **do**
    for $l_{in} \in \hat{\mathcal{E}_P}$ **do**
        if $HalfDuplex(l_{in}, \mathcal{S}^z) == False$ **then**
            $\mathcal{S}^z = \mathcal{S}^z \cup l_{in}$
            $Flag = \mathbf{LP_1}(\mathcal{S}^\mathbf{z}, \gamma^\mathbf{z})$
            if Flag $== False$ **then**
                $\mathcal{S}^z = \mathcal{S}^z \setminus l_{in}$
            end
        end
    end
end
// Include all *power* links
$z = |\mathcal{S}| + 1$, $\mathcal{S}^z = \emptyset$
for $l_{in} \in \hat{\mathcal{E}_P}$ **do**
    $\mathcal{S}^z = \mathcal{S}^z \cup l_{in}$, $p_i^z = P_{max}$
end
$\mathcal{S} = \mathcal{S} \cup \mathcal{S}^z$
return $\mathcal{S}$

4.3.2 Backscattering Sets Generator (BSG)

The basic idea of BSG is to preferentially add *backscattering* links that use the minimum backscattering power to meet the sensitivity threshold Ψ_{min}. BSG aims to enable the largest number of tags to backscatter simultaneously by reducing the interference between tags. For each router transmission set $\mathcal{S}^z$, BSG first depicts the said backscatter communication graph $\mathcal{G}_{\mathcal{S}^z}(\mathcal{V}^z, \mathcal{E}_B^z)$. After BSG adds a *backscattering* link l_{nx} into one backscattering set in collection $B(\mathcal{S}^z)$, it uses an LP to check whether the routers in set $\mathcal{S}^z$ will enable link l_{nx}, and whether link l_{nx} is able to co-exist with the other backscattering links in the backscattering set. BSG terminates after it constructs a collection of backscattering sets for all existing router transmission sets in $\mathcal{S}$.

Algorithm 4 shows the details of BSG. Given each router transmission set $\mathcal{S}^z$, the function *ConstructG()* returns the communication graph derived by set $\mathcal{R}(\mathcal{S}^z)$ and

$\mathcal{P}(\mathcal{S}^z)$, where tags use the maximum backscattering coefficient. Next, BSG greedily adds a *backscattering* link from set $\mathcal{E}_B^z$ into each backscattering set $\mathcal{B}_m^z$; see lines 7-22. The function *MinTx($\mathcal{E}_B^\star$)* returns a link $l_{nx}^\star$ that requires the minimum backscattered power at tag n to meet its receiver sensitivity. The function $\mathbf{LP_2}(\mathcal{B}_\mathbf{m}^\star, \theta_\mathbf{m}^\mathbf{z})$ returns *feasible* when all *backscattering* links in the backscattering set $\mathcal{B}_m^\star$ satisfy the SINR threshold θ_m^z. BSG allows each tag to lower its backscattering coefficient in order to co-exist with other tags. Hence, it also determines the backscattering coefficient of each transmitting tag of links in set $\mathcal{B}_m^\star$ by using the function $\mathbf{LP_2}(\mathcal{B}_\mathbf{m}^\star, \theta_\mathbf{m}^\mathbf{z})$. Links that have been assigned to a backscattering set are then removed from $\mathcal{E}_B^z$ for further consideration. This means BSG only activates each *backscattering* link in set $\mathcal{E}_B^z$ once in each collection $B(\mathcal{S}^z)$.

The function $\mathbf{LP_2}()$ determines the backscattering coefficient at each transmitting tag in set $\mathcal{B}_m^\star$. It solves an LP, where the objective is to maximize the total backscattering coefficient of all tags activated in backscattering set $B_m^\star$. Mathematically, $\mathbf{LP_2}()$ solves the following LP:

$$\underset{\rho_x^\star}{\text{maximize}} \quad \sum_{l_{nx} \in \mathcal{B}_m^\star} \rho_n^\star \tag{4.19a}$$

$$\text{subject to} \quad 0 \leq \rho_n^\star \leq 1, \forall l_{nx} \in \mathcal{B}_m^\star, \tag{4.19b}$$

$$\frac{P_{nx}^\star}{\sum_{u \in \mathcal{V}_T \setminus n} P_{uy}^\star + \sigma} \geq \theta_m^z, \forall l_{nx} \in \mathcal{B}_m^\star, \tag{4.19c}$$

$$P_{nx}^\star \geq \psi_{min}, \forall l_{nx} \in \mathcal{B}_m^\star. \tag{4.19d}$$

Note that the total incident power of RF-signals at backscattering tag n, i.e., P_n, is computed as per Eq. (4.3) given set $\mathcal{P}(\mathcal{S}^z)$. Constraint (4.19b) ensures the backscattering coefficients will not exceed their lower or upper bound. All backscattering links in backscattering set $\mathcal{B}_m^\star$ must satisfy SINR threshold $\theta_m^\star$; see constraint (4.19c). Moreover, constraint (4.19d) states that the backscattering coefficient at tag n must ensure that the incident power at its receiver y meets sensitivity requirement ψ_{min}.

Algorithm 4: *BSG.*

Input: $\mathcal{S}$, θ_m^z
Output: $\mathbf{B}$

// Construct each collection $B(\mathcal{S}^z)$
for $z = 1 \rightarrow |\mathcal{S}|$ **do**
  Set each $\rho_n = 1$
  $\mathcal{G}_{\mathcal{S}^z}(\mathcal{V}^z, \mathcal{E}_B^z)$ = *ConstructG*$(\mathcal{R}(\mathcal{S}^z), \mathcal{P}(\mathcal{S}^z))$
  Set $m = 1$, $\mathcal{B}_m^\star = \emptyset$, $\mathcal{E}_B^\star = \mathcal{E}_B^z$
  // Construct each set $\mathcal{B}_m^z$ in $B(\mathcal{S}^z)$
  while $\mathcal{E}_B^z \neq \emptyset$ **do**
    $l_{nx}^\star$ = *MinTx*$(\mathcal{E}_B^\star)$
    if *HalfDuplex* $(l_{nx}^\star, \mathcal{S}^z \cup \mathcal{B}_m^\star)$ == *False* **then**
      $\mathcal{B}_m^\star = \mathcal{B}_m^\star \cup l_{nx}^\star$
      if $\mathbf{LP_2}(\mathcal{B}_m^\star, \theta_m^z)$ *is infeasible* **then**
        $\mathcal{B}_m^\star = \mathcal{B}_m^\star \setminus l_{nx}^\star$
      end
    end
    $\mathcal{E}_B^\star = \mathcal{E}_B^\star \setminus l_{nx}^\star$
    // Add a new set in $B(\mathcal{S}^z)$
    if $\mathcal{E}_B^\star \neq \emptyset$ **then**
      $\mathcal{E}_B^z = \mathcal{E}_B^z \setminus \mathcal{B}_m^\star$, $\mathcal{E}_B^\star = \mathcal{E}_B^z$
      $B(\mathcal{S}^z) = B(\mathcal{S}^z) \cup \mathcal{B}_m^\star$
      $m = m + 1$, $\mathcal{B}_m^\star = \emptyset$
    end
  end
  $\mathbf{B} = \mathbf{B} \cup B(\mathcal{S}^z)$
end
return B

4.4 Heuristic: CMF

This section outlines a heuristic called Centralized Max-Flow (CMF) to compute the highest flow rates over $|\mathcal{T}|$ time slots. Its basic idea is to iteratively find a path for each session in order to maximize the flow rate at all sessions. CMF has two phases, namely *Phase-1* and *Phase-2*. In *Phase-1*, CMF first finds one or more paths for each session by using a routing protocol. It then routes each session over the shortest path first. The goal of *Phase-2* is to decide a path for each session in order to maximize the flow rate of all sessions. In *Phase-2*, it iteratively uses the next shortest path to route each session. If the next path has a higher flow rate, CMF then updates the session's path. The process ends when CMF is not able to increase the flow rate of all sessions.

Algorithm 5 details the steps of CMF. The collection $\mathcal{H}^s = \{\mathbf{P}_1^s, \mathbf{P}_2^s, \ldots, \mathbf{P}_{H^s}^s\}$ records H^s feasible paths for session s, where the set $\mathbf{P}_m^s$ records all links that support the m-th path for session s. The collection $\mathcal{P} = \{\mathbf{P}^1, \mathbf{P}^2, \ldots, \mathbf{P}^{|\mathcal{F}|}\}$ represents a set of links selected by CMF to route each session; e.g., variable $\mathbf{P}^s$ equals $\mathbf{P}_m^s$ if CMF uses the m-th path for session s. Referring to lines 2-7, CMF routes each session over the shortest path. The function *Sortpath()* is used to sort all feasible paths of a session in ascending order of their number of hops to the session's destination. In line 8, CMF uses *LSM($\mathcal{P}$)* to derive a link schedule $\mathcal{S}^\star$ for links in each set $\mathbf{P}^s$ in collection $\mathcal{P}$; *LSM($\mathcal{P}$)* is presented in Section 4.4.1. It then uses $\mathbf{LP_3}(\mathcal{S}^\star, \mathcal{P})$ to calculate the flow rate of each session in order to maximize the sum of flow rates.

Algorithm 5: *CMF.*

Input: $G(\mathcal{V}, \mathcal{E})$, $\{\mathcal{H}^1, \mathcal{H}^2, \ldots, \mathcal{H}^{|\mathcal{F}|}\}$
Output: $\mathbf{P}$, δ
1 // *Phase-1*
2 **for** $s = 1, \ldots, |\mathcal{F}|$ **do**
3     $\mathcal{H}^s$ = *Sortpath($\mathcal{H}^s$)*
4 **end**
5 **for** $s = 1, \ldots, |\mathcal{F}|$ **do**
6     $\mathbf{P}^s = \mathbf{P}_1^s$
7 **end**
8 $\mathcal{S}^\star = LSM(\mathcal{P})$, $\delta = \mathbf{LP_3}(\mathcal{S}^\star, \mathcal{P})$
9 // *Phase-2*
10 **for** $s = 1, \ldots, |\mathcal{F}_R|$ **do**
11   **for** $m = 2, \ldots, H^s$ **do**
12         $\mathbf{P}^s = \mathbf{P}_m^s$
13         $\mathcal{S}^\star = LSM(\mathcal{P})$, $\delta^\star = \mathbf{LP_3}(\mathcal{S}^\star, \mathcal{P})$
14   **if** $\delta^\star < \delta$ **then**
15             $\mathbf{P}^s = \mathbf{P}_{m-1}^s$
16   *Break*
17   **end**
18         $\delta = \delta^\star$
19   **end**
20 **end**
21 **return** $\mathbf{P}, \delta$

In *Phase-2*, CMF greedily determines a path for each session and calculates the sum of flow rates at both tiers. In lines 10-20, starting from the first session s in

$\mathcal{F}_R$, CMF assigns session s a new path, where it replaces the links in $\mathbf{P}^s$ with those in set $\mathbf{P}^s_m$, meaning CMF routes session s over the m-th path. Note that CMF only changes the path for the selected session s, meaning the paths for other sessions are not changed; see line 12. Next, it uses *LSM($\mathcal{P}$)* to schedule links on the path of each session in $\mathcal{F}_R$. The function $\mathbf{LP_3}(\mathcal{S}^\star, \mathcal{P})$ is used to calculate the maximum sum of flow rate over all sessions. After that, CMF checks whether assigning a new path for session s improves the sum of flow rate at both tiers; see lines 14-17. CMF terminates after it checks all feasible paths for each session in $\mathcal{F}_R$.

The following paragraphs explain $\mathbf{LP_3}()$. Its inputs are the link schedule $\mathcal{S}^\star$ and paths in collection $\mathcal{P}$. It solves a relaxed LP, where it relaxes each binary variable of type α^z_t in formulation (4.17) to be a real number in the range [0,1]. Its objective is to maximize the sum of flow rates of all sessions in both tiers. Mathematically, $\mathbf{LP_3}()$ is defined as

$$\underset{f^{st}_{xy}, \hat{f}^{st}_{xy}, r^s_i, \hat{r}^s_n, x^z_{mt}}{\text{maximize}} \quad \sum_{s=1}^{|\mathcal{F}_T|} \hat{r}^s + \sum_{s=1}^{|\mathcal{F}_R|} r^s \tag{4.20a}$$

$$\text{subject to} \quad \sum_{t=1}^{|\mathcal{T}|} f^{st}_{ij} = h^s_{ij} r^s, \forall s \in \mathcal{F}_R, \forall l_{ij} \in \mathcal{E}_R, \tag{4.20b}$$

$$\sum_{t=1}^{|\mathcal{T}|} f^{st}_{nx} = h^s_{nx} \hat{r}^s, \forall s \in \mathcal{F}_T, \forall l_{nx} \in \mathcal{E}_B, \tag{4.20c}$$

$$(4.8), (4.12), (4.16). \tag{4.20d}$$

The new constraint (4.20b) and (4.20c) ensure flow conservation on each *inter-router* link and *backscattering* link. Specifically, the indicator $h^s_{ij} \in \{0, 1\}$ and $h^s_{nx} \in \{0, 1\}$ equal one if link l_{ij} and l_{nx} support the path used to route session s.

4.4.1 Link Scheduling Module (LSM)

The function *LSM()* aims to find a link schedule that ensures all source nodes are able to forward data over a *given* path. The function *LSM()* has two main steps. First, it generates a weight-aware link schedule that activates links used by one or

Algorithm 6: *LSM.*

Input: $\mathcal{P}$, $\mathcal{S}$

Output: $\mathcal{S}^\star$

$\mathcal{S}^\star = \emptyset$, $[\mathcal{U}_R, \mathcal{U}_T] = \mathit{UseLink}(\mathcal{P})$, $K = 1$
// Schedule each link once
while $\mathcal{U}_R \neq \emptyset$ **do**
  $z = \mathit{Index}(\mathcal{S}, \mathcal{U}_R)$
  for $k = K, \ldots, K + \mathbf{W}(\mathcal{S}^z)$ **do**
    $y_k = z$
  end
  $K = K + \mathbf{W}(\mathcal{S}^z)$, $\mathcal{U}_R = \mathcal{U}_R \setminus \mathcal{S}^z$ $\mathcal{U}_T = \mathcal{U}_T \setminus \mathcal{E}_B^z$
end
if $\mathcal{U}_T \neq \emptyset$ **then**
  $K = K + 1$, $y_K = |\mathcal{S}|$
end
// Repeat link schedule
for $t = 1 \ldots, |\mathcal{T}|$ **do**
  $k = t \ mod \ K$
  if $k \neq 0$ **then**
    $z = y_k$, $\mathcal{S}^\star = \mathcal{S}^\star \cup \mathcal{S}^z$
  else
    $z = |\mathcal{S}|$, $\mathcal{S}^\star = \mathcal{S}^\star \cup \mathcal{S}^z$
  end
end
return $\mathcal{S}^\star$

more paths at least once. The weight-aware schedule prioritizes links that are used in more paths as these links must be activated more often. Next, the computed link schedule then repeats periodically over $|\mathcal{T}|$ time slots.

First define the weight of each link. Specifically, the weight of link l_{ij} is defined as the number of paths in collection $\mathcal{P}$ that are supported by link l_{ij}. Let the weight of link l_{ij} be W_{ij}. Formally, it is calculated as per

$$W_{ij} = \sum_{s=1}^{\mathcal{F}_R} h_{ij}^s, \forall l_{ij} \in \mathcal{E}. \tag{4.21}$$

Next, define the weight of transmission set $\mathcal{S}^z$. Formally, it is calculated as per

$$W(\mathcal{S}^z) = \max\{W_{ij}\}_{l_{ij} \in \mathcal{S}^z}. \tag{4.22}$$

Algorithm 6 implements *LSM()*. It uses the collection of transmission sets $\mathcal{S}$ constructed by ALGO-TSG. The function *UseLink()* is used to extract all *inter-router* links and *backscattering* links recorded in each set of collection $\mathcal{P}$. These *inter-router* links and *backscattering* links are recorded in set $\mathcal{U}_R$ and $\mathcal{U}_T$, respectively. Next, in lines 3-12, the function *LSM()* derives a weight-aware link schedule, which activates links in $\mathcal{U}_R$ and $\mathcal{U}_T$ at least once. Let K denote the schedule length of the weight-aware link schedule, which is set to one initially. Each slot is indexed by k. In line 4, the function *Index*($\mathcal{S}$,$\mathcal{U}_R$) is used to return the index of the transmission set in collection $\mathcal{S}$ that matches the most number of links in set $\mathcal{U}_R$. Next, in lines 5-7, the corresponding transmission set $\mathcal{S}^z$ is activated in $\mathbf{W}(\mathcal{S}^z)$ time slots. This aims to improve the capacity of bottleneck links. Specifically, the index of active transmission set in slot k is recorded as y_k; see line 6. Next, the function *LSM()* adds an additional slot that consists of power links to activate any backscattering links not enabled by RF links; see lines 10-12. In lines 14-21, the function *LSM()* repeats the weight-aware link schedule in all time slots in set $\mathcal{T}$. For instance, the router transmission set activated in the first time slot is also activated in the $(K + 1)$-th time slot.

4.4.2 Discussion

This section concludes with some remarks on the implementation of CMF. Recall that CMF computes the following quantities: (i) the path used by each session, (ii) the amount of data generated by each source, (iii) the amount of traffic routed over each RF/backscattering link, (iv) a schedule that includes the transmission time of RF/backscattering links. Moreover, ALGO-TSG has computed the corresponding transmit power of routers and the backscattering coefficient of tags. In practice, these quantities can be programmed into routers and tags; e.g., routers can be configured to transmit at the computed power and at their assigned transmission time. Also, note that CMF can be run by a controller/gateway in software-defined wireless networks [189]. Specifically, the controller first runs CMF to compute the said quantities, then configures each router/backscatter accordingly. For example, it can install rules at routers to ensure sessions are routed on a computed path.

4.5 Analysis

This section presents (i) the total number of decision variables and constraints of MILP (4.17), (ii) the number of times ALGO-TSG calls MILP (4.18) and LP (4.19), which affects the computation time of ALGO-TSG, (iii), the total number of decision variables and constraints in LP (4.20), which affects the computation time of heuristic CMF, and (iv) the run-time complexity of heuristic CMF.

Proposition 6. *MILP* (4.17) *has* $|\mathcal{S}||\mathcal{T}|(M^z+1)+|\mathcal{F}|+|\mathcal{T}|(|\mathcal{E}_R||\mathcal{F}_R|+|\mathcal{E}_B||\mathcal{F}_T|)$ *decision variables and* $|\mathcal{F}_R||\mathcal{V}_R|+|\mathcal{F}_T||\mathcal{V}_T|+|\mathcal{T}|(|\mathcal{E}_B|+|\mathcal{E}_R|+|\mathcal{S}|+1)$ *constraints.*

Proof. First consider the number of decision variables in MILP (4.17). The decision variable α_t^z exists for each router transmission set and time slot. This gives $|\mathcal{S}||\mathcal{T}|$ decision variables of type α_t^z. Each transmission set $\mathcal{S}^z$ supports M^z backscattering sets, which gives $|\mathcal{S}||\mathcal{T}|M^z$ decision variables of type x_{mt}^z. Next, the number of decision variable r^s and $\hat{r}^s$ is equal to the number of sessions, i.e., $|\mathcal{F}_R|$ and $|\mathcal{F}_T|$. For each *inter-router* link l_{ij} and *backscattering* link l_{nx}, variable f_{ij}^{st} and $\hat{f}_{nx}^{st}$ are used to represent the traffic of session s routed over the link in each time slot t. Hence, there are $|\mathcal{E}_R||\mathcal{T}||\mathcal{F}_R|$ decision variables of type f_{nx}^{st} and $|\mathcal{E}_B||\mathcal{T}||\mathcal{F}_R|$ decision variables of type $\hat{f}_{nx}^{st}$. In total, there are $|\mathcal{S}||\mathcal{T}|(M^z+1)+|\mathcal{F}|+|\mathcal{T}|(|\mathcal{E}_R||\mathcal{F}_R|+|\mathcal{E}_B||\mathcal{F}_T|)$ decision variables, as claimed.

Next, consider the constraints of MILP (4.17). There is a constraint (4.7) for each time slot t, and constraint (4.8) for each router transmission set and time slot. This gives $|\mathcal{T}|(1+|\mathcal{S}|)$ constraints of type (4.7) and (4.8) in total. Next, there is a flow conservation constraint for the source node, destination node and each relay node of each session. Hence, there are $|\mathcal{F}_R||\mathcal{V}_R|$ constraints of type (4.9), (4.10) and (4.11), and $|\mathcal{F}_T||\mathcal{V}_T|$ constraints of type (4.13), (4.14) and (4.15) in total. Next, each *inter-router* link and *backscattering* link has a capacity constraint for each time slot. Hence, there are $|\mathcal{E}_R||\mathcal{T}|$ constraints of type (4.12), and $|\mathcal{E}_B||\mathcal{T}|$ constraints of type (4.16), respectively. In total, there are $|\mathcal{F}_R||\mathcal{V}_R|+|\mathcal{F}_T||\mathcal{V}_T|+|\mathcal{T}|(|\mathcal{E}_B| + |\mathcal{E}_R| + 1 + |\mathcal{S}|)$ constraints for MILP (4.17). This completes the proof. □

The next proposition shows the number of decision variables and constraints for LP (4.20), which is used by CMF to derive the flow rate of each session.

Proposition 7. *ALGO-TSG calls MILP (4.18) exactly* $|\mathcal{E}_R|(|\mathcal{E}_R| + |\mathcal{E}_P|)$ *times and LP (4.19)* $|\mathcal{S}|\frac{|\mathcal{E}_B|(1+|\mathcal{E}_B|)}{2}$ *times in the worst case.*

Proof. Referring to Algorithm 2, in *Phase-1*, ALGO-TSG calls MILP (4.18) for each transmission set and each *inter-router* links. In *Phase-2*, ALGO-TSG calls MILP (4.18) for each transmission set and each *power* link. As there are $|\mathcal{E}_R|$ router transmission sets generated in *Phase-1*, ALGO-TSG calls MILP (4.18) exactly $|\mathcal{E}_R|(|\mathcal{E}_R| + |\mathcal{E}_P|)$ times in total.

Referring to Algorithm 4, ALGO-TSG calls LP (4.19) for each backscattering set and each *backscattering* link. In the worst case, each router transmission set enables $|\mathcal{E}_B|$ *backscattering* links. Note that ALGO-TSG activates at least one *backscattering* link in a backscattering set, and only schedules each link once. Hence, for each router transmission set, ALGO-TSG calls LP (4.19) the following number of times:

$$|\mathcal{E}_B| + (|\mathcal{E}_B| - 1) + (|\mathcal{E}_B| - 2) + \cdots + 1 = \frac{|\mathcal{E}_B|(1 + |\mathcal{E}_B|)}{2}. \tag{4.23}$$

As there are $|\mathcal{S}|$ router transmission sets, in the worst case, ALGO-TSG calls LP (4.19) $|\mathcal{S}|\frac{|\mathcal{E}_B|(1+|\mathcal{E}_B|)}{2}$ times in total. This completes the proof. □

Proposition 8. *LP (4.20) has* $|\mathcal{F}|+|\mathcal{T}|(|\mathcal{E}_R||\mathcal{F}_R| + |\mathcal{E}_B||\mathcal{F}_T|) + |\mathcal{S}||\mathcal{T}|M^z$ *decision variables and* $|\mathcal{F}_R||\mathcal{E}_R|+|\mathcal{F}_T||\mathcal{E}_B|+|\mathcal{T}|(|\mathcal{S}| + |\mathcal{E}_R| + |\mathcal{E}_B|)$ *constraints.*

Proof. This proof starts with the decision variables of LP (4.20). The number of variable r^s and $\hat{r}^s$ is equal to the number of source routers and source nodes, respectively. For each time slot and each session, there is a variable f_{ij}^{st} or f_{nx}^{st} for an *inter-router* link or a *backscattering* link, and to indicate the active time of each backscattering set. Consequently, there are $|\mathcal{F}|+|\mathcal{T}|(|\mathcal{E}_R||\mathcal{F}_R|+|\mathcal{E}_B||\mathcal{F}_T|)+|\mathcal{S}||\mathcal{T}|M^z$ decision variables of LP (4.20) in total, as claimed.

As for the number of constraints in LP (4.20), there are $|\mathcal{F}_R||\mathcal{E}_R|$ constraints of type (4.20b), and $|\mathcal{F}_T||\mathcal{E}_B|$ constraints of type (4.20c), respectively. In addition, there are $|\mathcal{T}||\mathcal{S}|$ constraints of type (4.8). Next, there are $|\mathcal{E}_R||\mathcal{T}|$ constraints of type (4.12), and $|\mathcal{E}_B||\mathcal{T}|$ constraints of type (4.16), respectively.

In total, there are $|\mathcal{F}_R||\mathcal{E}_R|+|\mathcal{F}_T||\mathcal{E}_B|+|\mathcal{T}|(|\mathcal{S}|+|\mathcal{E}_R|+|\mathcal{E}_B|)$ constraints of LP (4.20), as claimed □

The next proposition concerns CMF.

Proposition 9. *CMF has a run-time complexity of* $\mathcal{O}((\sum_{s=1}^{|\mathcal{F}_R|} H^s(|\mathcal{E}_R|^3|\mathcal{F}_R|\log(|\mathcal{E}_R|)+|\mathcal{T}|+\mathbf{n}^3/log(\mathbf{n})))$.

Proof. First consider to compute the time complexity of *LSM()*. Note that the function *UseLink*($\mathcal{P}$) has a run-time complexity of $\mathcal{O}(|\mathcal{E}_R|+|\mathcal{E}_B|)$. In lines 3-9, the function *LSM()* iteratively selects a router transmission set with the maximum weight and decides its active time. First note that *Index()* has time $\mathcal{O}(|\mathcal{E}_R|^2\log(|\mathcal{E}_R|))$. In the worst case, each router transmission set only contains one active link and has the highest weight $\mathbf{W}(\mathcal{S}^z)=|\mathcal{F}_R|$. This requires complexity $\mathcal{O}(|\mathcal{E}_R|^3|\mathcal{F}_R|\log(|\mathcal{E}_R|))$ for lines 3-9. Each line from step 10 to step 12 takes complexity $\mathcal{O}(1)$. Next, each line from step 14 to step 21 has time $\mathcal{O}(1)$. This means lines 14-21 has a run-time complexity of $\mathcal{O}(|\mathcal{T}|)$. Hence, the time complexity of *LSM()* is $\mathcal{O}(|\mathcal{E}_R|^3|\mathcal{F}_R|\log(|\mathcal{E}_R|)+|\mathcal{T}|)$.

now consider the complexity of CMF. Lines 2-4 take $\mathcal{O}(|\mathcal{F}|H^s\log(H^s))$ because *SortPath()* requires a run-time complexity of $\mathcal{O}(H^s\log(H^s))$ for each session s. Lines 5-7 take $\mathcal{O}(|\mathcal{F}|)$. Solving LP (4.20) requires time $\mathcal{O}(\mathbf{n}^3/log(\mathbf{n}))$ using the interior-point method [191]; $\mathbf{n}$ is the number of variables. Thus, line 8 takes $\mathcal{O}(|\mathcal{E}_R|^3|\mathcal{F}_R|\log(|\mathcal{E}_R|)+|\mathcal{T}|+\mathbf{n}^3/log(\mathbf{n}))$. In *Phase-2*, CMF iteratively updates a path used by one session. Lines 11-19 in the worst case repeats $H^s - 1$ times, and thus have a complexity of $\mathcal{O}(H^s(|\mathcal{E}_R|^3|\mathcal{F}_R|\log(|\mathcal{E}_R|) + |\mathcal{T}| + \mathbf{n}^3/log(\mathbf{n})))$. As there are $|\mathcal{F}_R|$ source routers, lines 10-20 requires $\mathcal{O}(\sum_{s=1}^{|\mathcal{F}_R|} H^s(|\mathcal{E}_R|^3|\mathcal{F}_R|\log(|\mathcal{E}_R|) + |\mathcal{T}| + \mathbf{n}^3/log(\mathbf{n})))$. The run-time complexity of CMF is thus $\mathcal{O}((\sum_{s=1}^{|\mathcal{F}_R|} H^s(|\mathcal{E}_R|^3|\mathcal{F}_R|\log(|\mathcal{E}_R|) + |\mathcal{T}| + \mathbf{n}^3/log(\mathbf{n})))$, as claimed. □

4.6 Evaluation

This chapter conducts all experiments in Python 3.8, and solves the proposed MILP using the commercial solver Gurobi 9.0.1. It considers up to 30 routers, randomly placed on a 50 × 50 m^2 square area. Each router transmits at a frequency of $f_1 = 2.4$ GHz. It deploys up to 60 tags. Each tag has a transmission range of 0.5 meters [54]. The receiver sensitivity at both tags and routers is set to Ψ = -75 dBm. The SINR threshold and data rate used by *inter-router* links are as per the Cisco data sheet [196]. Further, according to to [197], tags support BPSK, QPSK, and 16-PSK. The background noise level σ is -90 dBm. Table 4.2 summarizes parameter values.

This chapter compares MILP (4.17) and CMF against Serial Linear Programming Rounding (SLPR) [198]. Briefly, SLPR aims to maximize link throughput. It solves an LP to determine the most number of links that can co-exist simultaneously. In addition, SLPR assigns a higher capacity to links with large traffic demand. Note SLPR does not consider routing. To employ SLPR, Dijkstra's algorithm is used to compute the shortest path for each session in $\mathcal{F}_R$. After that, SLPR is used to schedule links on the path from each session.

ALGO-TSG benchmarks against Joint Scheduling and Power Control (JSPC) [199]. First, note that JSPC only schedules *inter-router* links. Thus, JSPC does not consider backscattering links. Given a set of *inter-router* links, JSPC aims to schedule each link at least once. JSPC generates router transmission sets as follows: (i) select all unscheduled *inter-router* links into a transmission set, (ii) use an LP to optimize the transmit power of links selected in step (i) such that all links are able to co-exist with one another. If no such transmit power exists, remove the link with the minimum SINR value. The previous steps are then repeated until there is a feasible transmit power, (iii) store the resulting transmission set of step (ii) and mark all links in the said transmission set as *scheduled*. After that, repeat from step (i) until all *inter-router* links have been scheduled into a transmission set.

Note that MILP (4.17) accepts router transmission sets generated by ALGO-TSG or JSPC to derive a final schedule that maximizes the sum of flow rates at both tiers. To compare ALGO-TSG and JSPC fairly in the problem of this chapter, define the following two approaches:

- MILP-TSG. The transmission sets generated by ALGO-TSG are used by MILP (4.17) to derive a schedule that maximizes the sum of flow rates at both tiers. Specifically, MILP-TSG decides (i) the active time of each router transmission set and backscattering set, and (ii) the traffic over each *inter-router* link and each *backscattering* link.

- MILP-JSPC. MILP (4.17) accepts as input the router transmission sets generated by JSPC. It derives a schedule that maximizes the sum of flow rates at *Tier-1* by determining (i) the active time of each router transmission set, and (ii) the traffic on each *inter-router* link.

Given the above schemes, Figure 3.3 summarizes how these schemes link together to jointly optimize link schedule transmit power control, backscattering coefficient control, and routing in a two-tier IoT network for data collection. The major difference lies in how they construct transmission sets, how they optimize the transmit power of routers, how they select paths for packet delivery, and whether they apply backscattering.

This set of simulations studies MILP-TSG, MILP-JSPC, CMF, and SLPR with (i) a different number of routers $|\mathcal{V}_R|$, (ii) a different number of flows $|\mathcal{F}_R|$ and $|\mathcal{F}_T|$, (iii) maximum transmit power at routers P_{max}, and (iv) different SINR thresholds γ

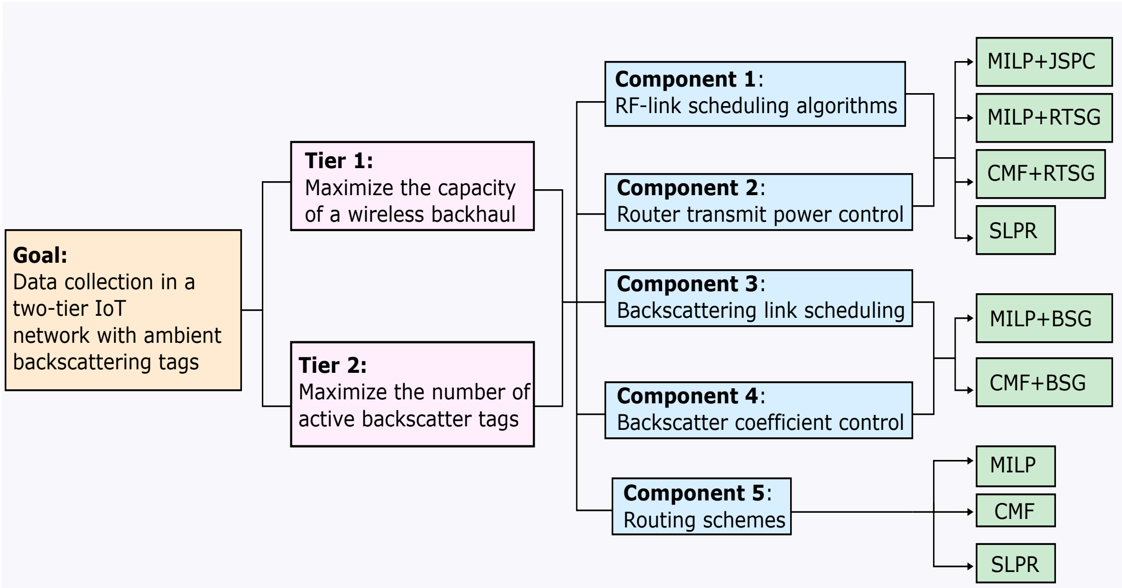

Figure 4.3: Approaches to maximize the sum flow rates in a two-tier data collection IoT network.

and θ. Table 4.2 lists necessary parameter values. Each experiment is run 50 times; each run has random source and destination routers and tags.

Table 4.2: Parameter values.

Parameter	**Value(s)**	**Parameter**	**Value(s)**
$\lvert\mathcal{V}_R\rvert$	20 to 30	$\lvert\mathcal{V}_T\rvert$	30 to 60
$\lvert\mathcal{F}_R\rvert$	5 to 10	$\lvert\mathcal{F}_T\rvert$	5 to 10
L	$50 \times 50\ m^2$	$\lvert\mathcal{T}\rvert$	30
R_x	10 m	R_n	0.5 m
α	20 dB	β	2
d_0	1 m	P_{max}	1-5 watts
λ	0.125 m	σ	-90 dBm
γ	5 to 13 dB	θ	3 to 15 dB
Ψ	-75 dBm	τ	1 sec

4.6.1 Optimality gap

This section aims to evaluate the optimality gap between the proposed algorithms, i.e., Algo-TSG and CMF, to the optimal solution of problem (4.17) computed by exhausted search. As in Section 3.6.2, exhaustive search only applies to small-scale networks. This section considers small-scale networks with that consist of ten backscatter tags and at most ten routers. There are two data flows between routers, and two data flows routed over tags; i.e., $|\mathcal{F}_R| = 2$ and $|\mathcal{F}_T| = 2$. Referring to Figure 4.4, observe that the optimality gap between the optimal solution and the proposed solutions grows with network scales; the gap between the optimal solution and MILP-TSG grows from 0.01 to 0.15. This is because Algo-TSG is only capable of computing a limited number of transmission sets, i.e.,$|\mathcal{E}_R| + 1$ transmission sets and $|\mathcal{E}_B|$ backscattering sets; see Section 4.3. This means the number of transmission sets computed by Algo-TSG increases linearly with network scale. On the other hand, the number of all possible transmission sets grows exponentially. Consequently, the gap between the number of available transmission sets computed by Algo-TSG and the true number of transmission sets results in the gap between the MILP-TSG and CMF and the optimal solution.

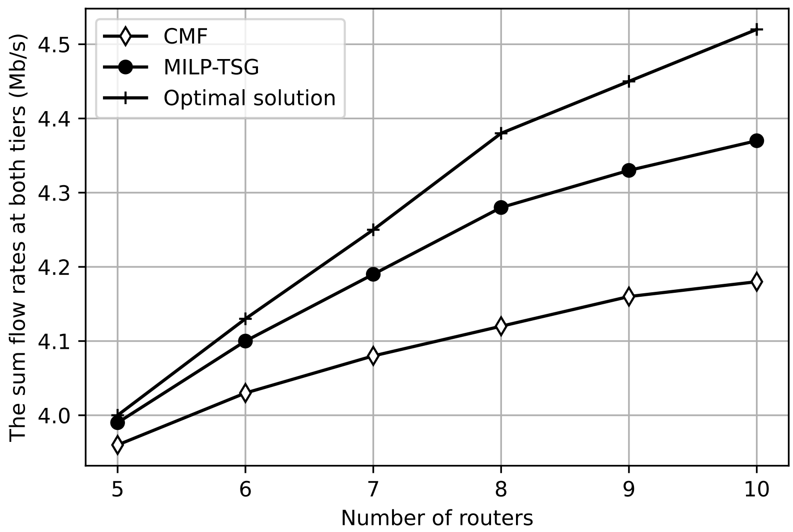

Figure 4.4: The optimality gap between MILP-TSG, CMF and the optimal solution. The reason for this gap is the proposed link schedulers only use a portion number of feasible transmission sets.

4.6.2 Router density

This section increases the number of routers $|\mathcal{V}_R|$ from 20 to 30. The number of tags is set to $|\mathcal{V}_T| = 60$. The SINR threshold for all links is $\gamma = 5 = \theta = 5$ dB. There are five source routers and five source tags; i.e., $|\mathcal{F}_R| = 5$ and $|\mathcal{F}_T| = 5$.

Referring to Figure 4.5, the sum of flow rates of MILP-TSG, MILP-JSPC, CMF, and SLPR increases with more routers. This is because there are more links, which helps avoid bottleneck links. Moreover, for MILP-TSG and CMF, the number of tags that are able to backscatter increases when there are more routers. Hence, there are more source tags that are able to forward their data to their corresponding destination, leading to source tags with a higher flow rate.

As shown in Figure 4.5, for MILP-TSG, its sum of flow rates is on average 22.81% higher than that of MILP-JSPC. This is reasonable as MILP-JSPC does not support backscattering communications. As there are more backscattering communications with an increasing number of routers, the gap between MILP-TSG and MILP-JSPC gradually becomes larger. In addition, JSPC only schedules each link once, meaning it has a small number of transmission sets. As a result, fewer routers transmit simultaneously when they use JSPC. Moreover, MILP-TSG outperforms CMF. This is because MILP-TSG avoids routing sessions using a long path. Note that CMF considers routing sessions over long paths. As a result, more links and transmission sets are activated, meaning the active time and capacity of each link is reduced. Consequently, the sum of flow rates decreases.

4.6.3 SINR thresholds

This section sets the number of routers and tags to $|\mathcal{V}_R| = 20$ and $|\mathcal{V}_T| = 60$, respectively. The number of source routers and source tags are set to $|\mathcal{F}_R| = 5$ and $|\mathcal{F}_T| = 10$, respectively. First, this set of experiments studies how different SINR thresholds at routers affect network throughput. The SINR threshold for tags is fixed at $\theta = 5$ dB. Referring to Figure 4.6, the sum of flow rates gradually increases as the SINR threshold γ increases from 5 to 13 dB. This is because when the SINR threshold increases, each link acquires a higher transmission rate, i.e., from 6 to 24 Mb/s. The sum of flow rates of MILP-TSG increases slower after $\gamma = 7$ dB. This

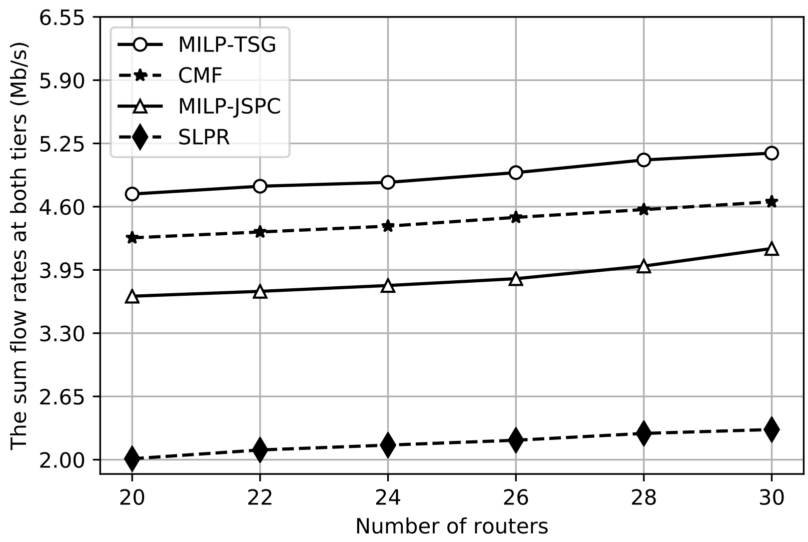

Figure 4.5: Comparison of the maximum network throughput achieved by MILP-TSG, CMF, MILP-JSPC, and SLPR with varying number of routers. The network throughput of MILP-TSG is on average 12.43%, 22.81%, and 92.45% higher than the throughput of CMF, MILP-JSPC and SLPR, respectively. This is because with more routers, there are correspondingly more backscattering links in router transmission sets, which lead to higher capacity.

is because there are fewer routers that are able to transmit simultaneously, which results in fewer links that have a non-zero capacity. Consequently, fewer source routers are able to forward data to their destination.

Referring to Figure 4.6, the gap between MILP-TSG and CMF becomes larger with increasing γ value. This is because CMF aims to activate all source routers. However, MILP-TSG only considers routing sessions over links with a high capacity. As each active link has a low capacity when using CMF, the gap between MILP-TSG and CMF becomes larger as the SINR threshold γ increases. Moreover, the sum of flow rates of MILP-JSPC is higher than CMF after $\gamma = 7$ dB. This is because the capacity of *inter-router* links is much higher than that of *backscattering* links after $\gamma = 7$ dB, which is 12 Mb/s and 1.33 Mb/s, respectively. However, CMF regularly activates *power* links and route sessions using a long path, which reduces the sum of flow rates of source routers.

Next, this set of experiments studies network throughput when tags have a high

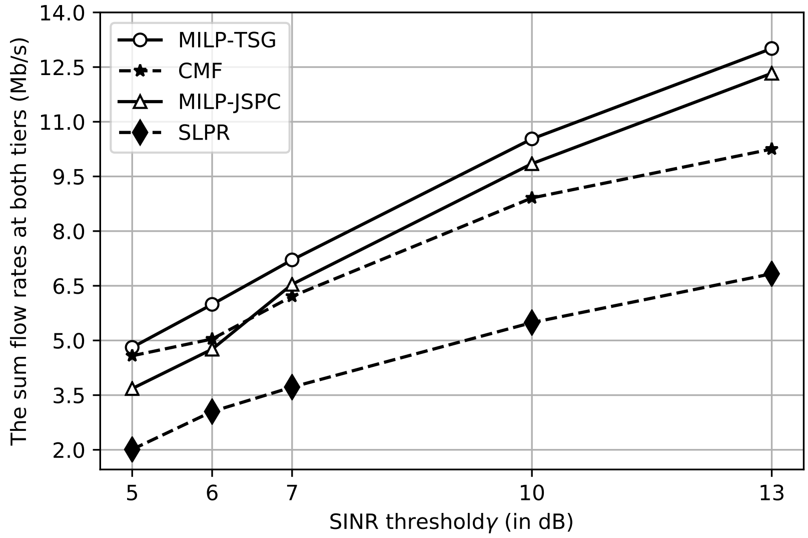

Figure 4.6: Impact of SINR threshold γ on the maximum network throughput when $\theta = 5$ dB. MILP-JSPC outperforms CMF when $\gamma = 13$ dB. This is because MILP-JSPC achieves a higher capacity for active *inter-router* links.

data rate of 5 Mb/s. To this end, the SINR threshold for tags is set to $\theta = 15$ dB. Referring to Figure 4.7, the gap between MILP-TSG and MILP-JSPC becomes larger as compared to when θ is 5 dB. This is because tags have a high transmission rate of 5 Mbps when θ is 15 dB. Next, the sum of flow rates of CMF and MILP-TSG only increases slightly when γ rises from 5 to 6 dB. This is because increasing the SINR threshold γ results in a smaller number of backscattering links that are powered by each router transmission set. Consequently, the sum of source rates at tags reduces. *Inter-router* links have a higher capacity when γ increases. This indicates a trade-off between the source rate at routers and tags when setting the SINR threshold γ and θ. Moreover, the gap between MILP-TSG and CMF increases from 14.31% to 20.13% as the SINR threshold γ increases from 5 to 13 dB. This is because CMF only activates *power* links for a short time as compared to MILP-TSG. As a result, CMF results in source tags having a lower flow rate as compared to MILP-TSG. On the other hand, the gap between CMF when $\theta = 5$ dB and CMF when $\theta = 15$ dB becomes smaller as γ increases. This is because the number of active backscattering links in each time slot is inversely proportional to SINR threshold γ.

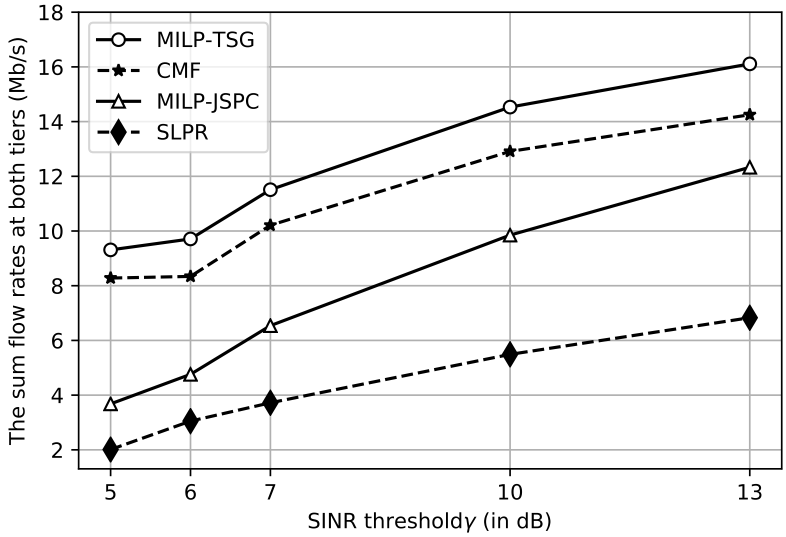

Figure 4.7: Impact of SINR threshold γ on the maximum network throughput when $\theta = 15$ dB. The network throughput of MILP-TSG is on average 18.51% higher than the throughput of CMF. This is because MILP-TSG uses a small number of *power* links to power tags.

4.6.4 Number of sources

This section now investigates how the number of source routers and tags impacts the sum of flow rates. Note that the total number of routers and tags are fixed, i.e., $|\mathcal{V}_R| = 20$ and $|\mathcal{V}_T| = 60$. These set of experiments set the SINR threshold γ and θ to 5 dB.

Number of source routers

This section first studies how the number of sessions routed over *inter-router* links affects the sum of flow rates. To this end, these set of experiments consider $|\mathcal{F}_R| \in \{5, 6, 7, 8, 9, 10\}$ and $|\mathcal{F}_T| = 10$. As per Figure 4.8, the sum of flow rates increases when $|\mathcal{F}_R|$ rises from five to ten. When there are more source routers, the probability of including a session with a short path is higher. MILP-TSG and MILP-JSPC are able to find a link schedule that often activates links used by shorter paths. In addition, MILP-TSG places traffic over *inter-router* links that power more tags, meaning the sum of source rates at tags increases. On the other hand, we observe that the sum of flow rates of CMF and SLPR decreases when $|\mathcal{F}_R|$ increases from five to ten. This is because the schedule computed by CMF and SLPR activates links over long paths. This means CMF computes a longer schedule containing more router transmission sets. Note that CMF outperforms SLPR. This is reasonable as SLPR does not have backscattering communications. Moreover, CMF, with the help of the Dijkstra algorithm, is able to decide a path for each session that leads to the maximum sum of flow rates at routers. In addition, the schedule computed by CMF ensures links in selected paths to have a higher capacity. This helps improve the flow rate at each source router.

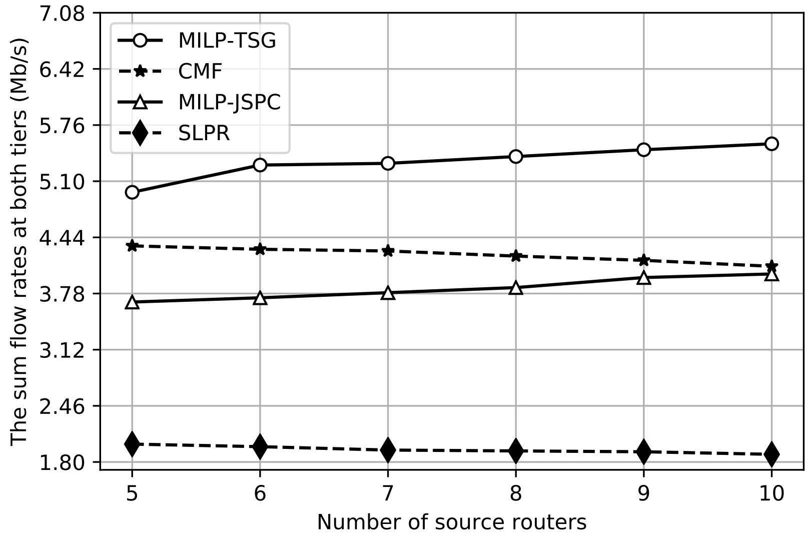

Figure 4.8: The impact on network throughput with a varying number of source routers. The network throughput of MILP-TSG is on average 39.53% higher as compared to CMF. This is because CMF uses more *inter-router* links and router transmission sets to route sessions with a long path.

Number of source tags

This section considers the following number of source tags: $|\mathcal{F}_T| \in \{5, 6, 7, 8, 9, 10\}$. The number of source routers is set to $|\mathcal{F}_R| = 5$. In Figure 4.9, the sum of flow rates increases when $|\mathcal{F}_T|$ increases from five to ten. For MILP-TSG and CMF, this is reasonable as more source tags are able to forward their data to their destination. The sum of flow rates of MILP-TSG is on average 16.93% higher than that of CMF. This is because MILP-TSG is able to use router transmission sets that lead to more tags performing backscattering communications. Note that the sum of flow rates of MILP-JSPC and SLPR does not vary with an increasing number of tags. This is because they do not support backscattering communications. As a result, the gap between MILP-JSPC and MILP-TSG becomes larger as there are more source tags. We see the same trend for CMF and SLPR.

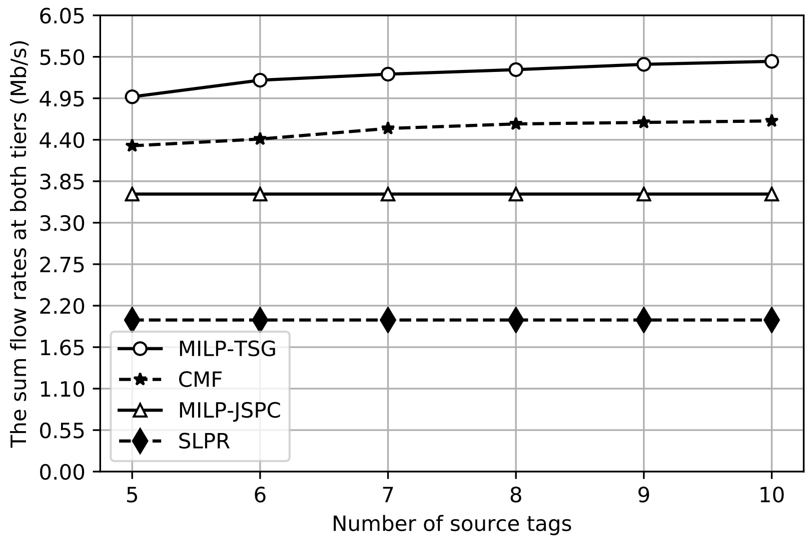

Figure 4.9: The maximum network throughput with the number of source tags. MILP-TSG has on average 16.93% higher throughput as compared to CMF; i.e., MILP-TSG is able to power more tags without using a large number of *inter-router* links. The number of tags does not affect the throughput of MILP-JSPC and SLPR

4.6.5 Maximum transmit power

In the following set of simulations, the maximum transmit power of routers ranges from 1 to 5 Watts. Referring to Eq. (4.3) and (4.4), a high transmit power enables more backscattering links. Referring to Figure 4.10, the sum of flow rates of MILP-TSG and CMF increases with the maximum transmit power at routers. Specifically, the sum of flow rates of MILP-TSG increases from 5.21 to 6.49 Mb/s, whereby the sum of flow rates of CMF increases from 4.55 to 5.25 Mb/s, respectively. For MILP-TSG and CMF, more tags are able to backscatter when routers have a higher transmit power. This reduces the probability of only using *power* links to support backscattering communications, which improves the source rate at routers. In addition, more source tags are able to forward data when there are more *backscattering links*. As a result, the rate at source tags also increases when routers use a higher transmit power. We observe that the maximum transmit power of routers does not affect the throughput of MILP-JSPC. This is because JSPC only schedules each *inter-router* link once. As a result, increasing the maximum transmit power of routers does not affect the number of links in a transmission set. The throughput of SLPR increases from 2.01 to 2.12 Mb/s. This is because SLPR allows more links to co-exist when P_{max} increases.

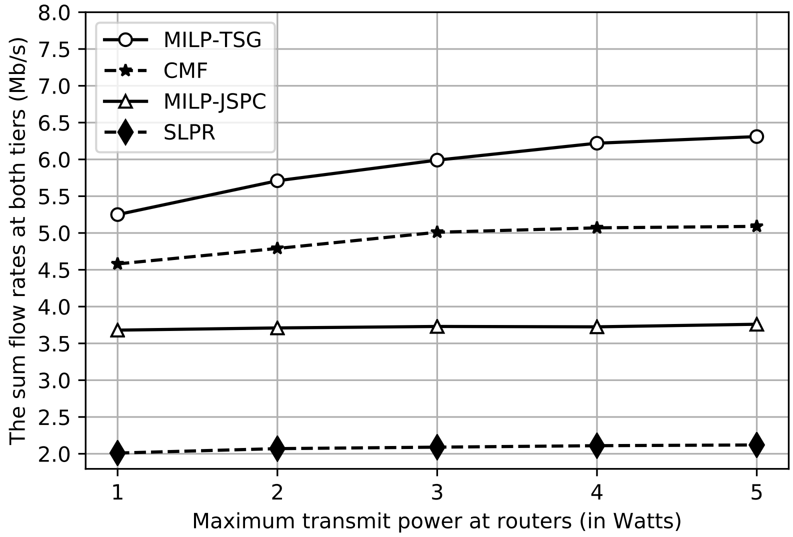

Figure 4.10: A comparison of MILP-TSG, CMF, MILP-JSPC, and SLPR under varying maximum transmit power at routers. MILP-TSG has on average 15.61% higher throughput than CMF. This shows that a high transmit power helps increase coverage. The maximum transmit power at routers has negligible impact on the throughput of MILP-JSPC and SLPR.

4.7 Conclusion

This chapter considers a novel backscatter-assisted two-tier wireless backhaul network where tags communicate via passive backscattering and routers communicate via active RF transmissions. It formulates a MILP that is used to jointly optimize the active time of RF links and backscattering links, and traffic over links in order to maximize the sum flow rates of source nodes. Further, this chapter outlines a heuristic called ALGO-TSG to generate transmission sets for routers and tags. In addition, this chapter outlines a heuristic called CMF to jointly decide the path used for each session and a transmission schedule. The simulation results show that network throughput can be increased by using a backscatter-aided link scheduler.

The work in this chapter assumes perfect CSI. However, in practice, devices may not be able to afford the energy cost of estimating and transmitting CSI to routers. To this end, the next chapter considers a problem whereby a power beacon or charger only has imperfect CSI and does not know the energy level of devices.

Chapter 5

Data collection in a RF-charging network with imperfect CSI

This chapter considers data collection in an RF-charging network with imperfect CSI. It considers a dedicated power beacon that delivers energy to devices under imperfect CSI. These devices are responsible for relaying a sample from a source to a sink. The *goal* is to minimize the energy consumption of the power beacon and ensure the sample arrives at the sink by a deadline with a probability level. The problem at hand is to optimize the charging policy for the power beacon to cope with the said probabilistic requirement. To this end, this chapter contains a chance-constrained program that can be used to determine the optimal charging policy of a power beacon. In addition, it outlines two algorithms named S-POPA and BO-POPA to approximate the optimal solution to the problem.

To illustrate the said research problem and corresponding challenges, consider sample delivery in the RF-charging network shown in Figure 5.1. Source S transmits a sample to the sink over multiple hops. There are also two relay devices, namely N_1 and N_2. All devices harvest RF energy from a power beacon (PB) that uses a switched-beam antenna. Assume the sample must arrive by $\Delta = 4$ frames. Consider two charging policies: the PB transmits with maximum or minimum transmit power. In both strategies, the PB allocates its transmit power uniformly over all its antennas. Moreover, due to time-varying channel gains, devices require different transmit power to forward a sample in each frame. Figure 5.1 shows the cumulative distribution function (CDF) of sample arrival times. We see that the probability of a sample arriving before the end of frame t_4 is only 30% when the PB uses the minimum transmit power. On the other hand, this probability is approximately 90% when the PB transmits with the maximum power. Hence, there is a trade-off between the energy consumption of the PB and the sample arrival time. A key challenge is that the PB must determine a transmit power over random channel power gains and non-causal channel state information (CSI) and energy level information at devices. Specifically, the PB does not know the channel gains to each device, and also the channel gains between devices.

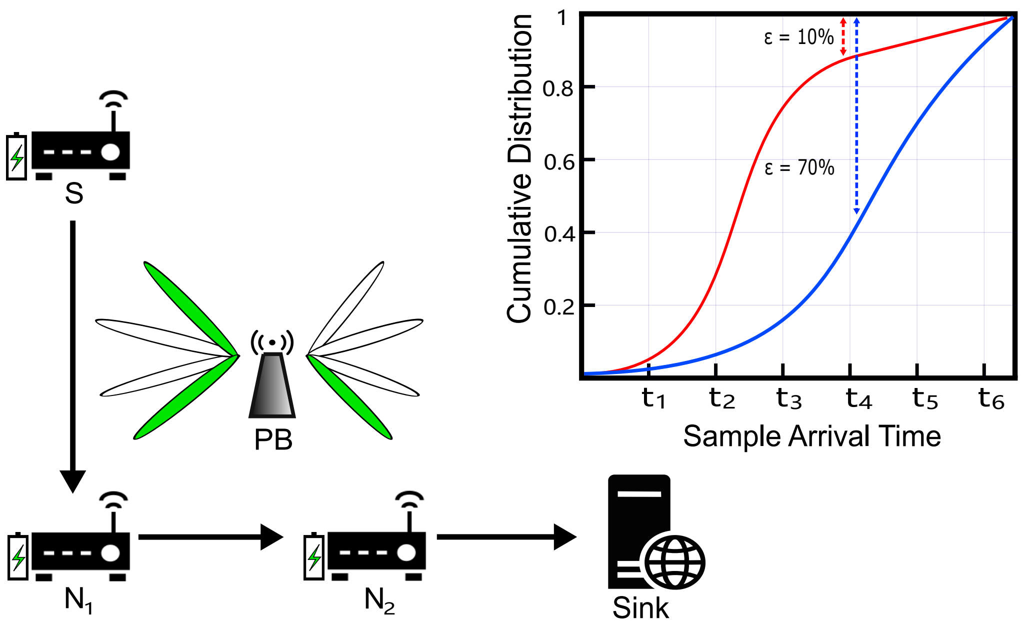

Figure 5.1: An example wireless powered network with a PB. The CDF of sample arrival times (in frames) when the PB uses the maximum and minimum transmit power are denoted by a red and blue curve, respectively. A sample from source S must arrive at the Sink within $\Delta = 4$ frames with probability $(1 - \epsilon)$. The value of ϵ is 0.1 and 0.7 when the PB uses the maximum and minimum transmit power, respectively.

The *aim* of this chapter is to design solutions that minimize the total transmit power of PB, and ensure samples arrive at a sink within Δ frames with probability $(1-\epsilon)$; the term ϵ is the probability that a sample fails to reach the sink within Δ frames. Ideally, if the PB is aware of channel gain conditions and the energy level of devices, it will be able to optimize its transmit power accordingly. In contrast, this chapter considers the challenging case where the PB does not have the said information. This assumption is made for practical reason as it is expensive to collect CSI from devices.

Sections 5.1 and 5.2 respectively present the system and problem. Section 5.3 presents an algorithm to solve the formulated chance-constrained stochastic program. Section 5.4 and Section 5.5 present S-POPA and BO-POPA, respectively. Section 5.6 presents evaluation methodology and results. Finally, Section 5.7 concludes this chapter.

5.1 Preliminaries

5.1.1 Network model

This chapter studies a wireless-powered network with a sink/gateway o and source device s. The source generates a sample and sends it to the sink via multi-hop communications over a fixed path. Let set $\mathcal{V} = \{n_1, \ldots, n_{|\mathcal{V}|}\}$ denote a set of relay devices on the path; each element is indexed by i according to their hop number from source s towards sink o. There is a PB, denoted as m, that charges all source and relay devices. In addition, the PB uses switched-beam antennas, where there are a set of $\mathcal{K}$ antennas; each single-lobe of a PB is indexed by k. The PB has no energy constraint.

Time is discrete. Define $\mathcal{T} = \{1, \ldots, T\}$ as a set of frames; each frame t has duration τ. This chapter assumes a *harvest-then-transmit* protocol [200] for devices. The structure of a frame is shown in Figure 5.2. Specifically, PB m first charges source device s and relays for duration τ_C. This is followed by a set of $|\mathcal{V}|+1$ data slots that are assigned to a distinct device on the path. This means if all devices on the path have sufficient energy, a sample will arrive at the end of a frame. For ease of exposition, assume $\tau_C = \tau_D = 1$ second. This allows the terms power and energy to be used interchangeably.

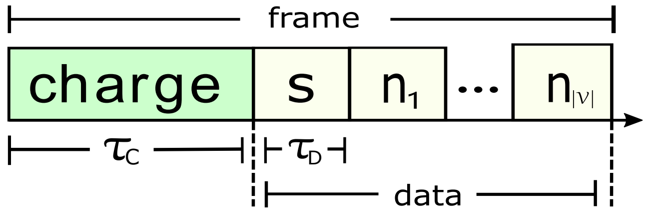

Figure 5.2: Frame structure. An energy slot and multiple data slots are denoted as green and yellow boxes, respectively.

This chapter assumes block Rayleigh channel fading, where channel power gains vary independently from frame to frame but remain constant in each frame. Let g_{mi}^{tk} denote the channel power gain between antenna k of PB m and receiver i in frame t, respectively. Formally, it is

$$g_{mi}^{tk} = \chi\alpha\left(\frac{d_{mi}}{d_0}\right)^{\beta}, \forall k \in \mathcal{K}, \forall t \in \mathcal{T}. \tag{5.1}$$

The Euclidean distance between PB m and receiver i is d_{mi}, χ is the Exponential distributed random variable with unit mean. The path loss at reference distance $d_0 = 1$ meter is α, and the path loss exponent is β. In addition, let $\mathbf{g}_{mi}^t = \{g_{mi}^{tk}\}_{k\in\mathcal{K}}$ denote a vector of channel power gains between receiver i and antennas of PB m in frame t. Define vector $\mathbf{g} = \{\mathbf{g}_{mi}^t\}$, whereby $\forall i \in \mathcal{V} \cup s, \forall t \in T$, as a collection of channel power gains from PB m to *all* devices over $\mathcal{T}$ frames.

This chapter assumes block fading Rayleigh channels. Let $\hat{g}_{ij}^t$ denote the channel power gain between device-i and device-j in frame t. Similarly, let the vector $\hat{\mathbf{g}} = \{\hat{g}_{ij}^t\}$ denote to the channel gains between all devices including source s and sink o across $\mathcal{T}$ frames, whereby $\forall i \in \mathcal{V} \cup s, \forall j \in \mathcal{V} \cup o, \forall t \in \mathcal{T}$.

Table 5.1: A summary of notations

Notation	Description
$\mathcal{V}$	A set of relays
$\mathcal{T}$	A set of frames
$\mathcal{K}$	A set of antennas on the PB
$\mathcal{H}$	A set of energy conversion efficiencies
$\mathcal{P}$	A collection of switched-beam patterns
δ	SNR threshold for transmission
ρ_i^t	The required transmit power for device i in frame t
a_i^t	Whether device i transmit in frame t
λ_o	The sample arrival time
p_{mk}^z	The transmit power over antenna k in the z-th switched-beam pattern
w_{mz}^t	The switched-beam pattern for frame t
$\boldsymbol{\pi}$	A vector of w_{mz}^t for all frame t
$\boldsymbol{\xi}$	A vector of channel power gains for all devices and all frames
$\mathbf{c}_{mi}^t$	A vector of channel coefficient between PB m and device i in frame t
e_i^t	The received power for device i in frame t
b_i^t	The energy level for device i in frame t
B_{max}	The battery capacity of devices

5.1.2 Transmission model

A transmitter sends a sample to a receiver only if the Signal-to-Noise Ratio (SNR) at the receiver exceeds a threshold δ. Hence, in each frame t, a transmitter i transmits to receiver j when the SNR satisfies

$$\frac{p_i^t \hat{g}_{ij}^t}{N_0} \geq \delta, \tag{5.2}$$

where N_0 is the ambient noise power level and p_i^t is the transmit power of device-i in frame t. In practice, the value of δ corresponds to a desired data rate, denoted as $C(\delta)$ in bps.

Let S denote the sample size in bits. In addition, define δ_{min} as the minimum SNR threshold that satisfies $C(\delta_{min})\tau_D \geq S$. Let ρ_i^t represent the required transmit power to send a sample in frame t, whereby each ρ_i^t is calculated as per $\rho_i^t = \frac{\delta_{min} N_0}{\hat{g}_{ij}^t}$. Let vector $\boldsymbol{\rho} = \{\rho_s^1, \rho_1^1 \ldots \rho_{|\mathcal{V}|}^T\}$ represent the required transmit power of source s and all relay devices over $\mathcal{T}$ frames. Note this chapter does not consider circuit power as it is a constant, meaning it only scales simulation results and does not change its findings.

Source s only generates one sample over $\mathcal{T}$ frames, whereby the sample is forwarded to sink o by all relay devices in set $\mathcal{V}$. Each relay device n_i is able to transmit in frame t only if it has received the sample from its neighbor n_{i-1}. This means the sample is forwarded hop-by-hop on the path. Let the binary variable $a_i^t \in \{0, 1\}$ equal one when the source or relay device-i transmits a sample in frame t. Mathematically, there exists the following so-called flow conservation constraint for each relay device in set $\mathcal{V}$:

$$a_i^t \leq \sum_{z=1}^{t} a_{i-1}^z, \forall i \in \mathcal{V}, \forall t \in \mathcal{T}, \tag{5.3}$$

where constraint (5.3) ensures that relay n_i only transmits after the transmission of relay n_{i-1}. Briefly, if relay n_{i-1} does not transmit within t frames, the right-hand side of Eq. (5.3) is zero. This in turn prevents relay n_i from any transmission in frame t, i.e., the term a_i^t is forced to zero for $t, t+1, \ldots$. Recall that the relays in set $\mathcal{V}$ are sorted according to their hop number from the source towards the sink; see Figure 5.2. This also means relay $n_{|\mathcal{V}|}$ is only able to transmit a sample in frame t if the sample has been transmitted by each device $i \in \{s, n_1, \ldots, n_{|\mathcal{V}|-1}\}$ in t frames.

Next, the source or each relay device only transmits at most once across $\mathcal{T}$ frames as there is only one sample generated at source s. Mathematically, each relay must satisfy

$$\sum_{t=1}^{\mathcal{T}} a_i^t \leq 1, \forall i \in \mathcal{V} \cup s. \tag{5.4}$$

Let the binary variable $u_o^t \in \{0, 1\}$ equal one if the sample does not arrive at sink o in frame t. This means each $u_o^t \in \{0, 1\}$ is set to zero only if the source and all relays have transmitted the sample within frames $1, \ldots, t$. Specifically, sink o receives a sample when relay $n_{|\mathcal{V}|}$ forwards a sample. This means the value of each u_o^t depends on the transmission of relay $n_{|\mathcal{V}|}$ in frame t. Mathematically, variable u_o^t is calculated as per

$$u_o^t = 1 - \sum_{z=1}^{t} a_{|\mathcal{V}|}^z, \forall t \in \mathcal{T}. \tag{5.5}$$

According to constraint (5.3), any device that fails to transmit a sample within t frames will result in the term $\sum_{z=1}^{t} a_{|\mathcal{V}|}^z$ being set to zero. This in turn sets each u_o^t to one as per Eq. (5.5).

Next, the sample arrival time λ_o is calculated as per

$$\lambda_o = \sum_{t=1}^{\mathcal{T}} u_o^t + 1. \tag{5.6}$$

In other words, the sample arrival time is equal to the sum of each variable u_o^t across $\mathcal{T}$ frames plus one. As an example, if the sample arrives at the sink in frame-2, meaning the term u_o^1 is equal to one and each term in $[u_o^2, \ldots, u_o^{\mathcal{T}}]$ is zero. Consequently, the sample arrival time is calculated as per $\sum_{t=1}^{\mathcal{T}} u_o^t + 1 = 1 + 1 = 2$.

5.1.3 Switched-Beam Antennas

The PB adopts switched-beam antennas as doing so obviates the need to collect CSI from devices and to ensure a well-conditioned channel gain matrix. Specifically, the PB has a set of $\mathcal{K}$ antennas that it uses to create switched-beam patterns. The PB m has $|\mathcal{K}|$ predefined single-lobe beams; each single-lobe beam has a coverage of $360/|\mathcal{K}|$ degree. Advantageously, the PB is capable of generating different switched-beam patterns by weighting single-lobe beams. Define the maximum transmit power at the PB as P_{max}. Following [201], let $\mathcal{P} = \{\mathbf{p}_1, \ldots, \mathbf{p}_Z\}$ denote a collection of Z available switched-beam patterns; each element is indexed by z and represents a vector of weights of $|\mathcal{K}|$ beams. In addition, let p_k^z represent the weight allocated to beam k for pattern $\mathbf{p}_z$. For each pattern $\mathbf{p}_z$ in collection $\mathcal{P}$, the weight allocated to $|\mathcal{K}|$ beams must satisfy

$$\sum_{k=1}^{|\mathcal{K}|} p_{mk}^z \leq P_{max}. \tag{5.7}$$

Define binary variable $w_{mz}^t \in \{0, 1\}$ to equal one when PB m uses beam pattern $\mathbf{p}_z$ in frame t. Mathematically, there exists the following constraint to select a beamforming pattern for PB m in each frame t:

$$\sum_{z=1}^{Z} w_{mz}^t \leq 1, \forall t \in \mathcal{T}. \tag{5.8}$$

5.1.4 RF Energy-harvesting

The source s and relay n are equipped with a single antenna. The received power at devices depends on the channel power gains and switched-beam patterns at the PB [201]. Specifically, define the received power coefficient c_{mki}^t at device-i when PB m uses the single-lobe beam k in frame t. This coefficient corresponds to the case when PB m uses single-lobe beam k with transmit power P_{max}. Next, let vector $\mathbf{c}_{mi}^t = \{c_{mki}^t\}_{k \in \mathcal{K}}$ denote a vector of the said received power coefficients between device-i and PB m in frame t. Further, let vector $\mathbf{c} = \{c_{ms}^1, \ldots, c_{m|\mathcal{V}|}^T\}$ be the received power coefficients of all devices over T frames. Note that the received power coefficients of devices are unknown to the PB. Let the variable e_i^t denote the total received power at device-i from the PB in frame t. Mathematically, the received power at device-i in each frame t is calculated as per

$$e_i^t = \sum_{z=1}^{Z} \mathbf{p}_z^{\mathsf{T}} w_{mz}^t \mathbf{c}_{mi}^t + N_0, \forall i \in \mathcal{V}, \forall t \in \mathcal{T}, \tag{5.9}$$

where the symbol T denotes the transpose of a vector, N_0 is the random circuit noise power with zero-mean.

This chapter considers a practical energy-harvesting model with non-linear energy conversion rates [192]. To be specific, the energy conversion rate is modeled as a function of incident power, where the function is derived from an actual datasheet of energy conversion efficiency via curve fitting [35]. Let $\zeta()$ be the said function that takes each incident power e_i^t as input and returns the energy conversion rate accordingly. In addition, let b_i^t denote the battery level of device-i at the end of each frame t. Mathematically, the energy evolution of each device in each frame is calculated as per

$$b_i^t = b_i^{t-1} + \zeta(e_i^t)\tau_C - a_i^t \rho_i^t \tau_D, \forall i \in \mathcal{V}, \forall t \in \mathcal{T}. \tag{5.10}$$

In other words, the energy level of device-i at the end of frame t is equal to the energy level at the end of frame $t-1$ plus the energy collected in frame t minus the energy consumed by its transmission.

Each device has a battery capacity of B_{max} to store its harvested energy. Energy arrival at a device-i may exceed its available battery storage in frame t as per Eq. (5.10), i.e., when $\zeta(e_i^t)\tau_D > B_{max} - b_i^{t-1}$. To this end, an energy consumption constraint for the source and each device-i in set $\mathcal{V}$ is defined as per

$$\sum_{t=1}^{T} a_i^t \rho_i^t \tau_D \leq B_{max}, \forall i \in \mathcal{V} \cup s, \tag{5.11}$$

where constraint (5.11) specifies that each device-i is only able to use the amount of energy stored in its battery. This also means each device consumes a maximum B_{max} amount of energy to transmit a sample in one of the $\mathcal{T}$ frames.

5.2 Problem Definition

The *aim* of this chapter is to minimize the total transmit power of PB m, while ensuring that the sample from source s arrives at sink o within Δ frames with a probability of at least $(1-\epsilon)$. The problem at hand has the following decision variables: (i) a beamforming pattern used by PB m in each frame t, i.e., w^t_{mz}, and (ii) whether each device i harvests sufficient energy in each frame t, and whether the device transmits in each frame t, i.e., each a^t_i.

The next discussion focuses on linearization. The first is the non-linear energy conversion rate function $\zeta()$. This chapter adopts the piece-wise linear approximation method in [202, 203]. Specifically, the possible received power is divided into $|\mathcal{H}|$ non-overlapping intervals; each interval h has a corresponding energy conversion efficiency η_h. Let the range of interval h be $[L_h, H_h)$, where L_h and H_h is respectively the lower and upper bound of interval h. In addition, define binary variable $I^t_{ih} \in \{0, 1\}$, which is set to one when the received power e^t_i falls into interval h. Next, Eq. (5.10) and Eq. (5.11) can be rewritten as follows:

$$b^t_i = b^{t-1}_i + \tau_C \sum_{h\in\mathcal{H}} e^t_i I^t_{ih} \eta_h - a^t_i \rho^t_i \tau_D, \forall i \in \mathcal{V}, \forall t \in \mathcal{T}, \tag{5.12}$$

$$I^t_{ih} L_h \leq e^t_i I^t_{ih} \leq I^t_{ih} H_h, \forall i \in \mathcal{V}, \forall t \in \mathcal{T}, \forall h \in \mathcal{H}, \tag{5.13}$$

$$\sum_{h\in\mathcal{H}} I^t_{ih} = 1, \forall i \in \mathcal{V}, \forall t \in \mathcal{T}. \tag{5.14}$$

Constraint (5.12) specifies an energy conversion efficiency corresponding to a given received power level. Specifically, an energy conversion efficiency η_h is adopted when the received power e^t_i falls in interval h. Constraint (5.13) sets each I^t_{ih} to one if the received power e_i^t is within the range $[L_h, H_h)$. Otherwise, each I_{ih}^t is forced to zero. Constraint (5.14) ensures a given received power e_i^t only corresponds to one energy conversion rate and one interval.

Next, constraints (5.12)-(5.13) are to be linearized due to the product of two decision variables, i.e., e_i^t and I_{ih}^t. To this end, replace $e_i^t I_{ih}^t$ with a variable X_{ih}^t, and rewrite them as

$$b_i^t = b^{t-1} + \tau_C \sum_{h \in \mathcal{H}} X_{ih}^t \eta_h - a_i^t \rho_i^t \tau_D, \forall i \in \mathcal{V}, \forall t \in \mathcal{T}, \tag{5.15}$$

$$I_{ih}^t L_h \leq X_{ih}^t \leq I_{ih}^t H_h, \forall i \in \mathcal{V}, \forall t \in \mathcal{T}, \forall h \in \mathcal{H}, \tag{5.16}$$

$$X_{ih}^t \leq I_{ih}^t \Phi, \forall i \in \mathcal{V}, \forall t \in \mathcal{T}, \forall h \in \mathcal{H}, \tag{5.17}$$

$$0 \leq X_{ih}^t \leq e_i^t, \forall i \in \mathcal{V}, \forall t \in \mathcal{T}, \forall h \in \mathcal{H}, \tag{5.18}$$

$$X^t \geq e_i^t - (1 - I_{ih}^t)\Phi, \forall i \in \mathcal{V}, \forall t \in \mathcal{T}, \forall h \in \mathcal{H}. \tag{5.19}$$

Constraint (5.15) is the linearized energy evolution of each device in each frame. Constraint (5.16) specifies an interval for a given received power level e_i^t. Next, when the value of I_{ih}^t is one, the value of X_{ih}^t is forced to the value of e_i^t as per constraint (5.18) and (5.19). This means device-i adopts the energy conversion efficiency η_h accordingly. Otherwise, variable X_{ih}^t is set to zero by constraint (5.16) if the value of I_{ih}^t is zero. The constant Φ is the upper bound of the received power level e_i^t, which is set to $\Phi = |\mathcal{M}|P_{max}$.

Next, is the definition of the probabilistic function $G(\boldsymbol{\pi}, \boldsymbol{\xi})$. Let the random vector $\boldsymbol{\xi} = [\mathbf{c}, \boldsymbol{\rho}]$ correspond to (i) the received power coefficient between PB m and energy-harvesting devices across $\mathcal{T}$ frames, and (ii) the required transmit power for source and relays to send a sample across $\mathcal{T}$ frames. Second, the decision variable $\boldsymbol{\pi}$ corresponds to a set of switched-beam patterns used by PB m in each frame. In addition, each device needs a transmission schedule based on its energy level.

Formally, the function $G(\boldsymbol{\pi}, \boldsymbol{\xi})$ is represented as

$$G(\boldsymbol{\pi}, \boldsymbol{\xi}) = \lambda_o - \Delta. \tag{5.20}$$

Specifically, the value of $G(\boldsymbol{\pi}, \boldsymbol{\xi})$ is less than or equal to zero only if solution $\boldsymbol{\pi}$ ensures the sample arrival time λ_o is no larger than Δ for all realizations of $\boldsymbol{\xi}$. Otherwise, the value of function $G(\boldsymbol{\pi}, \boldsymbol{\xi})$ is larger than zero, meaning the source or relays meet an energy shortfall over random channel gains given solution $\boldsymbol{\pi}$. Next, the probabilistic constraint for the proposed chance-constrained problem is

$$Pr\{G(\boldsymbol{\pi}, \boldsymbol{\xi}) \leq 0\} \geq (1 - \epsilon), \tag{5.21}$$

where the probability ϵ and threshold Δ are given. The symbol ϵ is the probability that a sample fails to arrive sink within Δ frames. Note that Eq. (5.21) requires the joint probability distribution of all realizations of the random vector $\boldsymbol{\xi}$.

Formally, a chance-constrained stochastic model for the proposed problem is formulated as per

$$\begin{aligned} \min_{w_{mz}^t, a_i^t} \quad & \sum_{t=1}^{T} \sum_{m=1}^{|\mathcal{M}|} \sum_{z=1}^{|\mathcal{Z}|} \sum_{k=1}^{|\mathcal{K}|} p_{mk}^z w_{mz}^t \\ s.t. \quad & (5.3) - (5.6), \quad (5.7) - (5.11), \\ & (5.12) - (5.19), \quad (5.20) - (5.21). \end{aligned} \tag{5.22}$$

There are a number of challenges when solving the problem of this chapter. The first challenge is imperfect CSI and random channel power gains. This means PB m is not able to decide its transmit power allocation or switched-beam pattern based on channel power gains and energy level at devices. In addition, the required energy to transmit a sample also varies with random channel gains in each frame. Consequently, when PB m randomly transmits in each frame, the source and relay devices may experience an energy shortfall across $\mathcal{T}$ frames. This in turn increases sample arrival time. The second challenge is solving chance-constrained stochastic problem (5.22). It is a challenging problem because (i) checking the feasibility of a given solution $\boldsymbol{\pi}$ requires the calculation of a multivariate integral, and (ii) the chance constraint function $G(\boldsymbol{\pi}, \boldsymbol{\xi})$ is usually not convex [204]. In addition, calculating the optimal solution for the true problem (5.22) needs the actual probability distribution of random variables. However, the actual probability distribution is difficult to obtain in practice.

5.3 Sample Average Approximation

This chapter adopts SAA [57] to approximate the optimal solution to the true problem (5.22) with Monte Carlo sampling. In particular, the actual distribution of $\boldsymbol{\xi}$ in problem (5.22) is replaced by its empirical distribution [57]. First, consider to rewrite the probability constraint function (5.21) for a corresponding SAA problem as follows: $q(\boldsymbol{\pi}) \leq \epsilon$, where $q(\boldsymbol{\pi}) = Pr\{G(\boldsymbol{\pi}, \boldsymbol{\xi}) > 0\}$. This means the probability of the sample arriving after Δ frames for all realizations of $\boldsymbol{\xi}$ is at most ϵ for solution $\boldsymbol{\pi}$. Next, let $\boldsymbol{\xi}^1, \ldots, \boldsymbol{\xi}^N$ be a set of N i.i.d scenarios or realizations of the random vector $\boldsymbol{\xi}$ derived from an empirical distribution; each scenario is denoted as $\boldsymbol{\xi}^j$. This means the probability function $q(\boldsymbol{\pi})$ with N i.i.d scenarios can be approximated as per

$$\hat{q}_N(\boldsymbol{\pi}) = \frac{1}{N} \sum_{j=1}^{N} \mathbb{1}_{(0,\infty)}(G(\boldsymbol{\pi}, \boldsymbol{\xi}^j)), \tag{5.23}$$

where the indicator function $\mathbb{1}_{(0,\infty)}(G(\boldsymbol{\pi}, \boldsymbol{\xi}^j))$ is equal to one when the probabilistic function satisfies $G(\boldsymbol{\pi}, \boldsymbol{\xi}^j) > 0$. Otherwise, it returns a value of zero for the input solution $\boldsymbol{\pi}$ and scenario $\boldsymbol{\xi}^j$.

Next, consider to formulate a mixed integer linear program (MILP) with N i.i.d scenarios for the SAA problem:

$$\min_{w_{mz}^t,\, a_i^{jt}} \quad \sum_{t=1}^{T}\sum_{m=1}^{|\mathcal{M}|}\sum_{z=1}^{|\mathcal{Z}|}\sum_{k=1}^{|\mathcal{K}|} p_{mk}^{z} w_{mz}^{t} \tag{5.24a}$$

$$\text{s.t.} \quad (5.3)-(5.6), (5.9)-(5.10), (5.14)-(5.20), \tag{5.24b}$$

$$\sum_{j=1}^{N} y_j \le \epsilon N, \tag{5.24c}$$

$$G(\boldsymbol{\pi}, \boldsymbol{\xi}^j) \le \Phi y_j, j = 1, \ldots, N \tag{5.24d}$$

Note that constraints (5.24b) exist for each scenario $\boldsymbol{\xi}^j$. This means each relay can have a different activation and energy level in each scenario, which in turn results in a different sample arrival time in each scenario $\boldsymbol{\xi}^j$. To this end, let auxiliary decision variable a_i^{jt} indicate the activation of relay i in frame t under channel conditions given in scenario $\boldsymbol{\xi}^j$. Note that there is a set of new variables $y_1, \ldots, y_N$, and new constraints in MILP (5.24). First, the binary variable $y_j \in \{0, 1\}$ equals zero when solution $\boldsymbol{\pi}$ ensures the sample arrives at sink o within Δ frames for scenario $\boldsymbol{\xi}^j$. Constraint (5.24c) specifies that the sink o fails to receive a sample within Δ frames in at most ϵN scenarios, i.e., $\hat{q}_N(\boldsymbol{\pi}) \le \epsilon$. Constraint (5.24d) specifies $G(\boldsymbol{\pi}, \boldsymbol{\xi}^j) \le 0$ only if the value of y_j is zero. In addition, if the value of y_j is non-zero, constraint (5.24d) is disabled by a big number Φ[1], where Φ is set to $(T - \Delta + 1)$, i.e., the upper bound of function $G(\boldsymbol{\pi}, \boldsymbol{\xi})$.

The solution for the SAA problem converges to the optimal solution to the true problem (5.22) as the value of N approaches infinity [57]. However, notice that MILP (5.24) becomes computationally intractable with an increasing number of binary variables, i.e., y_j. To this end, consider to use a different probability level γ to replace ϵ in constraint (5.24c), where $\gamma \le \epsilon$. This helps the solution for MILP (5.24) to be a feasible point to the true problem (5.22) when there is only given a small number of scenarios [57], e.g., $N \le 100$.

[1]This is also known as the big-M method.

5.3.1 Solution Quality

This chapter adopts the validation procedure in [57] to evaluate a candidate solution for the SAA problem (5.24) versus the optimal solution of the true problem (5.22). Specifically, for a given candidate solution $\boldsymbol{\pi}$ that specifies a switched-beam pattern schedule of the PB, the validation procedure includes (i) whether $\boldsymbol{\pi}$ is a feasible point for the true problem (5.22), and (ii) if $\boldsymbol{\pi}$ is a feasible point, it next evaluates the optimality gap between the total transmit power of the PB for the SAA problem (5.24) and the total transmit power of the PB for the true problem (5.22).

The validation procedure starts by validating whether a candidate solution $\boldsymbol{\pi}$ is a feasible solution to the true problem (5.22). To this end, it first generates a large number of N' scenarios via Monte Carlo sampling, denoted as $\boldsymbol{\xi}^1, \ldots, \boldsymbol{\xi}^{N'}$. It then estimates $q(\boldsymbol{\pi})$ by computing $\hat{q}_{N'}(\boldsymbol{\pi})$ as per Eq. (5.23) given N' scenarios. Next, it is well known that the Binomial distribution approximates the Normal distribution for large N'. This means the validation procedure is able to estimate $q(\boldsymbol{\pi})$ using a Normal distribution with mean $q(\boldsymbol{\pi})$ and variance $q(\boldsymbol{\pi})(1 - q(\boldsymbol{\pi}))/N'$. Mathematically, the $(1 - \beta)$ confidence upper bound of $q(\boldsymbol{\pi})$ estimated by $\hat{q}_{N'}(\boldsymbol{\pi})$ is

$$U_{\beta,N'}(\boldsymbol{\pi}) = \hat{q}_{N'}(\boldsymbol{\pi}) + z_\beta \sqrt{\hat{q}_{N'}(\boldsymbol{\pi})(1 - \hat{q}_{N'}(\boldsymbol{\pi}))/N'}, \tag{5.25}$$

where $z_\beta = \Phi^{-1}(1 - \beta)$ is the $(1 - \beta)$-quantile of the standard Normal distribution; $\Phi^{-1}(.)$ is the inverse CDF of the standard Normal distribution. When the value of $U_{\beta,N'}(\boldsymbol{\pi})$ is not larger than ϵ, solution $\boldsymbol{\pi}$ is feasible to the true problem (5.22) with a confidence level of $(1 - \beta)$.

The method to validate the lower bound of the objective value of the true problem (5.22) is as follows. First, given the Binomial distribution where the probability of success is q, then its CDF is calculated as per

$$B(L; q, N) = \sum_{l=0}^{L} \binom{N}{i} q^l (1 - q)^{N-l}, \tag{5.26}$$

where Eq. (5.26) represents the cumulative probability of at most L successes in N trials. By Eq. (5.26), it is able to calculate the probability that the value of function $G(\boldsymbol{\pi}, \boldsymbol{\xi}^j)$ is larger than zero for at most γN times in N scenarios for solution $\boldsymbol{\pi}$ accordingly. Mathematically, let θ_N denote the probability of $\hat{q}_N(\boldsymbol{\pi}) \leq \gamma$, which is computed as per

$$\theta_N = Pr\{\hat{q}_N(\boldsymbol{\pi}) \leq \gamma\} = B(\gamma N; \epsilon, N). \tag{5.27}$$

Next, the validation procedure generates M i.i.d samples via Monte Carlo sampling, where each sample consists of N i.i.d scenarios. Let $\hat{v} = \{\hat{v}^1, \ldots, \hat{v}^M\}$ be a set of M corresponding optimal objective value of SAA problem (5.24). Next, it sorts all objective values in the set $\hat{v}$ in ascending order, i.e., $\hat{v}^1 \leq \hat{v}^2, \ldots, \leq \hat{v}^M$. Lastly, in order to obtain the lower bound of the true objective value with a confidence interval of $(1-\beta)$, it computes the largest integer L that satisfies

$$B(L-1; \theta_N, M) \leq \beta. \tag{5.28}$$

As per [57], the L-th largest objective value in the sorted set $\hat{v}$, i.e., $\hat{v}^L$, is a lower bound of the objective value of the true problem (5.22) with probability at least $(1-\beta)$.

5.3.2 Solutions Generation

This section outlines a procedure to generate a feasible solution to the true problem (5.22). Algorithm 7 starts by setting the failure probability ϵ and γ, and confidence level $(1-\beta)$. Next, the algorithm initializes the value of M, N, and N', respectively. In *Phase-1*, Algorithm 7 computes the $(1-\beta)$ confidence lower bound of the objective value of the true problem (5.22). After the value of M, N, ϵ and γ are given, Algorithm 7 first computes the value of L as per Eq. (5.28). In lines 5-8, Algorithm 7 solves MILP (5.24) M times, and generates a set of candidate solutions

$\{\boldsymbol{\pi}_1, \ldots, \boldsymbol{\pi}_M\}$ and objective values $\{\hat{v}_1, \ldots, \hat{v}_M\}$. As aforementioned, Algorithm 7 sorts all objective values in ascending order, and finds the L-th largest objective value $\hat{v}^L$. In line 9, Algorithm 7 selects the corresponding solution to the objective value $\hat{v}^L$, and denotes the solution as $\boldsymbol{\pi}^\star$.

In *Phase-2*, Algorithm 7 evaluates whether the selected solution $\boldsymbol{\pi}^\star$ from *Phase-1* is a feasible point to the true problem (5.22). In lines 13-15, note that the algorithm only needs to compute the number of times that the value of function $G(\boldsymbol{\pi}^\star, \boldsymbol{\xi}^j)$ is larger than zero. This also means N' can be set significantly larger than N as *Phase-2* does not involve solving MILP (5.24) exactly. In lines 16-19, if the selected solution $\boldsymbol{\pi}^\star$ is a feasible point to the true problem (5.22), Algorithm 7 returns $\boldsymbol{\pi}^\star$ as an output. Otherwise, it next validates whether the corresponding solution to the objective value $\hat{v}^{L+1}$ in the sorted set $\hat{v}$ is feasible, and repeats lines 11-19. If all candidate solutions are not a feasible point to the true problem, Algorithm 7 increases the value M and N and decreases the value of γ, and repeats lines 2-19.

Algorithm 7 needs to solve MILP (5.24) a large number of times in order to approximate the optimal solution to the true problem. To do so, SAA requires a large number of i.i.d scenarios to guarantee the solution is feasible with confidence level $(1 - \beta)$. Unfortunately, MILP (5.24) becomes computationally intractable as the number of integer decision variables increases with the number of scenarios.

5.4 A sampling method for probabilistic optimal power allocation

This section outlines a Sampling-based Probabilistic Optimal Power Allocation (S-POPA) method to approximate the optimal solution to problem (5.22). Briefly, S-POPA generates a set of candidate solutions, whereby each candidate solution represents the power allocation used by the PB. In addition, S-POPA assigns each candidate solution a reward value and a probability of being sampled based on its

Algorithm 7: Solutions Generation Procedure.

Set $\epsilon, \gamma, \beta, M, N, N'$
while *no solution is feasible* **do**
  // Phase-1: Generate candidate solutions
  Compute the value L as per Eq. (5.28)
  for *1,2,. . . ,M* **do**
    Solve MILP (5.24)
    Add the objective value of MILP into set $\hat{v}$
  end
  Sort the objective values in set $\hat{v}$
  // Phase-2: Solution feasibility validation
  for *L,. . . ,M* **do**
    Let the solution of $\hat{v}^L$ be $\boldsymbol{\pi}^\star$
    Generate N' i.i.d scenarios
    Compute $\hat{q}_{N'}(\boldsymbol{\pi}^\star)$ as per Eq. (5.23)
    Compute $U_{\beta,N'}(\boldsymbol{\pi}^\star)$ as per Eq. (5.25)
    if $U_{\beta,N'}(\boldsymbol{\pi}^\star) \leq \epsilon$ **then**
      return $\boldsymbol{\pi}^\star$
    end
  end
  Increase M and N, decrease γ
end

reward value. Specifically, there is a probability mass function (PMF) over these candidate solutions. Then in each iteration, using this PMF, S-POPA samples a candidate solution and determines its quality, i.e., whether the sampled candidate solution is a feasible point to the true problem with confidence level $(1 - \beta)$. After that, S-POPA updates the reward value of the sampled solution based on its quality and the total transmit power of the PB, and updates the PMF. After a given maximum number of iterations, S-POPA selects the candidate solution that has the highest reward value and checks whether the selected solution is a feasible point to the true problem (5.22).

The following paragraphs present the main steps of S-POPA; see Figure 5.3. It has R sampling rounds, whereby each sampling round consists of E sampling iterations. First, S-POPA starts each round by randomly generating $|\mathcal{A}|$ candidate solutions. Specifically, let $\mathcal{A}(r) = \{\boldsymbol{\pi}_1^r, \ldots, \boldsymbol{\pi}_{|\mathcal{A}|}^r\}$ represent the set of candidate solutions for use in the r-th round; each element is denoted as $\boldsymbol{\pi}_i^r$. In addition,

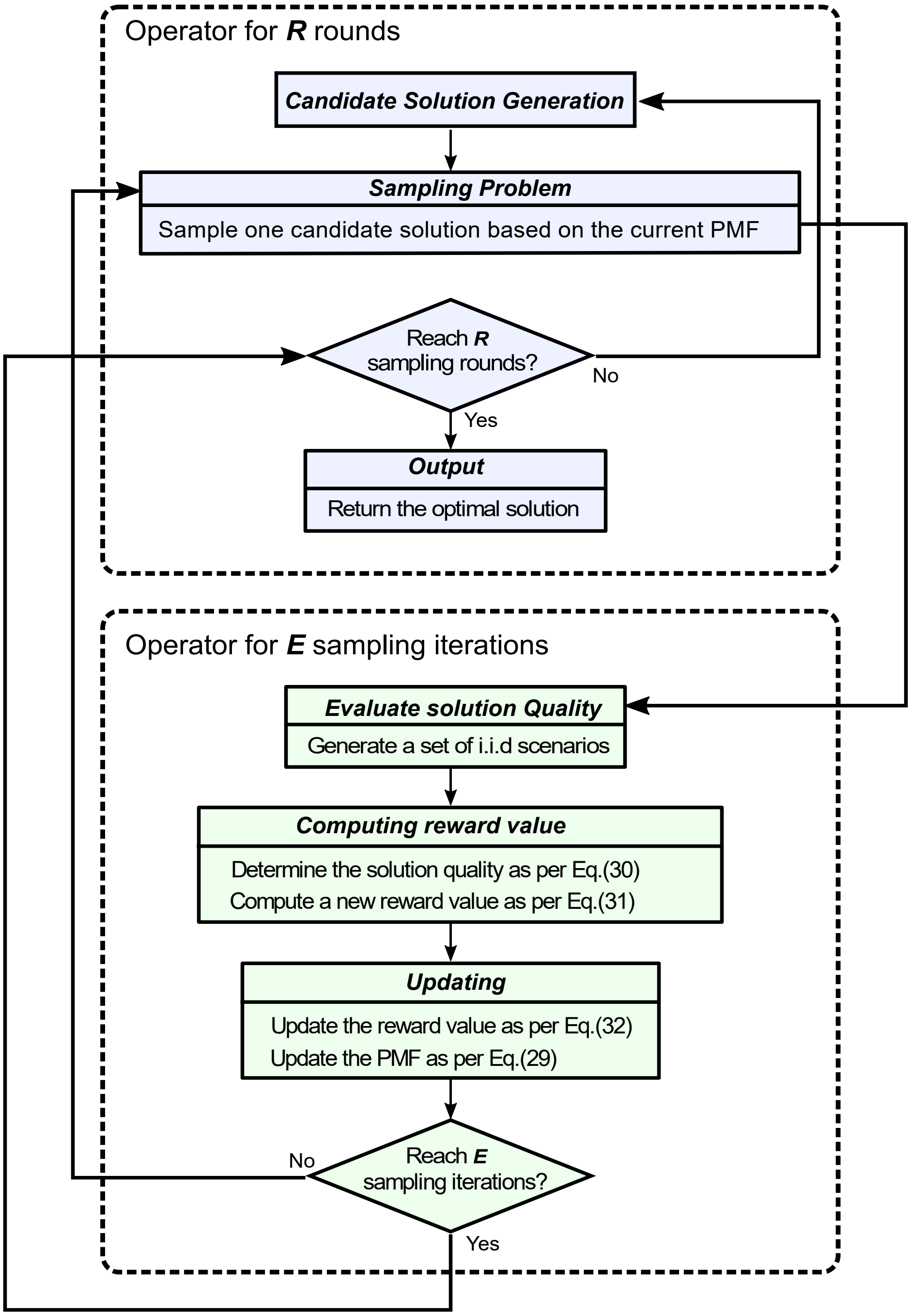

Figure 5.3: The main procedures of S-POPA.

let $\mathbf{P}(\boldsymbol{\pi}_i^r)$ denote the total transmit power of the PB for the candidate solution $\boldsymbol{\pi}_i^r$. Next, let $\omega(\boldsymbol{\pi}_i^r)$ and $Pr(\boldsymbol{\pi}_i^r)$ denote the reward value and the PMF for the candidate solution $\boldsymbol{\pi}_i^r$, respectively. In addition, the probability of selecting each candidate solution $\boldsymbol{\pi}_i^r$ in $\mathcal{A}(r)$ is computed via the *Softmax* function as per

$$Pr(\boldsymbol{\pi}_i^r) = \frac{e^{\omega(\boldsymbol{\pi}_i^r)}}{\sum_{j=1}^{|\mathcal{A}|} e^{\omega(\boldsymbol{\pi}_j^r)}}. \tag{5.29}$$

In other words, for each candidate solution, the probability of being sampled is proportional to its reward value. In particular, S-POPA assigns each candidate solution in $\mathcal{A}(r)$ with an initial reward value of one. This also means each candidate solution has an equal probability of $\frac{1}{|\mathcal{A}|}$ initially. Next, in each iteration of the r-th round, S-POPA carries out the following steps:

(i) S-POPA samples a solution $\boldsymbol{\pi}_i^r$ from the set $\mathcal{A}(r)$ according to its probability $Pr(\boldsymbol{\pi}_i^r)$.

(ii) In order to validate the quality of the sampled solution $\boldsymbol{\pi}_i^r$, S-POPA generates $\hat{N}$ i.i.d scenarios. Specifically, it computes the number of times that the probabilistic constraint, i.e., $G(\boldsymbol{\pi}_i^r, \boldsymbol{\xi}) \leq 0$, is satisfied over $\hat{N}$ trials. Let the said number be $\hat{L}$. Note that the value of $\hat{L}$ follows a Binomial distribution. To this end, S-POPA adopts the *Clopper-Pearson* method to validate whether solution $\boldsymbol{\pi}_i^r$ is a feasible point to the true problem with confidence level $(1-\beta)$. Let $C_{LB}(\boldsymbol{\pi}_i^r)$ denote the said $(1-\beta)$ confidence *Clopper-Pearson* interval lower bound. Mathematically, the value of $C_{LB}(\boldsymbol{\pi}_i^r)$ given solution $\boldsymbol{\pi}_i^r$ is calculated as per

$$\sum_{l=0}^{\hat{L}} \binom{\hat{N}}{l} (C_{LB}(\boldsymbol{\pi}_i^r))^l (1 - C_{LB}(\boldsymbol{\pi}_i^r))^{\hat{N}-l} = \frac{(1-\beta)}{2}, \tag{5.30}$$

(iii) S-POPA computes a reward value for the sampled solution $\boldsymbol{\pi}_i^r$ according to its quality. First, let $v(\boldsymbol{\pi}_i^r)$ denote the reward function for solution $\boldsymbol{\pi}_i^r$. Mathematically, the reward function is given by

$$v(\boldsymbol{\pi}_i^r) = e^{-\mathbf{P}(\boldsymbol{\pi}_i^r)}\kappa(C_{LB}(\boldsymbol{\pi}_i^r)), \tag{5.31}$$

where the reward function (5.31) specifies that the computed reward value of solution $\boldsymbol{\pi}_i^r$ is inversely proportional to the sum of transmit power at the PB. In addition, $\kappa(C_{LB}(\boldsymbol{\pi}_i^r))$ is a piece-wise function for the value of $C_{LB}(\boldsymbol{\pi}_i^r)$. In particular, S-POPA sets a large value for $\kappa(C_{LB}(\boldsymbol{\pi}_i^r))$ when $C_{LB}(\boldsymbol{\pi}_i^r)$ is no less than $(1-\epsilon)$. Otherwise, it sets the value of $\kappa(C_{LB}(\boldsymbol{\pi}_i^r))$ to be less than one. This ensures the computed reward value $v(\boldsymbol{\pi}_i^r)$ is less than the initial reward value when the sampled solution $\boldsymbol{\pi}_i^r$ is not a feasible point to the true problem.

(iv) The reward value $\omega(\boldsymbol{\pi}_i^r)$ in an iteration is updated as per

$$\omega(\boldsymbol{\pi}_i^r) = \hat{\alpha}\omega'(\boldsymbol{\pi}_i^r) + (1-\hat{\alpha})v(\boldsymbol{\pi}_i^r) \tag{5.32}$$

where $\omega'(\boldsymbol{\pi}_i^r)$ is the reward value of $\boldsymbol{\pi}_i^r$ in the previous iteration. In addition, this chapter sets the value of $\hat{\alpha}$ to equal 0.9 as per [205].

(v) S-POPA updates the PMF over all solutions in the $\mathcal{A}(r)$ by using the updated reward value $\omega(\boldsymbol{\pi}_i^r)$, which is calculated as per Eq. (5.29) accordingly.

After E iterations of the r-th round, S-POPA selects the optimal solution $\boldsymbol{\pi}_\star^r$ that has the largest reward value. Next, S-POPA computes the $(1-\beta)$ confidence upper bound for solution $\boldsymbol{\pi}_\star^r$ as per Eq. (5.25). If the value of confidence upper bound $U_{\beta,N'}(\boldsymbol{\pi}_\star^r)$ is larger than the value of ϵ, meaning solution $\boldsymbol{\pi}_\star^r$ is not feasible to the true problem with probability $(1-\beta)$, S-POPA then removes the candidate solution $\boldsymbol{\pi}_\star^r$ by replacing $\boldsymbol{\pi}_\star^r$ with $\boldsymbol{\pi}_\star^{r-1}$. Given $\boldsymbol{\pi}_\star^r$ and the value of $\mathbf{P}(\boldsymbol{\pi}_\star^r)$, S-POPA generates a set of new candidate solutions for use in the $(r+1)$-th round. Specifically, the total transmit power at the PB of each candidate solution sampled in the $(r+1)$-th round must be equal to or smaller than that of the solution $\boldsymbol{\pi}_\star^r$. This helps S-POPA to focus on candidate solutions with low transmit power as the number of rounds increases, thereby improving the sampling efficiency. Mathematically, a set of available candidate solutions sampled in the $(r+1)$-th round is given by

$$\mathcal{A}(r+1) = \{\boldsymbol{\pi}_i^{r+1} | \mathbf{P}(\boldsymbol{\pi}_i^{r+1}) \leq \mathbf{P}(\boldsymbol{\pi}_\star^r), 1 \leq i \leq |\mathcal{A}|\}. \tag{5.33}$$

After R sampling rounds, S-POPA terminates and returns a candidate solution with the highest reward value and being a feasible point to the true problem (5.22) as output.

The next proposition states the computational complexity of S-POPA method.

Proposition 10. *S-POPA has a run-time complexity of* $\mathcal{O}(R(E(\hat{N}|\mathcal{V}|T + 2|\mathcal{A}| + 1) + \hat{N}|\mathcal{V}|T))$.

Proof. In the initialization stage of each round, S-POPA creates $|\mathcal{A}|$ candidate solutions. This results in a computational complexity of $\mathcal{O}(|\mathcal{A}|)$. Then for each iteration, S-POPA samples one candidate solution based on its probability. This results in a computational complexity of $\mathcal{O}(|\mathcal{A}|)$. To validate the quality of a sampled solution in each iteration, S-POPA checks whether each device harvests sufficient energy to transmit a sample in each frame given each scenario. This gives us a time complexity of $\mathcal{O}(\hat{N}|\mathcal{V}|T)$ as there are $\hat{N}$ scenarios, $|\mathcal{V}|$ devices and $\mathcal{T}$ frames. Next, computing each Eq. (5.30)-(5.32) incurs a computation complexity of $\mathcal{O}(1)$. Computing the PMF for $|\mathcal{A}|$ candidate solutions results in a computation complexity of $\mathcal{O}(|\mathcal{A}|)$. Consequently, the combined computation complexity in each iteration is $\mathcal{O}(\hat{N}|\mathcal{V}|T + 2|\mathcal{A}| + 1)$. At the end of each round, the computation time to compute the $(1-\beta)$ confidence upper bound for a sampled solution is $\hat{N}|\mathcal{V}|T$. Considering S-POPA has R rounds and each round has E iterations, the computation complexity of S-POPA is $\mathcal{O}(R(E(\hat{N}|\mathcal{V}|T + 2|\mathcal{A}| + 1) + \hat{N}|\mathcal{V}|T))$, as claimed. □

5.5 A Bayesian Optimization algorithm for power allocation

Bayesian optimization is a well-known method to solve expensive optimization problems where the objective function is non-convex or cannot be mathematically defined [206]. Given the reward function (5.31), notice that the solution with the highest reward value is the optimal solution to the true problem with confidence level $(1-\beta)$. However, sampling all possible power allocations from a continuous search space is computationally intractable. In addition, the reward function (5.31) is non-concave. This means computing the global optimal solution of a given reward function (5.31) analytically is hard.

To this end, this chapter outlines a Bayesian Optimization based Probabilistic Optimal Power Allocation (BO-POPA) algorithm to approximate the optimal solution to the true problem (5.22). Bayesian optimization is based on Bayesian Theorem. Specifically, Bayesian optimization allows us to construct a surrogate model of any reward function via a number of sampling iterations. The surrogate model approximates a given reward function, and also indicates the uncertainty level for the prediction value at each possible power allocation. Advantageously, we are able to compute an approximation of the optimal solution to the true problem by evaluating the surrogate model.

First, define a new reward objective function $f(\boldsymbol{\pi})$ for use by BO-POPA rather than employing Eq. (5.31). The reward value of a solution depends on the total transmit power at the PB and its quality, i.e., whether the solution is a feasible point to the true problem with confidence level $(1-\beta)$. Mathematically, the reward function $f(\boldsymbol{\pi})$ is given by

$$f(\boldsymbol{\pi}) = \mathbf{P}(\boldsymbol{\pi}) + \kappa'(C_{LB}(\boldsymbol{\pi}))TP_{max}, \tag{5.34}$$

where $\mathbf{P}(\boldsymbol{\pi})$ denote the total transmit power of the PB for power allocation $\boldsymbol{\pi}$ over

$\mathcal{T}$ frames, the value of $C_{LB}(\boldsymbol{\pi})$ is the $(1-\beta)$ *Clopper-Pearson* confidence interval lower bound when solution $\boldsymbol{\pi}$ is sampled as per Eq. (5.30). In addition, the binary variable $\kappa'(C_{LB}(\boldsymbol{\pi}))$ is equal to zero only when the value of p_{LB} is less than or equal to the value of ϵ. This means the optimal solution to the objective function $f(\boldsymbol{\pi})$ must be a feasible point to the true problem with confidence level $(1-\beta)$. Next, BO-POPA derives the optimal power allocation $\boldsymbol{\pi}^\star$ that satisfies

$$\boldsymbol{\pi}^\star = \arg\min_{\boldsymbol{\pi}\in\boldsymbol{\Pi}} f(\boldsymbol{\pi}) \tag{5.35}$$

where $\boldsymbol{\pi}^\star$ is the optimal power allocation solution, symbol $\boldsymbol{\Pi}$ is the search space for all possible power allocations used for the PB over $\mathcal{T}$ frames.

The surrogate model of the given objective function $f(\boldsymbol{\pi})$ is defined as $\hat{f}(\boldsymbol{\pi})$. In Bayesian optimization, the surrogate model is typically a Gaussian Process (GP) model [207]. A GP is uniquely defined by a mean function $\mu(\boldsymbol{\pi})$, and a covariance kernel function $k(\boldsymbol{\pi}_i, \boldsymbol{\pi}_j)$ that represents the correlation between solution $\boldsymbol{\pi}_i$ and $\boldsymbol{\pi}_j$. Typically, assume values on the surrogate model $\hat{f}(\boldsymbol{\pi})$ are jointly Gaussian distributed with zero means. In addition, BO-POPA employs the *Marten* class kernel function [206]. Given a set of sampled solutions $\{\boldsymbol{\pi}_1, \ldots, \boldsymbol{\pi}_M\}$, BO-POPA is able to compute a covariance kernel matrix $\mathbf{K}$ with a dimension of $M \times M$; each element is the covariance of a pair of sampled solutions. Employing the covariance kernel matrix $\mathbf{K}$ allows BO-POPA to compute the GP posterior distribution of the surrogate function $\hat{f}(\boldsymbol{\pi})$. Specifically, the prediction $\hat{f}(\boldsymbol{\pi}')$ at any possible solution $\boldsymbol{\pi}'$ that has not been sampled follows a Gaussian distribution, where its mean $\mu(\boldsymbol{\pi}')$ and variance $\sigma^2(\boldsymbol{\pi}')$ are respectively calculated as per [207]:

$$\mu(\boldsymbol{\pi}') = \mathbf{k}^T\mathbf{K}^{-1}[f(\boldsymbol{\pi}_1), \ldots, f(\boldsymbol{\pi}_M)], \tag{5.36}$$

$$\sigma^2(\boldsymbol{\pi}') = k(\boldsymbol{\pi}', \boldsymbol{\pi}') - \mathbf{k}^T\mathbf{K}^{-1}\mathbf{k}, \tag{5.37}$$

where $\mathbf{k} = [k(\boldsymbol{\pi}', \boldsymbol{\pi}_1), \ldots, k(\boldsymbol{\pi}', \boldsymbol{\pi}_M)]$ is a vector of covariance terms between the new $\boldsymbol{\pi}'$ and each sampled solution.

This paragraph now outlines the main steps of BO-POPA; see Algorithm 8. The BO-POPA algorithm consists of M' sampling iterations. Let $\mathcal{D}$ denote a set of sampled data, where each element $(\boldsymbol{\pi}_i, f(\boldsymbol{\pi}_i))$ is a tuple that represents the sampled solution and its corresponding reward value in the i-th iteration. First, each iteration i starts by selecting a power allocation $\boldsymbol{\pi}_i$ that maximizes an acquisition function $u(\boldsymbol{\pi}|\mathcal{D})$. In practice, there are numerous acquisition functions, where BO-POPA employs the Expected Improvement (EI) acquisition function outlined in [208]. Specifically, the EI acquisition function $u(\boldsymbol{\pi}|\mathcal{D})$ requires the GP posterior distribution computed from a set of observed samples $\{\boldsymbol{\pi}_1, \dots, \boldsymbol{\pi}_{i-1}\}$ and data $\{f(\boldsymbol{\pi}_1), \dots, f(\boldsymbol{\pi}_{i-1})\}$ in set $\mathcal{D}$. Next, BO-POPA generates a set of $\hat{N}$ i.i.d scenarios to evaluate the solution quality of the sampled power allocation by computing its confidence interval lower bound p_{LB}. After that, BO-POPA computes the corresponding objective value $f(\boldsymbol{\pi}_i)$ of solution $\boldsymbol{\pi}_i$, and adds the observed data $(\boldsymbol{\pi}_i, f(\boldsymbol{\pi}_i))$ into the set $\mathcal{D}$ accordingly. Next, BO-POPA updates the GP model and computes the GP posterior distribution as per Eq. (5.36) and Eq. (5.37). After M' iterations, BO-POPA fits the surrogate GP model $f(\boldsymbol{\pi})$ for a set of observed samples in the set $\mathcal{D}$. Lastly, it computes an optimal power allocation $\boldsymbol{\pi}^\star$ with the minimum prediction value $\hat{f}(\boldsymbol{\pi}^\star)$ on the surrogate model $\hat{f}(\boldsymbol{\pi})$.

Algorithm 8: *BO-POPA.*

for i = *1, 2, . . . ,* M' **do**
  Find a power allocation $\boldsymbol{\pi}_i$ that maximizes the acquisition function $u()$:
  $\boldsymbol{\pi}_i = \arg\max_{\boldsymbol{\pi}\in\boldsymbol{\Pi}} u(\boldsymbol{\pi}|\mathcal{D})$
  Generate $\hat{N}$ i.i.d scenarios and compute p_{LB} of $\boldsymbol{\pi}_i$.
  Compute the objective value $f(\boldsymbol{\pi}_i)$.
  Add data $(\boldsymbol{\pi}_i, f(\boldsymbol{\pi}_i))$ into set $\mathcal{D}$
  Update the GP model $\hat{f}(\boldsymbol{\pi})$ upon the observed data set $\mathcal{D}$
end
Find the optimal solution $\boldsymbol{\pi}^\star$ by evaluating GP model:
$\boldsymbol{\pi}^\star = \arg\min_{\boldsymbol{\pi}\in\boldsymbol{\Pi}} \hat{f}(\boldsymbol{\pi})$
return $\boldsymbol{\pi}^\star$

5.5.1 Discussion

Note that the major difference between SAA, S-POPA, and BO-POPA lies in how they derive a charging policy that approximates the true problem. Specifically, SAA determines a charging policy by repeatedly solving the MILP with N chance constraints M times. As solving the MILP is computationally intractable when the value of N is large, solving SAA can be time consuming and may not apply to large-scale networks. S-POPA approximates the optimal solution to the true problem by iteratively sampling possible solutions that have higher reward values, and it narrows its search region in each round. To this end, a critical issue for S-POPA is to determine the number of sampling rounds and iterations that ensure the computed solution meets the chance requirements of the true problem. BO-POPA constructs a GP model to approximate the true problem (5.22) and updates the model based on sampled solutions. Advantageously, BO-POPA is able to return an approximation to the true problem within a limited number of samples. Further, sampling more solutions helps improve the accuracy of the GP model to the true problem.

5.6 Evaluation

This chapter conducts all simulations in Python 3.9 and commercial solver Gurobi 9.3 [190]. The source and relays are uniformly deployed within a square area of 10 m $\times$ 10 m. Each device has a battery capacity of 200 mJ. The SNR threshold and data rate of each device is respectively set to 5 dB and 250 kb/s based on the datasheet of WaspMote [209] and IEEE 802.15.4 standard [210]. The non-linear energy conversion rates at devices are derived from the datasheet of P2110B RF-energy harvester [192]; as shown in Table 5.3. The PB has three antennas and a maximum transmit power of 1 Watt. It is placed at the center of the said square area. The path-loss at the reference distance of 1 m is set to 20 dB, and the path-loss exponent β is set to 2.5. The noise power level N_0 is set to -90 dBm/Hz.

Furthermore, the value of sample arrival deadline is equal to the number of frames, i.e., $\Delta = |\mathcal{T}|$. Table 5.2 lists parameter values adopted in all simulations.

Table 5.2: Parameter values.

Parameter	**Value(s)**	**Parameter**	**Value(s)**
α	20 dB	β	2
$\lvert\mathcal{V}\rvert$	1 to 9	Δ	2 to 10
L	$10 \times 10\ m^2$	S	250 kb
δ	5 dB	$C(\delta)$	250 kb/s
P_{max}	1 Watt	N_0	-90 dBm
R	20 to 100	E	200
$\lvert\mathcal{A}\rvert$	100	M'	100
N'	10^5	$\hat{N}$	200

Table 5.3: Received power and energy conversion rates.

Interval	**Received power (in mW)**	η
I_6	≥ 10.0	5%
I_5	[5.0, 10.0]	55%
I_4	[0.8, 5.0]	60%
I_3	[0.6, 0.8]	55%
I_2	[0.08, 0.6]	35%
I_1	[0.0, 0.08]	5%

5.6.1 Solution quality of SAA method

The first set of simulations evaluates the solution quality of SAA. This section aims to evaluate how the 95% confidence level upper bound of the computed solution varies with the number of scenarios. To this end, the number of scenarios in each sample varies from ten to sixty with an interval of ten in this set of simulations. The value of Δ is set to three and there are three hops from the source to the destination. The failure rate ϵ is 0.2. To apply SAA, this section considers two failure levels, namely $\gamma = 0.1$ and $\gamma = 0.2$, to solve MILP (5.24).

Referring to Figure 5.4, the gap between the 95% confidence level upper bound and failure rate ϵ decreases as the number of scenarios increases. As expected, the solution quality of SAA improves with more scenarios. In addition, the gap between the 95% confidence level upper bound and ϵ decreases when a smaller γ is used by MILP (5.24). For example, when there are 60 scenarios, the 95% confidence level upper bound for $\gamma = 0.2$ remains higher than ϵ. Hence, the solution for SAA when using $\gamma = \epsilon = 0.2$ is not a feasible point to the true problem. Observe that the 95% confidence level upper bound is 0.195 when $\gamma = 0.1$. This indicates that a small γ helps SAA generate feasible solutions by using a small number of i.i.d scenarios.

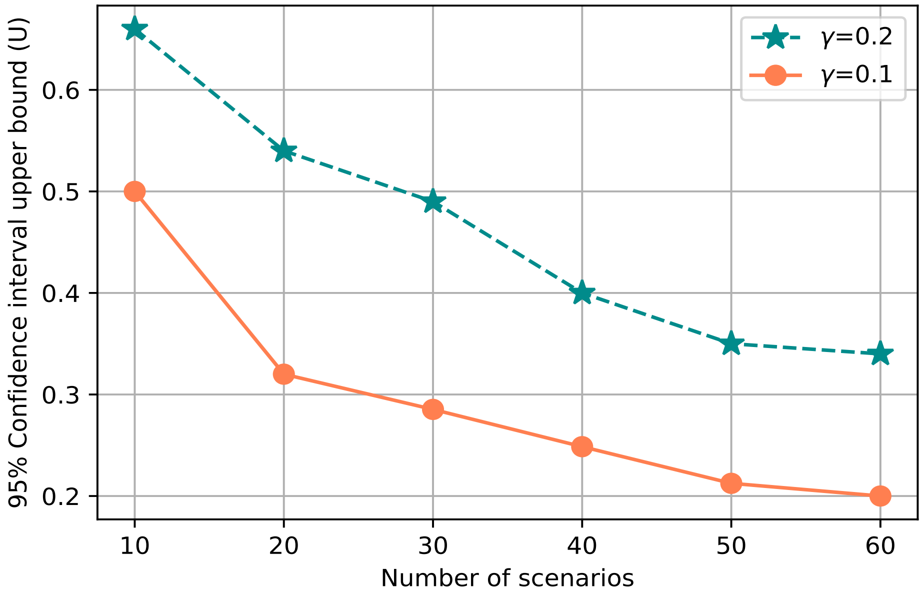

Figure 5.4: Confidence upper bound versus the number of scenarios. The gap between the 95% confidence level upper bound and ϵ when using $\gamma = 0.1$ reduces from 0.51 to 0.19. The gap between the 95% confidence level upper bound and ϵ when using $\gamma = 0.2$ reduces from 0.67 to 0.34. The result shows that the solution quality improves with more scenarios and a small γ value.

5.6.2 Robustness requirements

Here, this set of simulations investigates how different values of ϵ affect the minimum total transmit power of the PB. The value of γ is set to half the value of ϵ. This section fixes the number of devices to three, i.e., the source is connected to the sink via two hops. The value of Δ is fixed to five. As for MILP (5.24), the value of M and N is set to 200 and 100, respectively.

Referring to Figure 5.5(a), the minimum total transmit power at the PB reduces with an increasing value of failure rate ϵ. For example, the minimum total transmit power at the PB reduces from 2.22 to 1.21 Watts. The minimum total transmit power at the PB reduces from 2.8 to 1.37 Watts and 3.02 to 1.5 Watts for S-POPA and BO-POPA, respectively. This is because when the value of ϵ increases, the sample arrival time is allowed to exceed the given deadline Δ in more scenarios. Consequently, the PB is able to use a lower transmit power to charge devices as the power allocation permits more failures. In addition, an increasing value of ϵ allows S-POPA and BO-POPA to sample solutions that have a lower *Clopper-Pearson* interval lower bound. As a result, S-POPA and BO-POPA result in the PB using a lower transmit power.

Referring to Figure 5.5(a), SAA outperforms S-POPA and BO-POPA. Specifically, when using SAA, the minimum total transmit power of the PB is on average 13.62% and 19.58% lower than that of S-POPA and BO-POPA, respectively. This is because the power allocation at the PB computed by S-POPA and BO-POPA does not change over multiple frames. This means S-POPA and BO-POPA are not able to adjust the PB's power allocation according to channel gains in different frames. The PB must transmit in all frames, including frames that have low channel power gains. In addition, the PB must also continuously transmit after all devices harvest a sufficient amount of energy. In SAA, the PB is able to switch its beamforming patterns to charge devices that on average have higher channel gains in each frame. Thus, SAA results in a lower total transmit power at the PB to charge devices as compared to S-POPA and BO-POPA. Moreover, the performance of S-POPA and BO-POPA depends on the number of sampling iterations. The solutions computed by S-POPA and BO-POPA approximate the optimal solution to the true problem as more sampling iterations are employed.

The following set of experiments next investigate how the different values of ϵ affect solutions quality. Figure 5.5(b) shows the 95% confidence level upper bound for SAA, S-POPA and BO-POPA as per Eq. (5.25). Referring to Figure 5.5(b), the 95% confidence level upper bound of SAA increases from 0.098 to 0.395 as the value of ϵ becomes larger. The reason is because an increasing ϵ value allows more transmission failures. In addition, we note that the 95% confidence level upper bound for SAA is lower than ϵ when the failure rate ϵ varies from 0.1 to 0.4. This means each solution for a given failure rate ϵ is a feasible point to the true problem with a 95% confidence level. Next, we note that the 95% confidence level upper bound for S-POPA and BO-POPA also increases proportionally to the value of ϵ. In addition, the gap between the upper bound for S-POPA and ϵ is on average 9.14% lower than the gap between the upper bound for BO-POPA and ϵ. This means the solution for S-POPA is closer to the true problem as compared to BO-POPA. The reason is because S-POPA is able to re-sample a solution that has a *Clopper-Pearson* interval lower bound that is close to ϵ. This prevents S-POPA from assigning a low reward to a solution in one sampling iteration due to random scenarios with poor channel power gains. However, BO-POPA only samples each point once to compute the surrogate model. This means any infeasible solutions where the PB uses a low transmit power is heavily punished due to poor channel gains in one iteration. Hence, solutions that approximate the optimal solution to the true problem are more likely to be assigned a poor objective value by the surrogate function. As a result, when using BO-POPA, the PB uses a higher transmit power to ensure the power allocation is a feasible point to the true problem with a high probability.

5.6.3 Number of relay devices

Here, the following set of experiments evaluates how the number of relay devices affects the total transmit power. The number of relays $|\mathcal{V}|$ increases from one to nine with an interval of one, meaning the sample is forwarded from the source to the sink via two to ten hops. The value of Δ is set to five. This section sets $M = 200$ and $N = 100$ scenarios. The value of ϵ is set to 0.2.

As shown in Figure 5.6, the total transmit power at the PB increases propor-

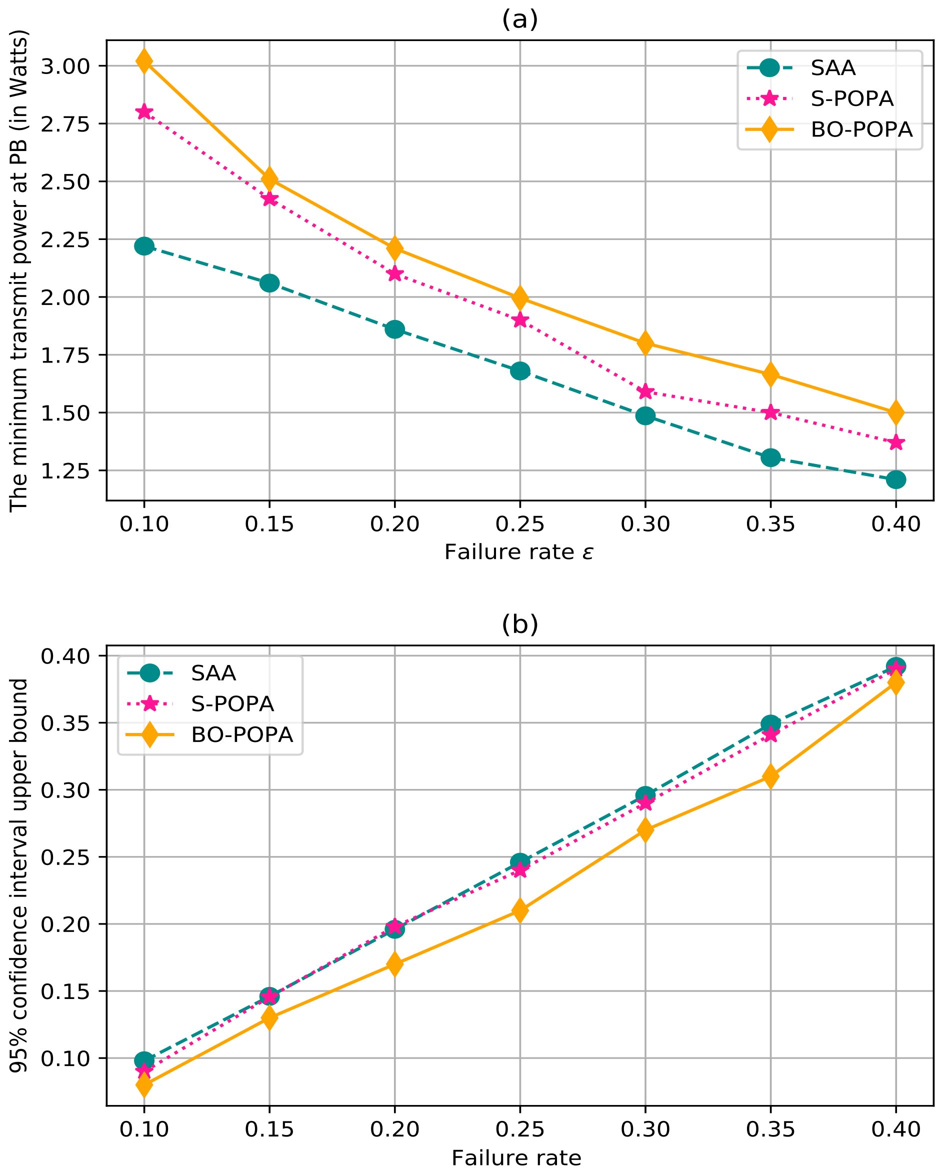

Figure 5.5: The minimum total transmit power at the PB (a), Confidence upper bound versus the number of scenarios(b). The result shown in (a) shows that the minimum total transmit power at the PB decreases with the value of ϵ. This is because a higher ϵ means a higher tolerance for transmission failures. In (b), the result shows all solutions are feasible points to the true problem with a confidence level of 95%.

tionally with the number of hops. For example, the minimum total transmit power at the PB computed by SAA increases from 1.89 to 5.49 as the number of relays $|\mathcal{V}|$ increases from one to nine. Then for S-POPA and BO-POPA, the total transmit power at the PB increases from 2.10 to 5.85 and 2.21 to 6.62 Watts, respectively. This is because the power allocation at the PB must satisfy the energy requirement of more relays. As there are more relays and more channel power gains, the probability that the PB charges devices even when the channel is poor increases. Hence, the PB has to raise its transmit power to charge devices that have poor channel gains in order to satisfy their energy requirement. In addition, the probability of relay devices transmitting over poor channel increases as there are more transmissions within Δ frames. Relay devices that experience poor channel gains will request more RF energy from the PB, which increases the transmit power of the PB.

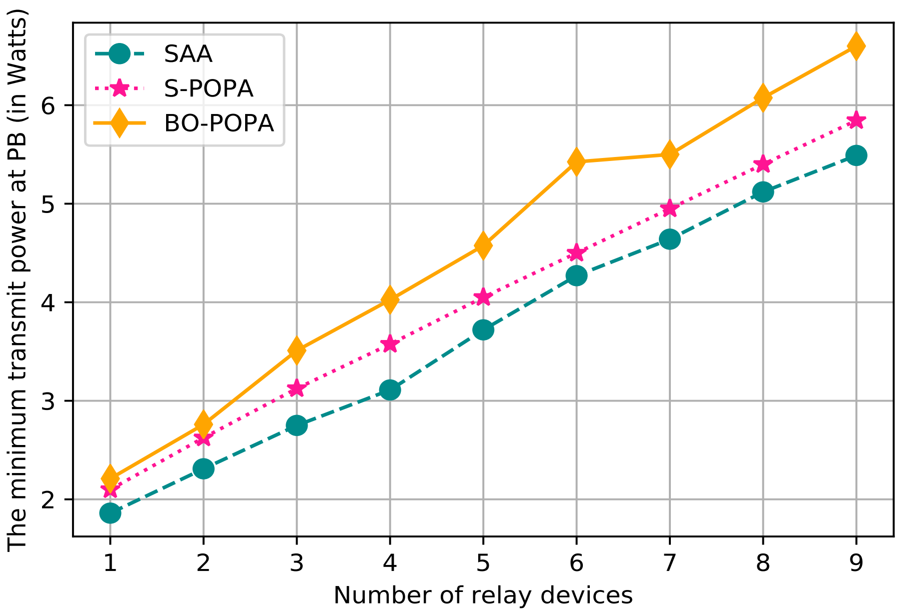

Figure 5.6: Comparison between the minimum total transmit power at the PB computed by SAA, S-POPA, and BO-POPA. The result shows that the minimum total transmit power at the PB increases as more relays request RF energy from the PB.

5.6.4 Sample arrival time threshold

In the last set of simulations, the focus is to investigate the relation between the total transmit power at the PB and threshold Δ. The number of relay devices $|\mathcal{V}|$ is fixed to three. The failure rate ϵ is set to 0.2, where this section considers $M = 200$ samples and each sample consists of $N = 100$ i.i.d scenarios.

As shown in Figure 5.7, the minimum total transmit power of the PB computed by SAA decreases from 4.58 to 1.25 Watts as Δ increases from one to ten. The minimum total transmit power at the PB computed by S-POPA and BO-POPA decreases from 5.46 to 1.61 Watts and 6.78 to 1.63 Watts, respectively. This is because a larger Δ value means relays have more time in order to harvest energy. This reduces the probability that a sample fails to arrive at the sink due to the energy shortfall at relays. In addition, relays are able to transmit in frames where the channel gains are higher on average, which helps utilize their harvested energy better. On the other hand, when using SAA, the PB is able to allocate its transmit power to charge relays that transmit with a high probability in each frame. This also helps to reduce the total transmit power of the PB.

Another observation is that the minimum total transmit power at the PB does not reduce continuously for an increasing threshold Δ value. This is because the energy conversion rate is non-linear. Recall that the power allocation computed by S-POPA and BO-POPA remains the same from frame to frame. Hence, a lower transmit power at the PB means the transmit power in all frames decreases equally. Consequently, if the PB reduces its transmit power to a low level, the source and relays have to harvest energy by using a low energy conversion efficiency of 5% over all frames. This results in devices to experience an energy shortfall as the sum of harvested energy over all frames is insufficient for transmission. As a result, the PB first reduces its transmit power as Δ increases, and maintains its transmit power level to prevent devices from using a low energy conversion efficiency in all frames.

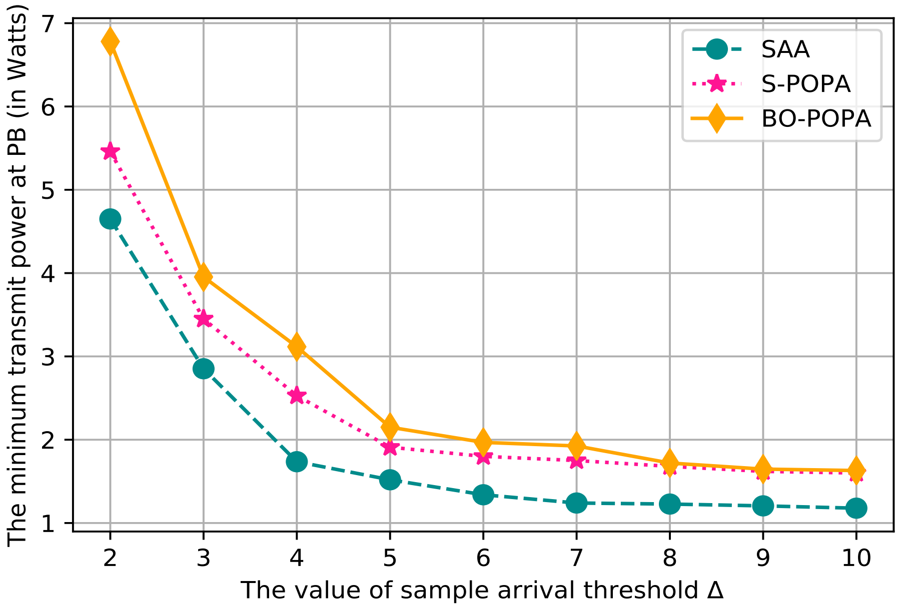

Figure 5.7: The minimum total transmit power of the PB versus sample arrival threshold Δ. The objective value of the SAA in on average 23.16% and 31.90% lower than that of S-POPA and BO-POPA, respectively. This is because S-POPA and BO-POPA require the PB to transmit with a fixed power level. In SAA, the switched-beam pattern of the PB in each frame depends on the sample delivery of N i.i.d scenarios given in MILP (5.24a).

5.7 Conclusion

This chapter has studied the problem of delivering samples to a sink node from a source device by a given deadline. A key challenge is that the PB that charges devices is unaware of their channel gains or energy information. To this end, this chapter develops a chance-constrained stochastic program to minimize the total transmit power at the PB subject to samples arriving at a sink with a given probability. This chapter solves the program using the SAA method, and also proposes two algorithms named S-POPA and BO-POPA to approximate the optimal solution. Numerical results show the minimum total transmit power at the PB is dependent on (i) the given sample delivery failure probability, (ii) the number of relay devices, and (iii) the sample arrival threshold Δ. In addition, SAA outperforms S-POPA and BO-POPA because S-POPA and BO-POPA are not able to adjust the beam patterns from frame to frame. Lastly, BO-POPA uses fewer sampling iterations and has a lower computation time as compared with SAA and S-POPA. However, the transmit power at the PB computed by BO-POPA is higher than that of SAA and S-POPA.

Chapter 6

Conclusion

This thesis considers data collection problems in multi-hop two-tier IoT networks. The first tier is a multi-hop wireless backhaul that is composed of routers. The second tier consists of a multi-hop RF energy-harvesting network or multi-hop ambient backscattering network. It focuses on the following research question: *how to jointly optimize energy provision and device activation in a two-tier multi-hop IoT network for data collection?* This question ensures devices in the second tier of an IoT network are able to harvest sufficient energy for data transmissions. Further, it ensures wireless links in the first tier have sufficient capacity to carry flows between routers. A major challenge is that the energy arrivals at devices depend on the transmissions of routers. Further, these routers operate over the same frequency band; i.e., they share limited channel resources. Another challenge is to efficiently deliver energy to devices and schedule the activation of devices in order to collect data.

This thesis first considers routing and link scheduling in a two-tier wireless backhaul network. The first tier consists of routers and the second tier consists of RF energy-harvesting IoT devices that rely on routers for energy. The goal is to derive the shortest TDMA link schedule that satisfies the traffic demand of routers and the energy demand of IoT devices. To this end, this thesis formulates an LP to jointly derive a routing and link schedule solution. This thesis also proposes a heuristic link scheduler called TSG to generate transmission sets and to derive the transmit power allocation of routers. In addition, this thesis outlines a novel routing metric that considers the number of RF energy-harvesting devices on a given path. TSG on average achieves 31.25% shorter schedules as compared to competing schemes. Finally, the proposed routing metric results in link schedules that are at most 24.75% longer than those computed by LP.

Second, this thesis considers routing and link scheduling in a two-tier backscatter-assisted wireless IoT network. The goal is to maximize the network throughput at both tiers. To this end, it outlines an MILP that jointly optimizes link scheduling for both RF links and backscattering links, and routing. It also presents a heuristic called ALGO-TSG to compute transmission sets for use by the proposed MILP. In addition, it also outlines a heuristic called CMF to maximize network throughput by jointly considering routing and link scheduling. The simulation results in Chapter 4 show that 1) the network throughput achieved by ALGO-TSG at both tiers is 29.80% higher as compared to the case without backscattering, and 2) the throughput of CMF is on average 21.36% lower than the throughput computed by MILP.

Lastly, this thesis considers sample delivery in a multi-hop network where a power beacon charges devices with imperfect CSI. Devices forward samples from a source to a sink, where the sample has a deadline. The goal is to minimize the energy consumption at a power beacon and ensure samples arrive at a sink by their deadline with a given probability level. To cope with imperfect CSI and probabilistic constraints, this thesis contains a chance-constrained stochastic program for the problem at hand. It employs the SAA method to approximate the optimal solution to the problem. This thesis also outlines two novel approximation methods for the problem, namely S-POPA and BO-POPA. Numerical results show that the performance of S-POPA and BO-POPA achieves on average 86.91% and 79.25% of the transmit power computed by SAA.

There are many possible future research directions. First, this thesis only considers routers that operate on the same frequency band. A possible research direction is to employ routers and devices that are equipped with multiple radios. This means routers and devices can operate on different channels, which yields more concurrent transmissions and increase both network capacity and energy delivered to devices. Consequently, an IoT system can collect more data packets from devices. A promising research problem is to jointly optimize channel assignment, link scheduling, and routing in a two-tier RF-energy harvesting IoT network. In terms of energy delivery and data transmission, this thesis only considers non-causal energy arrival processes and CSI. This means a controller is aware of future CSI to compute an optimal solution. A possible research direction is to consider data collection in a two-tier IoT network with causal CSI. In this case, routers and devices only have past and present CSI. To deal with causal CSI, a possible research problem is to adopt model predictive control, Markov decision process (MDP), and reinforcement learning techniques to name a few to optimize energy delivery policy and link scheduling. Another research direction is to consider information freshness optimization in an RF-charging network with imperfect CSI. In this case, multiple source devices will forward data packets to a sink via multi-hop communication. Different from Chapter 5, a power beacon needs to harvest energy from solar and experiences random energy arrival. In addition, it may be aware of which devices samples are at. This way, a fundamental problem is to jointly optimize energy delivery policy, routing, and device activation schedule in order to optimize information freshness.

Bibliography

[1] S. Chen, H. Xu, D. Liu, B. Hu, and H. Wang, "A vision of IoT: Applications, challenges, and opportunities with china perspective," *IEEE Internet of Things Journal*, vol. 1, pp. 349–359, Aug. 2014.

[2] I. Lee and K. Lee, "The internet of things (IoT): Applications, investments, and challenges for enterprises," *Business Horizons*, vol. 58, pp. 431–440, July 2015.

[3] Y. Zhou, D. Zhang, and N. Xiong, "Post-cloud computing paradigms: a survey and comparison," *Tsinghua Science and Technology*, vol. 22, pp. 714–732, Dec. 2017.

[4] Z. Yin, Y. Che, and W. He, "A hierarchical group control method of electrical loads in smart home," in *6th International Conference on Power Electronics Systems and Applications*, (Hong Kong, China), pp. 1–6, Dec. 2015.

[5] A. Fernández-Ares, A. Mora, M. Arenas, P. García-Sanchez, G. Romero, V. Rivas, P. Castillo, and J. Merelo, "Studying real traffic and mobility scenarios for a smart city using a new monitoring and tracking system," *Future Generation Computer Systems*, vol. 76, pp. 163–179, Nov. 2017.

[6] A. Solano, N. Duro, R. Dormido, and P. González, "Smart vending machines

in the era of internet of things," *Future Generation Computer Systems*, vol. 76, pp. 215–220, Nov. 2017.

[7] M. Srinivas, S. Benedict, and B. C. Sunny, "IoT cloud based smart bin for connected smart cities - a product design approach," in *10th International Conference on Computing, Communication and Networking Technologies (ICCCN)*, (Kanpur, India), pp. 1–5, July 2019.

[8] N. Gondchawar, R. Kawitkar, *et al.*, "IoT based smart agriculture," *International Journal of advanced research in Computer and Communication Engineering*, vol. 5, no. 6, pp. 838–842, 2016.

[9] M. S. Mekala and P. Viswanathan, "A survey: Smart agriculture IoT with cloud computing," in *International conference on Microelectronic Devices, Circuits and Systems (ICMDCS)*, (Vellore, India), pp. 1–7, Aug. 2017.

[10] V. Gupta, H. S. Gill, P. Singh, and R. Kaur, "An energy efficient fog-cloud based architecture for healthcare," *Journal of Statistics and Management Systems*, vol. 21, pp. 529–537, June 2018.

[11] J. M. Talavera, L. E. Tobón, J. A. Gómez, M. A. Culman, J. M. Aranda, D. T. Parra, L. A. Quiroz, A. Hoyos, and L. E. Garreta, "Review of IoT applications in agro-industrial and environmental fields," *Computers and Electronics in Agriculture*, vol. 142, pp. 283–297, Nov. 2017.

[12] J. Ruan and Y. Shi, "Monitoring and assessing fruit freshness in IOT-based e-commerce delivery using scenario analysis and interval number approaches," *Information Sciences*, vol. 373, pp. 557–570, Dec. 2016.

[13] C. le Zhong, Z. Zhu, and R.-G. Huang, "Study on the IOT architecture and access technology," in *2017 16th International Symposium on Distributed Computing and Applications to Business, Engineering and Science (DCABES)*, (Anyang, China), pp. 113–116, Oct. 2017.

[14] G. Hiertz, D. Denteneer, L. Stibor, Y. Zang, X. Costa, and B. Walke, "The ieee 802.11 universe," *IEEE Communications Magazine*, vol. 48, pp. 62–70, Jan. 2010.

[15] J.-S. Lee, Y.-W. Su, and C.-C. Shen, "A comparative study of wireless protocols: Bluetooth, UWB, ZigBee, and wi-fi," in *33rd Annual Conference of the IEEE Industrial Electronics Society*, (Taipei, Taiwan), pp. 56–61, Nov. 2007.

[16] Akashdeep, K. S. Kahlon, and H. Kumar, "Survey of scheduling algorithms in ieee 802.16 PMP networks," *Egyptian Informatics Journal*, vol. 15, pp. 25–36, Mar. 2014.

[17] G. M. Garrido, J. Sedlmeir, Ömer Uludağ, I. S. Alaoui, A. Luckow, and F. Matthes, "Revealing the landscape of privacy-enhancing technologies in the context of data markets for the IoT: A systematic literature review," *Journal of Network and Computer Applications*, vol. 207, p. 103465, Nov. 2022.

[18] A. Ali, Y. Ming, S. Chakraborty, and S. Iram, "A comprehensive survey on real-time applications of WSN," *Future Internet*, vol. 9, p. 77, Nov. 2017.

[19] F. Alizadeh-Shabdiz and S. Subramaniam, "Analytical models for single-hop and multi-hop ad hoc networks," *Mobile Networks and Applications*, vol. 11, pp. 75–90, Dec. 2005.

[20] M. Campista, P. Esposito, I. Moraes, L. Costa, O. Duarte, D. Passos, C. de Albuquerque, D. Saade, and M. Rubinstein, "Routing metrics and protocols for wireless mesh networks," *IEEE Network*, vol. 22, pp. 6–12, Jan. 2008.

[21] C. Shannon, "The zero error capacity of a noisy channel," *IEEE Transactions on Information Theory*, vol. 2, pp. 8–19, Sept. 1956.

[22] S. Weber, J. Andrews, X. Yang, and G. de Veciana, "Transmission capacity of wireless ad hoc networks with successive interference cancellation," *IEEE Transactions on Information Theory*, vol. 53, pp. 2799–2814, Aug. 2007.

[23] R. Nelson and L. Kleinrock, "Spatial TDMA: A collision-free multihop channel access protocol," *IEEE Transactions on Communications*, vol. 33, pp. 934–944, Sept. 1985.

[24] J. Yick, B. Mukherjee, and D. Ghosal, "Wireless sensor network survey," *Computer Networks*, vol. 52, pp. 2292–2330, Aug. 2008.

[25] T. Amgoth and P. K. Jana, "Energy-aware routing algorithm for wireless sensor networks," *Computers and Electrical Engineering*, vol. 41, pp. 357–367, Jan. 2015.

[26] S. Lin, F. Miao, J. Zhang, G. Zhou, L. Gu, T. He, J. A. Stankovic, S. Son, and G. J. Pappas, "ATPC," *ACM Transactions on Sensor Networks*, vol. 12, pp. 1–31, Mar. 2016.

[27] Z. Zhang, H. Pang, A. Georgiadis, and C. Cecati, "Wireless power transfer-an overview," *IEEE Transactions on Industrial Electronics*, vol. 66, pp. 1044–1058, Feb. 2019.

[28] N. V. Huynh, D. T. Hoang, X. Lu, D. Niyato, P. Wang, and D. I. Kim, "Ambient backscatter communications: A contemporary survey," *IEEE Communications Surveys and Tutorials*, vol. 20, no. 4, pp. 2889–2922, 2018.

[29] A. A. S. Mohamed, A. Meintz, P. Schrafel, and A. Calabro, "In-vehicle assessment of human exposure to EMFs from 25-kW WPT system based on near-field analysis," in *IEEE Vehicle Power and Propulsion Conference (VPPC)*, (Chicago, IL, USA), pp. 1–6, Aug. 2018.

[30] J. Huh, S. W. Lee, W. Y. Lee, G. H. Cho, and C. T. Rim, "Narrow-width inductive power transfer system for online electrical vehicles," *IEEE Transactions on Power Electronics*, vol. 26, pp. 3666–3679, Dec. 2011.

[31] A. M. Jawad, R. Nordin, S. K. Gharghan, H. M. Jawad, and M. Ismail, "Op-

portunities and challenges for near-field wireless power transfer: A review," *Energies*, vol. 10, p. 1022, July 2017.

[32] N. Shinohara, "Trends in wireless power transfer: WPT technology for energy harvesting, mllimeter-wave/THz rectennas, MIMO-WPT, and advances in near-field WPT applications," *IEEE Microwave Magazine*, vol. 22, pp. 46–59, Jan. 2021.

[33] D. Arnitz and M. S. Reynolds, "MIMO wireless power transfer for mobile devices," *IEEE Pervasive Computing*, vol. 15, pp. 36–44, Oct. 2016.

[34] J. Garnica, R. A. Chinga, and J. Lin, "Wireless power transmission: From far field to near field," *Proceedings of the IEEE*, vol. 101, pp. 1321–1331, June 2013.

[35] C. Song, Y. Huang, J. Zhou, J. Zhang, S. Yuan, and P. Carter, "A high-efficiency broadband Rectenna for ambient wireless energy harvesting," *IEEE Transactions on Antennas and Propagation*, vol. 63, pp. 3486–3495, Aug. 2015.

[36] X. Zhang, J. Grajal, M. López-Vallejo, E. McVay, and T. Palacios, "Opportunities and challenges of ambient radio-frequency energy harvesting," *Joule*, vol. 4, pp. 1148–1152, June 2020.

[37] P. Zhang, H. Yi, H. Liu, H. Yang, G. Zhou, and L. Li, "Back-to-back microstrip antenna design for broadband wide-angle RF energy harvesting and dedicated wireless power transfer," *IEEE Access*, vol. 8, pp. 126868–126875, July 2020.

[38] O. Galinina, H. Tabassum, K. Mikhaylov, S. Andreev, E. Hossain, and Y. Koucheryavy, "On feasibility of 5g-grade dedicated RF charging technology for wireless-powered wearables," *IEEE Wireless Communications*, vol. 23, pp. 28–37, Apr. 2016.

[39] T. Wu and H.-C. Yang, "RF energy harvesting with cooperative beam selection

for wireless sensors," *IEEE Wireless Communications Letters*, vol. 3, pp. 585–588, Dec. 2014.

[40] T. D. P. Perera, D. N. K. Jayakody, S. K. Sharma, S. Chatzinotas, and J. Li, "Simultaneous wireless information and power transfer (SWIPT): Recent advances and future challenges," *IEEE Communications Surveys and Tutorials*, vol. 20, no. 1, pp. 264–302, 2018.

[41] G. Wang, F. Gao, R. Fan, and C. Tellambura, "Ambient backscatter communication systems: Detection and performance analysis," *IEEE Transactions on Communications*, vol. 64, pp. 4836–4846, Nov. 2016.

[42] B. Kellogg, A. Parks, S. Gollakota, J. R. Smith, and D. Wetherall, "Wi-fi backscatter," in *Proceedings of the 2014 ACM conference on SIGCOMM*, (Chicago, Illinois, USA), pp. 607–618, Aug. 2014.

[43] D. Bharadia, K. R. Joshi, M. Kotaru, and S. Katti, "BackFi: high throughput wifi backscatter," *ACM SIGCOMM Computer Communication Review*, vol. 45, pp. 283–296, Sept. 2015.

[44] P. ZHANG, M. Rostami, P. Hu, and D. Ganesan, "Enabling practical backscatter communication for on-body sensors," in *Proceedings of the 2016 ACM SIGCOMM Conference*, (Florianopolis, Brazil), pp. 370–383, Aug. 2016.

[45] V. Liu, A. Parks, V. Talla, S. Gollakota, D. Wetherall, and J. R. Smith, "Ambient backscatter: Wireless communication out of thin air," *ACM SIGCOMM Computer Communication Review*, vol. 43, pp. 39–50, Sept. 2013.

[46] J. Qian, A. N. Parks, J. R. Smith, F. Gao, and S. Jin, "IoT communications with M-PSK modulated ambient backscatter: Algorithm, analysis, and implementation," *IEEE Internet of Things Journal*, vol. 6, pp. 844–855, Feb. 2019.

[47] V. Talla, M. Hessar, B. Kellogg, A. Najafi, J. R. Smith, and S. Gollakota, "LoRa backscatter," *Proceedings of the ACM on Interactive, Mobile, Wearable and Ubiquitous Technologies*, vol. 1, pp. 1–24, Sept. 2017.

[48] S. N. Daskalakis, J. Kimionis, A. Collado, G. Goussetis, M. M. Tentzeris, and A. Georgiadis, "Ambient backscatterers using FM broadcasting for low cost and low power wireless applications," *IEEE Transactions on Microwave Theory and Techniques*, vol. 65, pp. 5251–5262, Dec. 2017.

[49] J. Ryoo, J. Jian, A. Athalye, S. R. Das, and M. Stanacevic, "Design and evaluation of "BTTN": A backscattering tag-to-tag network," *IEEE Internet of Things Journal*, vol. 5, pp. 2844–2855, Aug. 2018.

[50] M. Hua, L. Yang, C. Li, Z. Zhu, and I. Lee, "Bistatic backscatter communication: Shunt network design," *IEEE Internet of Things Journal*, vol. 8, pp. 7691–7705, May 2021.

[51] R. Duan, X. Wang, H. Yigitler, M. U. Sheikh, R. Jantti, and Z. Han, "Ambient backscatter communications for future ultra-low-power machine type communications: Challenges, solutions, opportunities, and future research trends," *IEEE Communications Magazine*, vol. 58, pp. 42–47, Feb. 2020.

[52] J. Fei, K.-W. Chin, C. Yang, and M. Ros, "Data collection in multihop mobile sink-aided backscatter IoT networks," *IEEE Internet of Things Journal*, vol. 9, pp. 12001–12013, July 2022.

[53] A. Y. Majid, M. Jansen, G. O. Delgado, K. S. Yildirim, and P. Pawelczak, "Multi-hop backscatter tag-to-tag networks," in *IEEE INFOCOM-IEEE Conference on Computer Communications*, (Paris, France), pp. 721–729, Apr. 2019.

[54] C. Liu, Z. J. Haas, and Z. Tian, "On the design of multi-hop tag-to-tag routing

protocol for large-scale networks of passive tags," *IEEE Open Journal of the Communications Society*, vol. 1, pp. 1035–1055, 2020.

[55] O. Goussevskaia, Y. A. Oswald, and R. Wattenhofer, "Complexity in geometric SINR," in *8th ACM international symposium on Mobile ad hoc networking and computing - MobiHoc '07*, (Montreal Quebec Canada), pp. 100–109, Sept. 2007.

[56] A. Crauser, K. Mehlhorn, U. Meyer, and P. Sanders, "A parallelization of dijkstra's shortest path algorithm," in *Mathematical Foundations of Computer Science* (L. Brim, J. Gruska, and J. Zlatuška, eds.), (Berlin, Heidelberg), pp. 722–731, Aug. 1998.

[57] B. K. Pagnoncelli, S. Ahmed, and A. Shapiro, "Sample average approximation method for chance constrained programming: Theory and applications," *Journal of optimization theory and applications*, vol. 142, p. 399–416, Aug. 2009.

[58] H. Ju and R. Zhang, "Throughput maximization in wireless powered communication networks," *IEEE Transactions on Wireless Communications*, vol. 13, pp. 418–428, Jan. 2014.

[59] H. Ju and R. Zhang, "Optimal resource allocation in full-duplex wireless-powered communication network," *IEEE Transactions on Communications*, vol. 62, pp. 3528–3540, Oct. 2014.

[60] S. Bi and R. Zhang, "Placement optimization of energy and information access points in wireless powered communication networks," *IEEE Transactions on Wireless Communications*, vol. 15, pp. 2351–2364, Mar. 2016.

[61] W. Ejaz, S. Kandeepan, and A. Anpalagan, "Optimal placement and number of energy transmitters in wireless sensor networks for RF energy transfer," in

IEEE 26th Annual International Symposium on Personal, Indoor, and Mobile Radio Communications, (Hong Kong, China), pp. 1238–1243, Aug. 2015.

[62] H. Tabassum and E. Hossain, "On the deployment of energy sources in wireless-powered cellular networks," *IEEE Transactions on Communications*, vol. 63, pp. 3391–3404, Sept. 2015.

[63] O. M. Rosabal, O. L. A. Lopez, H. Alves, S. Montejo-Sanchez, and M. Latva-Aho, "On the optimal deployment of power beacons for massive wireless energy transfer," *IEEE Internet of Things Journal*, vol. 8, pp. 10531–10542, July 2021.

[64] K. Moon, K. M. Kim, Y. Kim, and T.-J. Lee, "Device-selective energy request in RF energy-harvesting networks," *IEEE Communications Letters*, vol. 25, pp. 1716–1719, May 2021.

[65] L. Liu, R. Zhang, and K.-C. Chua, "Multi-antenna wireless powered communication with energy beamforming," *IEEE Transactions on Communications*, vol. 62, no. 12, pp. 4349–4361, 2014.

[66] D. K. P. Asiedu, S. Mahama, C. Song, D. Kim, and K.-J. Lee, "Beamforming and resource allocation for multiuser full-duplex wireless-powered communications in IoT networks," *IEEE Internet of Things Journal*, vol. 7, pp. 11355–11370, Dec. 2020.

[67] Q. Sun, G. Zhu, C. Shen, X. Li, and Z. Zhong, "Joint beamforming design and time allocation for wireless powered communication networks," *IEEE Communications Letters*, vol. 18, pp. 1783–1786, Oct. 2014.

[68] Z. Xiang and M. Tao, "Robust beamforming for wireless information and power transmission," *IEEE Wireless Communications Letters*, vol. 1, pp. 372–375, Aug. 2012.

[69] R. Zhang and C. K. Ho, "MIMO broadcasting for simultaneous wireless information and power transfer," *IEEE Transactions on Wireless Communications*, vol. 12, pp. 1989–2001, May 2013.

[70] Q. Shi, L. Liu, W. Xu, and R. Zhang, "Joint transmit beamforming and receive power splitting for MISO SWIPT systems," *IEEE Transactions on Wireless Communications*, vol. 13, pp. 3269–3280, June 2014.

[71] X. Zhou, R. Zhang, and C. K. Ho, "Wireless information and power transfer in multiuser OFDM systems," *IEEE Transactions on Wireless Communications*, vol. 13, pp. 2282–2294, Apr. 2014.

[72] M. Y. Naderi, P. Nintanavongsa, and K. R. Chowdhury, "RF-MAC: A medium access control protocol for re-chargeable sensor networks powered by wireless energy harvesting," *IEEE Transactions on Wireless Communications*, vol. 13, pp. 3926–3937, July 2014.

[73] M. Moradian and F. Ashtiani, "Throughput analysis of a slotted aloha-based network with energy harvesting nodes," in *IEEE 23rd International Symposium on Personal, Indoor and Mobile Radio Communications - (PIMRC)*, (Sydney, NSW, Australia), pp. 351–356, Sept. 2012.

[74] H.-H. Choi and W. Shin, "Harvest-until-access protocol based on slotted ALOHA for wireless powered dense networks," in *International Conference on Electronics, Information, and Communication (ICEIC)*, (Auckland, New Zealand), pp. 1–6, Jan. 2019.

[75] Z. A. Eu and H.-P. Tan, "Probabilistic polling for multi-hop energy harvesting wireless sensor networks," in *IEEE International Conference on Communications (ICC)*, (Ottawa, ON, Canada), pp. 271–275, June 2012.

[76] T. D. Nguyen, J. Y. Khan, and D. T. Ngo, "A distributed energy-harvesting-

aware routing algorithm for heterogeneous IoT networks," *IEEE Transactions on Green Communications and Networking*, vol. 2, pp. 1115–1127, Dec. 2018.

[77] P. Gong, Q. Xu, and T. M. Chen, "Energy harvesting aware routing protocol for wireless sensor networks," in *9th International Symposium on Communication Systems, Networks and Digital Sign (CSNDSP)*, (Manchester, UK), pp. 171–176, July 2014.

[78] C. Lin, L. Tang, and X. Zhang, "Joint resource allocation and cooperative transmission in distributed wireless powered communication networks," in *IEEE International Conference on Communication Systems (ICCS)*, (Chengdu, China), pp. 337–342, Dec. 2018.

[79] D. Mishra and S. De, "Optimal power allocation and relay placement for wireless information and RF power transfer," in *IEEE International Conference on Communications (ICC)*, (Kuala Lumpur, Malaysia), pp. 1–6, May 2016.

[80] B. Lyu, T. Qi, H. Guo, and Z. Yang, "Throughput maximization in full-duplex dual-hop wireless powered communication networks," *IEEE Access*, vol. 7, pp. 158584–158593, Oct. 2019.

[81] Z. Yun and S. Han, "Demo abstract: RT-WPCN: A multi-hop real-time wireless powered communication network," in *IEEE 27th Real-Time and Embedded Technology and Applications Symposium (RTAS)*, (Nashville, TN, USA), pp. 526–527, May 2021.

[82] R. Du, A. Ozcelikkale, C. Fischione, and M. Xiao, "Towards immortal wireless sensor networks by optimal energy beamforming and data routing," *IEEE Transactions on Wireless Communications*, vol. 17, pp. 5338–5352, Aug. 2018.

[83] X. Liu, Z. Wen, D. Liu, J. Zou, and S. Li, "Joint source and relay beamforming design in wireless multi-hop sensor networks with SWIPT," *Sensors*, vol. 19, p. 182, Jan. 2019.

[84] S. Lee and R. Zhang, "Cognitive wireless powered network: Spectrum sharing models and throughput maximization," *IEEE Transactions on Cognitive Communications and Networking*, vol. 1, pp. 335–346, Sept. 2015.

[85] J. Kim, H. Lee, C. Song, T. Oh, and I. Lee, "Sum throughput maximization for multi-user MIMO cognitive wireless powered communication networks," *IEEE Transactions on Wireless Communications*, vol. 16, pp. 913–923, Feb. 2017.

[86] X. Lu, P. Wang, D. Niyato, and E. Hossain, "Dynamic spectrum access in cognitive radio networks with RF energy harvesting," *IEEE Wireless Communications*, vol. 21, pp. 102–110, June 2014.

[87] D. Jiang, X. Ying, Y. Han, and Z. Lv, "Collaborative multi-hop routing in cognitive wireless networks," *Wireless Personal Communications*, vol. 86, pp. 901–923, Sept. 2015.

[88] T. V. Nguyen, T.-N. Do, V. N. Q. Bao, D. B. da Costa, and B. An, "On the performance of multihop cognitive wireless powered d2d communications in WSNs," *IEEE Transactions on Vehicular Technology*, vol. 69, pp. 2684–2699, Mar. 2020.

[89] G. Zheng, Z. Ho, E. A. Jorswieck, and B. Ottersten, "Information and energy cooperation in cognitive radio networks," *IEEE Transactions on Signal Processing*, vol. 62, pp. 2290–2303, May 2014.

[90] C. Zhai, J. Liu, and L. Zheng, "Cooperative spectrum sharing with wireless energy harvesting in cognitive radio networks," *IEEE Transactions on Vehicular Technology*, vol. 65, pp. 5303–5316, July 2016.

[91] K.-W. Chin, "On energy and data delivery in wireless local area networks with RF charging nodes," in *27th International Telecommunication Networks*

and Applications Conference (ITNAC), (Melbourne, VIC, Australia), pp. 1–7, Nov. 2017.

[92] Y. Wang, K.-W. Chin, and S. Soh, "Link scheduling in wireless networks with RF energy harvesting nodes," *IEEE Transactions on Green Communications and Networking*, vol. 3, pp. 302–316, June 2019.

[93] M. Z. Sarwar and K.-W. Chin, "On supporting legacy and RF energy harvesting devices in two-tier OFDMA heterogeneous networks," *IEEE Access*, vol. 6, pp. 62538–62551, Oct. 2018.

[94] "The full-stack solution for all smart devices." https://csa-iot.org/all-solutions/zigbee/, May 2014.

[95] "Airfuel rf standard." https://airfuel.org/airfuel-rf/.

[96] P. Santi, R. Maheshwari, G. Resta, S. Das, and D. M. Blough, "Wireless link scheduling under a graded SINR interference model," in *Proceedings of the 2nd ACM international workshop on Foundations of wireless ad hoc and sensor networking and computing*, (New Orleans, Louisiana, USA), pp. 3–12, May 2009.

[97] M. Alicherry, R. Bhatia, and L. E. Li, "Joint channel assignment and routing for throughput optimization in multi-radio wireless mesh networks," in *Proceedings of the 11th annual international conference on Mobile computing and networking*, (Cologne Germany), pp. 58–72, Aug. 2005.

[98] J. Yuan, Z. Li, W. Yu, and B. Li, "A cross-layer optimization framework for multihop multicast in wireless mesh networks," *IEEE Journal on Selected Areas in Communications*, vol. 24, pp. 2092–2103, Nov. 2006.

[99] Y. Wang, W. Wang, X.-Y. Li, and W.-Z. Song, "Interference-aware joint routing and TDMA link scheduling for static wireless networks," *IEEE Transactions on Parallel and Distributed Systems*, vol. 19, pp. 1709–1726, Dec. 2008.

[100] X.-Y. Li, A. Nusairat, Y. Wu, Y. Qi, J. Zhao, X. Chu, and Y. Liu, "Joint throughput optimization for wireless mesh networks," *IEEE Transactions on Mobile Computing*, vol. 8, pp. 895–909, July 2009.

[101] F. Sivrikaya and B. Yener, "Minimum delay routing for wireless networks with STDMA," *Wireless Networks*, vol. 15, pp. 755–772, Oct. 2007.

[102] P. Cappanera, L. Lenzini, A. Lori, G. Stea, and G. Vaglini, "Optimal joint routing and link scheduling for real-time traffic in TDMA wireless mesh networks," *Computer Networks*, vol. 57, pp. 2301–2312, Aug. 2013.

[103] S. Kompella, J. E. Wieselthier, A. Ephremides, H. D. Sherali, and G. D. Nguyen, "On optimal SINR-based scheduling in multihop wireless networks," *IEEE/ACM Transactions on Networking*, vol. 18, pp. 1713–1724, Dec. 2010.

[104] Y. Sadi and S. C. Ergen, "Minimum length scheduling with packet traffic demands in wireless ad-hoc networks," *IEEE Transactions on Wireless Communications*, vol. 13, pp. 3738–3751, July 2014.

[105] M. Johansson and L. Xiao, "Cross-layer optimization of wireless networks using nonlinear column generation," *IEEE Transactions on Wireless Communications*, vol. 5, pp. 435–445, Feb. 2006.

[106] M. Sanchez, J. Zander, and T. Giles, "Combined routing and scheduling for spatial TDMA in multihop ad hoc networks," in *The 5th International Symposium on Wireless Personal Multimedia Communications*, (Honolulu, HI, USA), pp. 781–785, Oct. 2002.

[107] W. Wang, X. Liu, and D. Krishnaswamy, "Robust routing and scheduling in wireless mesh networks under dynamic traffic conditions," *IEEE Transactions on Mobile Computing*, vol. 8, pp. 1705–1717, Dec. 2009.

[108] J. Luo, A. Iyer, and C. Rosenberg, "Throughput-lifetime trade-offs in multihop

wireless networks under an SINR-based interference model," *IEEE Transactions on Mobile Computing*, vol. 10, pp. 419–433, Mar. 2011.

[109] C. Buratti and R. Verdone, "Joint scheduling and routing with power control for centralized wireless sensor networks," *Wireless Networks*, vol. 24, pp. 1699–1714, Dec. 2016.

[110] R. Cruz and A. Santhanam, "Optimal routing, link scheduling and power control in multihop wireless networks," in *IEEE INFOCOM. Twenty-second Annual Joint Conference of the IEEE Computer and Communications Societies (IEEE Cat. No.03CH37428)*, (San Francisco, CA, USA), pp. 702–711, Mar. 2003.

[111] R. Bhatia and M. Kodialam, "On power efficient communication over multi-hop wireless networks: joint routing, scheduling and power control," in *IEEE INFOCOM*, (Hong Kong, China), pp. 1457–1466, Mar. 2004.

[112] P. Gupta and P. Kumar, "The capacity of wireless networks," *IEEE Transactions on Information Theory*, vol. 46, pp. 388–404, Mar. 2000.

[113] S. Jafar and M. Fakhereddin, "Degrees of freedom for the MIMO interference channel," *IEEE Transactions on Information Theory*, vol. 53, pp. 2637–2642, July 2007.

[114] M. Cheng, Q. Ye, and X. Cheng, "Simultaneous routing and multiplexing in ad hoc networks with MIMO links," in *IEEE International Conference on Communications (ICC)*, (Budapest, Hungary), pp. 1414–1418, June 2013.

[115] B. Zhang, X. Jia, K. Yang, and R. Xie, "Multi-path routing and stream scheduling with spatial multiplexing and interference cancellation in MIMO networks," in *IEEE 33rd International Conference on Distributed Computing Systems Workshops*, (Philadelphia, PA, USA), pp. 256–261, July 2013.

[116] H. Wang, K.-W. Chin, and S. Soh, "On minimizing data forwarding schedule in multi transmit/receive wireless mesh networks," *IEEE Access*, vol. 4, pp. 1570–1582, Apr. 2016.

[117] M. Bansal and A. Trivedi, "Cross-layer design of multi-radio multi-channel capable MIMO-based WMNs," in *IEEE Wireless Communications and Networking Conference (WCNC)*, (Paris, France), pp. 1686–1691, Apr. 2012.

[118] R. Bhatia and L. Li, "Throughput optimization of wireless mesh networks with MIMO links," in *26th IEEE International Conference on Computer Communications*, (Anchorage, AK, USA), pp. 2326–2330, May 2007.

[119] X. Qin, X. Yuan, Y. Shi, Y. T. Hou, W. Lou, and S. F. Midkiff, "Joint flow routing and DoF allocation in multihop MIMO networks," *IEEE Transactions on Wireless Communications*, vol. 15, pp. 1907–1922, Mar. 2016.

[120] M. Bansal and A. Trivedi, "Fair rate allocation, routing, and stream control scheduling in MIMO-based WMNs," in *National Conference on Communications (NCC)*, (Kharagpur, India), pp. 1–5, Feb. 2012.

[121] L. Luo, D. Raychaudhuri, and H. Liu, "Channel assignment, stream control, scheduling and routing in multi-radio MIMO wireless mesh networks," in *IEEE International Conference on Communications Workshops*, (Dresden, Germany), pp. 1–5, June 2009.

[122] P. Wang, J. Matyjas, and M. Medley, "Resource allocation in MIMO-based ad hoc networks," in *45th Annual Conference on Information Sciences and Systems*, (Baltimore, MD, USA), pp. 1–6, Mar. 2011.

[123] H. Vangala, R. Meshram, and V. Sharma, "Joint routing, scheduling and power control in multihop MIMO networks with MAC and broadcast links," in *IEEE Wireless Communications and Networking Conference (WCNC)*, (Paris, France), pp. 2582–2587, Apr. 2012.

[124] Y.-H. Lin, T. Javidi, R. L. Cruz, and L. B. Milstein, "Distributed link scheduling, power control and routing for multi-hop wireless MIMO networks," in *Fortieth Asilomar Conference on Signals, Systems and Computers*, (Pacific Grove, CA, USA), pp. 122–126, Nov. 2006.

[125] H. Kordbacheh, H. D. Oskouei, and N. Mokari, "Robust cross-layer routing and radio resource allocation in massive multiple antenna and OFDMA-based wireless ad-hoc networks," *IEEE Access*, vol. 7, pp. 36527–36539, Mar. 2019.

[126] K.-W. Chin, L. Wang, and S. Soh, "Joint routing and links scheduling in two-tier multi-hop RF-energy harvesting networks," *IEEE Communications Letters*, vol. 20, pp. 1864–1867, Sept. 2016.

[127] C. Zhao, S. Chen, C. Wu, F. Chen, and Y. Ji, "Accelerated sampling optimization for RF energy harvesting wireless sensor network," *IEEE Access*, vol. 6, pp. 52161–52168, Sept. 2018.

[128] R. Doost, K. R. Chowdhury, and M. D. Felice, "Routing and link layer protocol design for sensor networks with wireless energy transfer," in *IEEE Global Telecommunications Conference GLOBECOM*, (Miami, FL, USA), pp. 1–5, Dec. 2010.

[129] L. Huang and M. J. Neely, "Utility optimal scheduling in energy harvesting networks," in *Proceedings of the Twelfth ACM International Symposium on Mobile Ad Hoc Networking and Computing - MobiHoc '11*, (Paris France), pp. 1–11, May 2011.

[130] H.-T. Roh and J.-W. Lee, "Cross-layer optimization for wireless sensor networks with RF energy transfer," in *International Conference on Information and Communication Technology Convergence (ICTC)*, (Busan, Korea (South)), pp. 122–126, Oct. 2014.

[131] T. He, K.-W. Chin, and S. Soh, “On maximizing min flow rates in rechargeable wireless sensor networks,” *IEEE Transactions on Industrial Informatics*, vol. 14, pp. 2962–2972, July 2018.

[132] T. He, K.-W. Chin, S. Soh, C. Yang, and J. Wen, “On maximizing max–min source rate in wireless-powered internet of things,” *IEEE Internet of Things Journal*, vol. 7, pp. 11276–11289, Nov. 2020.

[133] T. He, K.-W. Chin, S. Soh, and Z. Zhang, “A novel distributed resource allocation scheme for wireless-powered cognitive radio internet of things networks,” *IEEE Internet of Things Journal*, vol. 8, pp. 15486–15499, Oct. 2021.

[134] C. Wen, B. Zhu, and Y. Zhu, “JBRC: Jointly balanced routing and charging scheme for RF energy harvesting wireless sensor networks,” in *21st Asia-Pacific Network Operations and Management Symposium (APNOMS)*, (Daegu, Korea (South)), pp. 91–95, Sept. 2020.

[135] P. Movva, K. K. Kamarajugadda, and T. R. Polipalli, “An energy aware cluster-based routing and adaptive semi-synchronized MAC for energy harvesting WSN,” *International Journal of Communication Systems*, vol. 35, May 2022.

[136] M. Pierobon, J. M. Jornet, N. Akkari, S. Almasri, and I. F. Akyildiz, “A routing framework for energy harvesting wireless nanosensor networks in the terahertz band,” *Wireless Networks*, vol. 20, pp. 1169–1183, Nov. 2013.

[137] E. M. Royer and C. E. Perkins, “Ad-hoc on-demand distance vector routing,” in *Proceedings of the 2nd IEEE Workshop on Mobile Computing Systems and Applications*, vol. 2, (New Orleans, LA, USA), pp. 90–100, Feb. 1999.

[138] Y. Wang, S. Yan, W. Yang, Y. Huang, and C. Liu, “Energy-efficient covert communications for bistatic backscatter systems,” *IEEE Transactions on Vehicular Technology*, vol. 70, pp. 2906–2911, Mar. 2021.

[139] C. Perez-Penichet, D. Piumwardane, C. Rohner, and T. Voigt, "A fast carrier scheduling algorithm for battery-free sensor tags in commodity wireless networks," in *IEEE INFOCOM-IEEE Conference on Computer Communications*, (Toronto, ON, Canada), pp. 994–1003, July 2020.

[140] C. Perez-Penichet, D. Piumwardane, C. Rohner, and T. Voigt, "TagAlong: Efficient integration of battery-free sensor tags in standard wireless networks," in *19th ACM/IEEE International Conference on Information Processing in Sensor Networks (IPSN)*, (Sydney, NSW, Australia), pp. 169–180, Apr. 2020.

[141] X. Liu, Y. Gao, and F. Hu, "Optimal time scheduling scheme for wireless powered ambient backscatter communications in IoT networks," *IEEE Internet of Things Journal*, vol. 6, pp. 2264–2272, Apr. 2019.

[142] F. Jameel, T. Ristaniemi, I. Khan, and B. M. Lee, "Simultaneous harvest-and-transmit ambient backscatter communications under rayleigh fading," *EURASIP Journal on Wireless Communications and Networking*, vol. 2019, June 2019.

[143] X. Cao, Z. Song, B. Yang, M. A. Elmossallamy, L. Qian, and Z. Han, "A distributed ambient backscatter MAC protocol for internet-of-things networks," *IEEE Internet of Things Journal*, vol. 7, pp. 1488–1501, Feb. 2020.

[144] G. Yang, D. Yuan, Y.-C. Liang, R. Zhang, and V. C. M. Leung, "Optimal resource allocation in full-duplex ambient backscatter communication networks for wireless-powered IoT," *IEEE Internet of Things Journal*, vol. 6, pp. 2612–2625, Apr. 2019.

[145] M. J. Kim, J. Kim, and S. M. Kim, "Multi-tag selection in cognitive ambient backscatter communications for next-generation IoT networks," *Wireless Communications and Mobile Computing*, vol. 2022, pp. 1–12, Jan. 2022.

[146] D. Li, W. Peng, and F. Hu, "Capacity of backscatter communication systems with tag selection," *IEEE Transactions on Vehicular Technology*, vol. 68, pp. 10311–10314, Oct. 2019.

[147] D. Li, "Fairness-based multiuser scheduling for ambient backscatter communication systems," *IEEE Wireless Communications Letters*, vol. 9, pp. 1150–1154, Aug. 2020.

[148] P. Hou, J. Gong, and J. Zhao, "A physical layer security enhancement scheme under the ambient backscatter system," *Symmetry*, vol. 13, no. 1, 2021.

[149] G. Maselli, M. Piva, and J. A. Stankovic, "Adaptive communication for battery-free devices in smart homes," *IEEE Internet of Things Journal*, vol. 6, pp. 6977–6988, Aug. 2019.

[150] A. H. Halbouni, M. A. B. A. Ghani, and M. H. Habaebi, "Aloha-NOMA for ambient backscatter m2m communication in IoT networks with random power levels and frequency channel assignment," in *IEEE 7th International Conference on Smart Instrumentation, Measurement and Applications (ICSIMA)*, (Bandung, Indonesia), pp. 111–116, Aug. 2021.

[151] B. Ji, B. Xing, K. Song, C. Li, H. Wen, and L. Yang, "The efficient BackFi transmission design in ambient backscatter communication systems for IoT," *IEEE Access*, vol. 7, pp. 31397–31408, Feb. 2019.

[152] "Epc uhf gen2 air interface protocol." https://www.gs1.org/sites/default/files/docs/epc/gs1-epc-gen2v2-uhf-airinterface_i21_r_2018-09-04.pdf, July 2018.

[153] "Iso/iec 18000-6:2013." https://www.iso.org/standard/59644.html, Jan. 2013.

[154] P. V. Nikitin, S. Ramamurthy, R. Martinez, and K. V. S. Rao, "Passive tag-

to-tag communication," in *IEEE International Conference on RFID (RFID)*, (Orlando, FL, USA), pp. 177–184, Apr. 2012.

[155] A. Ahmad, X. Sha, A. Athalye, S. Das, P. Djuric, and M. Stanacevic, "Collaborative backscatter based on phase channel estimation in passive RF tag networks," in *IEEE International Conference on RFID Technology and Applications (RFID-TA)*, (Delhi, India), pp. 128–131, Oct. 2021.

[156] C. Liu and Z. J. Haas, "Routing protocol design in tag-to-tag networks with capability-enhanced passive tags," in *IEEE 28th Annual International Symposium on Personal, Indoor, and Mobile Radio Communications (PIMRC)*, (Montreal, QC, Canada), pp. 1–6, Oct. 2017.

[157] Y. Liu, P. Ren, and Q. Du, "Cooperative routing and transmission over multi-hop network of RFID tags," in *IEEE 94th Vehicular Technology Conference (VTC2021-Fall)*, (Norman, OK, USA), pp. 1–5, Sept. 2021.

[158] J. Zhao, W. Gong, and J. Liu, "X-tandem: Towards multi-hop backscatter communication with commodity WiFi," in *Proceedings of the 24th Annual International Conference on Mobile Computing and Networking*, (New Delhi India), pp. 497–511, Oct. 2018.

[159] H. Niu and S. Jagannathan, "A cross layer routing scheme for passive RFID tag-to-tag communication," in *39th Annual IEEE Conference on Local Computer Networks*, (Edmonton, AB, Canada), pp. 438–441, Sept. 2014.

[160] D. Li, W. Peng, and Y.-C. Liang, "Hybrid ambient backscatter communication systems with harvest-then-transmit protocols," *IEEE Access*, vol. 6, pp. 45288–45298, Aug. 2018.

[161] B. Lyu, Z. Yang, G. Gui, and Y. Feng, "Wireless powered communication networks assisted by backscatter communication," *IEEE Access*, vol. 5, pp. 7254–7262, Mar. 2017.

[162] Y. Liu, K.-W. Chin, and C. Yang, "Maximizing sampling data upload in ambient backscatter-assisted wireless-powered networks," *IEEE Internet of Things Journal*, vol. 8, pp. 12266–12278, Aug. 2021.

[163] Y. Long, G. Huang, D. Tang, S. Zhao, and G. Liu, "Achieving high throughput in wireless networks with hybrid backscatter and wireless-powered communications," *IEEE Internet of Things Journal*, vol. 8, pp. 10896–10910, July 2021.

[164] S. Gong, L. Gao, J. Xu, Y. Guo, D. T. Hoang, and D. Niyato, "Exploiting backscatter-aided relay communications with hybrid access model in device-to-device networks," *IEEE Transactions on Cognitive Communications and Networking*, vol. 5, pp. 835–848, Dec. 2019.

[165] J. Xu, J. Li, S. Gong, K. Zhu, and D. Niyato, "Passive relaying game for wireless powered internet of things in backscatter-aided hybrid radio networks," *IEEE Internet of Things Journal*, vol. 6, no. 5, pp. 8933–8944, 2019.

[166] Y. Zhuang, X. Li, H. Ji, H. Zhang, and V. C. M. Leung, "Optimal resource allocation for RF-powered underlay cognitive radio networks with ambient backscatter communication," *IEEE Transactions on Vehicular Technology*, vol. 69, pp. 15216–15228, Dec. 2020.

[167] S. Xiao, H. Guo, and Y.-C. Liang, "Resource allocation for full-duplex-enabled cognitive backscatter networks," *IEEE Transactions on Wireless Communications*, vol. 18, pp. 3222–3235, June 2019.

[168] T. T. Anh, N. C. Luong, D. Niyato, Y.-C. Liang, and D. I. Kim, "Deep reinforcement learning for time scheduling in RF-powered backscatter cognitive radio networks," in *IEEE Wireless Communications and Networking Conference (WCNC)*, (Marrakesh, Morocco), pp. 1–7, Apr. 2019.

[169] N. V. Huynh, D. T. Hoang, D. N. Nguyen, E. Dutkiewicz, D. Niyato, and P. Wang, "Optimal and low-complexity dynamic spectrum access for RF-

powered ambient backscatter system with online reinforcement learning," *IEEE Transactions on Communications*, vol. 67, pp. 5736–5752, Aug. 2019.

[170] W. Wang, D. T. Hoang, D. Niyato, P. Wang, and D. I. Kim, "Stackelberg game for distributed time scheduling in RF-powered backscatter cognitive radio networks," *IEEE Transactions on Wireless Communications*, vol. 17, pp. 5606–5622, Aug. 2018.

[171] D. T. Hoang, D. Niyato, P. Wang, D. I. Kim, and Z. Han, "The tradeoff analysis in RF-powered backscatter cognitive radio networks," in *IEEE Global Communications Conference (GLOBECOM)*, (Washington, DC, USA), pp. 1–6, Dec. 2016.

[172] R. Kishore, S. Gurugopinath, P. C. Sofotasios, S. Muhaidat, and N. Al-Dhahir, "Opportunistic ambient backscatter communication in RF-powered cognitive radio networks," *IEEE Transactions on Cognitive Communications and Networking*, vol. 5, pp. 413–426, June 2019.

[173] Z. Yao, Y. Wang, J. Ba, J. Zong, S. Feng, and Z. Wu, "Deadline-aware and energy-efficient dynamic flow scheduling in data center network," in *13th International Conference on Network and Service Management (CNSM)*, (Tokyo, Japan), pp. 1–4, Nov. 2017.

[174] J. Liu, B. Zhao, Q. Xin, J. Su, and W. Ou, "DRL-ER: An intelligent energy-aware routing protocol with guaranteed delay bounds in satellite mega-constellations," *IEEE Transactions on Network Science and Engineering*, vol. 8, pp. 2872–2884, Oct. 2021.

[175] Y. Zhou, E. C.-H. Ngai, M. R. Lyu, and J. Liu, "POWER-SPEED: A power-controlled real-time data transport protocol for wireless sensor-actuator networks," in *IEEE Wireless Communications and Networking Conference*, (Hong Kong, China), pp. 3736–3740, Mar. 2007.

[176] O. Chipara, Z. He, G. Xing, Q. Chen, X. Wang, C. Lu, J. Stankovic, and T. Abdelzaher, "Real-time power-aware routing in sensor networks," in *14th IEEE International Workshop on Quality of Service*, (New Haven, CT, USA), pp. 83–92, June 2006.

[177] J. Heo, J. Hong, and Y. Cho, "EARQ: Energy aware routing for real-time and reliable communication in wireless industrial sensor networks," *IEEE Transactions on Industrial Informatics*, vol. 5, pp. 3–11, Feb. 2009.

[178] "802.15.4-2015 - ieee standard for low-rate wireless networks." https://ieeexplore.ieee.org/document/7460875, Apr. 2016.

[179] Z. Shelby and C. Bormann, *6LoWPAN: The wireless embedded Internet*. John Wiley & Sons, 2011.

[180] J. Lou, X. Yuan, S. Kompella, and N.-F. Tzeng, "Boosting or hindering: AoI and throughput interrelation in routing-aware multi-hop wireless networks," *IEEE/ACM Transactions on Networking*, vol. 29, pp. 1008–1021, June 2021.

[181] A. Arafa and S. Ulukus, "Age-minimal transmission in energy harvesting two-hop networks," in *In IEEE Global Communications Conference*, (Singapore), pp. 1–6, Dec. 2017.

[182] K. Chen, F. Benkhelifa, H. Gao, J. A. McCann, and J. Li, "Minimizing age of information in multihop energy-harvesting wireless sensor network," *IEEE Internet of Things Journal*, vol. 9, pp. 25736–25751, Dec. 2022.

[183] T. He, K.-W. Chin, Z. Zhang, T. Liu, and J. Wen, "Optimizing information freshness in RF-powered multi-hop wireless networks," *IEEE Transactions on Wireless Communications*, vol. 21, pp. 7135–7147, Sept. 2022.

[184] M. A. Abd-Elmagid, N. Pappas, and H. S. Dhillon, "On the role of age of information in the internet of things," *IEEE Communications Magazine*, vol. 57, pp. 72–77, Dec. 2019.

[185] Z. Zou, P. Soldati, H. Zhang, and M. Johansson, "Energy-efficient deadline-constrained maximum reliability forwarding in lossy networks," *IEEE Transactions on Wireless Communications*, vol. 11, pp. 3474–3483, Oct. 2012.

[186] X. Lu, P. Wang, D. Niyato, D. I. Kim, and Z. Han, "Wireless networks with RF energy harvesting: A contemporary survey," *IEEE Communications Surveys and Tutorials*, vol. 17, no. 2, pp. 757–789, 2015.

[187] S. Lee and R. Zhang, "Cognitive wireless powered network: Spectrum sharing models and throughput maximization," *IEEE Transactions on Cognitive Communications and Networking*, vol. 1, pp. 335–346, Sept. 2015.

[188] S. Borbash and A. Ephremides, "Wireless link scheduling with power control and SINR constraints," *IEEE Transactions on Information Theory*, vol. 52, pp. 5106–5111, Nov. 2006.

[189] I. T. Haque and N. Abu-Ghazaleh, "Wireless software defined networking: A survey and taxonomy," *IEEE Communications Surveys and Tutorials*, vol. 18, pp. 2713 – 2737, May 2016.

[190] "Gurobi optimizer reference manual." https://www.gurobi.com/, 2022.

[191] F. A.Potra and S. J.Wright, "Interior-point methods," *Journal of Computational and Applied Mathematics*, vol. 124, pp. 281–302, Dec. 2000.

[192] L. PowerCast, "Powercast pcc114 powerharvester receiver data sheet (2018)." https://www.powercastco.com/, 2018.

[193] P.-J. Wan, O. Frieder, X. Jia, F. Yao, X. Xu, and S. Tang, "Wireless link scheduling under physical interference model," in *IEEE INFOCOM*, (Shanghai, China), pp. 1–10, Apr. 2011.

[194] K. Chin, S. Soh, and C. Meng, "Novel scheduling algorithms for concurrent transmit/receive wireless mesh networks," *Elsevier Computer Networks*, vol. 56, pp. 1200–1214, Mar. 2012.

[195] S. Barré, C. Paasch, and O. Bonaventure., "Multipath TCP: From theory to practice.," in *IEEE 21st International Conference on Advanced Information Networking and Applications Workshops*, (Valenncia, Spain), pp. 1–7, May 2011.

[196] "Cisco wireless mesh access points design deployment guide release 7.3 x." https://www.cisco.com/c/en/us/td/docs/wireless/technology/mesh/7-3/design/guide/Mesh.pdf., Aug. 2012.

[197] D. Bharadia, K. Joshi, M. Kotaru, and S. Katti, "High throughput WiFi backscatter," in *ACM SIGCOMM Computer Communication Review*, (London, United Kingdom), pp. 17–21, Aug. 2015.

[198] J. Tang, G. Xue, C. Chandler, and W. Zhang, "Link scheduling with power control for throughput enhancement in multihop wireless networks," *IEEE Transactions on Vehicular Technology*, vol. 55, pp. 733–742, May 2006.

[199] T. ElBatt and A. Ephremides, "Joint scheduling and power control for wireless ad hoc networks," *IEEE Transactions on Wireless communications*, vol. 3, pp. 74–85, Jan. 2004.

[200] C. Yang, K.-W. Chin, and Y. Liu, "On maximizing sampling time of RF-harvesting sensor nodes over random channel gains," in *IEEE International Conference on Communications*, (Kansas City, MO, USA), pp. 1–7, May 2018.

[201] H.-S. Lee and J.-W. Lee, "Contextual learning-based wireless power transfer beam scheduling for IoT devices," *IEEE Internet of Things Journal*, vol. 6, pp. 9606–9620, Dec. 2019.

[202] E. Boshkovska, D. W. K. Ng, N. Zlatanov, A. Koelpin, and R. Schober, "Robust resource allocation for MIMO wireless powered communication networks based on a non-linear EH model," *IEEE Transactions on Wireless communications*, vol. 65, pp. 1984–1999, May 2017.

[203] C. Frenzen, T. Sasao, and J. T. Butler, "On the number of segments needed in a piecewise linear approximation," *Journal of Computational and Applied Mathematics*, vol. 234, pp. 437–446, May 2010.

[204] A. Charnes and W. W. Cooper, "Chance-constrained programming," *Manag. Sci.*, vol. 6, pp. 73–79, October 1959.

[205] A. Hammoudeh and L. Al-Sharif, "Estimating the elevator traffic system arrival rate using exponentially weighted moving average (EWMA)," in *IEEE Jordan Conference on Applied Electrical Engineering and Computing Technologies*, (Aqaba, Jordan), pp. 1–5, Oct. 2017.

[206] B. Shahriari, K. Swersky, Z. Wang, R. P. Adams, and N. de Freitas, "Taking the human out of the loop: A review of bayesian optimization," *Proceedings of the IEEE*, vol. 104, pp. 148–175, Jan. 2016.

[207] C. E. Rasmussen and C. K. I. Williams, *Gaussian Processes for Machine Learning*. Cambridge, MA, USA: MIT press, 2005.

[208] J. Mockus, V. Tiesis, and A. Zilinskas, "The application of bayesian methods for seeking the extremum," *Towards Global Optimisation*, vol. 2, no. 2, pp. 117–129, 1978.

[209] "Waspmote datasheet." http://Waspwww.libelium.com/downloads/documentation/waspmote_datasheet.pdf., Mar. 2018.

[210] S. Chen, J. Yao, and Y. Wu, "Analysis of the power consumption for wireless sensor network node based on Zigbee," *Procedia Engineering*, vol. 29, pp. 1994–1998, Feb. 2012.